UNIVERSITÀ
DEGLI STUDI
DI PADOVA

Head Office: Università degli Studi di Padova

Center:

Centro di Ateneo di Studi e Attività Spaziali "Giuseppe Colombo" CISAS

Ph.D. COURSE IN: Scienze, Tecnologie e Misure Spaziali
CURRICULUM: Scienze e Tecnologie per Applicazioni Satellitari e Aeronautiche (STASA)
SERIES XXXI

Discontinuous mechanical problems studied with a Peridynamics-based approach

Thesis written with the financial contribution of "FONDAZIONE CARIPARO"

Coordinator: Ch.mo Prof. Giampiero Naletto
Supervisor: Ch.mo Prof. Ugo Galvanetto
Co-Supervisor: Ch.mo Prof. Mirco Zaccariotto

Ph.D. student : Soheil Bazazzadeh

To my parents,

without whom none of my success would be possible

SUMMARY

The classical theory of solid mechanics is rooted in the assumption of a continuous distribution of mass within a body. It employs partial differential equations (PDEs) with significant smoothness to obtain displacements and internal forces of the body. Although classical theory has been applied to wide range of engineering problems, PDEs of the classical theory cannot be applied directly on a discontinuity such as cracks. Peridynamics is considered to be an alternative and promising nonlocal theory of solid mechanics that, by replacing PDEs of classical theory with integral or integro-differential equations, attempts to unite the mathematical modelling of continuous media, cracks and particles within a single framework. Indeed, the equations of peridynamic are based on the direct interaction of material points over finite distances. Another concept, derived from the peridynamic approach to cope with engineering problems with discontinuities, is that of the peridynamic differential operator (PDDO). The PDDO uses the non-local interaction of the material points in a way similar to that of peridynamics. PDDO is capable to recast partial derivatives of a function through a nonlocal integral operator whose kernel is free of using any correction function. In this dissertation, application of peridaynamics and PDDO, to three different important engineering problems including fatigue fracture, thermo-mechanics and sloshing phenomena, is examined comprehensively.

To cope with fatigue fracture problems, an algorithm has been developed in such a way that the increment of damage due to fatigue is added to that due to the static increment of the opening displacement. A one degree of freedom cylinder model has been used to carry out an efficient comparison of the computational performance of three fatigue degradation strategies. The three laws have been implemented in a code using bond based peridynamics (BBPD) to

simulate fatigue crack propagation. Both the cylinder model and the bond base peridynamics code provide the same assessment of the three fatigue degradation strategies.

To deal with thermo-mechanical problems, an effective way is proposed to use a variable grid size in a weakly coupled thermal shock peridynamic model. The proposed numerical method is equipped with stretch control criterion to transform the grid discretization adaptively in time. Hence, finer grid spacing is only applied in limited zones where it is required. This method is capable of predicting complex crack patterns in the model. By introducing fine grid discretization over the boundaries of the model the surface (softening) effect can be reduced. The accuracy and performance of the model are examined through problems such as thermo-elastic and thermal-shock induced fracture in ceramics.

Finally to investigate sloshing phenomena, the PDDO has been applied to the solution of problems of liquid sloshing in 2D and 3D tanks with potential flow theory and Lagrangian description. Moreover, liquid sloshing in rectangular tanks containing horizontal and vertical baffles are investigated to examine the robustness and accuracy of PDDO. With respect to other approaches such as meshless local Petrov-Galerkin (MLPG), volume of fluid (VOF) and and local polynomial collocation methods the examples are solved with a coarser grid of nodes. Using this new approach, one is able to obtain results with a high accuracy and low computational cost.

Publications

Articles

• **Bazazzadeh, S.,** Shojaei, A., Zaccariotto, M., Galvanetto, U., **"Application of the Peridynamic differential operator to the solution of sloshing problems in tanks"** Engineering computations. (In press DOI (10.1108/EC-12-2017-0520).

• Zaccariotto, M., Sarego, G., Dipasquale, D., Shojaei, A., **Bazazzadeh, S.,** Mudric, T., Duzzi, M. and Galvanetto, U., **"Discontinuous mechanical problems studied with a peridynamics-based approach"** Aerotecnica Missili & Spazio, The Journal of Aerospace Science, Technology and Systems 96 (2017): 54-67.

• **Bazazzadeh, S.,** Zaccariotto, M., Galvanetto, U., **"Fatigue degradation strategies to simulate crack propa-gation using peridynamic based computational methods "** Latin American journal of solid and structures. (Under review).

• **Bazazzadeh, S.,** Mossaiby, F., Zaccariotto, M., Galvanetto, U. "**Simulation of thermo-mechanical problems in ceramics using an adaptive multi-grid peridynamic method**". (In preparation)

Conferences

• **Bazazzadeh, S**., Shojaei, A., Zaccariotto, M**.**, Galvanetto, U., **Simulation of 3D nonlinear sloshing in tanks by Peridynamic differential operator mesh-free method**. 10th International Conference Engineering Computational Technology, Sitges, Barcelona, Spain, Sep 4-6, 2018.

• **Bazazzadeh, S**., Shojaei, A., Zaccariotto, M**.**, Galvanetto, U., **Simulation of two-dimensional sloshing phenomenon by Peridynamic differential operator mesh-free method**. 10th European solid mechanics conference, Bologna, Italy, July 2-6, 2018.

• Zaccariotto, M., Shojaei, A,. Ni, T,. **Bazazzadeh, S.,** Ongaro, G., Dal Pozzolo, M., Galvanetto U., **Crack propagation problems studied with a peridynamics-based approach**. 28th International Workshop on Computational Mechanics of Materials, Glasgow, UK Sep 10 – 12, 2018.

• **Bazazzadeh, S**., Zaccariotto, M**.**, Galvanetto, U., **A simple assesment of damage under high-cycle fatigue-driven delamination** .14th International Conference on Fracture, Rhodes, Greece, June 18-23, 2017.

• **Bazazzadeh, S**., Zaccariotto, M**.**, Galvanetto, U., **Determination of the fatigue damage in delamination of composite materials**.16th International Conference on New Trends in Fatigue and Fracture Dubrovnik, Croatia, May 24 - 27, 2016.

- Galvanetto, U**.,** Zaccariotto, M**.**, Mudric, T., Shojaei, A., **Bazazzadeh, S.,** Tomasi, D., **"A Simple Way to Couple Peridynamic Grids to FEM Meshes for the Solution of Static Problems**" International Mechanical Engineering Congress and Exposition Phoenix, Ariz, USA, Nov 11 - 17, 2016.

Acknowledgements

Firstly, I would like to express my sincere gratitude to my supervisor Prof. Ugo Galvanetto and my co-supervisor Prof. Mirco Zaccariotto for the continuous support of my Ph.D study and related research, for their patience, motivation, and immense knowledge. Their guidance helped me in all the time of research and writing of this thesis. I could not have imagined having a better advisor and mentor for my Ph.D study.

I must express my gratitude to Prof. Bijan Boroomand and Prof. Farshid Mossaiby for their useful suggestions. Their helps played a key role in some parts of my research.

A special thanks to my family. Words cannot express how grateful I am to my father, mother, and my sister for all of the sacrifices that they have made on my behalf. They have regularly encouraged me to believe in myself.

I would also like to thank all of my friends Arman, Greta, Mattia, Giulia, Daniele, Teo, Tao, Novella, Ashkan and Hasan who supported me in writing, and encourage me to strive towards my goal.

Finally, I would like to thank the University of Padua, not only for providing the CARIPARO funding which allowed me to undertake this research, but also for giving me the opportunity to attend conferences and meet so many interesting people.

Table of acronyms

Partial differential equations	PDEs
Peridynamic differential operator	PDDO
Bond based peridynamics	BBPD or BB-PD
State-based peridynamic	SB-PD
Ordinary state based peridynamics	OSB-PD
Non-ordinary state based peridynamics	NOSB-PD
Meshless local Petrov-Galerkin	MLPG
Volume of fluid	VOF
Linear elastic fracture mechanics	LEFM
Finite element method	FEM
Boundary element method	BEM
Extended finite element method	XFEM
Cohesive zone model	CZM
Computational fluid dynamics	CFD
Arbitrary Lagrangian–Eulerian	ALE
Radial basis function collocation method	RBFCM
Exponential basis functions	EBFs
Smoothed Particle Hydrodynamics	SPH
Reproducing Kernel Particle Method	RKPM
Generalized Finite Difference Method	GFDM
Moving least-squares	MLS
Prototype microelastic brittle	PMB
Dynamic free surface boundary conditions	DFSBC

Chapter 1 Introduction

Natural phenomena are often described by partial differential equations, which assume the continuity of both the unknowns and the field domain where the equations are defined. Such assumptions break down when simulation of problems containing discontinuities, such as cracks, comes into the picture.

In this chapter, a brief review on the literature of various topics, related to the discontinuity in engineering problems, is investigated. Then, the advantages and disadvantages of several major approaches to solve engineering problems with discontinuity, in particular those aimed at modeling fatigue fracture, thermo-mechanical and sloshing phenomena are discussed.

1.1 Fatigue phenomena in structural mechanics

Until a few decades ago, machines and components only were designed based on classical methods of strength calculation. In spite of precise calculation, damage occurred repeatedly in aircraft and aerospace structures, ships, rail vehicles and reactor components with catastrophic consequences. Sensational events such as crashes of Comet aircraft in 1953 and 1954 (Blumenauer and Pusch 1993) and recently, the catastrophic Aloha Airlines accident,

(Fig.(1.1)) have shown that considerably more research is needed with respect to the safe design of machines, components and structures.

Figure 1.1. Destruction of the canopy due to material fatigue during an Aloha Airlines flight in 1988 (Richard and Sander 2016).

Fatigue is a weakening process of a component, which is subjected to fluctuating stresses, at stress levels much lower than its monotonic fracture strength. Fatigue is categorized as a time-dependent failure that may happen without any recognisable warning. In fact, 95 percent of all mechanical failures are attributed to the fatigue phenomenon (Richard and Sander 2016).

Therefore, fatigue is a major cause of structural failure in engineering structures. Prediction of fracture propagation under cyclic loading is a challenging problem for two main reasons: from a theoretical point of view the discontinuous nature of fracture phenomena conflicts with the underlying mathematical structure of classical continuum mechanics, and from a more practical side the slow damaging effect of a large number of load cycles (high cycle fatigue) is not easy to model. Fatigue failure generally is divided into three distinct phases, namely: crack initiation, incremental crack growth, and the final fracture.

Basically, theoretical models to describe the fatigue phenomenon are categorised into three different classes: fatigue-life models, phenomenological models, and progressive damage models. (Degrieck and Van Paepegem 2001) . Fatigue-life models use cyclic stress amplitude VS number of cycles to failure (S-N) curves to predict fatigue life without consideration of crack initiation and propagation. Phenomenological models describe the degradation of macroscopically observable material properties due to fatigue loading and progressive damage models take into account the actual underlying damage mechanisms to predict fatigue degradation of the continuum.

The classical approach to fatigue problems, also referred to as Stress Controlled Fatigue or High Cycle Fatigue, provides information about material behaviour under cyclic loads through S-N or Wöhler diagrams. This diagram is generated by fatigue tests made on cylindrical test bars. This approach is based on the *safe life* philosophy for designing against fatigue fracture; hence, the number of the stress cycles to failure can be estimated through it. Although S-N curves have been applied for numerous fatigue failure analyses, they have some shortcomings. The major drawback of these curves is that they are obtained by testing standard specimens under laboratory conditions. Therefore, the tests are not completely capable of capturing the manufacturing defects. Moreover, obtaining these curves for High Cycle Fatigue is time-consuming and expensive. A typical example of S-N (Wöhler) diagrams is given below.

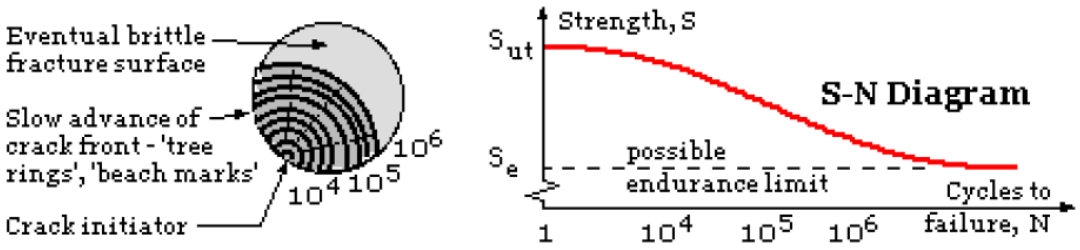

Figure 1.2. A typical example of S-N (Wöhler) diagrams (Richard and Sander 2016).

Generally, fracture and damage are due to the small defects or cracks that are already in the components, e.g. manufacture faults or arise later as a result of imposing service loads. The size of these cracks might grow and thus lead to the second or third stage of fatigue, fracture growth or failure of the whole structure.

For processes of crack propagation, the conditions directly at the crack tip are significant. Based on classical continuum theory, infinite (singular) stresses emerge at crack tips (Griffith 1921). This conclusion underpinned the concept of Linear Elastic Fracture Mechanics (LEFM).

Based on LEFM, pre-existing crack is essential to consider the crack growth in a material. By using additional criteria such as critical energy release rate or stress intensity factor, this theory is equipped for the solution of crack propagation problems. Moreover, the plastic zone at the crack tip is small compared to the crack or component dimensions and the global behaviour of the structure is linear elastic.

LEFM theory is still capable of simulating many engineering problems by applying the Finite Element Method (FEM) as the numerical solution. Nevertheless, the failure analysis cannot be carried out always satisfactorily due to complex issues such as dislocations, presence of micro cracks and anisotropy.

FEM is the most popular computational technique for structural computations. It is robust and has been thoroughly developed for static, dynamic, linear and nonlinear mechanical systems. FEM, or various modified versions of the FEM, have been used to simulate fatigue crack growth (Allix and Corigliano 1996; Branco et al. 2015; Leray et al. 2008; Point and Sacco 1996; Schellekens and Borst 1993). The boundary element method (BEM) is also applied to fatigue crack problems (Benedetti and Aliabadi 2010; Benedetti and Aliabadi 2015; Benedetti et al. 2009; Kuhn and Partheymüller 1999). Using the FEM approach the component is divided into finite elements. In the case of crack problems, both crack edges have to be assigned separate nodes. FEM models are based on the classical continuum mechanics theory, which cannot directly be used to simulate problems with discontinuities since they require extra relationships that control the crack growth speed and direction. Due to the singular stress fields near the crack, generally a very fine mesh is needed in the crack tip area. This derives from the theory that the governing equations of FEM is derived. In order to numerically solve problems with discontinuities within the framework of classical mechanics, special techniques are needed. For example, the FEM with a re-meshing technique is widely used to model fatigue crack growth (Branco et al. 2015). However, implementation of automatic remeshing techniques is not easy in 3D cases (Baydoun and Fries 2012), and it is costly to remesh geometries when multiple cracks exist. Hence, while FEM models remain the most popular for structural computation, it is limited and suffers from the presence of undefined spatial derivatives at the crack surface.

The extended finite element method (XFEM) allows cracks to pass through the elements leading to better approximations of crack paths without remeshing. It has been introduced by (Belytschko and Black 1999). Moes and Belytchko have included a traction-separation law to

model cohesive cracking (Moës and Belytschko 2002). Lately, this method has been used to simulate 3D fatigue crack growth (Shi et al. 2010). Nevertheless, one common problem for XFEM is that additional criteria are needed to guide crack growth speed, direction, and coalescence or branching.

Cohesive zone model (CZM) is a model in which formation of the fracture is regarded as a gradual phenomenon where separation of the surfaces involved in the crack takes place across an extended crack tip known as cohesive zone. Accordingly, cohesive tractions emerge in this zone to resist the separation of the layers. The CZM model firstly developed by (Dugdale 1960) and (Barenblatt 1962). They investigated the inelastic behaviour of materials at the crack tip using CZM theory. Based on their assumption a plastic zone exists near the crack tip where stresses act across the crack. This cohesive zone removes the problem of an infinite stress concentration along a lower-dimensional crack-front by spreading out the area where mechanical energy is spent to create the crack surfaces. The significant merits of this model over conventional models such as LEFM are:

- It is capable of efficiently predict the behaviour of uncracked structures with blunt notches, while the presence of an initial crack is essential for LEFM to be applicable.
- The non-linear zone dimension is arbitrary, while in other methods this dimension must be negligible in comparison with other dimensions.

Cohesive forces occur in CZM when material elements are being pulled apart. While the cohesive surfaces separate, traction raise up to its maximum level and then reduces to zero which results in whole separation. Despite physical separation, CZM maintains continuity conditions mathematically. Hence, it eliminates stress singularity and limits it to the strength

of the material. The cohesive zones under Barenblatt and Dugdale assumptions are represented in Figure 1.3 respectively. In Dugdale model, the stress along the cohesive zone is constant and it is suitable for macroscale modelling; however, in Barenblatt's model the stresses relate to molecular cohesive forces. The Barenbatt's model is under two main assumptions (Konstanze 2014):

1. The length of the cohesive zone, l_{cz} , is small compared to other dimensions and remains constant for a given material.
2. The distribution of the stresses is based on $\sigma(x)$, where x is the distance from crack tip, this distribution is independent of the global loading conditions.

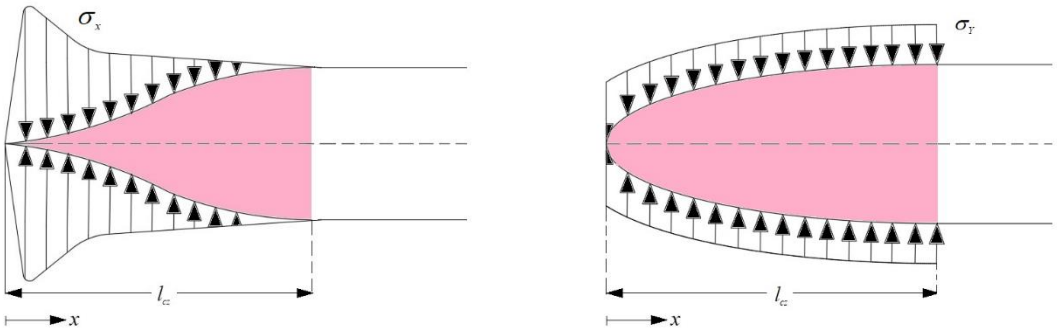

(a) (b)

Figure 1.3. (a) Barenblatt cohesive zone model and (b) Cohesive zone model by Dugdale (Konstanze 2014).

The first application of the cohesive zone model within the FEM framework was proposed by Hillerborg for mode I (Hillerborg et al. 1976); however, the CZM model proposed by Hillerborg to Barenblatt's model is that the cohesive stress is not a function of the distance from the crack tip, x , but is the function of crack width. In cohesive zone FEM models, It is essential to have a prior knowledge of actual crack path; since in the simulation, crack can only propagate in the parts where cohesive zone elements are located. Interface elements equipped

with cohesive zone models have been used (Alfano and Crisfield 2001; Alfano and Crisfield 2003; Benedetti and Aliabadi 2013; Blackman et al. 2003; Chen et al. 1999; Crisfield and Alfano 2002; Ostergaard et al. 2011; Qiu et al. 2001) in the cases in which the crack path is predictable. However, due to the complexity of the problem, usually advanced knowledge of crack path in practice is not available. Mesh dependency is another limitation of the use of cohesive zone FEM models.

Peridynamics, a recently presented continuum theory, has been proposed by Silling in (Silling 2000) to overcome the restrictions related to the differential formulation of methods based on the classical theory. It is a non-local continuum theory which is considered to be an alternative and promising nonlocal theory of solid mechanics that is formulated suitably for discontinuous problems such as crack propagation. Peridynamics is based on integral equations and does not make use of spatial differentiation, for these reasons it is better suited to describe problems affected by discontinuities (Bobaru et al. 2016; Madenci and Oterkus 2014; Silling 2000). A distinguishing feature of the peridynamic approach is that it allows for spontaneous formation, interaction, and growth of discontinuities in a consistent framework (Xu et al. 2008). It is also capable of being coupled with other methods based on the classical continuum theory as a strategy to address their shortcomings for problems involving damage (Seleson et al. 2013; Seleson et al. 2015; Shojaei et al. 2017; Wildman et al. 2017; Zaccariotto et al. 2018; Zaccariotto et al. 2017). Using this method, promising results have been obtained in dynamic brittle fracture in glass (Ha and Bobaru 2010; Ha and Bobaru 2011; Hu et al. 2013; Kilic and Madenci 2009), fiber-reinforced composites (Ghajari et al. 2014; Hu et al. 2012), functionally graded materials (Cheng et al. 2015) and corrosion damage (Chen and Bobaru 2015; Chen et al. 2016).

A peridynamic model for fatigue cracking has been proposed in the recent past by Silling and Askari (Silling and Askari 2014), which enables the simulation, in a single model, of the three phases of fatigue failure: crack initiation, fatigue growth and final failure controlled by quasi-static crack growth. In (Silling and Askari 2014), dynamic relaxation method is used to obtain the static solution, and fatigue crack growth is demonstrated by using a standard compact tension test and torsional load on a rod. Based on this study (Silling and Askari 2014), peridynamic based software can simulate crack initiation without any initial crack; however, this issue is still open and the fatigue examples in this study avoid this problem by adopting an initial crack. References (Zhang and Bobaru 2016; Zhang et al. 2016a) study fatigue crack propagation to obtain the static solution by using a conjugate gradient energy minimization method, which is matrix-free and much faster than dynamic relaxation method, see (Le 2014). Two critical damage parameters that improve computational efficiency and maintain stability in the numerical solution process are also introduced. In a recent work (Hu et al. 2015; Hu and Madenci 2017) peridynamics is applied to the prediction of fatigue life and residual strength in composite laminates. Moreover, by using peridynamic approach, mixed-mode fatigue crack propagation has been investigated in (Jung and Seok 2017). Other studies to simulate fatigue phenomena based on the peridynamic theory can be found in (Baber and Guven 2017; Jung and Seok 2016; Oterkus et al. 2010).

1.2 Thermal shock in brittle materials

Thermal shock is a phenomenon characterized by significant inhomogeneous stresses suddenly occurring in brittle material such as ceramic due to a transient temperature. Complex crack patterns may emerge on ceramics as a crucial outcome of thermal shock induced stresses.

Ceramics have a wide range of application in high-temperature industries such as aircraft propulsion (Levine et al. 2002; Opeka et al. 2004), hypersonic vehicles, marine propulsion and thermal protection structures due to their stability above the melting point of metal alloys. Hence, a basic understanding of thermal shock failure is required in the design of the aforementioned structures (Padture et al. 2002).

Numerous experimental and numerical studies have been done over the last few decades to investigate the mechanisms of thermal shock failure in ceramics. Among the experimental studies, Jiang *et al* (Jiang et al. 2012) and Shao *et al* (Shao et al. 2011) have explored thermal shock in thin rectangular ceramic specimens, while in the studies by Honda and Liu (Honda et al. 2009; Honda et al. 2002; Liu et al. 2015) the thermal shock in circular ceramic specimens is explored comprehensively.

Thermal shock cracks generally exhibit periodic and hierarchical damage patterns. In the studies by (Bažant et al. 1979; Nemat-Nasser 1978; Nemat-Nasser et al. 1978), the length and stability of the crack patterns have been scrutinized theoretically. Among the theoritical studies, thermal shock resistance has been investigated from the viewpoint of stress and energy (Hasselman 1963; Kingery 1955). Later, thermal shock parameters related to the fracture initiation, crack propagation and arrest criteria of ceramic specimens were investigated in (Hasselman 1969; Schneider 1991). An energy minimization method was also proposed by (Jenkins 2005), to determine the crack depth and spacing array in a shrinking slab due to sudden temperature variation.

Yet, available computational techniques based on the classical theory of continuum mechanics cannot accurately describe how complex crack patterns nucleate and evolve. Hence, several researchers have introduced a wide range of computational techniques to solve the problem

and equipped computational methods based on the classical theory with the capability to precisely describe crack propagation phenomena. Among the numerical methods, the Boundary Element Method (BEM) was used to simulate quenching thermal shock (see (Bahr et al. 1988; Tarasovs and Ghassemi 2014)). Later, the eXtended Finite Element Method (XFEM) with nodal enrichment (Menouillard and Belytschko 2011; Rokhi and Shariati 2013; Zamani and Eslami 2010), the phase field method (Bourdin et al. 2014; Chu et al. 2017), damage-mechanics-based model (Tang et al. 2016) and non-local damage model (Li et al. 2015) have all been applied to reproduce the multiple cracking patterns in the quenching test with different levels of success. The majority of these techniques make use of *ad-hoc* modifications and simplifying assumptions. Furthermore, their application to 3D problems generally turns out to be very complex.

As explained in Section 1.1 Peridynamics theory addresses discontinuous problems in solid mechanics. In (Kilic and Madenci 2009; Xu et al. 2018), single and multiple pre-existing initial cracks due to prescribed thermal temperature history (without applying any thermo-mechanical coupling) are simulated by the peridynamic approach. Furthermore, the peridynamic formulation was developed for multiphysics problem e.g. thermal diffusion in (Gerstle et al. 2007). Soon afterwards, heat transfer equations for 1D and 2D problems were reformulated in (Bobaru and Duangpanya 2010) and (Bobaru and Duangpanya 2012) respectively. Moreover, Oterkus *et al* (Oterkus et al. 2014b) carried out a detailed investigation of thermal diffusion problems by using state-based peridynamic (SB-PD) theory.

Recently, thermo-mechanical coupled problems via peridynamic approach is receiving increasing attention from researchers. An important feature of peridynamic in thermo-mechanical problems is to apply the same discretization to study both thermal transient and

mechanical problems. Additionally, both models are capable of simulating the onset of fracture surfaces. In 2014, Agwai and Oterkus *et al* investigated thermo-elastic problems without any crack propagations via the peridynamic numerical approach (Agwai 2011; Oterkus et al. 2014a). Lately, thermal cracking of uranium dioxide in fuel pellets and simulation of thermal shock cracking in ceramics using bond-based peridynamic (BB-PD) have been thoroughly explored in (Oterkus and Madenci 2017). Furthermore, in (D'Antuono and Morandini 2017), 2D and 3D thermal-shocks of ceramic slabs are simulated via SB-PD solution. Other applications of the peridynamic theory to simulate thermal-shock crack propagation in brittle materials e.g. rocks can be traced in (Wang et al. 2018a; Wang et al. 2018b).

Peridynamic computational methods are computationally more expensive than the methods based on classical theories e.g. FEM due to their non-local nature. However, in conventional peridynamic approach, a constant horizon size and uniform grid should be assumed all over the domain in order to get rid of ghost forces and spurious reflections of waves. Hence, the efficiency of the peridynamic approach is strongly affected when the fine grid spacing is used all over the domain; however, the finest grid size is only needed in the zones which suffer from discontinuity or surface effects (Gu et al. 2017a). There have been many attempts so far to maintain the computational accuracy and reduce computational time of peridynamic approach such as coupling of peridynamic models with other methods (Seleson et al. 2013; Shojaei et al. 2016; Zaccariotto et al. 2018), parallel computing techniques (Lee et al. 2017; Mossaiby et al. 2017) and adaptive refinement algorithms (Dipasquale et al. 2014; Gu et al. 2017a; Ren et al. 2016; Shojaei et al. 2018) . Among aforementioned adaptive refinement techniques, the one introduced by Shojaei *et al* (Shojaei et al. 2018) is used to solve dynamic problems such as elastic waves and cracks propagation with a high accuracy and low computational cost.

1.3 Sloshing problems in tanks

Sloshing of tanks with free surface fluid is the concern of many engineering applications as in ballast tanks of ships (see (Mitra et al. 2012)), interaction of dam-reservoirs, fuel tank of aircraft or aerospace structures and marine transportation of liquefied natural gas. The sloshing problem is a dominant phenomenon when the frequency of an external motion is near the first natural frequency of the system. Consequently, an intensive oscillation occurs in tanks and hence they need to be well-designed for preventing damage to the structures. Insertion of baffles inside the liquid tanks is one of the common ways to tackle this problem (see (Ibrahim 2005; Liu and Lin 2009)).

In the process of computational fluid dynamics (CFD), there are three well-known methods to simulate fluid flow i.e. Eulerian, Lagrangian and Arbitrary Lagrangian–Eulerian (ALE) approaches. In an Eulerian description, fluid is permitted to flow through a fixed set of computational grids (See (Zienkiewicz and Taylor 2000)). On the other hand, in a Lagrangian description, which recently received a considerable attention in CFD, computational grids move with the fluid domain and its boundaries. Lagrangian description can be traced in studies by (Boroomand et al. 2016; Idelsohn et al. 2003; Radovitzky and Oritz 1998; Ramaswamy and Kawahara 1986; Ramaswamy and Kawahara 1987b; Shingareva and Celaya 2007; Wu et al. 2016; Zandi et al. 2012). In intermediate description, which is known as ALE, computational grid movement is independent of fluid motion. This approach and its applications can be found in the studies by (Durate et al. 2004; Lo and Young 2004; Nithiarasu 2005; Ramaswamy and Kawahara 1987a; Zhang et al. 2015).

Liquid sloshing in a tank can be investigated numerically, analytically and experimentally. In (Faltinsen 1987), the author proposed an analytical solution based on potential flow theory for

linear sloshing problems. In the works by (Choun and Yun 1996; Choun and Yun 1999) sloshing in a bottom-mounted rectangular block tank using the small amplitude wave theory is investigated. In the work by (Faltinsen et al. 2005), linear and nonlinear problems have been presented using experimental results and analytical solutions. For analytical/experimental studies, one may trace the studies by (Akyildiz and Unal 2005; Akyildiz and Unal 2006).

As the development of computer technology, the use of numerical tools in the absence of analytical solutions has become increasingly popular. Linear and nonlinear numerical approaches have been proposed to efficiently and accurately simulate the non-breaking waves in the sloshing problems (see for instance (Boroomand et al. 2016; Boroomand et al. 2017; Chen and Nokes 2005; Chen et al. 2007b; Frandsen 2004; Pal 2012a; Ramaswamy and Kawahara 1986; Shobeyri and Yourdkhani 2017; Wu and Chang 2011; Zandi et al. 2012; Zandi et al. 2017; Zhang et al. 2016b).

Among the aforementioned numerical studies the finite element method (FEM) needs mesh generation inside the domain as well as the boundaries at each time step which makes the problem more time consuming and complicated; however, in other numerical methods such as the boundary element method (BEM) mesh generation is only needed on the boundaries. Recently, a new type of numerical approaches known as mesh-free methods (Nguyen et al. 2008) is the interest of many scientists. The advantage of these methods is that no mesh generation is needed neither in the domain nor on the boundaries. In the past decades, many mesh-free methods have been proposed to accurately and efficiently model the non-breaking waves in the sloshing problem, such as radial basis function collocation method (RBFCM), exponential basis functions (EBFs), Smoothed Particle Hydrodynamics (SPH), Reproducing Kernel Particle Method (RKPM), Generalized Finite Difference Method (GFDM), etc.

To exemplify, the RBFCM is a mesh-free approach which is capable of modeling 2D/3D nonlinear sloshing problems using few sets of collocation points both inside the domain and on the boundaries. Another mesh-free method, which is capable of simulating linear/nonlinear sloshing based on pressure theory, is known as the EBFs (Boroomand et al. 2010; Shojaei et al. 2015). It falls within the category of Trefftz methods (Chen et al. 2009; Chen et al. 2007a). In this method a linear summation of EBFs is assumed as an approximation to the solution. This collocation technique is used only on a set of boundary nodes; however, it cannot be used in problems with singular points due to the smoothness of the basis functions.

The SPH method was firstly developed by Gingold and Monaghan to investigate astrophysical problems (Gingold and Monaghan 1977). This method is based on a non-local interaction of the material points (or particles) located in a subdomain of finite distance (domain of interactions). The domain of interaction is defined by a smoothing or characteristic length where the field variable function and its derivatives are approximated. Additionally, the field variable function has to be smoothed by a kernel, which has significant influence on the proper satisfaction of boundary conditions. Later, this method has been generalized and developed to cope with CFD problems (Ren et al. 2014; Shao et al. 2012).

The Reproducing Kernel Particle Method (RKPM) (Li and Liu 1998; Li and Liu 1999a; Li and Liu 1999b) also utilizes non-local interactions between the particles. It can remove some of the shortcomings of SPH by introducing a correction function to the kernel of integral transformation. RKPM employs the fundamental notions of the convolution theorem, window functions and multiresolution analysis. However, the issue of the boundary conditions persists and for different boundary conditions with respect to the order of spatial derivatives, different correction functions are needed.

GFDM is one of the most promising domain-type meshless methods. This method firstly proposed by Benito et al in 2001 (Benito et al. 2001) has then been used in many engineering problems (Gu et al. 2017b; Salete et al. 2017; Zhang et al. 2016b; Zhang et al. 2016c). One of the significant merits of this scheme is to produce a well-conditioned sparse system of linear equations by coupling the Taylor series expansions and the weighted moving least-squares (MLS). In fact, derivatives of field variables can be evaluated at each node by linear combinations of nearby function values with various weighting coefficients without any mesh generation nor numerical quadrature. More recently, this simple method has been used in the solution of moving-boundary problems (Zhang et al. 2016b; Zhang et al. 2016c).

Lately, a new mesh-free method known as PDDO has been proposed by Madenci. (Madenci et al. 2016; Madenci et al. 2017). Indeed, PDDO and its concept comes from the Peridynamic theory which enables to reformulate classical continuum mechanics based on non-local interaction of a material point with other points within a finite distance known as *horizon*. Later, this feature was used in PDDO to obtain a non-local scalar field and its derivatives up to any order over a domain. Furthermore, the intensity of interaction between the material points is specified via a weight function. The capability of this operator is to construct solutions to ordinary, partial differential equations and derivatives of scattered data.

Another appealing feature of this method is to recast the numerical differentiation up to an arbitrary order through integration by using orthogonality properties of Peridynamic functions. Therefore, field equation and its derivatives are valid everywhere in the domain/boundaries regardless of the singularities or jump discontinuities. One of the advantages of this numerical approach is to obtain a unified solution for PDEs without any special treatment or derivative reduction process. Aforementioned merits of PDDO inspired the author to apply this mesh-

free method to liquid sloshing problems in which the derivatives of the scalar field plays an important role to the accuracy of velocities and geometry updating (Bazazzadeh et al. 2019). Installing baffles inside liquid tanks is also a crucial issue in liquid sloshing problems (Liu and Lin 2009; Shao et al. 2015). Due to the fact that usually baffles are very thin, many numerical methods are still incapable of capturing the detailed flow phenomenon near the baffle tip. The method applied in the present study (PDDO), can be considered as a good candidate for such type of problems, as it can calculate the derivatives of the potential flow, near the singular points such as the tip of the baffle, with a suitable accuracy (Bazazzadeh et al. 2019).

1.4 Outlines of the present study

The chapters of the thesis are organized as follows:

In Chapter 2 an overview of the peridynamic formulation and its discretization by a meshless approach is presented.

In Chapter 3, a cylinder model (Galvanetto et al. 2009) is used to efficiently compare the computational performance of three fatigue laws. Three fatigue degradation strategies have been implemented in conjunction with a bilinear constitutive law. The computational performance of the three fatigue degradation strategies is examined by making use of various discretization parameters. Then the same constitutive laws and fatigue degradation strategies are implemented in a peridynamic based computational code.

In Chapter 4, we aim to use a variable grid size for the solution of thermal shock problems with a peridynamic framework as the extension of the study performed by (Shojaei et al. 2018).

In Chapter 5, the PDDO numerical solution is applied to solve 2D/3D incompressible fluid flow problems. To this end, a second order finite difference algorithm for time marching of the

solution is employed. Then, the efficiency of the method in the presence of geometric discontinuities such as installing horizontal/vertical baffles is investigated.

Chapter 6, contains a summary of the findings as well as overall conclusions and insights obtained from the research. Additionally, suggestions for future research are made.

Chapter 2 Overview of the peridynamic theory

2.1 Equations of motion

Assume that a body, composed of material points with an initial configuration Ω, occupies a 2D/3D space. The generic position of each material point in the reference configuration is represented by $\mathbf{x}$ (hereinafter referred to as point $\mathbf{x}$) (see Figure 2.1). Each point interacts with other surrounding points even if they are not in contact, provided that the distance between them is less than a threshold value δ called the *horizon*. The relative position or bond between material points, $\mathbf{x}$ and $\mathbf{x}'$, with respect to the reference configuration is defined as:

$$\boldsymbol{\xi} = \mathbf{x} - \mathbf{x}' \tag{2.1}$$

also for the relative displacement of these two material points we have:

$$\boldsymbol{\eta} = \mathbf{u}(\mathbf{x}', t) - \mathbf{u}(\mathbf{x}, t) \tag{2.2}$$

A peridynamic vector state $\underline{\mathbf{A}}$ is a mapping that associates a vector denoted $\underline{\mathbf{A}}\langle \mathbf{x}' - \mathbf{x} \rangle$ with each bond $\boldsymbol{\xi} = \mathbf{x} - \mathbf{x}'$ within a neighborhood of any point $\mathbf{x}$.

An infinitesimal volume, dV_x, is associated to each point. Based on SB-PD, the equation of the motion, at time instant $t > 0$, can be written as

$$\rho(\mathbf{x}) \frac{\partial^2 \mathbf{u}}{\partial t^2}(x, t) = \int_{H(\mathbf{x})} \left(\underline{\mathbf{T}}[\mathbf{x}, t]\langle \mathbf{x}' - \mathbf{x} \rangle - \underline{\mathbf{T}}[\mathbf{x}', t]\langle \mathbf{x} - \mathbf{x}' \rangle \right) dV_{\mathbf{x}'} + \mathbf{b}(\mathbf{x}, t) \tag{2.3}$$

Hereinafter the bold letters represent vectors, one dot and two dots over a letter represent first order and second order time derivatives, respectively, $\underline{\mathbf{T}}$ stands for the force vector state field,

which the material point $\mathbf{x}'$ exerts on material point $\mathbf{x}$. In Eq. (2.3), by keeping $\mathbf{x}$ fixed and altering material point $\mathbf{x}'$ with the volume of $dV_{\mathbf{x}'}$, the integral is performed over $H(\mathbf{x})$, which is the sphere of radius δ centered in $\mathbf{x}$ i.e. two material points interact only within a finite distance, δ . ρ, $\mathbf{u}$ and $\mathbf{b}$ are the mass density, displacement field and body density force respectively. It should be mentioned that the governing equation of motion in peridynamics shares some similarities with that of traditional molecular dynamics as a summation of interactions between neighboring material points/particles are involved in both. In molecular dynamics, a material is viewed as a collection of individual particles of finite size; however, from the peridynamic view-point a material is a collection of material points of infinitesimally small size. Therefore, peridynamics is a continuum theory.

As a consequence of the integration domain assumed in Eq (2.3), the equation of motion of peridynamics is restricted to the integration of the of the forces in $H(\mathbf{x})$ which is a spherical neighborhood (in 3D) centered at the material point $\mathbf{x}$, defined by:

$$H(\mathbf{x}) = \left\{ \mathbf{x}' \in \mathrm{R}^3 \,\middle|\, \|\mathbf{x}' - \mathbf{x}\| < \delta \right\} \tag{2.4}$$

for two-dimensional and one-dimensional problems $H(\mathbf{x})$ becomes a circle or a line, respectively.

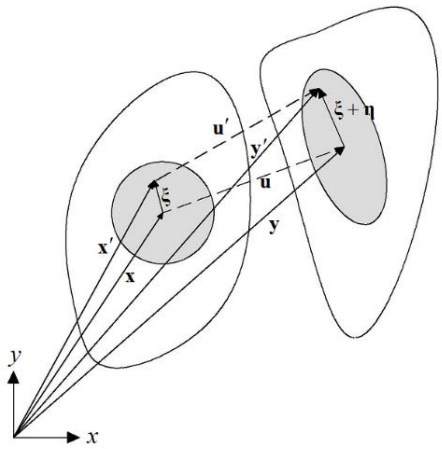

Figure 2.1. Kinematics of the reference and deformed configurations for a peridynamic continuum.

In ordinary state based peridynamics (OSB-PD) pairwise force states are not equal ($\underline{\mathbf{T}}[\mathbf{x}', t]\langle \mathbf{x} - \mathbf{x}' \rangle \neq -\underline{\mathbf{T}}[\mathbf{x}, t]\langle \mathbf{x}' - \mathbf{x} \rangle$) although they are co-axial (see Figure 2.2 (b)); however, in non-ordinary state based peridynamics (NOSB-PD) pairwise force states are neither equal nor co-axial (see Figure 2.2 (c)). On the other hand, in BB-PD the interaction between two material points is totally independent of other bonds. Hence, the force state field that two points exert on each other are equal in magnitude but opposite in sign ($\underline{\mathbf{T}}[\mathbf{x}', t]\langle \mathbf{x} - \mathbf{x}' \rangle = -\underline{\mathbf{T}}[\mathbf{x}, t]\langle \mathbf{x}' - \mathbf{x} \rangle$) (see Figure 2.2 (a)). Therefore, Eq. (2.3) can be simplified for BB-PD and takes the following form:

$$\rho(\mathbf{x})\ddot{\mathbf{u}}(\mathbf{x}, t) = \int_{H(x)} \mathbf{f}(\mathbf{u}(\mathbf{x}', t) - \mathbf{u}(\mathbf{x}, t), \mathbf{x}' - \mathbf{x}) dV_{\mathbf{x}'} + \mathbf{b}(\mathbf{x}, t) \tag{2.5}$$

in which, $\mathbf{u}$, $\mathbf{b}(\mathbf{x}, t)$ and $\mathbf{f}$ are the displacement, applied body force per unit of volume and the pairwise force function of each bond respectively.

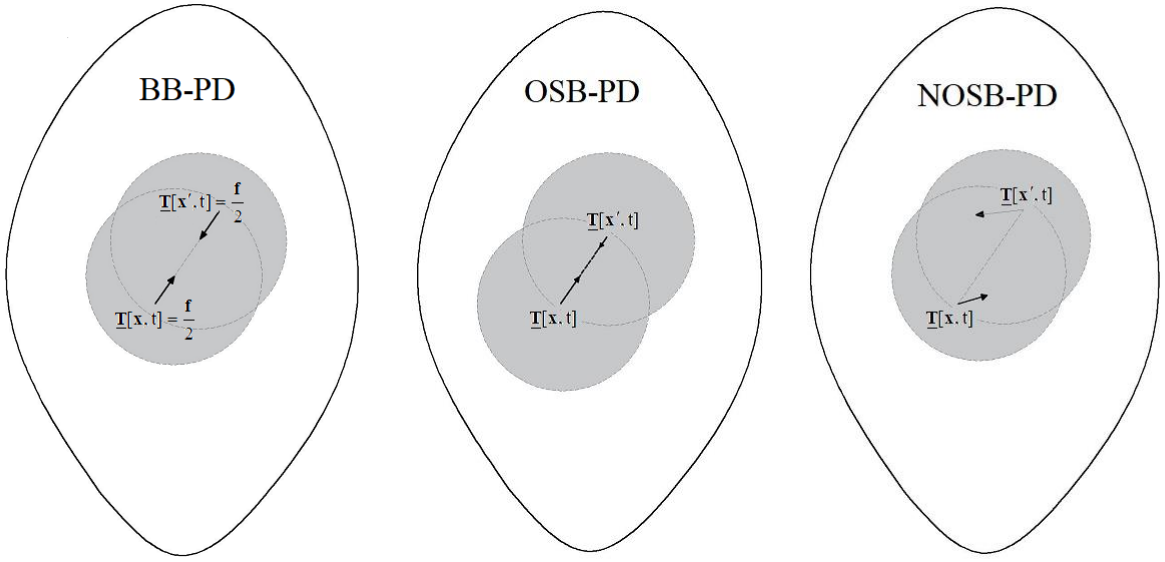

Figure 2.2. (a) BB-PD Pairwise equilibrated force densities (b) OSB-PD Ordinary unequal aligned force densities (c) NOSB-PD arbitrarily oriented force densities.

Based on the given definitions, $\|\boldsymbol{\xi}\|$ is the undeformed bond length and $\|\boldsymbol{\xi}+\boldsymbol{\eta}\|$ is the deformed bond length; see Figure 2.1.

Based on Newton's third law, the force function, $\mathbf{f}$, the following condition for conservation of linear momentum should be satisfied:

$$\mathbf{f}(-\boldsymbol{\eta},-\boldsymbol{\xi}) = -\mathbf{f}(\boldsymbol{\eta},\boldsymbol{\xi}) \tag{2.6}$$

Moreover, conservation of angular momentum requires:

$$(\boldsymbol{\eta}+\boldsymbol{\xi})\times\mathbf{f}(\boldsymbol{\eta},\boldsymbol{\xi}) = \mathbf{0} \tag{2.7}$$

which means the force vector between two material points must be parallel to their current relative position $\boldsymbol{\eta}+\boldsymbol{\xi}$.

As a consequence, looking at Eqs (2.6) and (2.7), a general form of $\mathbf{f}(\boldsymbol{\eta},\boldsymbol{\xi})$ can be expressed as (Silling 2000):

$$\mathbf{f}(\boldsymbol{\eta},\boldsymbol{\xi}) = F(\boldsymbol{\eta},\boldsymbol{\xi})(\boldsymbol{\eta}+\boldsymbol{\xi}), \quad \forall\boldsymbol{\eta},\boldsymbol{\xi} \tag{2.8}$$

in which, $F(\boldsymbol{\eta},\boldsymbol{\xi})$ stands for an appropriate scalar valued function.

2.2 Elasticity

In BB-PD elastic behavior (elasticity) of a material is considered by defining the concept of *microelasticity*. A material is known as microelastic if it satisfies the following condition (Silling 2000):

$$\oint_{\Gamma} \mathbf{f}(\boldsymbol{\eta},\boldsymbol{\xi}) \cdot d\boldsymbol{\eta} = 0, \quad \forall \text{closed curve } \Gamma, \quad \forall \boldsymbol{\xi} \neq \mathbf{0} \tag{2.9}$$

where $d\boldsymbol{\eta}$ is the differential vector path length along Γ. From line integral represented in Eq. (2.9), similar to elasticity in the classic theory, it can be noticed that the net work done by the response force along any closed curve is zero i.e. it is path independent. Based on Stoke's Theorem, if $\mathbf{f} = (f_1, f_2, f_3)$ is continuously differentiable with respect to $\boldsymbol{\eta} = (\eta_1, \eta_2, \eta_3)$, then a necessary condition for Eq. (2.9) to hold is:

$$\nabla_{\eta} \times \mathbf{f}(\boldsymbol{\eta},\boldsymbol{\xi}) = \left(\frac{\partial f_3}{\partial \eta_2} - \frac{\partial f_2}{\partial \eta_3}\right)\vec{\mathbf{i}} + \left(\frac{\partial f_1}{\partial \eta_3} - \frac{\partial f_3}{\partial \eta_1}\right)\vec{\mathbf{j}} + \left(\frac{\partial f_2}{\partial \eta_1} - \frac{\partial f_1}{\partial \eta_2}\right)\vec{\mathbf{k}} = \mathbf{0}, \quad \forall \boldsymbol{\xi} \neq \mathbf{0} \tag{2.10}$$

Since the force field is conservative and irrotational, one can calculate the peridynamic force from a scalar-valued differentiable function w known as *micropotential* by:

$$\mathbf{f}(\boldsymbol{\eta},\boldsymbol{\xi}) = \frac{\partial w}{\partial \boldsymbol{\eta}}(\boldsymbol{\eta},\boldsymbol{\xi}), \quad \forall \boldsymbol{\eta},\boldsymbol{\xi} \tag{2.11}$$

It can be proved that the micropotential depends only on the relative displacement vector, $\boldsymbol{\eta}$, through the scalar distance between the deformed points (Silling and Askari 2005b). Therefore, for isotropic microelastic peridynamic models a scalar-valued function $\hat{w}$ is defined by:

$$w(\boldsymbol{\eta},\boldsymbol{\xi}) = \hat{w}(\|\boldsymbol{\eta}+\boldsymbol{\xi}\|,\boldsymbol{\xi}), \quad \forall \boldsymbol{\eta},\boldsymbol{\xi} \tag{2.12}$$

By replacing of the above equation in Eq. (2.11), regarding Eq. (2.8) a general peridynamic force function, aligned with the relative position vector, for microelastic material is achieved by:

$$\mathbf{f}(\boldsymbol{\eta},\boldsymbol{\xi}) = H(\|\boldsymbol{\eta}+\boldsymbol{\xi}\|,\boldsymbol{\xi})(\boldsymbol{\eta}+\boldsymbol{\xi}), \quad \forall \boldsymbol{\eta},\boldsymbol{\xi} \tag{2.13}$$

in which, H is a scalar-valued even function:

$$H(p,\boldsymbol{\xi}) = \frac{\partial \hat{w}}{\partial p}(p,\boldsymbol{\xi}), \quad p = \|\boldsymbol{\eta}+\boldsymbol{\xi}\|, \quad \forall \boldsymbol{\eta},\boldsymbol{\xi} \tag{2.14}$$

Above equation is similar to that in Eq. (2.8) although, in Eq. (2.14), the dependence of the scalar part of the expression on the relative distance is concluded.

2.3 Linear form of the peridynamic

In the general framework of peridynamics large deformation is permitted. This theory can be applied to various problems regarding large deformations. By making the assumption of a small deformation, such that $(\|\boldsymbol{\eta}+\boldsymbol{\xi}\|-\|\boldsymbol{\xi}\|)/\|\boldsymbol{\xi}\| << 1$ for all $\boldsymbol{\xi}$. A Taylor expansion on $\boldsymbol{\eta}$ of first order to Eq (2.8) a peridynamic force function can be written by:

$$\mathbf{f}(\boldsymbol{\eta},\boldsymbol{\xi}) = \mathbf{C}(\boldsymbol{\xi})\boldsymbol{\eta} + \mathbf{f}(\mathbf{0},\boldsymbol{\xi}) \tag{2.15}$$

in which $\mathbf{C}$ is a second-order tensor , known as *micromodulus,* of the peridynamic force, and thus it can be calculated as:

$$\mathbf{C}(\boldsymbol{\xi}) = \frac{\partial \mathbf{f}}{\partial \boldsymbol{\eta}}(\mathbf{0},\boldsymbol{\xi}) \tag{2.16}$$

the above formula can be expanded by:

$$\mathbf{C}(\boldsymbol{\xi}) = \frac{\partial \mathbf{f}}{\partial \boldsymbol{\eta}}(\mathbf{0},\boldsymbol{\xi}) = \begin{bmatrix} \frac{\partial f_1}{\partial \eta_1}(\mathbf{0},\boldsymbol{\xi}) & \frac{\partial f_1}{\partial \eta_2}(\mathbf{0},\boldsymbol{\xi}) & \frac{\partial f_1}{\partial \eta_3}(\mathbf{0},\boldsymbol{\xi}) \\ \frac{\partial f_2}{\partial \eta_1}(\mathbf{0},\boldsymbol{\xi}) & \frac{\partial f_2}{\partial \eta_2}(\mathbf{0},\boldsymbol{\xi}) & \frac{\partial f_2}{\partial \eta_3}(\mathbf{0},\boldsymbol{\xi}) \\ \frac{\partial f_3}{\partial \eta_1}(\mathbf{0},\boldsymbol{\xi}) & \frac{\partial f_3}{\partial \eta_2}(\mathbf{0},\boldsymbol{\xi}) & \frac{\partial f_3}{\partial \eta_3}(\mathbf{0},\boldsymbol{\xi}) \end{bmatrix} \tag{2.17}$$

Also with respect to Eq (2.8), the micromodulus tensor can be achieved by:

$$\mathbf{C}(\boldsymbol{\xi}) = \boldsymbol{\xi} \otimes \frac{\partial F}{\partial \boldsymbol{\eta}}(\mathbf{0},\boldsymbol{\xi}) + F(\mathbf{0},\boldsymbol{\xi})\mathbf{I} \tag{2.18}$$

in which, $\otimes$ is the dyadic or tensor product between two vectors and $\mathbf{I}$ is an identity matrix which yields a tensor of second order. The condition expressed in Eq (2.10) for a microelastic material implies that:

$$\frac{\partial f_i}{\partial \eta_j} = \frac{\partial f_j}{\partial \eta_i}, \quad \text{for } i, j = 1,2,3 \tag{2.19}$$

Accordingly, by introducing the above condition to Eq (2.16), one can conclude the mircromodulus must be symmetric for a linear microelastic material as:

$$\mathbf{C}(\boldsymbol{\xi}) = \mathbf{C}^T(\boldsymbol{\xi}), \quad \forall \boldsymbol{\xi} \tag{2.20}$$

To satisfy of the above expression, sufficient and necessary condition is that there should be a scalar-valued even function $\lambda(\boldsymbol{\xi})$ through which (Silling 2000):

$$\boldsymbol{\xi} \otimes \frac{\partial F}{\partial \boldsymbol{\eta}}(\mathbf{0},\boldsymbol{\xi}) = \lambda(\boldsymbol{\xi})\boldsymbol{\xi} \otimes \boldsymbol{\xi} \tag{2.21}$$

in which

$$\lambda(\boldsymbol{\xi}) = \frac{\boldsymbol{\xi}}{\|\boldsymbol{\xi}\|^2} \frac{\partial F}{\partial \boldsymbol{\eta}}(\mathbf{0},\boldsymbol{\xi}) \tag{2.22}$$

Hence, for a symmetric micromodulus we have:

$$\mathbf{C}(\boldsymbol{\xi}) = \lambda(\boldsymbol{\xi})\boldsymbol{\xi} \otimes \boldsymbol{\xi} + F(0,\boldsymbol{\xi})\mathbf{I} \tag{2.23}$$

Consequently, the linearized bond-based peridynamic force function can be explicitly reformulated in a general form as:

$$\mathbf{f}(\boldsymbol{\eta},\boldsymbol{\xi}) = \left[\boldsymbol{\lambda}(\boldsymbol{\xi})\boldsymbol{\xi} \otimes \boldsymbol{\xi} + F(\mathbf{0},\boldsymbol{\xi})\mathbf{I}\right]\boldsymbol{\eta} + \mathbf{f}(\mathbf{0},\boldsymbol{\xi}) \tag{2.24}$$

For a microelastic material, using $F(\boldsymbol{\eta},\boldsymbol{\xi}) = H(p,\boldsymbol{\xi})$ (Silling 2000), presents:

$$\lambda(\boldsymbol{\xi}) = \frac{1}{\|\boldsymbol{\xi}\|}\frac{\partial H}{\partial p}(\|\boldsymbol{\xi}\|,\boldsymbol{\xi}), \quad p = \|\boldsymbol{\xi} + \boldsymbol{\eta}\| \tag{2.25}$$

Finally, the linearized peridynamic force function for a microelastic material is obtained as:

$$\mathbf{f}(\boldsymbol{\eta},\boldsymbol{\xi}) = \left[\frac{1}{\|\boldsymbol{\xi}\|}\frac{\partial H}{\partial p}(\|\boldsymbol{\xi}\|,\boldsymbol{\xi}) + H(\mathbf{0},\boldsymbol{\xi})\mathbf{I}\right](\boldsymbol{\xi} \otimes \boldsymbol{\xi})\boldsymbol{\eta} + \mathbf{f}(\mathbf{0},\boldsymbol{\xi}) \tag{2.26}$$

2.4 Force per unit area

Force per unit area establishes a link between the BB-PD and the classic theory of elasticity. Assuming that an infinite body Ω undergoes a homogeneous deformation, one may choose a point $\mathbf{x}$ in Ω and a unit vector $\mathbf{n}$ passing through the point. The body is divided into two parts Ω^- and Ω^+ by a plane normal to the vector as (Figure 2.3):

$$\Omega^+ = \{\mathbf{x}' \in \Omega : (\mathbf{x}' - \mathbf{x}) \cdot \mathbf{n} \geq 0\}, \quad \Omega^- = \{\mathbf{x}' \in \Omega : (\mathbf{x}' - \mathbf{x}) \cdot \mathbf{n} \leq 0\} \tag{2.27}$$

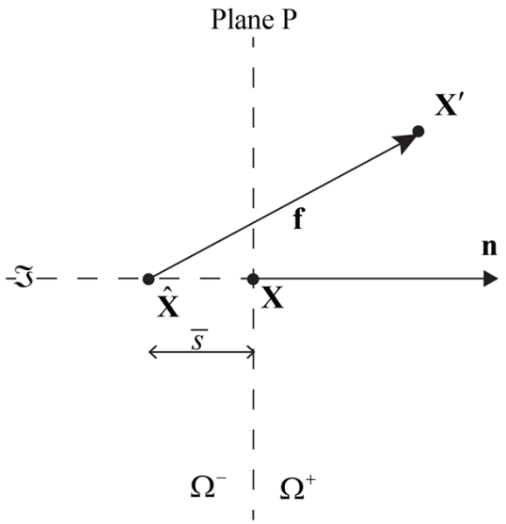

Figure 2.3. Definition of areal force density (Silling 2000).

Assuming that $\Im$ is a set of collinear points in Ω^-, one can write:

$$\Im = \left\{ \hat{\mathbf{x}} \in \Omega^- : \hat{\mathbf{x}} = \mathbf{x} - \bar{s}\mathbf{n}, 0 \le \bar{s} < \infty \right\} \tag{2.28}$$

In the direction of $\mathbf{n}$ the *areal force density*, $\boldsymbol{\tau}(\mathbf{x},\mathbf{n})$, at $\mathbf{x}$ is defined (Silling 2000):

$$\boldsymbol{\tau}(\mathbf{x},\mathbf{n}) = \int_{\Im}\int_{\Omega^+} \mathbf{f}(\mathbf{u}' - \hat{\mathbf{u}}, \mathbf{x}' - \hat{\mathbf{x}}) dV_{\mathbf{x}'} d\hat{l} \tag{2.29}$$

where, $d\hat{l}$ stands for the differential path length over $\Im$.

Assuming that homogenous deformation is independent of $\mathbf{x}$, one can propose a meaningful representation of a stress tensor as:

$$\boldsymbol{\tau}(\mathbf{x},\mathbf{n}) = \boldsymbol{\sigma}\mathbf{n}, \quad \forall \mathbf{n} \tag{2.30}$$

Since the calculation of the force per unit area, $\boldsymbol{\tau}$, is performed with respect to the reference configuration, stress tensor presented in Eq. (2.30) is a Piola-Kirchhoff stress tensor.

Force vector state field, $\underline{\mathbf{T}}$, for a 2D plane stress model is given by

$$\underline{\mathbf{T}}[\mathbf{x},\mathrm{t}]\langle\mathbf{x}'-\mathbf{x}\rangle=\left(\frac{2(2\nu-1)}{\nu-1}\left(k'\vartheta+\frac{\lambda}{3}\left(\underline{\omega}\left(\underline{e}^{d}-\alpha T_{avg}\|\boldsymbol{\xi}\|\right)\right)\bullet\underline{x}\right)\frac{\underline{\underline{\omega x}}}{q}+\lambda\underline{\underline{\omega e}}^{d}\right)\frac{\underline{\mathbf{Y}}[\mathbf{x},\mathrm{t}]\langle\mathbf{x}'-\mathbf{x}\rangle}{\left\|\underline{\mathbf{Y}}[\mathbf{x},\mathrm{t}]\langle\mathbf{x}'-\mathbf{x}\rangle\right\|} \tag{2.31}$$

in which k' and λ are the material parameters which relates to Young's modulus E and Poisson's ratio ν, while the position of point $\mathbf{x}$ at time t is denoted by $\mathbf{y}(\mathbf{x},t)=\mathbf{x}+\mathbf{u}(\mathbf{x},t)$. Therefore, one may obtain the extension scalar state as

$$e[\mathbf{x},t]\langle\boldsymbol{\xi}\rangle=\|\mathbf{y}(\mathbf{x}',t)-\mathbf{y}(\mathbf{x},t)\|-\|\boldsymbol{\xi}\| \tag{2.32}$$

where the deviatoric component is given by

$$\underline{e}^{d}=\underline{e}-\frac{\vartheta}{3}\underline{x} \tag{2.33}$$

In Eq. (2.31), α is the thermal expansion coefficient and $\underline{\omega}$ is a scalar influence function that allocates a weight to each bond with different $\boldsymbol{\xi}$. The mean value of the change in temperatures, T_{avg}, in Eq. (2.31), between two material points is defined as

$$T_{avg}=\frac{(\theta-\theta_0)+(\theta'-\theta_0)}{2} \tag{2.34}$$

in which, θ_0, represents the reference temperature whereas θ and θ' indicate the temperature at material points $\mathbf{x}$ and $\mathbf{x}'$ respectively.

Furthermore, the weighted-volume corresponding to $H(\mathbf{x})$ is demonstrated by $q=\underline{\omega x}\bullet\underline{x}$. In Eq. (2.31) and Eq. (2.33), the peridynamic counterpart of volume dilatation that indicates the relative volume change $\Delta V/V$ in plane stress case can be expressed by

$$\vartheta=\frac{2(2\nu-1)}{\nu-1}\frac{\underline{\underline{\omega x}}\bullet\underline{e}}{q} \tag{2.35}$$

2.5 Unstressed configuration condition

A configuration is known as unstressed if the following condition is observed (Silling 2000):

$$\boldsymbol{\tau}(\mathbf{x},\mathbf{n}) = \mathbf{0}, \quad \forall \mathbf{n} \tag{2.36}$$

Above condition restricts the scalar-valued function F discussed in this chapter.

Setting $\mathbf{x} = 0$ and taking $\mathbf{n} = \mathbf{e}_1$, one may rewrite Eq. (2.28) as:

$$\hat{\mathbf{x}} = -\bar{s}\mathbf{e}_1 \tag{2.37}$$

in which, $\mathbf{e}_1$ is chosen based on a set of orthonormal basis vectors as $\{\mathbf{e}_1, \mathbf{e}_2, \mathbf{e}_3\}$.

Then we have:

$$\boldsymbol{\xi} = \mathbf{x}' - \hat{\mathbf{x}} = \mathbf{x}' + \bar{s}\mathbf{e}_1 \tag{2.38}$$

Furthemore, according to the Eq. (2.8), for $\boldsymbol{\eta} = 0$, one can write:

$$\mathbf{f}(\boldsymbol{\eta},\boldsymbol{\xi}) = \mathbf{f}(\mathbf{0},\boldsymbol{\xi}) = F(\mathbf{0},\boldsymbol{\xi})\boldsymbol{\xi} \tag{2.39}$$

Similarly, the areal force density, by Eq. (2.29), in the direction of $\mathbf{e}_1$ is given by:

$$\boldsymbol{\tau}(\mathbf{0},\mathbf{e}_1) = \int_0^{\infty}\int_{\Omega^+} F(\mathbf{0},\mathbf{x}' + \bar{s}\mathbf{e}_1)(\mathbf{x}' + \bar{s}\mathbf{e}_1)dV_{X'}d\bar{s} \tag{2.40}$$

Since corresponding arguments in Eq. (2.40) are expressed in the vector form, one may convert the integration variables into spherical coordinates as (see Figure 2.4):

$$\xi_1 = r\cos(\theta), \quad \xi_2 = r\sin(\theta)\cos(\phi), \quad \xi_3 = r\sin(\theta)\sin(\phi) \tag{2.41}$$

in which $r = \|\boldsymbol{\xi}\|$. Hence, Eq (2.40) can be written as:

$$\tau(\mathbf{0},\mathbf{e}_1) = \int_0^{\infty}\int_0^{r}\int_0^{\cos^{-1}(\bar{s}/r)}\int_0^{2\pi} F(0,r)(r\cos\theta)r^2\sin\theta d\phi d\theta d\bar{s}dr = \frac{2\pi}{3}\int_0^{\infty} F(0,r)r^4 dr \tag{2.42}$$

Therefore, based on Eq. (2.36), Eq. (2.42) can be written as:

$$\psi = \frac{2\pi}{3}\int_0^\infty F(0,r)r^4 dr = 0 \tag{2.43}$$

The above formula denotes the aforementioned restriction on F (Silling 2000).

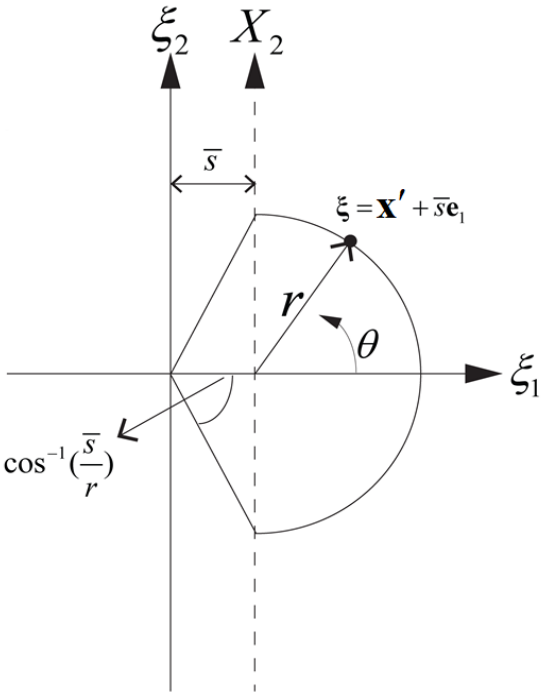

Figure 2.4. *Changing of the coordinates (Silling 2000).*

2.6 Poisson's ratio in bond-based peridynamics

The assumptions of the BB-PD theory impose a fixed value of the Poisson's ratio. This limitation is due to the nature of bonds that are characterized based on only pairwise interactions. This limitation is solved in the state-based version of peridynamics (Silling et al. 2007), however, SB-PD is computationally much more expensive than the BB-PD. In this section, it has been proven how a fixed value for Poisson's ratio is determined by equating the stress tensor of the areal force density concept with that obtained by the classical stress tensor.

The two stress tensors are compared considering the same strain in a homogeneous linear elastic body.

Assuming an infinite linear unstressed microelastic body, in the reference configuration, undergoes a homogeneous deformation as $u_1 = c_{11}X$ and $u_2 \equiv u_3 \equiv 0$, one can replace the displacement components in Eqs. (2.1) and (2.2) as:

$$\eta_1 = c_{11}\xi_1, \quad \eta_2 \equiv \eta_3 \equiv 0 \tag{2.44}$$

Note that $\{u_1, u_2, u_3\}$ are the components of the displacement field $\mathbf{u}$ (Silling 2000).

One may substitute the obtained relative displacements (Eq. (2.44)) into Eq. (2.24) and write:

$$\mathbf{f}(\boldsymbol{\eta}, \boldsymbol{\xi}) = \begin{Bmatrix} c_{11}[\lambda(\boldsymbol{\xi})\xi_1^3 + F(\mathbf{0}, \boldsymbol{\xi})\xi_1] \\ c_{11}\lambda(\boldsymbol{\xi})\xi_1^2\xi_2 \\ c_{11}\lambda(\boldsymbol{\xi})\xi_1^2\xi_3 \end{Bmatrix} \tag{2.45}$$

Similarly, the nine components of the stress tensor $\boldsymbol{\sigma}$ can be determined with respect to Eq. (2.29) by:

$$\sigma_{ij} = \tau_j(\mathbf{e}_i) = \int_{\Im}\int_{\Omega^+} f_j dV_{\mathbf{X}'} d\hat{l}, \quad \text{for } i, j = 1,2,3 \tag{2.46}$$

Derivation of the first three components, using the change of variable rule, explained in Eq. (2.41), gives:

$$\begin{aligned} \sigma_{11} = \tau_1(\mathbf{e}_1) &= \int_{\Im}\int_{\Omega^+} f_1 dV_{X'} d\hat{l} \\ &= c_{11}\int_0^{\infty}\int_0^{r}\int_0^{\cos^{-1}(\bar{s}/r)}\int_0^{2\pi}[\lambda(r)(r\cos\theta)^3 + F(0,r)(r\cos\theta)]r^2\sin\theta d\phi d\theta d\bar{s} dr \\ &= c_{11}\left[\frac{2\pi}{5}\int_0^{\infty}\lambda(r)r^6 dr + \frac{2\pi}{3}\int_0^{\infty}F(0,r)r^4 dr\right] = c_{11}(\Lambda + \psi) \end{aligned} \tag{2.47}$$

$$\sigma_{12} = \tau_2(\mathbf{e}_1) = \int_{\Im}\int_{\Omega^+} f_2 dV_{\mathbf{X}'} d\hat{l}$$
$$= c_{11}\int_0^{\infty}\int_0^{r}\int_0^{\cos^{-1}(\bar{s}/r)}\int_0^{2\pi}[\lambda(r)(r\cos\theta)^2 r\sin\theta\cos\phi]r^2\sin\theta d\phi d\theta ds dr \qquad (2.48)$$
$$= 0$$

$$\sigma_{13} = \tau_3(\mathbf{e}_1) = \int_{\Im}\int_{\Omega^+} f_3 dV_{\mathbf{X}'} d\hat{l}$$
$$= c_{11}\int_0^{\infty}\int_0^{r}\int_0^{\cos^{-1}(\bar{s}/r)}\int_0^{2\pi}[\lambda(r)(r\cos\theta)^2 r\sin\theta\sin\phi]r^2\sin\theta d\phi d\theta ds dr \qquad (2.49)$$
$$= 0$$

in which, on the basis of Eq. (2.43) $\psi = 0$, and Λ is defined by:

$$\Lambda = \frac{2\pi}{5}\int_0^{\infty}\lambda(r)r^6 dr \qquad (2.50)$$

Likewise, other six components of $\boldsymbol{\sigma}$ can be calculated. To illustrate, for the components in the direction of $\mathbf{e}_2$ the variables in Eq. (2.41) should be changed to:

$$\xi_1 = r\sin(\theta)\sin(\phi),\quad \xi_2 = r\cos(\theta),\quad \xi_3 = r\sin(\theta)\cos(\phi) \qquad (2.51)$$

then we obtain:

$$\boldsymbol{\sigma} = c_{11}\begin{bmatrix}\Lambda & 0 & 0\\ 0 & \frac{\Lambda}{3} & 0\\ 0 & 0 & \frac{\Lambda}{3}\end{bmatrix} \qquad (2.52)$$

On the other hand, the stress tensor based on classical theory of isotropic linear elasticity can be written as:

$$\boldsymbol{\sigma} = \begin{bmatrix}\bar{\lambda}+2\bar{\mu} & \bar{\lambda} & \bar{\lambda}\\ \bar{\lambda} & \bar{\lambda}+2\bar{\mu} & \bar{\lambda}\\ \bar{\lambda} & \bar{\lambda} & \bar{\lambda}+2\bar{\mu}\end{bmatrix}\begin{Bmatrix}c_{11}\\ 0\\ 0\end{Bmatrix} \qquad (2.53)$$

which can be simplified as:

$$\boldsymbol{\sigma} = c_{11}\begin{bmatrix} \bar{\lambda}+2\bar{\mu} & 0 & 0 \\ 0 & \bar{\lambda} & 0 \\ 0 & 0 & \bar{\lambda} \end{bmatrix} \tag{2.54}$$

in which, $\bar{\mu}$ and $\bar{\lambda}$ are the shear modulus and Lame's first parameter, respectively.

Equating Eq. (2.52) with Eq. (2.54) gives the following results:

$$\bar{\lambda} = \bar{\mu} = \frac{\Lambda}{3}, \quad \nu = \frac{1}{4}, \quad E = \frac{5\Lambda}{6} \tag{2.55}$$

in which, ν and E indicate the Poisson's ratio and Young's modulus, respectively. Based on aforementioned analysis, the obtained results indicate that for a linear microelastic isotropic material under a homogenous deformation using BB-PD model, the value of the Poisson's ratio is fixed to 0.25. The unknown term Λ, is dependent of ν and E and is not directly measurable (Silling 2000).

Likewise, it can be proven that Poisson's ratio for plane strain cases is $\nu = 1/4$ and for plane stress cases is $\nu = 1/3$ (Huang et al. 2015).

2.7 Prototype microelastic brittle (PMB) material model

One of the simple constitutive models, which has been widely used in peridynamics framework, is the *prototype microelastic brittle* (PMB) (see (Silling and Askari 2005b)). In PMB type material, there is a linear relationship between peridynamic force, $\mathbf{f}$, and the mechanical *bond stiffness* c_{ME}. One may establish this relationship via the bond relative elongation or stretch. This stretch is defined as:

$$s = \frac{\|\boldsymbol{\xi}+\boldsymbol{\eta}\| - \|\boldsymbol{\xi}\|}{\|\boldsymbol{\xi}\|} \tag{2.56}$$

For a PMB type material it is easy to insert the failure of a bond by considering that peridynamic bonds can be broken only when their stretch exceeds the elastic limit, s_0 , known as the *critical stretch* (Silling and Askari 2005b). The details on how to determine it will be presented in Section 2.8. Once the bond fails it cannot be recovered i.e. failure is an irreversible phenomenon. Furthermore, the bond does not fail in compression.

In the scalar valued function H , defined in Eq. (2.13), there is a linear relationship between the bond stiffness and the bond stretch:

$$H(\|\boldsymbol{\eta}+\boldsymbol{\xi}\|,\boldsymbol{\xi}) = \frac{c_{ME}(\boldsymbol{\xi})\mu(\boldsymbol{\xi})\left(s-\alpha T_{avg}\right)}{\|\boldsymbol{\eta}+\boldsymbol{\xi}\|} \tag{2.57}$$

in which, μ is a history dependent scalar-valued function that takes either a value of 0 or 1 depending on the status of the bond as:

$$\mu(\boldsymbol{\xi}) = \begin{cases} 1 & \text{if } \ s(\boldsymbol{\xi},t') < s_0, \quad 0 < t' < t \\ 0 & \text{else} \end{cases} \tag{2.58}$$

Therefore, the peridynamic force function for a PMB material can be written as:

$$\mathbf{f}(\mathbf{u}'-\mathbf{u},\mathbf{x}'-\mathbf{x},t) = \mu(\xi,t)\, c_{ME}\ (s-\alpha T_{avg})\frac{\boldsymbol{\xi}+\boldsymbol{\eta}}{\|\boldsymbol{\xi}+\boldsymbol{\eta}\|} \tag{2.59}$$

For the sake of simplicity, one can take $\xi = \|\boldsymbol{\xi}\|$ and $\eta = \|\boldsymbol{\eta}+\boldsymbol{\xi}\|$. Based on the definition of stretch it can be concluded that $\eta = (s-\alpha T_{avg})\xi$ and thus with respect to Eq. (2.57) we have:

$$H = c_{ME}(s-\alpha T_{avg}) = c_{ME}(\frac{\eta}{\xi}) \tag{2.60}$$

Under "small displacement" assumption, one can take $c_{ME}(\boldsymbol{\xi})$ as a constant function so that the above equations is simplified by:

$$\mathbf{f}(\boldsymbol{\eta},\boldsymbol{\xi}) = c_{ME}\left(s-\alpha T_{avg}\right)\mu(\boldsymbol{\xi})\frac{\boldsymbol{\xi}}{\|\boldsymbol{\xi}\|} \quad \text{if} \quad \|\boldsymbol{\eta}\| \ll \|\boldsymbol{\xi}\| \tag{2.61}$$

Based on Eq (2.11) the potential energy density of a bond, or the micropotential of a single bond can be obtained by:

$$\hat{w} = \int \xi H d\eta = \int \xi c_{ME} (\frac{\eta}{\xi^2}) d\eta = \frac{c_{ME} \eta^2}{2\xi} = \frac{c_{ME} (s - \alpha T_{avg})^2 \xi}{2} \tag{2.62}$$

The total elastic potential energy W at that point can be computed by integrating the above micropotential over all the bonds within the neighborhood of a given point

$$W(\mathbf{x}) = \frac{1}{2} \int_{H_X} w(\boldsymbol{\eta}, \boldsymbol{\xi}) dV_{X'} \tag{2.63}$$

The factor $1/2$ before the integral is due to the fact that the potential energy of a bond is shared between its two interacting points. Then, by substituting Eq (2.62) in Eq (2.63) and using spherical coordinates we have:

$$W = \frac{1}{2} \int_0^{\delta} (\frac{c_{ME} (s - \alpha T_{avg})^2 \xi}{2}) 4\pi \xi^2 d\xi = \frac{\pi c_{ME} (s - \alpha T_{avg})^2 \delta^4}{4} \tag{2.64}$$

In the framework of the classical theory of elasticity, it is also possible to calculate the strain energy density of a point using the following given tensors:

$$\boldsymbol{\varepsilon}_{ij} = \delta_{ij} s \tag{2.65}$$

$$\sigma_{ij} = 2\bar{\mu} \boldsymbol{\varepsilon}_{ij} + \bar{\lambda} \delta_{ij} \boldsymbol{\varepsilon}_{kk} \tag{2.66}$$

The Eqs. (2.65) and (2.66) can be rewritten in a matrix form as:

$$\boldsymbol{\varepsilon} = \begin{bmatrix} (s - \alpha T_{avg}) & 0 & 0 \\ 0 & (s - \alpha T_{avg}) & 0 \\ 0 & 0 & (s - \alpha T_{avg}) \end{bmatrix} \tag{2.67}$$

$$\boldsymbol{\sigma} = \begin{bmatrix} (2\bar{\mu} + 3\bar{\lambda})(s - \alpha T_{avg}) & 0 & 0 \\ 0 & (2\bar{\mu} + 3\bar{\lambda})(s - \alpha T_{avg}) & 0 \\ 0 & 0 & (2\bar{\mu} + 3\bar{\lambda})(s - \alpha T_{avg}) \end{bmatrix} \tag{2.68}$$

The strain energy density in the classical theory of elasticity is determined by:

$$W=\frac{1}{2}\sigma_{ij}\varepsilon_{ij}=\frac{3}{2}(2\bar{\mu}+3\bar{\lambda})(s-\alpha T_{avg})^2=3E(s-\alpha T_{avg})^2=\frac{9K(s-\alpha T_{avg})^2}{2},\quad \nu=1/4 \quad (2.69)$$

where K is the bulk modulus of the material. Considering the restriction of $\nu=1/4$ in Section 2.6 the rest of the parameters can be stated as follows:

$$\bar{\mu}=\frac{E}{2(1+\nu)}=\frac{2E}{5} \quad (2.70)$$

$$\bar{\lambda}=\frac{E\nu}{(1-2\nu)(1+\nu)}=\frac{2E}{5} \quad (2.71)$$

$$K=\frac{E}{3(1-2\nu)}=\frac{2E}{3} \quad (2.72)$$

Hence, bond constant c_{ME} can be obtained by Equating Eq (2.64) with Eq (2.69) as follows:

$$c_{ME}=\frac{18K}{\pi\delta^4}=\frac{12E}{\pi\delta^4} \qquad \text{3D case} \quad (2.73)$$

The same procedure to find the restricted Poisson's ratio and to determine the bond constant can be followed for a two-dimensional peridynamic model. In this way, the elastic energy can be calculated for both plane stress and plane strain conditions. Then the following results can be obtained (Huang et al. 2015):

$$\begin{cases} c_{ME}=\dfrac{9E}{\pi\,\delta^3} & \text{Plane stress} \\ c_{ME}=\dfrac{48E}{5\pi\,\delta^3} & \text{Plane strain} \end{cases} \quad (2.74)$$

Moreover, for the 1D case one can write (Bobaru et al. 2008):

$$c_{ME}=\frac{2E}{A\delta^2} \quad (2.75)$$

where A is the cross section area.

2.8 Failure criterion

In this section, we briefly discuss the introduction of failure into a BB-PD model. As discussed earlier for a PMB material the failure criterion is based on a maximum stretch (or critical stretch) s_0 that a bond can withstand during its performance. A schematic diagram of the peridynamic force versus the bond stretch for a PMB material is represented in Figure 2.5. In order to obtain s_0, the procedure introduced in (Silling and Askari 2005b) is followed. Macroscopic material properties such as the critical energy release rate of the material G_0 can be linked to The critical bond stretch, s_0.

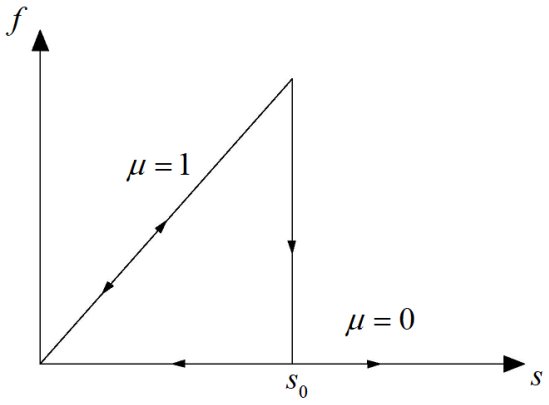

Figure 2.5. peridynamic force versus bond stretch.

A crack grows when the energy per unit area of fracture surface is dissipated. In peridynamics, separation of a body into two parts occurs when all the bonds (across a fracture surface) that initially connected the points on the opposite sides are broken. By assuming a complete separation of the fracture surface and neglecting the other dissipative mechanisms, one is able to find the relationship between s_0 and G_0.

The required work to break a single bond in PMB material can be calculated by:

$$w_0 = \int_0^{s_0} \xi H(s) d\eta = \int_0^{s_0} H(s)\xi^2 ds = \frac{c{s_0}^2 \xi}{2} \tag{2.76}$$

It is needed to break all the bonds crossing a surface to obtain a new fracture surface. The energy per unit surface area, required to break all the bonds, is taken to be equal to the critical energy release rate G_0 derived from Griffith's theory (Griffith 1921). This criterion is nonlocal since the Griffith's criterion is based on the energy balance of the whole material surrounding the crack. The mentioned released energies, due to propagation of crack, can be related as:

$$G_0 = \int_0^{2\pi} \int_0^{\delta} \int_z^{\delta} \int_0^{\arccos(\frac{z}{\xi})} (\frac{c{s_0}^2 \xi}{2}) \xi^2 \sin\phi d\phi d\xi dz d\theta = \frac{\pi c{s_0}^2 \delta^5}{10} \tag{2.77}$$

Evaluation of fracture energy, G_0. For each point *p* along the dashed line, $0 \le z \le \delta$, the work required to break the bonds connecting *p* to each point *q* in the spherical cap is summed by the integrals in Eq. (2.77) using a spherical coordinate system centered at *p*.

where the domain of integration and the variables are illustrated in Figure 2.6.

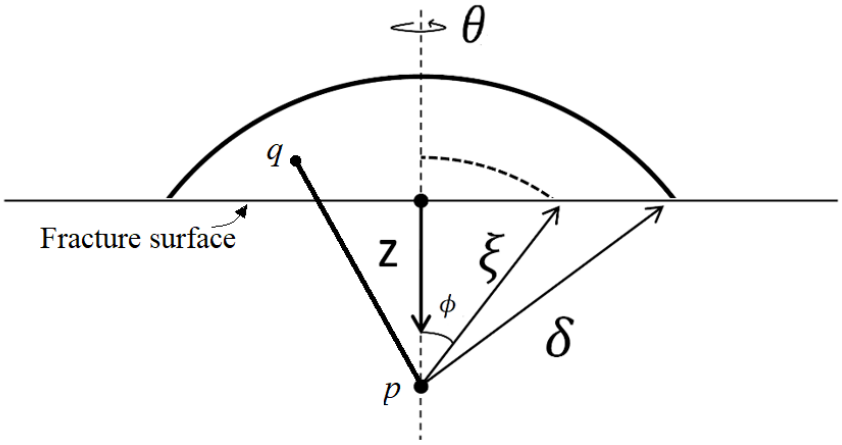

Figure 2.6. Variables involved in the computation of the critical stretch value.

Furthermore, it is possible to obtain critical stretch, s_0, in terms of the critical energy release rate of the material G_0 (Ha and Bobaru 2010; Silling and Askari 2005b).

$$s_0 = \begin{cases} \sqrt{\dfrac{5G_0}{6E\delta}} & 3D \\ \sqrt{\dfrac{4G_0}{9E\delta}} & \text{Plane stress} \\ \sqrt{\dfrac{5G_0}{12E\delta}} & \text{Plane strain} \end{cases} \tag{2.78}$$

A bond is considered broken and is removed from the following calculations when

$$s - \alpha T_{avg} \geq s_0 \tag{2.79}$$

The damage level of point $\mathbf{x}$ at time t can be expressed by

$$\phi(\mathbf{x}, t) = 1 - \frac{\int_{H(x)} \mu(\xi, t) dV_{x'}}{\int_{H(x)} dV_{x'}} \tag{2.80}$$

In Eq. (2.80), ϕ , indicates the ratio of the number of broken bonds to the total number of bonds originally connected to the point $\mathbf{x}$. The damage level , ϕ, takes a value between 0 and 1, $0 \leq \phi \leq 1$. $\phi = 1$ means there is no interaction between the point and all surrounding points within its horizon, while $\phi = 0$ denotes an undamaged state.

2.9 Spatial Discretization of the model

We discretize the solution domain with a set of grid points called *nodes* (see Figure 2.7), to approximate the peridynamic equation.

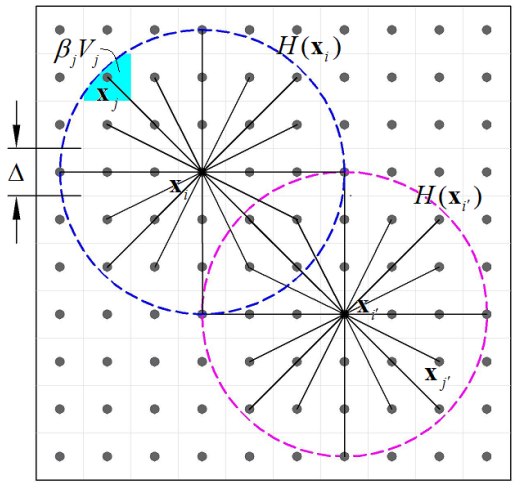

Figure 2.7. Peridynamic material points and their interactions.

By adapting the one-point Gauss quadrature rule to proceed with the spatial integration, one can discretize Eq. (2.5) as

$$\rho(\mathbf{x})\ddot{\mathbf{u}}(\mathbf{x},t)=\sum_{j=1}^{N}\mathbf{f}(\mathbf{u}(\mathbf{x}_j,t)-\mathbf{u}(\mathbf{x}_i,t),\mathbf{x}_j-\mathbf{x}_i)\,\beta_j(\boldsymbol{\xi})V_j+\mathbf{b}(\mathbf{x},t) \tag{2.81}$$

where, i is the point of interest and j denotes the family nodes located in the horizon of a node i . V_j represents the volume of the collocation point $\mathbf{x}_j$. Moreover, β_j is the volume correction factor which determines the portion of V_j falls within the neighbourhood of source node $\mathbf{x}_i$. In this study, β_j value is determined as proposed in (Yu et al. 2011):

$$\beta_j=\begin{cases}1 & \text{for} \quad \|\boldsymbol{\xi}\|\le\delta-0.5\Delta x \\ \dfrac{\delta+0.5\Delta x-\|\boldsymbol{\xi}\|}{\Delta x} & \text{for} \quad \delta-0.5\Delta x<\|\boldsymbol{\xi}\|\le\delta+0.5\Delta x \\ 0 & \text{otherwise}\end{cases} \tag{2.82}$$

The node of interest at which the volume is centered in known as the *source node*. Eq. (2.82) expresses that the volume of nodes close to the boundary of the neighborhood $H(\mathbf{x}_i)$ falls only

partially within the horizon of the source node. Additionally, the distance between two adjacent nodes $\Delta x = \Delta y = \Delta$ is referred to as the *grid spacing*.

2.10 Dynamic relaxation method

Although peridynamics widely has been used to simulate dynamic crack propagation, a few of works focus on quasi-static problems. In this thesis, we use the explicit dynamic relaxation method to investigate thermo-mechanical problems (inertia effects are not considered). Dynamic relaxation method firstly introduced by Day (Day 1965) and then implemented into peridynamics for quasi-static solutions in (Huang et al. 2015; Kilic and Madenci 2010). To employ the dynamic relaxation method in peridynamic equation of the motion, one may introduce artificial damping in Eq. (2.81) as

$$\mathbf{\Lambda}\ddot{\mathbf{u}}(\mathbf{x},t) + C\mathbf{\Lambda}\dot{\mathbf{u}}(x,t) = \sum_{j=1}^{N} \mathbf{f}(\mathbf{u}(\mathbf{x}',t) - \mathbf{u}(\mathbf{x},t), \mathbf{x}' - \mathbf{x})\, \beta(\boldsymbol{\xi}) V_j + \mathbf{b}(\mathbf{x},t) \tag{2.83}$$

where $\mathbf{\Lambda}$ is the fictitious diagonal density matrix and C represents the damping coefficient. There are many different ways to determine the density matrix, $\mathbf{\Lambda}$; however, in this study it is taken as (see (Kilic and Madenci 2010; Underwood 1983))

$$\lambda_{ii} \geq \frac{1}{4}\Delta t^2 \sum_j \left| K_{ij} \right| \tag{2.84}$$

where K_{ij} is the stiffness matrix of the equation system under consideration. By considering the linearize version of the response function for small displacements, an absolute row sum of the stiffness matrix is given by

$$\sum_j \left| K_{ij} \right| = \sum_{i=1}^{N} \sum_{j=1}^{N_e} \beta_j \frac{\left| \boldsymbol{\xi}.\mathbf{e} \right|}{\left| \boldsymbol{\xi} \right|} \frac{9k}{\pi \ell^4} e^{-(|\boldsymbol{\xi}|/\ell)^2} \frac{1}{|\boldsymbol{\xi}|} \tag{2.85}$$

where $\mathbf{e}$ is a unit vector along x , y and z directions. ℓ , β_j , N , N_e and k are internal bond length, integration weight associated with point $\mathbf{x}'_j$, total number of nodes, number of collocation points in the *i*th subdomain and bulk modulus of the material respectively.

The values for damping ratio C is taken, $C = 10^6 : 10^7$ kg/(m^3.s), as proposed by (Huang et al. 2015).

In this thesis, time integration is performed by using the central-difference explicit integration. Given displacement and acceleration of each node $\mathbf{x}_i$ at t^n,($\mathbf{u}_i^n$, $\ddot{\mathbf{u}}_i^n$), velocities and displacements at $t^{n+1} = t_n + \Delta t_{ME}$ can be obtained by (Kilic and Madenci 2010):

$$\dot{\mathbf{u}}^{n+1/2} = \left[\left(2 - C\Delta t_{ME}\right) \dot{\mathbf{u}}^{n-1/2} + 2\,\Delta t_{ME} \boldsymbol{\Lambda}^{-1} \mathbf{F}^n \right] / \left[2 + C\,\Delta t_{ME}\right] \tag{2.86}$$

$$\mathbf{u}^{n+1} = \mathbf{u}^n + \Delta t_{ME}\, \dot{\mathbf{u}}^{n+1/2} \tag{2.87}$$

$$\dot{\mathbf{u}}_i^{n+1} = \dot{\mathbf{u}}_i^{n+1/2} + \frac{\Delta t_{ME}}{2} \ddot{\mathbf{u}}_i^{n+1} \tag{2.88}$$

Hence, the solver can advance to the next time step by:

$$\mathbf{u}_i^{n+1} = \mathbf{u}_i^n + \Delta t_{ME}\, \dot{\mathbf{u}}_i^n + \frac{(\Delta t_{ME})^2}{2} \ddot{\mathbf{u}}_i^n \tag{2.89}$$

where Δt_{ME} stands for the constant mechanical time step, In order to start the aforementioned integration the velocity at $t^{1/2}$ is given by

$$\dot{\mathbf{u}}^{1/2} = \Delta t_{ME}\, \boldsymbol{\Lambda}^{-1} \mathbf{F}^0 / 2 \tag{2.90}$$

2.11 Loading and boundary conditions

Application of boundary conditions in peridynamics is another significant issue which is different from the classical continuum theory. This difference is due to the nonlocal nature

of peridynamics. Since integral operators , rather than partial differential operators, are used to calculate the peridynamic equilibrium equations the traction boundary conditions should be applied over a volume similarly to body forces.

It is noteworthy that all the calculations are under the assumption that a source node is located inside an infinite body. This assumption is not valid for nodes close to the boundaries of the body. This problem is due to an unwilling effect called *softening effect* (Bobaru and Ha 2011; Kilic and Madenci 2010) for peridynamic models. The prescribed boundary condition, should be imposed over a layer of nodes across the corresponding boundaries. The thickness of the layer usually is taken as the horizon value δ.

2.12 Equations of thermal diffusion

The SB-PD theory for heat conduction problem was firstly introduced by Oterkus *et al* (Oterkus et al. 2014b). The non-local interaction between material points, for thermal diffusion problems using the peridynamic framework, is related to the exchange of heat energy. Hence, a material point is able to exchange heat with the points located in its integration domain, $H(\mathbf{x})$. (see Figure 2.7) Consequently, a transient form of the SB-PD thermal diffusion equation can be written as

$$\rho c_v \dot{\theta}(\mathbf{x},t) = \int_{H(x)} \underline{h}[\mathbf{x},t]\langle \mathbf{x}'-\mathbf{x}\rangle - \underline{h}[\mathbf{x}',t]\langle \mathbf{x}-\mathbf{x}'\rangle dV_{\mathbf{x}'} + h_s(\mathbf{x},t) \tag{2.91}$$

where $\underline{h}(\mathbf{x},t)$ represents the heat flow scalar state and $h_s(\mathbf{x},t)$ is the heat source due to volumetric heat generation. In Eq. (2.91), ρ, c_v and $\theta(\mathbf{x},t)$ are the density of the material, specific heat capacity and temperature at point $\mathbf{x}$ respectively.

One may assume that the heat density allocated to material points, $\mathbf{x}$ and $\mathbf{x}'$, is just a function of the temperature difference between these points i.e. the heat density flow that point $\mathbf{x}'$ exerts on point $\mathbf{x}$ ($\underline{h}[\mathbf{x},t]\langle\mathbf{x}'-\mathbf{x}\rangle$) and the point $\mathbf{x}$ exerts on point $\mathbf{x}'$ ($\underline{h}[\mathbf{x}',t]\langle\mathbf{x}-\mathbf{x}'\rangle$) are equal in magnitude but opposite in sign. Accordingly, the heat density flow in BB-PD for the heat diffusion problem takes the following form

$$f_h(\theta'-\theta,\mathbf{x}'-\mathbf{x}) = \underline{h}[\mathbf{x},t]\langle\mathbf{x}'-\mathbf{x}\rangle - \underline{h}[\mathbf{x}',t]\langle\mathbf{x}-\mathbf{x}'\rangle \equiv \frac{1}{2}f_h - (-\frac{1}{2}f_h) \tag{2.92}$$

Therefore, by substituting Eq.(2.92) in Eq.(2.91), the BB-PD heat conduction equation can be written as

$$\rho c_v \dot{\theta}(\mathbf{x},t) = \int_{H(\mathbf{x})} f_h(\theta',\theta,\mathbf{x}',\mathbf{x},t)dV_{\mathbf{x}'} + h_s \tag{2.93}$$

in which, the pairwise heat flow density function, f_h, is given by

$$f_h(\mathbf{x}',\mathbf{x},t) = c_{TH}\frac{\tau(\mathbf{x}',\mathbf{x},t)}{|\boldsymbol{\xi}|} \tag{2.94}$$

where, the temperature difference between the material points $\mathbf{x}'$ and $\mathbf{x}$ at any time, $\tau(\mathbf{x}',\mathbf{x},t)$, can be expressed by

$$\tau(\mathbf{x}',\mathbf{x},t) = \theta(\mathbf{x}',t) - \theta(\mathbf{x},t) \tag{2.95}$$

In Eq. (2.94), c_{TH} stands for the thermal microconductivity. This parameter can be determined by calculating the thermal potential of a material point. (see ref. (Bobaru and Duangpanya 2012; Oterkus et al. 2014b)). The thermal micro-modulus c_{TH} in terms of the thermal conductivity γ and of the horizon radius, δ, for 1D, 2D and 3D cases are given by

$$c_{TH} = \frac{2\gamma}{A\delta^2} \quad \text{one dimensional}$$
$$c_{TH} = \frac{6\gamma}{\pi h\delta^3} \quad \text{two dimensional} \tag{2.96}$$
$$c_{TH} = \frac{6\gamma}{\pi\delta^4} \quad \text{three dimensional}$$

in which, A and h represent the cross-section area and thickness respectively.

Time can be discretized into instants as $t_1, t_2, t_3, \ldots, t_n$. By adapting the one-point Gauss quadrature rule to proceed with the spatial integration, one can discretize Eq. (2.93) as

$$\rho c_v \dot{\theta}_i^n = \sum_{j=1}^{N} f_h(\tau^n(\mathbf{x}_j - \mathbf{x}_i)) V_j + h_{s(i)}^n \tag{2.97}$$

in which, n stands for time step number, i is the point of interest and j denotes the family nodes located in the horizon of a node i . V_j represents the volume of the collocation point $\mathbf{x}_j$. Various time integration can be adapted to numerically evaluate the Eq. (2.97). In this study, forward difference time marching scheme has been employed as

$$\theta_i^{n+1} = \theta_i^n + \frac{\Delta t_{TH}}{\rho c_v}\left\{\sum_{j=1}^{N} f_h(\tau^n(\mathbf{x}_j - \mathbf{x}_i)) V_j + h_{s(i)}^n\right\} \tag{2.98}$$

where, Δt_{TH} is the thermal time step size. It is necessary to restrict this time step size in order to assure the stability condition of the numerical integration. Based on a Von Neumann stability analysis in (Oterkus et al. 2014b; Silling and Askari 2005b), thermal stability condition can be expressed by

$$\Delta t_{TH} < \frac{\rho c_v}{\sum_{j=1}^{N} \frac{c_{TH}}{\|\boldsymbol{\xi}\|} V_j} \tag{2.99}$$

2.13 Thermal boundary conditions

Thermal diffusion boundary conditions might be imposed as temperature, θ , which stands for Dirichlet boundary conditions on the surface of the domain indicated by Γ_F . To impose this boundary condition, it is only necessary to assign a temperature field to each material point located at Γ_F (see Figure 2.8).

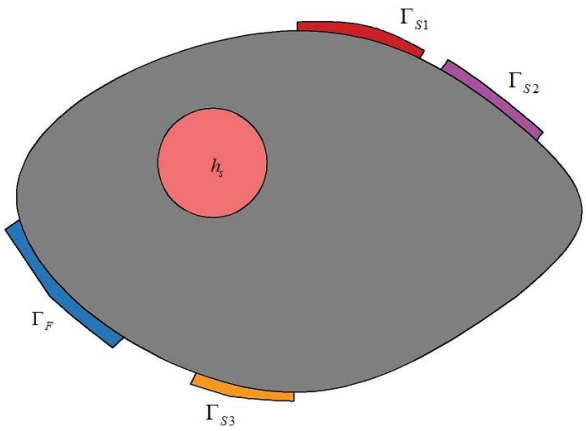

Figure 2.8. Thermal boundary conditions.

On the other hand, Neumann boundary condition can be imposed in the forms of heat flux, convection and radiation. In order to impose heat flux, a heat generation per unit volume (volumetric heat generation) should be assigned to the collocation points located at Γ_{S1} (see Figure 2.8) as

$$\tilde{Q} = \frac{\dot{Q}}{V_f} = \frac{-\int_{\Gamma_{S1}} \mathbf{q}.\mathbf{n}\, d\Gamma_{S1}}{\Gamma_{S1}\Delta} = -\frac{\mathbf{q}.\mathbf{n}}{\Delta} \tag{2.100}$$

in which $\tilde{Q}$ stands for volumetric heat generation. Furthermore, $\mathbf{q}$, V_f and Δ are the heat flux, volume of the material points and grid-spacing respectively.

Another type of Neumann boundary condition, which is used to simulate heat transfer between the surface of a body and its surrounding medium e.g. ceramic quenching test, is defined as the convection boundary condition. Convection boundary condition can be defined as

$$\mathbf{q}(\mathbf{x},t).\mathbf{n} = h\left(\theta(\mathbf{x},t) - \theta_\infty\right) \quad \mathbf{x} \in \Gamma_{S1} \tag{2.101}$$

where, h, is the convective heat transfer coefficient, θ_∞ and $\theta(\mathbf{x},t)$ are the temperature of the fluid surrounding the domain and the temperature of the body on Γ_{S2} surface respectively (see Figure 2.8). Consequently, similar to Eq. (2.100), volumetric heat generation due to convection boundary condition is given by

$$h_s(x,t) = \frac{1}{\Delta} h\left(\theta_\infty - \theta\left(\mathbf{x},t\right)\right) \quad \mathbf{x} \in \Gamma_{S2} \tag{2.102}$$

The third Neumann boundary condition is radiation. Similarly, heat generation per unit volume for radiation heat transfer is assigned to the material points located at Γ_{S3} (see Figure 2.8) as

$$h_s(\mathbf{x},t) = \frac{1}{\Delta} \varepsilon\sigma\left(\theta_{ss}^4 - \theta^4\left(\mathbf{x},t\right)\right) \quad \text{for } \mathbf{x} \in \Gamma_{S3} \tag{2.103}$$

where σ , ε and θ_{ss} are the Stefan-Boltzmann constant, emissivity of the surface and temperature of the surface surrounding the body respectively.

Chapter 3 Peridynamic implementation of different fatigue formulations

3.1 Introduction

The aim of this chapter is to develop new computational tools to study fatigue crack propagation in structural materials. In particular we compare the performance of different degradation strategies to study fatigue crack propagation phenomena adopting peridynamic based computational methods. Three fatigue degradation laws are proposed. The first and the third laws simulate the degradation process reducing the material stiffness as the number of load cycles increases, while the second fatigue law reduces the failure stretch as the number of load cycles increases. Initially a cylinder model is used to compare the computational performance of the three fatigue laws. Then the fatigue degradation strategies are implemented in a peridynamic framework to study fatigue crack propagation phenomena, very few papers adopt this method. The results obtained using the cylinder model allow a comparison on the robustness of the three degradation strategies with respect to variations of two discretization parameters: grid spacing and number of cycles per load increment. The findings of the cylinder model are confirmed then by peridynamic based simulations. Both cylinder model and peridynamic simulations show that the third proposed degradation law is unique in its combination of high accuracy, high stability and low computational cost.

3.2 Explanation of a mathematical cylinder model

The mathematical model consists of a cylinder of radius R which rolls on a horizontal surface initially composed of two coinciding zero-thickness layers, see Figure 3.1 (a) and ref. (Galvanetto et al. 2009). One of the layers is fixed and the other adheres to the surface of the cylinder at the contact point C. The upper layer remains adhered while the cylinder rotates and the contact point moves to the right (see Figure 3.1 (b)). In the initial state the contact point is at x=0 (see Figure 3.1), the rotation, θ, of the cylinder is zero and the line OA, on the cylinder cross section, is vertical. The value of the rotation of the cylinder is defined as the angle between the line OA and the vertical line connecting O to the current contact point.

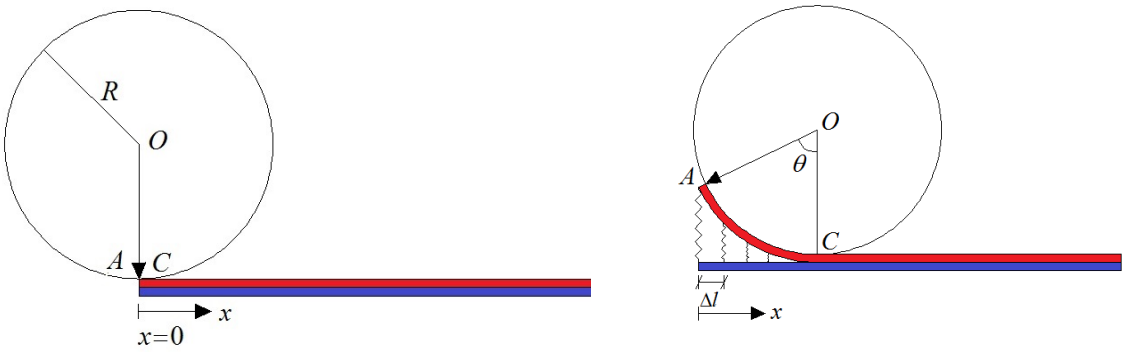

Figure 3.1. (a) Cylinder model in its initial configuration (b) The cylinder model after a rotation θ has occurred, adhesion between the layers is represented as a discrete system of springs.

If a clockwise moment is applied, the cylinder will rotate in the same direction and it will move to the right of its initial position and one layer will be lifted and separated from the other one, as shown in Figure 3.1 (b). An adhesion stress acting between the two layers opposes the motion of the cylinder. The model represents one of the two symmetric halves of the tip of a crack opening in mode I as depicted in Figure 3.2.

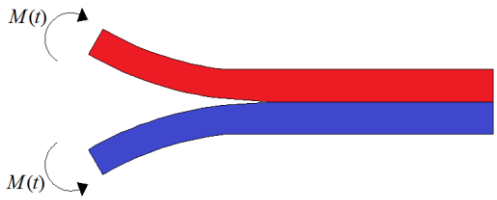

Figure 3.2. Pure moment loading for mode I specimen.

3.2.1 Continuum equations of the model

The model has only one degree of freedom, the rotation of the cylinder θ . The coordinate of the contact point X_{con} represents the crack length, which is linked to the rotation θ as

$$X_{con} = R\theta \tag{3.1}$$

The applied moment, M_a , is in equilibrium with the reaction moment, M_t , due to the stresses in the interface

$$M_t = \int_0^{X_{con}} \sigma(x)(X_{con} - x)\,dx \tag{3.2}$$

3.2.2 Discretization of the model

The motion of the cylinder detaches the two layers. The adhesion between them can be represented as a discrete system of vertical springs, with uniform spacing Δl, that oppose the separation, Figure 3.1.b. The springs are initially unstressed but become stressed as the two layers separate behind the advancing contact point.

A constitutive law for the springs has to be defined to describe the mechanical behavior of the interface which is progressively damaged: the force in the spring eventually reduces to zero (representing complete failure) as the layer separation increases.

The value of R is to be chosen as very large compared to the displacement at which the stretched springs fail so that the springs can be considered to remain vertical while they are stressed.

3.2.2.1 Kinematics

Once X_{con} is known and given the spring spacing Δl, it is easy to identify the number of springs that become active (n) and their coordinates x_i ($i = 1, 2, 3, \ldots n$) .

Figure 3.3 shows that simple geometry is sufficient to define the elongation v_i of the i-th spring and its distance d_i from the contact point.

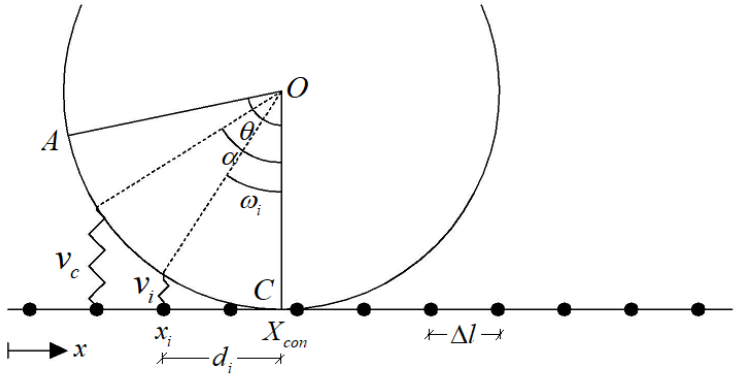

Figure 3.3. Angle, opening displacement and distance from contact point of springs.

Since the springs have a zero initial length, the elongation will be defined as the vertical displacement (v_i) of the top of the spring. Moreover it was previously mentioned that the spring eventually degrades as the displacement is increased and the stress finally reduces to zero. If v_c defines the critical displacement at which failure occurs, then the angle α at which such a displacement is achieved is given by (Figure 3.3):

$$\alpha = \cos^{-1}\left(\frac{R - v_c}{R}\right) \tag{3.3}$$

3.2.2.2 Equilibrium

As the cylinder advances, a number of springs become active. The interface stress (σ_i), which is a function of the opening displacement ($\sigma_i = f(\delta_i)$) can be obtained by using an interface constitutive law.

The interface stress of each spring can then be used to find the spring force (F_i) generated by multiplying this value σ_i by the area which the spring 'represents'. For dimensional reasons the cylinder is assumed to have a width of 1. The interface area associated with a typical spring is therefore $1 \cdot \Delta l$. An exception is for the area of the first spring which is taken as $1 \cdot \Delta l/2$. The value of the force for a typical spring is given by

$$F_i = 1 \cdot \Delta l \, \sigma_i \tag{3.4}$$

The moment (M_i) generated by the spring force with respect to the contact point (C) is obtained by multiplying the force by the distance to the current contact point

$$M_i = d_i \, F_i \tag{3.5}$$

and the total moment (M_t) generated by the springs is found by adding the moments M_i of all the active springs

$$M_t = \sum_{i=1}^{n} M_i \,, \tag{3.6}$$

This is the moment which has to be applied to the cylinder to maintain it in equilibrium for a given applied rotation. The critical moment M_c , which is the minimum value of the moment to break the interface is (Galvanetto et al. 2009):

$$M_c = G_c \, R \tag{3.7}$$

where G_c is the critical energy release rate. The moment M_c of the cylinder model can be found by imposing static equilibrium for a rotation of magnitude α.

3.3 Interface constitutive laws

As it was mentioned previously, a constitutive law is required to describe the behaviour of σ as a function of v. The constitutive law should be defined in such a way that for every value of δ there is a unique value of σ. In this research the bilinear interface constitutive law has been considered (Alfano and Crisfield 2001; Alfano and Crisfield 2003; Crisfield and Alfano 2002; Galvanetto et al. 2009; Peerlings et al. 2000; Qiu et al. 2001; Robinson et al. 2005). There are two parameters, additional to the critical displacement value, v_c, that are needed to define an interface constitutive law: the critical energy release rate (G_c) and the maximum stress value (σ_0). In the present case of the bilinear law the elastic limit relative displacement (v_0) is also required (Galvanetto et al. 2009; Peerlings et al. 2000; Robinson et al. 2005).

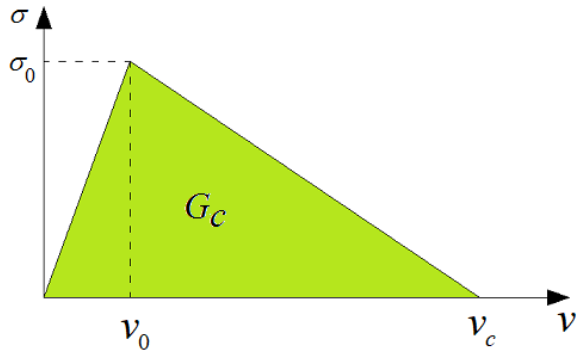

Figure 3.4. Mode I bilinear interface constitutive law.

The critical energy release rate is a physical quantity used in Linear Elastic Fracture Mechanics (LEFM) for defining a criterion of propagation of the delamination in the interface. Its value is measurable in lab tests. It is indirectly used in the definition of the constitutive laws by equating the areas under the stress-displacement curves to the critical energy release rates. Therefore, the total energy dissipated during the delamination is correctly computed at each point although it is not released instantaneously as is assumed in LEFM (Alfano and Crisfield 2001).

δ_0 is the maximum displacement for which the spring behavior is still linear elastic, whereas the ratio (σ_0 / v_0) is clearly linked to the stiffness of the interface.

The constitutive behavior for monotonic increasing relative displacement v will be described below.

The bilinear interface law, as seen in Figure 3.4, is divided into three parts: linear elastic, stiffness degradation and failure. In the first part a linear-elastic behavior is assumed for a relative displacement that is increased from zero, where there is no stress ($\sigma = 0$), until it

reaches the elastic limit v_0. At the elastic limit the stress assumes its maximum value, σ_0. The linear-elastic part of the law is described by the following expression:

$$\sigma = K v \qquad 0 \le v \le v_0 \tag{3.8}$$

where K is the initial stiffness of the interface and is given by

$$K = \sigma_0 / v_0 \tag{3.9}$$

The second part of the interface constitutive law defines the behavior between the elastic limit and the critical displacement v_c. Once the elastic limit is exceeded the interface starts to be degraded. This degradation is described by the following relationship:

$$\sigma = \sigma_0 \left(\frac{v_c - v}{v_c - v_0} \right) \qquad v_0 < v < v_c \tag{3.10}$$

The third and last part of the interface constitutive law is for relative displacement values that are equal or larger than the critical displacement value. When this critical displacement value is reached or exceeded the element fails irreversibly so that no stress can be carried by the interface:

$$\sigma = 0 \quad v \ge v_c \tag{3.11}$$

As it was stated previously the critical energy release rate G_c is equal to the area under the $v - \sigma$ curve, so in this case

$$G_c = \frac{v_c \sigma_0}{2} \tag{3.12}$$

Therefore of the four parameters G_c, v_c, v_0, σ_0 only three are independent.

The constitutive law of the interface can be written as well in terms of a damage variable *D* as:

$$\sigma = K(1-D)v \tag{3.13}$$

where the damage variable is:

$$\begin{cases} D = 0 & 0 \le v \le v_0 \\ D = \dfrac{v_c}{v}\left(\dfrac{v - v_0}{v_c - v_0}\right) & v_0 < v < v_c \\ D = 1 & v \ge v_c \end{cases} \tag{3.14}$$

The increment of the opening displacement from v_1 to v_2 ($v_2 > v_1$) causes an increment of the damage variable:

$$\Delta D = D_2 - D_1 = \frac{v_c v_0}{v_c - v_0}\left(\frac{1}{v_1} - \frac{1}{v_2}\right), \quad \textit{where} \quad v_0 < v_1 < v_c, v_0 < v_2 < v_c, v_2 > v_1 \tag{3.15}$$

3.4 Fatigue damage

If the fatigue phenomenon is involved a time-like independent variable has to be considered, the number of cycles *N* of the external load. The applied load history consists of two components: quasi-static ramping phase and fatigue phase as shown in Figure 3.5.

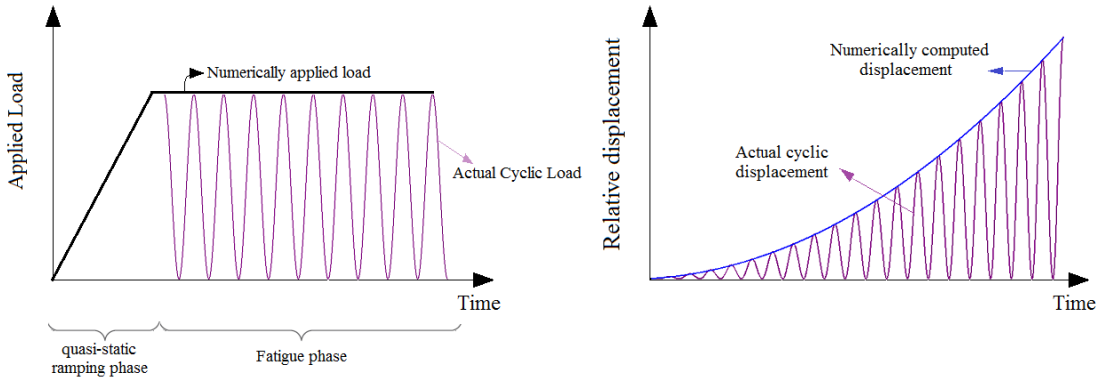

(a) (b)

Figure 3.5. (a) Envelope cyclic load approach and (b) envelope of the displacement for a large number of cycles.

In order to simplify the calculation process some assumptions are made (Peerlings et al. 2000). The first one is related to the cyclic load which is assumed to be sinusoidal and oscillating between zero and a maximum value. Since it would be very computationally expensive to simulate the relative displacement history for every load cycle in each spring, the load numerically applied to the structure is taken as constant and equal to the maximum value of the actual cyclic load as shown in Figure 3.5. Consequently, the relative displacement calculated at the crack tip will be the envelope of its true cyclic variation with time, as shown in Figure 3.5(b) (Galvanetto et al. 2009; Peerlings et al. 2000; Robinson et al. 2005).

We assume that the total damage rate in a spring can be obtained as the sum of the static and the fatigue damage rates as follows

$$\dot{D} = \dot{D}_s + \dot{D}_f \tag{3.16}$$

$\dot{D}_s$ is the rate of static damage due only to the increase in magnitude of v; $\dot{D}_f$ represent the fatigue damage increment due to the repetition of the load cycles and is greater than zero even

if v is constant. As the novelty of this work is in the fatigue part we use the same static damage rate based on the bilinear constitutive law for all different fatigue approaches.

3.4.1 Static damage rate

The static damage rate with respect to time can be obtained from Eq. (3.14) as

$$\dot{D}_s = \frac{\partial D_s}{\partial t} = \frac{v_0 v_c}{v_c - v_0} \frac{\dot{v}}{v^2} \qquad v_0 < v < v_c \tag{3.17}$$

One may integrate Eq. (3.17) over an increment of the number of load cycles (ΔN) as

$$D_{sN+\Delta N} - D_{sN} = \frac{v_0 v_c}{v_c - v_0} \left(\frac{1}{v_N} - \frac{1}{v_{N+\Delta N}} \right) \tag{3.18}$$

in which, D_{sN} and $D_{sN+\Delta N}$ denote the static damage component corresponding to the opening displacements v_N and $v_{N+\Delta N}$ where $v_{N+\Delta N} \geq v_N$. Eq. (3.18) provides the same expression as Eq. (3.15) and therefore clarifies that the static damage component is due only to the increment of the opening displacement.

Once the sum of static and fatigue damage increments has been computed, Eq. (3.13) is used to compute the stress in the spring.

Three strategies are considered to estimate the fatigue part of the damage.

3.4.2 First fatigue degradation strategy

In the first strategy, originally presented in (Galvanetto et al. 2009; Robinson et al. 2005) the fatigue rate is assumed to have the following form:

$$\dot{D}_f = \frac{\partial D_f}{\partial N} = Ce^{\lambda D}\left(\frac{v}{v_c}\right)^{\beta} \tag{3.19}$$

C, λ and β are parameters to be determined by fitting of experimental data. The physical meaning of Eq. (3.19) is that the fatigue damage rate is bigger for bigger relative displacement v and for higher values of the current total damage.

Integrating Eq. (3.19) over a number of loading cycles (ΔN), one may write the increment of fatigue damage as

$$D_{f\,N+\Delta N} - D_{f\,N} = \Delta N \frac{C}{1+\beta} e^{\lambda D_\mu}\left(\frac{v_\mu}{v_c}\right)^{1+\beta} \tag{3.20}$$

Moreover, based on the reference (Galvanetto et al. 2009), D_μ and v_μ are taken as

$$\begin{aligned} D_\mu &= (1-\mu)D_N + \mu D_{N+\Delta N} \\ v_\mu &= (1-\mu)v_N + \mu v_{N+\Delta N} \end{aligned} \tag{3.21}$$

where μ value is 0.7. Additionally, by putting (3.18) and (3.20) into Eq. (3.16), the total damage increment, based on the bilinear constitutive law and stiffness degradation damage (see Figure 3.6), can be obtained as

$$D_{N+\Delta N} - D_N = \underbrace{\frac{v_0 v_c}{v_c - v_0}\left(\frac{1}{v_N} - \frac{1}{v_{N+\Delta N}}\right)}_{static} + \underbrace{\Delta N \frac{C}{1+\beta} e^{\lambda D_\mu}\left(\frac{v_\mu}{v_c}\right)^{1+\beta}}_{fatigue} \tag{3.22}$$

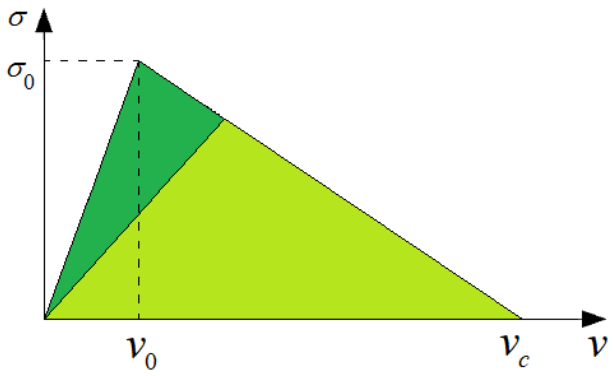

Figure 3.6. First (and third) fatigue law based on stiffness degradation strategy.

Note that in usual numerical procedures the only unknown variable in Eq. (3.22) is $D_{N+\Delta N}$, it appears on both sides of Eq. (3.22) which makes it implicit and nonlinear.

3.4.3 Second fatigue degradation strategy

The second fatigue degradation strategy, originally proposed by the authors in (Zaccariotto et al. 2015b), is based on the reduction of the value of the failure displacement, due to the fatigue phenomenon (Figure 3.7). It can be assumed that the failure elongation of a spring in each increment of load cycle, ΔN, is a function of displacement as follows.

$$v_{cN+\Delta N} = v_{cN} - B\,(v_{N+\Delta N} - v_0)^n\,\Delta N \tag{3.23}$$

where B and n are parameters related to the material behavior when it is subjected to fatigue load cycles and $v_{cN+\Delta N}$ is the failure displacement of a spring after $N+\Delta N$ loading cycles.

The total damage at the end of each load cycle increment can be obtained as

$$D_{N+\Delta N} = \frac{v_0 v_{cN+\Delta N}}{v_{cN+\Delta N} - v_0}\left(\frac{1}{v_0} - \frac{1}{v_{N+\Delta N}}\right) \tag{3.24}$$

Accordingly, the total damage increment in this approach is given by

$$D_{N+\Delta N} - D_N = \frac{v_0 v_{cN+\Delta N}}{v_{cN+\Delta N} - v_0}\left(\frac{1}{v_0} - \frac{1}{v_{N+\Delta N}}\right) - \frac{v_0 v_{cN}}{v_{cN} - v_0}\left(\frac{1}{v_0} - \frac{1}{v_N}\right) \tag{3.25}$$

In the above formula if $\Delta N \to 0$, only the static damage takes place due to the increment of external load so that Eq. (3.25) is simplified to

$$D_{N+\Delta N} - D_N = \frac{v_0 v_{cN}}{v_{cN} - v_0}\left(\frac{1}{v_0} - \frac{1}{v_{N+\Delta N}}\right) - \frac{v_0 v_{cN}}{v_{cN} - v_0}\left(\frac{1}{v_0} - \frac{1}{v_N}\right) = \underbrace{\frac{v_0 v_{cN}}{v_{cN} - v_0}\left(\frac{1}{v_N} - \frac{1}{v_{N+\Delta N}}\right)}_{\text{Static Damage}} \tag{3.26}$$

which is consistent with Eq. (3.18). In Eq. (3.24), the dependence on the number of cycles is implicit in $v_{cN+\Delta N}$ (see Eq. (3.23)) and in the value of the current displacement. Since $D_{N+\Delta N}$ doesn't appear on both sides of Eq. (3.25), this numerical approach, differently from the first strategy, is explicit.

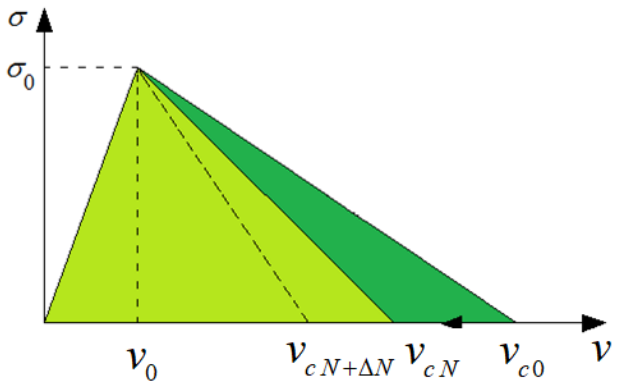

Figure 3.7. Second fatigue law, failure stretch shortening.

3.4.4 Third fatigue degradation strategy

In the third law, which has not presented before, it is assumed that the derivative of fatigue damage with regard to N is given in Eq. (3.27)

$$\dot{D}_f = \frac{\partial D_f}{\partial N} = A'\left(\frac{v}{v_c}\right)^{m'} \tag{3.27}$$

In the above formula, A' and m' are constants related to the material behavior while v represents the elongation of the spring. Eq. (3.27) differs from Eq. (3.19) because in (3.27) the damage rate does not depend on the current value of total damage D.

Updated fatigue damage for crack growth can be determined as (see references (Bak et al. 2016; Peerlings et al. 2000))

$$D_{f\,N+\Delta N} = D_{f\,N} + \int_N^{N+\Delta N} \frac{\partial D_f}{\partial N} dN \tag{3.28}$$

Using a mid-point rule, one may approximately calculate the integral of the fatigue damage rate as

$$\int_N^{N+\Delta N} \frac{\partial D_f}{\partial N} dN \approx A' \Delta N \left(\frac{1}{2}\left(\frac{v_N}{v_c} + \frac{v_{N+\Delta N}}{v_c}\right)\right)^{m'} \tag{3.29}$$

Accordingly, by combining Eq.s (3.29) and (3.18) in Eq. (3.16), the increment of total damage due to an increment ΔN of the number of cycles is given by the following expression, explicit in the unknown $D_{N+\Delta N}$:

$$D_{N+\Delta N} - D_N = \underbrace{\frac{v_0 v_c}{v_c - v_0}\left(\frac{1}{v_N} - \frac{1}{v_{N+\Delta N}}\right)}_{static} + \underbrace{A' \Delta N \left(\frac{1}{2}\left(\frac{v_N}{v_c} + \frac{v_{N+\Delta N}}{v_c}\right)\right)^{m'}}_{fatigue} \tag{3.30}$$

Note that in the third law, as in the first one, damage directly affects the stiffness of the springs as shown in Figure 3.6.

3.5 Comparison of the performance of the three fatigue degradation strategies applied to the cylinder model

In this section we compare the computational performances of the three fatigue degradation strategies proposed in Section 3.4. The fatigue phenomena considered are described by the following Paris law, based on the experimental data gathered from (Asp et al. 2001), (the specimen is under pure mode I loading):

$$\frac{\partial X_{con}}{\partial N} = C_I \left(\frac{G}{G_c} \right)^{m_I} \qquad G_0 < G < G_c \tag{3.31}$$

where C_I and m_I are material parameters, X_{con} and N represent the crack length and number of load cycle respectively. G , G_c and G_0 express the maximum, critical and threshold energy release rates respectively. For the cylinder model, using Eq. (3.7), one may rewrite Eq. (3.31) as

$$\frac{dX_{con}}{dN} = C_I \left(\frac{M_a}{M_c} \right)^{m_I} \tag{3.32}$$

C_I and m_I assume the values given in Table 3.1, provided in reference (Bak et al. 2017). In a log-log graph representing dX_{con} / dN vs G / G_c Paris law is a straight line, as shown by the red line in Figure 3.8.

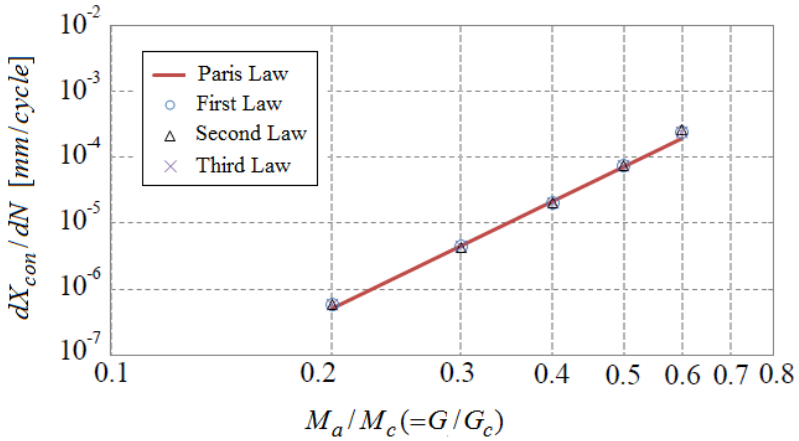

Figure 3.8. Paris law and results produced by the three fatigue degradation strategies..

Parameter	Value
C_1	0.00308 mm/cycle
m_1	5.4
G_c	0.260 Nmm/mm^2
R	100 mm
Δl	0.005 mm
ΔN	100
σ_0	30 N/mm^2
v_0	10^{-6} mm
v_c	0.01733 mm

Table 3.1. Parameter values of Paris law and cylinder model.

The parameters of the three fatigue degradation strategies are chosen so that they reproduce the Paris law and the relevant results are shown in Figure 3.8. The parameter values are shown in Table 3.2. These parameters should be chosen using a curve fitting approach to generate the same slope for the linear part of Paris law which means the same material used for the three fatigue degradation strategies.

Figure 3.9(a) and Figure 3.9(b) show the excellent agreement among the results obtained with the three fatigue laws for two cases $M_a = 0.2M_c$ and $M_a = 0.3M_c$. Given the initial static ramp of the load phase, the crack fatigue propagation starts from a value different from zero.

Fatigue laws	Model specific parameters
First	$C = 2\times10^6,\ \lambda = 0.5,\ \beta = 2.0$
Second	$B = 2540,\ n = 3.8$
Third	$A' = 1.099\times10^{-6},\ m' = 3.0$

Table 3.2. Parameters used in the three proposed fatigue degradation strategies.

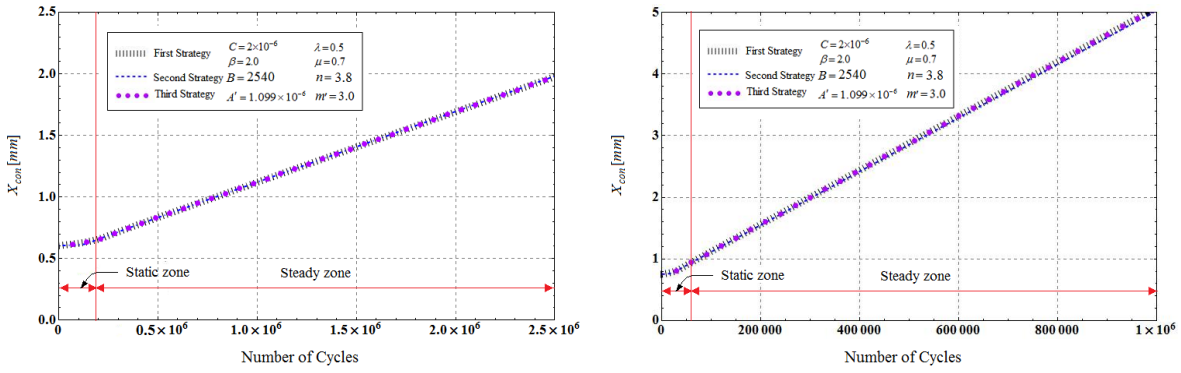

(a) (b)

Figure 3.9. Crack length X_{con} for (a) $M_a = 0.2M_c$ and (b) $M_a = 0.3M_c$ using the three different strategies in the cylinder model.

As depicted in Figure 3.9, the fatigue crack propagation is divided into two phases. At the beginning of crack propagation, one may observe a slow increase of the crack length, which demonstrates the crack initiation phase, and then the crack grows more quickly with a constant slope which determines the steady state part of fatigue crack propagation. It is also apparent

that the slope dX_{con}/dN is bigger for the case $M_a = 0.3M_c$. All three proposed approaches are able to produce the same slope, dX_{con}/dN, with an excellent agreement.

All the codes are developed using standard Matlab 2016 language.The run times reported later are measured on an Intel Core i7-6700HQ 2.60 GHz CPU, on a 64 bit Windows 10 Enterprise system.

It takes 59.84 CPUs and 57.32 CPUs to solve this example using the second and third fatigue laws respectively when $M_a = 0.2M_c$, while this computational time in the first law is 68.01 CPUs which is approximately 15-20% slower than the other two.

Normalized stress vs. displacement graphs are shown in Figure 3.10 for an energy release rate of $G = 0.5G_c$, i.e. the applied moment is $M_a = 0.5M_c$. The three graphs show the stress-elongation curve (σ–v curve) for the same spring in the constant slope propagation phase. The three approaches generate a similar curve due to the simultaneous action of increasing displacement and fatigue cycles. For all cases the area under the σ–v fatigue curve approximates well the green area which represents half of the area under the static bi-linear law.

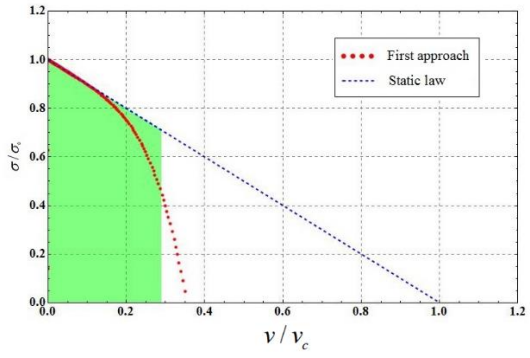

(a)

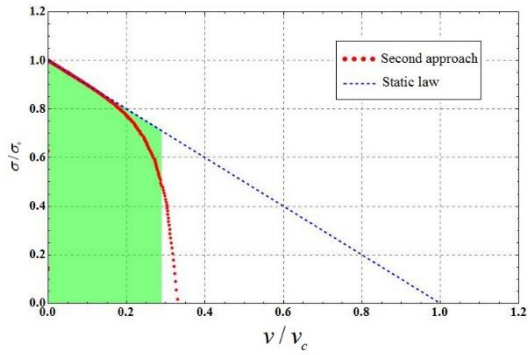

(b)

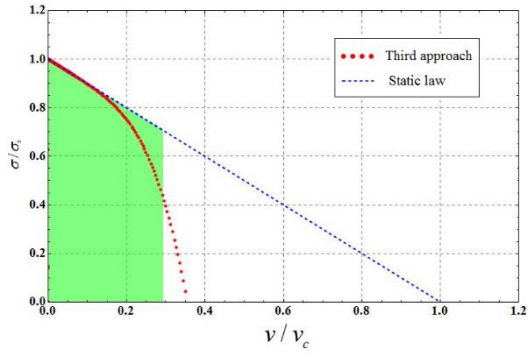

(c)

Figure 3.10. Single spring behavior under static and fatigue load using (a) the First, (b) the second and (c) the third approach. The green area represents half of the triangular area under the bi-linear law, which is a measure of the energy dissipated during static crack propagation.

In many practical problems, the applied G is not constant. So, following what was done also in (Bak et al. 2016), we compare the performance of the three fatigue degradation strategies when used with a variable G (i.e a M_a in the case of the cylinder model). We alter the applied moment instantly as shown in Figure 3.11. The response to this energy release change can be observed in the crack length vs. the number of load cycles as depicted Figure 3.11. It can be noticed that there is a good agreement between all proposed approaches and the Paris law. The results of the theoretical Paris law are obtained by integrating numerically Eq. (3.31) to

evaluate the crack length as a function of energy release rate as (see Reference (Bak et al. 2016))

$$X_{con} = \int C\left(\frac{G(X_{con})}{G_c}\right)^m dN \tag{3.33}$$

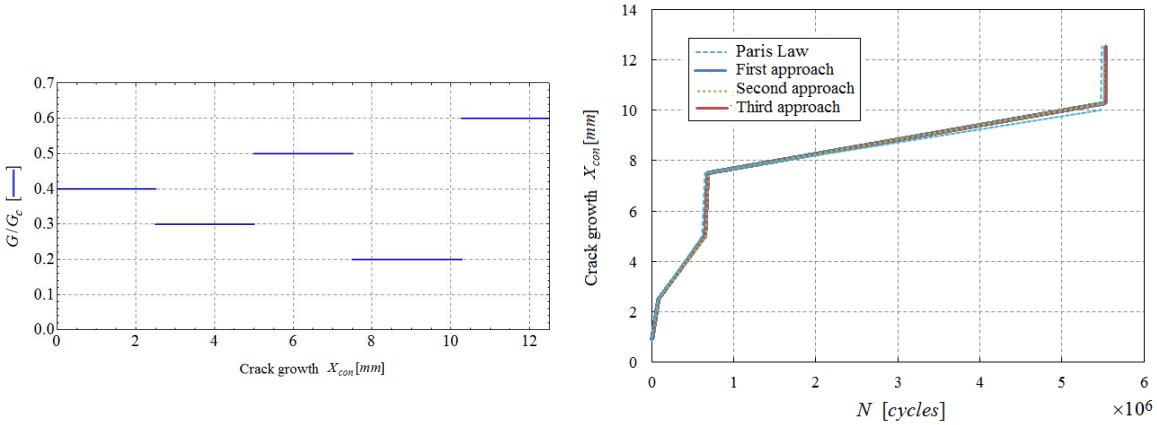

Figure 3.11. Blockwise constant energy release rate G in the cylinder model.

Moreover, in many engineering problems gradual energy release changes occur. Assuming the energy release rate as a function of crack length, one may change the loading condition in a way to obtain an increasing/decreasing energy release rate as depicted in Figure 3.12.

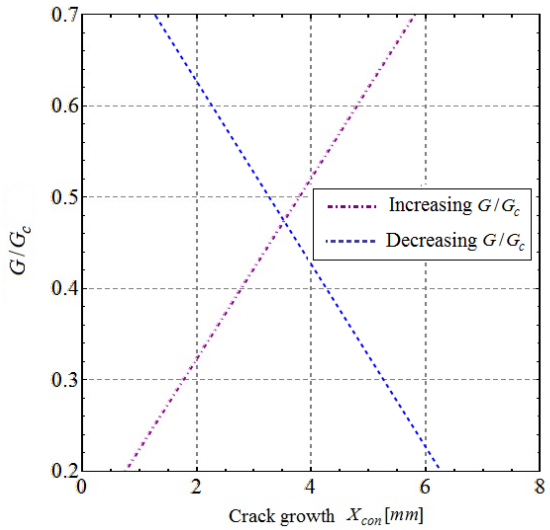

Figure 3.12. Simulation linear dependency of the energy release rate ratio $G(X_{con})/G_c$ on the crack length.

For increasing M_a the first fatigue degradation strategy provides results slightly better than the third law, whereas the results of the second law are worse. For decreasing M_a the three laws have a similar performance (see Figure 3.13).

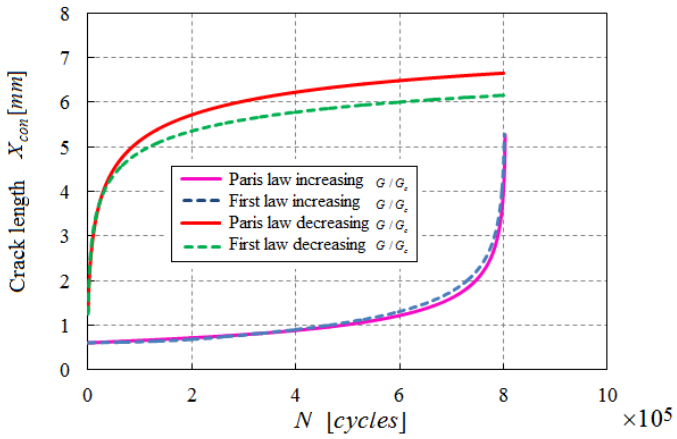

(a)

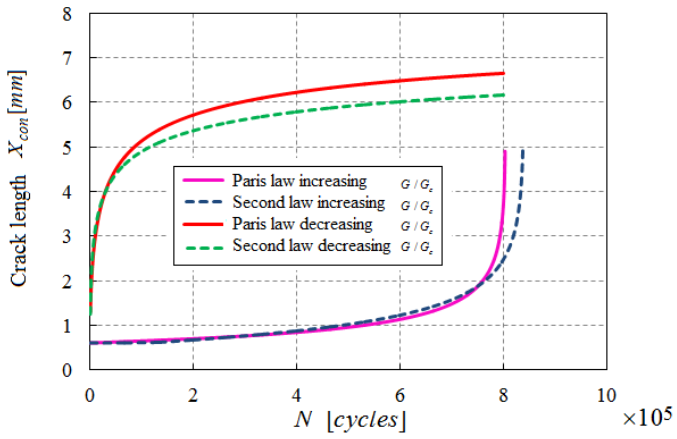

(b)

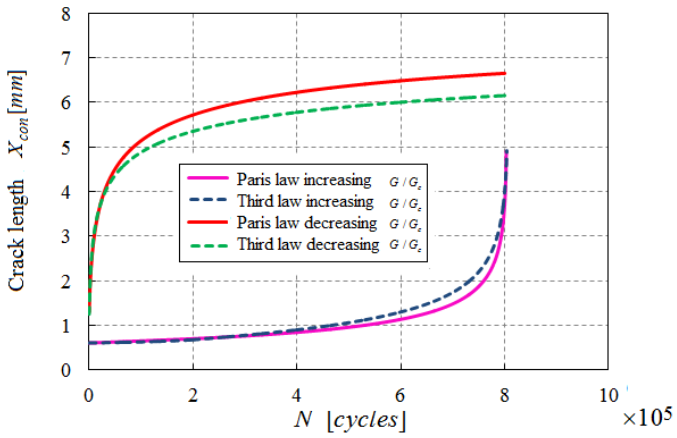

(c)

Figure 3.13. Crack growth for a linearly variable energy release rate as a function of the crack length using (a) the First, (b) the second and (c) the third approach.

3.5.1 Stability of the results with respect to variations of discretization parameters

The results presented in the previous section seem to suggest that the performance of the three degradation strategies are rather similar; the second law has a worse performance in the case of increasing M_a; and the first law requires a longer computational time than the other two, but the overall behavior of the three laws does not exhibit apparent differences. In this section we

want to compare the stability of the results provided by the three laws with respect to variations of two important discretization parameters: Δl, the spring spacing, and ΔN, the increment of load cycles in one step. The best approach is the one for which the slope dX_{con}/dN is affected the least by changes in Δl and ΔN. All parameters are given in Table 3.2. The applied moment is set to be $M_a = 0.2M_c$ and the "exact slope" is generated by adopting small values of ΔN (=100) and Δl (=0.005mm). The 'exact slope' is the same for all fatigue degradation strategies. Note that smaller values of Δl and ΔN increase the computational cost of the procedure but reduce the error in the slope dX_{con}/dN. We consider values of Δl in the range $0.005 \text{ mm} < \Delta l < 0.21 \text{ mm}$, which is divided into 206 uniform subintervals of amplitude equal to 0.001 mm. ΔN is considered in the range $100 < \Delta N < 60000$, which is divided into 600 uniform subintervals. Consequently, 123600 different parameter pairs are taken into account to produce three contour plots of the error, shown in Figure 3.14. For every pair of values (Δl ,ΔN) the relevant slope is computed and compared to the value of the 'exact slope'. Different colors in Figure 3.14 represent different percent errors in the computed slope with respect to 'exact slope'. Analyzing these error-plots, we observe that as Δl and ΔN increase the error in general rises. The region of small error (green zone) is much wider for the third law and much smaller for the second. Therefore, the third law, not only is computationally cheaper than the other methods for the same values of Δl and ΔN, but also can be used with larger values of Δl and ΔN.

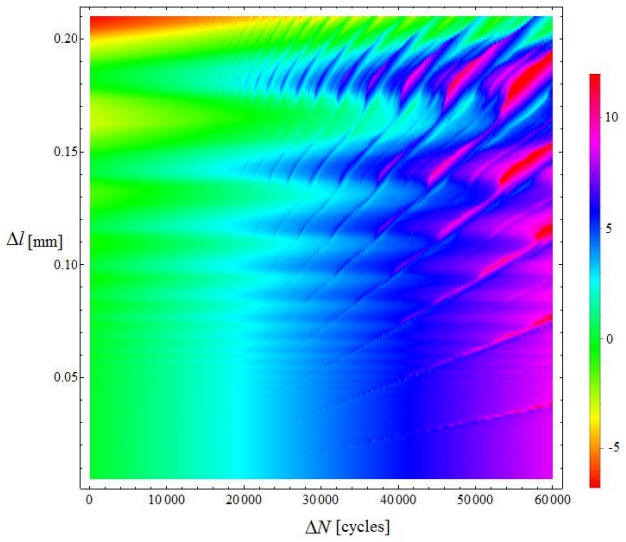
0.20
0.15
Δl [mm]
0.10
0.05
0
10 000
20 000
30 000
40 000
50 000
60 000
ΔN [cycles]
10
5
0
-5

(a)

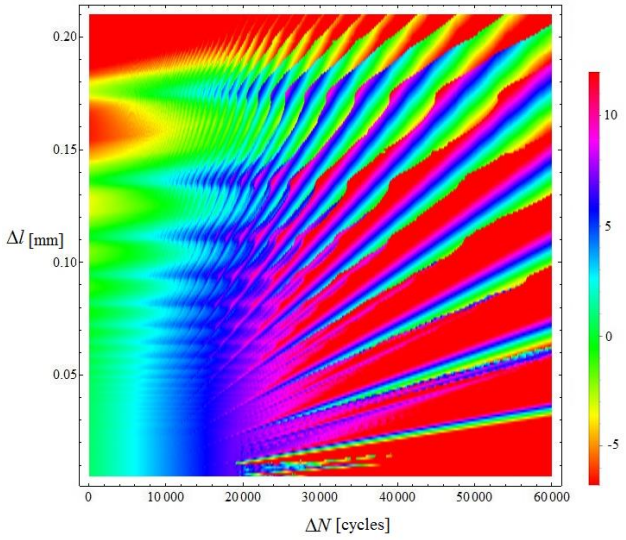
0.20
0.15
Δl [mm]
0.10
0.05
0
10 000
20 000
30 000
40 000
50 000
60 000
ΔN [cycles]
10
5
0
-5

(b)

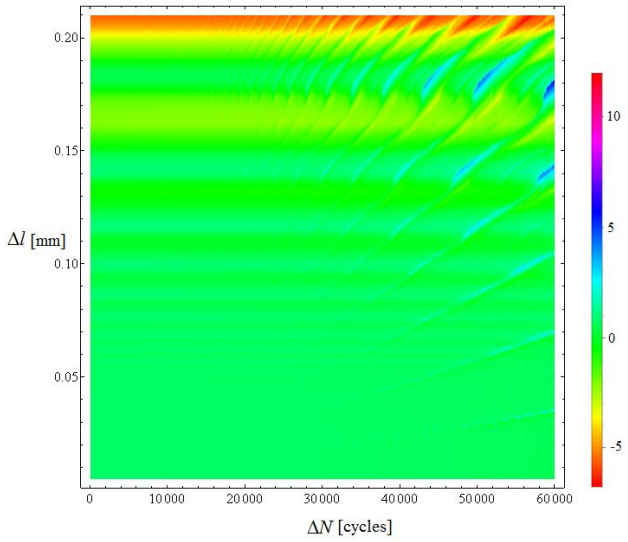

(c)

Figure 3.14. Error plots using bilinear constitutive law for (a) first (b) second and (c) third fatigue laws.

3.6 Peridynamics fatigue model

Bond based peridynamics (BBPD) is a non-local theory of continuum proposed in Reference (Silling 2000). Since the formulation of the theory avoids differentiations and is only based on spatial integration BBPD is particularly suited for describing crack propagation problems. For a point, $\mathbf{x}$, and time, t, the peridynamic static equilibrium equation is written as (see Figure 2.2 (a))

$$\mathbf{0} = \int_{H_x} \mathbf{f}(\mathbf{u}(\mathbf{x}',t) - \mathbf{u}(\mathbf{x},t), \mathbf{x}' - \mathbf{x}) \mathrm{dV}_{\mathbf{x}'} + \mathbf{b}(\mathbf{x},t) \quad for \quad \mathbf{x} \in \Omega \; and \; t \in [t_0, t_f] \tag{3.34}$$

3.6.1 Spatial Discretization

Solution domain is discretized with a set of grid as depicted in Figure 3.15, to approximate the peridynamic equation.

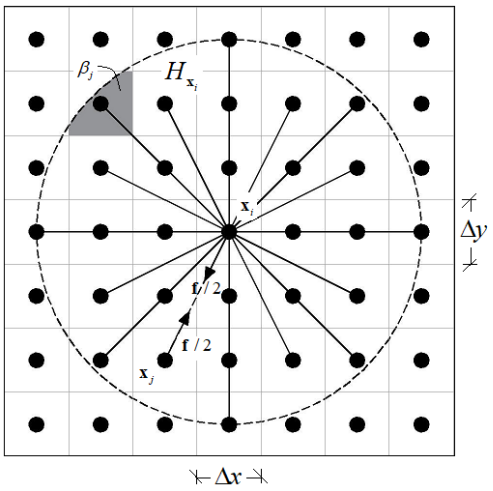

Figure 3.15. A spatial discretization for a peridynamic model.

By adapting the one-point Gauss quadrature rule to proceed with the spatial integration, one can discretize Eq. (3.34) as

$$0=\sum_{j=1}^{N}\mathbf{f}(\mathbf{u}(\mathbf{x}_j,t)-\mathbf{u}(\mathbf{x}_i,t),\mathbf{x}_j-\mathbf{x}_i)\,\beta_j(\boldsymbol{\xi})V_j+\mathbf{b}(\mathbf{x},t) \tag{3.35}$$

6.2 Pairwise force function

As described in Chapter 2,for a PMB material the stretch in a bond is related to the pairwise function $\mathbf{f}$ by Eq. (2.59) (Silling and Askari 2005a). When the stretch reaches its limit value, s_0, the bond breaks so that the global behaviour of the system is nonlinear. In this section the constitutive law of the bond $f=f(s)$ is assumed to be bilinear of the type presented in Section 3.4. The stretch of the bond plays the same role as the elongation of the spring. s_0 is the elastic limit, and s_c is the failure limit of the stretch, as shown in Figure 3.16. According to Reference (Zaccariotto et al. 2015a), G_0 in Eq. (2.78), is the energy required to start the damaging process.

The ratio between G_c and G_0, called k_r, is defined as (see Reference (Zaccariotto et al. 2015a)):

$$k_r = \frac{G_c}{G_0} = \frac{s_c}{s_0} \tag{3.36}$$

Equation (41) provides the value of s_c for the bilinear constitutive law.

(a) (b)

Figure 3.16. magnitude of the bond force f vs bond stretch s law: (a) elastic brittle material (b) elastic-progressively damaging material.

Using a bilinear constitutive law, one may define the pairwise force function magnitude, f, as

$$\begin{cases} f(\mathrm{s}) = c\,s & 0 \le s \le s_0 \\ f(\mathrm{s}) = c\,(1-D)\,s & s_0 < s < s_c \\ f(\mathrm{s}) = 0 & s \ge s_c \end{cases} \tag{3.37}$$

in which, D, represents the total damage (sum of the static damage and the fatigue damage) in the bond.

The damage rate is defined according to the equations shown in Section 3.3. Accordingly, static damage is given by

$$D_s = \begin{cases} \left(\frac{s_{\max} - s_0}{s_{\max}}\right)\left(\frac{s_c}{s_c - s_0}\right) & s < s_{\max} \wedge s_{\max} < s_0 \\ \left(\frac{s_{\max} - s_0}{s_{\max}}\right)\left(\frac{s_c}{s_c - s_0}\right) & s = s_{\max} > s_0 \end{cases} \tag{3.38}$$

where, $s_{\max}$ is the maximum value of the stretch in the deformation history of the bond. Likewise, the increment of static damage can be obtained with respect to Eq. (3.18) as follows

$$D_{sN+\Delta N} - D_{sN} = \frac{s_0 s_c}{s_c - s_0}\left(\frac{1}{s_N} - \frac{1}{s_{N+\Delta N}}\right) \tag{3.39}$$

Moreover, similar to the cylinder model, the increment of total damage in each bond for the first fatigue strategy is given by (see Eq. (3.22))

$$D_{N+\Delta N} - D_N = \underbrace{\frac{s_0 s_c}{s_c - s_0}\left(\frac{1}{s_N} - \frac{1}{s_{N+\Delta N}}\right)}_{static} + \underbrace{\Delta N \frac{C}{1+\beta} e^{\lambda D_\mu}\left(\frac{s_\mu}{s_c}\right)^{1+\beta}}_{fatigue} \tag{3.40}$$

where,

$$s_\mu = (1-\mu)\mathrm{s}_N + \mu s_{N+\Delta N} \tag{3.41}$$

Similarly, for the second fatigue law, the total damage of each bond at the end of a load cycle can be obtained as (see Eq. (3.24))

$$D_{N+\Delta N} = \frac{s_0 s_{cN+\Delta N}}{s_{cN+\Delta N} - s_0}\left(\frac{1}{s_0} - \frac{1}{s_{N+\Delta N}}\right) \tag{3.42}$$

Finally, for the third fatigue law, the increment of total damage of each bond, considering Section 3.4.4, can be written as (see Eq. (3.30)

$$D_{N+\Delta N} - D_N = \underbrace{\frac{s_0 s_c}{s_c - s_0}\left(\frac{1}{s_N} - \frac{1}{s_{N+\Delta N}}\right)}_{static} + \underbrace{A'\Delta N\left(\frac{1}{2}\left(\frac{s_N}{s_c} + \frac{s_{N+\Delta N}}{s_c}\right)\right)^{m'}}_{fatigue} \tag{3.43}$$

6.3. Nonlinearity of the system

The problem becomes nonlinear after the bonds get damaged, therefore, stiffness matrix of the structure is not constant anymore. Various techniques have so far been used to satisfy the equilibrium in the whole structure. In this thesis, the Newton-Raphson (N-R) method is adapted to solve Eq. (3.35) and update the stiffness matrix in each iteration.

Using the conventional finite element concept, one is able to write the relationship between external and internal forces as follows:

$$\mathbf{K}\mathbf{u} = \mathbf{F}_{ext} \tag{3.44}$$

in which, $\mathbf{K}$ represents the global stiffness matrix of the structure, $\mathbf{u}$ and $\mathbf{F}_{ext}$ stand for the nodal displacements and external force vector respectively.

An out of balance force in the whole system is generated due to the nonlinearity of the problem. Therefore, the out of balance force vector is represented by

$$\mathbf{g} = \mathbf{F}_{int} - \mathbf{F}_{ext} = \mathbf{K}\mathbf{u} - \mathbf{F}_{ext} \tag{3.45}$$

The equilibrium is satisfied when the norm of $\mathbf{g}$ is lower a given tolerance.

According to the Newton-Raphson solution, it is needed to calculate the derivatives of $\mathbf{g}$ with respect to the nodal displacement vector, $\mathbf{u}$, as follows

$$\frac{\partial \mathbf{g}}{\partial \mathbf{u}} = \frac{\partial}{\partial \mathbf{u}}\left(\mathbf{K}\mathbf{u} - \mathbf{F}_{ext}\right) = \mathbf{K} + \frac{\partial \mathbf{K}}{\partial \mathbf{u}}\mathbf{u} \tag{3.46}$$

At a given point in which $\mathbf{u} = \mathbf{u}_0$, the term $\frac{\partial \mathbf{g}}{\partial \mathbf{u}}|_{\mathbf{u}=\mathbf{u}_0}$ stands for the tangent stiffness matrix, $\mathbf{K}_T$. One may calculate each component of this matrix by

$$K_{T_{ij}} = K_{ij} + \sum_{m=1}^{N} \frac{\partial K_{im}}{\partial u_j} u_m \tag{3.47}$$

in which, *N,* represents the total number of degrees of freedom. *i* and *j* denote the rows and the columns of the $\mathbf{K}$ and $\mathbf{K}_T$ respectively. For a single bond, tangent stiffness matrix, $\mathbf{K}_T$, in different conditions is given by

$$\begin{cases} \mathbf{K}_T = \mathbf{K} & 0 \le s \le s_0 \\ \mathbf{K}_T = \mathbf{K} + \dfrac{\partial \mathbf{K}}{\partial \mathbf{u}} \mathbf{u} & s_0 < s < s_c \\ \mathbf{K}_T = \mathbf{0} & s \ge s_c \end{cases} \tag{3.48}$$

Above equation expresses that for a bond which still has elastic linear behavior the tangent stiffness matrix does not change and it is equal to the stiffness matrix of the bond. On the other hand, when a bond passes the linear elastic limit, s_0 , and its stretch is less than failure stretch, s_c , tangent stiffness matrix, $\mathbf{K}_T$ should be calculated from Eq. (3.47). In the case that the stretch of a bond exceeds the failure stretch, s_c , the bond is removed from the whole structure and its tangent stiffness matrix, $\mathbf{K}_T$ is equal to zero.

Numerical models with static damage have been comprehensively investigated in (Zaccariotto et al. 2015a). Deformations of the structures have been compared to the exact and FEM numerical solutions and the results are in a good agreement (Zaccariotto et al. 2015a). Since the main contribution of this work is on the fatigue damage, the authors just present the

examples with static and fatigue damage to further validate the fatigue degradation strategies in a peridynamic framework.

3.6.2 Double cantilever beam peridynamic example

In order to verify the indications of the cylinder model, a double cantilever beam is simulated with a BBPD based code as depicted in Figure 3.17. The beam has the length of $L = 0.0161$ m and width of $W = 0.0029$ m. Its Young's modulus and pre-crack length are specified as $E = 70$ GPa, $a = 0.005$ m. The applied moment is $M_a = 0.048$ Nm which is sufficient to introduce static damage in several bonds during the initial static ramp. Furthermore, based on Eq. (3.36): $k_r = 20$.

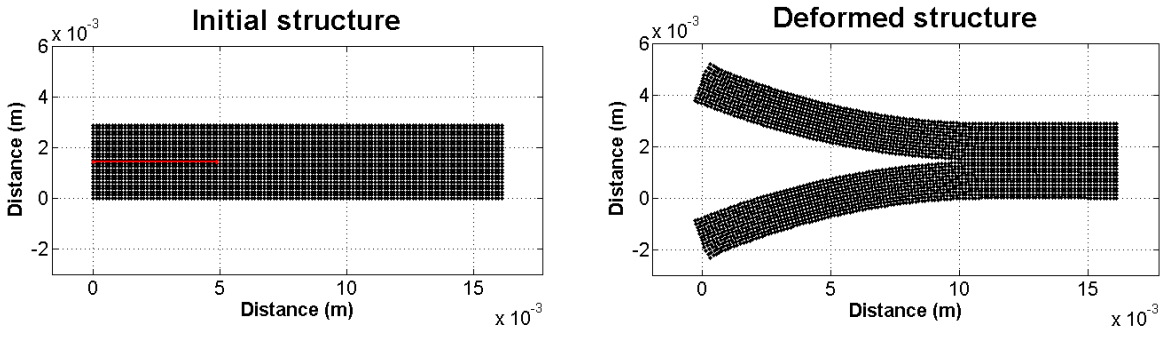

(a) (b)

Figure 3.17. Double cantilever beam model discretized with a BBPD software; (a) Initial structure with a pre crack of $a = 0.005$ m (b) Deformed structure after 4×10^6 load cycles (a scale factor of 20 has been applied to displacement values).

Assuming a constant horizon size, $\delta = 3.75\times10^{-4}$ m, and the grid spacing, Δl, namely $m = \delta / \Delta l$, we are able to examine the efficiency of each fatigue low by using m-convergence approach, three different values of m and Δl are used as: $m = 2, 3, 4$ and $\Delta l = 1.8971\times10^{-4}, 1.25\times10^{-4}, 9.4298\times10^{-5}$ m respectively. In Figure 3.18, the slope of the lines

'crack-length vs number of cycles' in the third law converge for m values equal to 3 and 4. Due to the fact that $m = 3$ is computationally less expensive than $m = 4$, $m = 3$ is employed for the rest of analysis.

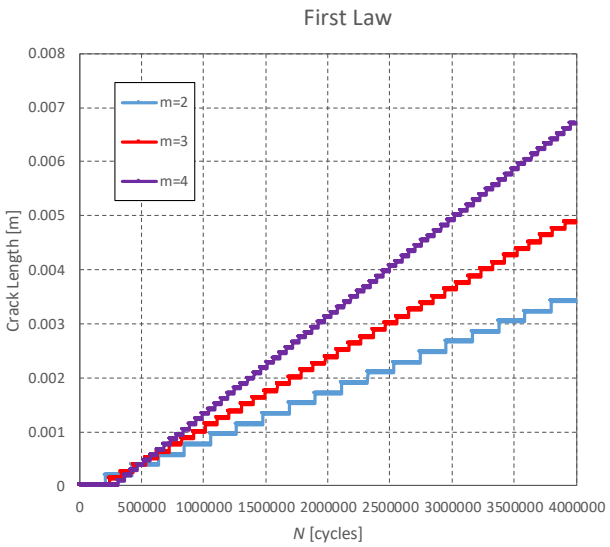

(a)

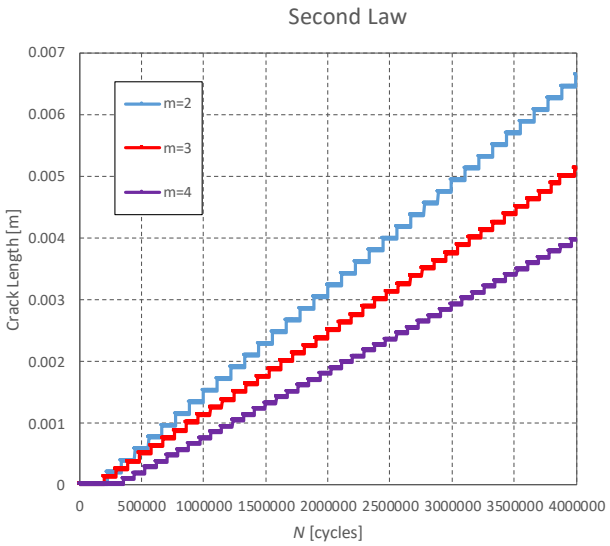

(b)

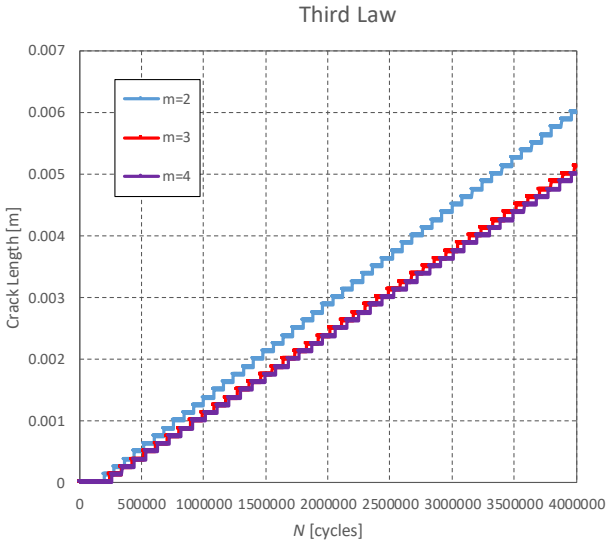

(c)

Figure 3.18. Slope of the lines 'crack-length vs number of cycles' by using fixed values of δ and ΔN ($\delta = 3.75 \times 10^{-4}$ and $\Delta N = 1000$) and different m values for the (a) first (b) second and (c) third fatigue laws.

This example has been solved using different grid spacing as $\Delta l = 6.27 \times 10^{-5}$ m , $\Delta l = 1.06 \times 10^{-4}$ m and $\Delta l = 1.25 \times 10^{-4}$ m ; and different increments of load cycles, ΔN= 1000, 10000 and 50000 for the first and the third proposed fatigue laws, in contrast, due to convergence problems we used smaller values of 500, 1000 and 10000 for the second fatigue law. (See Table 3.3).

In this example, the crack length with respect to the number of load cycles, N , is computed by using the three fatigue strategies (See Figure 3.20).

Table 3.3. Ranges of ΔN and Δl investigated using the first (purple triangle), the second (red square) and the third (green circle) fatigue laws

ΔN / Δl (m)	500	1000	10000	50000
6.27×10^{-5}	------	------	■	▲●
1.06×10^{-4}	■	▲■●	▲■●	▲●
1.25×10^{-4}	■	▲■●	▲■●	▲●

Assuming a constant parameter, $m = 3$, one can examine the efficiency of the fatigue laws via δ -convergence approach (see Figure 3.19). The horizon size, δ, is reduced and the grid spacing is equal to $\Delta l = \delta / m$.

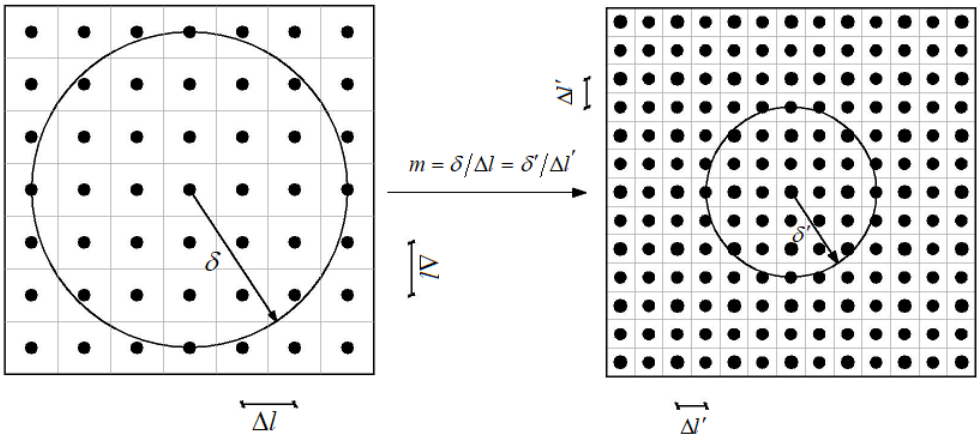

Figure 3.19. δ_H - Convergence with a fixed m ratio.

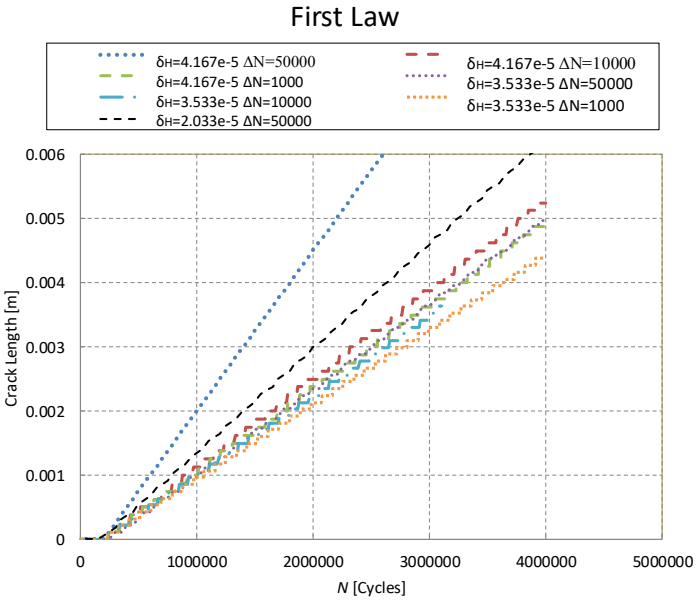
First Law
δH=4.167e-5 ΔN=50000
δH=4.167e-5 ΔN=1000
δH=3.533e-5 ΔN=10000
δH=2.033e-5 ΔN=50000
δH=4.167e-5 ΔN=10000
δH=3.533e-5 ΔN=50000
δH=3.533e-5 ΔN=1000
Crack Length [m]
0.006
0.005
0.004
0.003
0.002
0.001
0
0
1000000
2000000
3000000
4000000
5000000
N [Cycles]

(a)

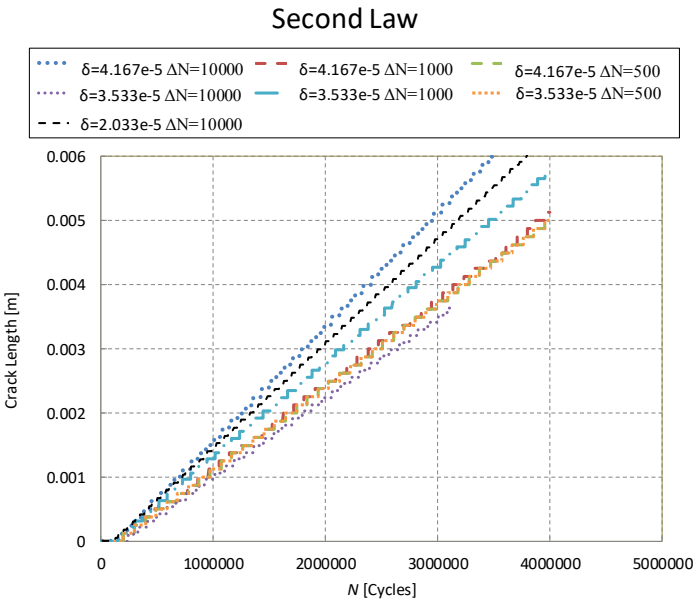
Second Law
δ=4.167e-5 ΔN=10000
δ=4.167e-5 ΔN=1000
δ=4.167e-5 ΔN=500
δ=3.533e-5 ΔN=10000
δ=3.533e-5 ΔN=1000
δ=3.533e-5 ΔN=500
δ=2.033e-5 ΔN=10000
Crack Length [m]
0.006
0.005
0.004
0.003
0.002
0.001
0
0
1000000
2000000
3000000
4000000
5000000
N [Cycles]

(b)

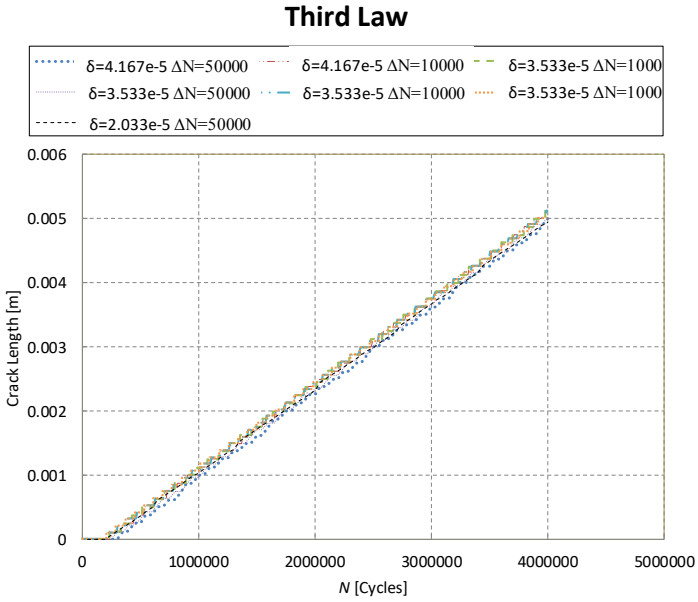

(c)

Figure 3.20. Number of cycles vs. crack length for different values of δ and ΔN for (a) the first (b) the second and (c) the third laws.

Figure 3.20 shows the second law to be much more sensitive to parameter variations than the other two: it does not work for ΔN= 50000 and for smaller values of ΔN provides results that are clearly more scattered than those produced by third law. Moreover the comparison between Figure 3.20 (a) and Figure 3.20 (b) shows that if the lines in Figure 3.20 (a) obtained for ΔN= 50000 are neglected, since there is no equivalent counterpart in Figure 3.20 (b), the results of the second law are worse even than those of the first law. Finally comparing Figure 3.20 (a) and Figure 3.20 (c) confirms the findings of the cylinder model: the third law is much more stable than the other two and provides very similar values of the slope of the line 'crack-length vs number of cycles' in a reasonably wide range of values of δ and ΔN.

Additionally, Figure 3.20 shows that the third fatigue law is less sensitive than the other two to the horizon size, δ .

Both the cylinder model and the DCB discretized with the peridynamic based code confirm that the third law is the best of the three considered in the present work because it is more stable with respect to the variations of the discretization parameters and it is cheaper from a computational point of view.

3.6.3 Experimental validation of the model

To further validate the presented numerical methods, we simulate a DCB test, which is taken from an experimental study (Juntti et al. 1999), using a BBPD code. Due to the good convergence and high computational speed of the third fatigue law which represented in previous sections, hereinafter we only use the third law for the rest of the examples. In this example, we investigate the effectiveness of the selected fatigue degradation strategy by comparing with the experimental data (Juntti et al. 1999). The specimen used for this simulation is shown in Figure 3.21. The beam has the length of $L = 0.15$ m, thickness of $W = 0.0031$ m and width of $B = 0.02$ m. Its Young's modulus, Poisson's ratio and pre-crack length are specified as $E = 120$ GPa, $\nu = 0.3$ and $a = 0.035$ m. Although the specimen is 3D we simplify it into a 2D plain strain peridynamic model. The specimen arms are loaded under pure mode I with opposing moments as depicted in Figure 3.2. (This type of loading with constant applied moment, M_a, cause a constant crack growth length so that the energy release rate is independent of crack length). Bilinear constitutive law parameters are set as: $G_c = 260$ J/m^2 and $k_r = 4.38$. Moreover, fatigue constant parameters of the selected fatigue approach are shown in Table 4.3.

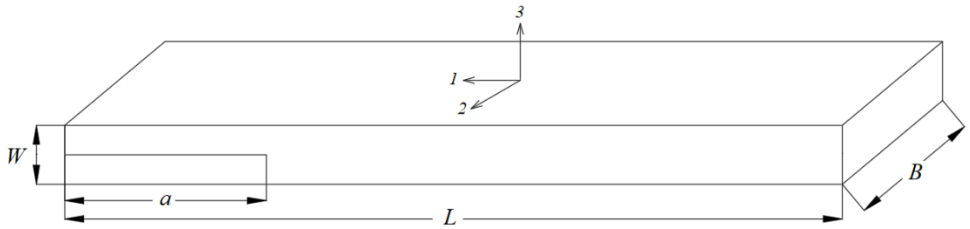

Figure 3.21. Geometry of the specimen.

The energy release rate under pure mode I for a DCB test, is related to the applied moment, M_a , as (Mi and Crisfield 1996)

$$G = \frac{M_a^2}{B E I} \tag{3.49}$$

where, I , is the second moment of area of the specimen arm.

Table 3.4. Parameters used in the proposed fatigue degradation strategies for the DCB model.

Fatigue law	Model specific parameters
Third	$A' = 10^7, m' = 4.0$

In a log-log graph representing dX_{con} / dN vs G / G_c , the third fatigue law using $m = 3$ and $m = 4$, is able to produce the linear part of Paris plot (see Figure 3.22).

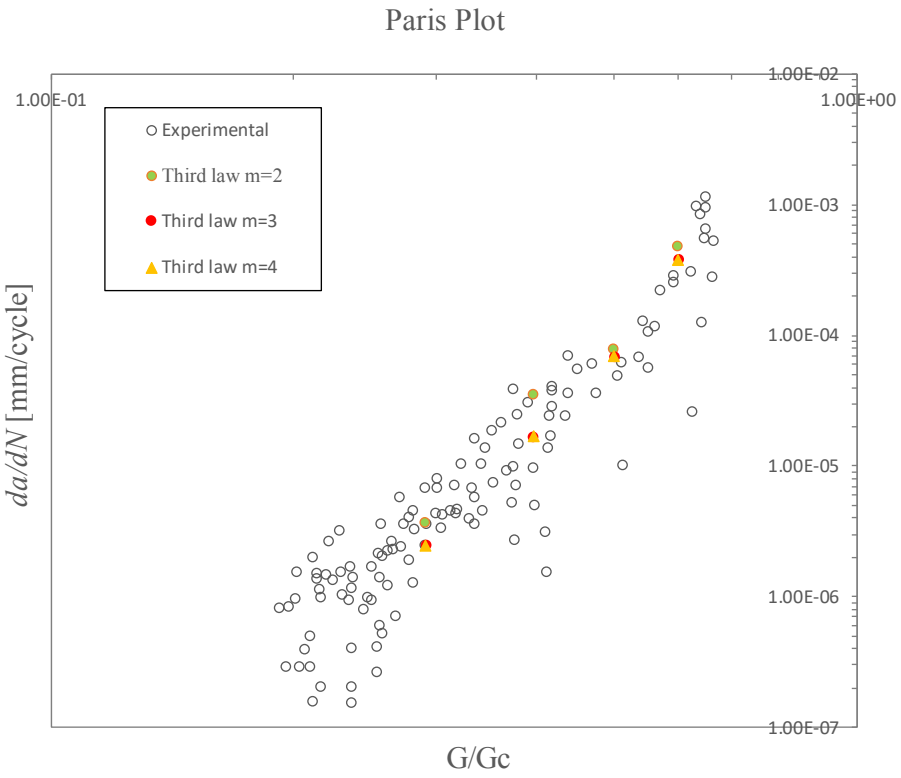

Figure 3.22. Paris plot for mode I with experimental and BBPD numerical results.

3.6.4 Center cracked beam with a hole

In this section, fatigue crack propagation is simulated in a single notched beam with a hole by using the third fatigue law (see Figure 3.23). Experimental data on this test can be found in (Miranda et al. 2003). As shown in Figure 3.23, the beam is loaded in two points at the top and supported in two other points at the bottom. This problem has been solved under plain strain conditions with the physical parameters of: $E = 205\,\text{GPa}$, $\nu = 0.3$, $a = 0.025\,\text{m}$ and $P = 100$ N. Bilinear constitutive law parameters are set as: $G_c = 1.07\times10^5\ \text{J/m}^2$, $\delta = 1.143\times10^{-3}$, $m = 4$ and $k_r = 4.00$. Moreover, fatigue constant parameters are taken as: $\text{A}' = 2.1\times10^8$ and $m' = 4.0$

.

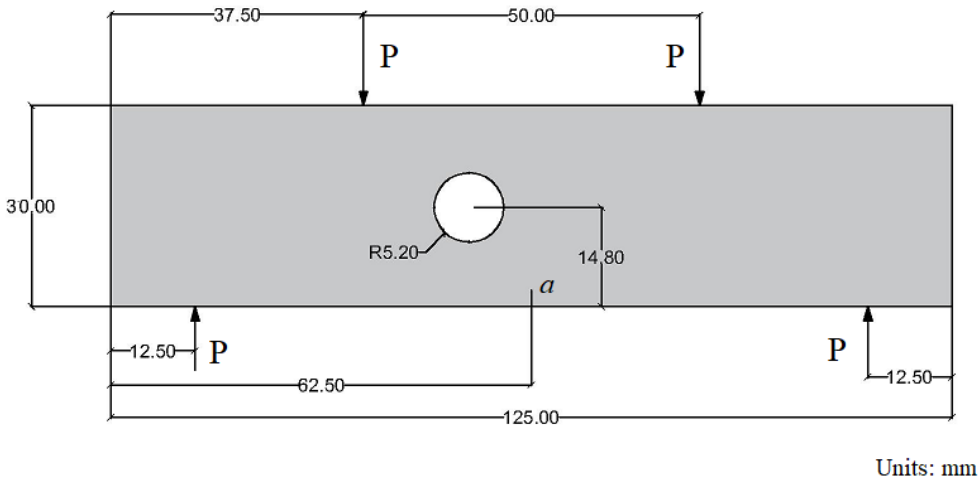

Figure 3.23. Beam with a center crack, loaded in two points and supported in two points.

The solution domain is discretized with a 106×438 uniform grid of nodes which results in 45,390 nodes. This example has been solved up to 6.7×10^5 load cycles using $\Delta N = 50000$ cycles. As shown in Figure 3.24, the crack path grows toward the center hole. Moreover, the crack path is in a very good agreement with experimental data in (Miranda et al. 2003).

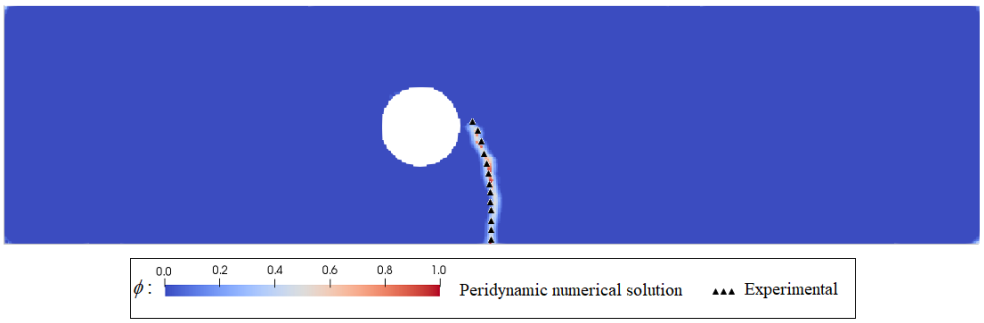

Figure 3.24. Comparison of the crack paths between numerical results and experimental results.

Chapter 4 Simulation of thermo-mechanical problems in brittle materials using an adaptive multi-grid peridynamic method

4.1 Introduction

In this chapter, a thermo-mechanical coupled peridynamic model using adaptive grid refinement technique is developed to investigate the complex crack propagation path in ceramics. By introducing couple grids with different spacing, an efficient algorithm is established to apply the refinement adaptively. Compared to the standard peridynamic model with the uniform grid, this approach allows to increase the resolution of analysis merely in the critical (discontinuous) zones. Moreover, no loss of volume is observed between different grid zones (Shojaei et al. 2018). Loss of volume is an important issue, and it can be considered as one of the sources of ghost forces (see (Bobaru and Ha 2011; Dipasquale et al. 2014)). The performance of this approach is explored in solving 2D thermo-elastic problems and then it is applied to study the fracture of disk shape ceramic specimens under central thermal shock. Finally, the proposed numerical approach is adapted to investigate thermal shock behavior of thin rectangular and circular slabs. The accuracy of the method is scrutinized by comparing the numerical results with the Finite Element Method (FEM), experimental data in the literature

and standard peridynamic with uniform discretization. An excellent agreement is achieved at a much smaller computational cost.

4.2 Problem description

Assume that the solution domain, Ω, is divided into two subdivisions: Ω^+ and Ω^-. The subdivision which is discretized by a grid spacing Δx^+ and a horizon δ^+ is known as Ω^+, whereas, the subdivision with the finer grid spacing $\Delta x^- < \Delta x^+$ and characterized by a horizon δ^- is represented by Ω^-. In this study, it is assumed that the finely discretized zone Ω^- grows only where it is essential (see Figure 4.1). This algorithm is used in order to efficiently optimize the use of computational resources.

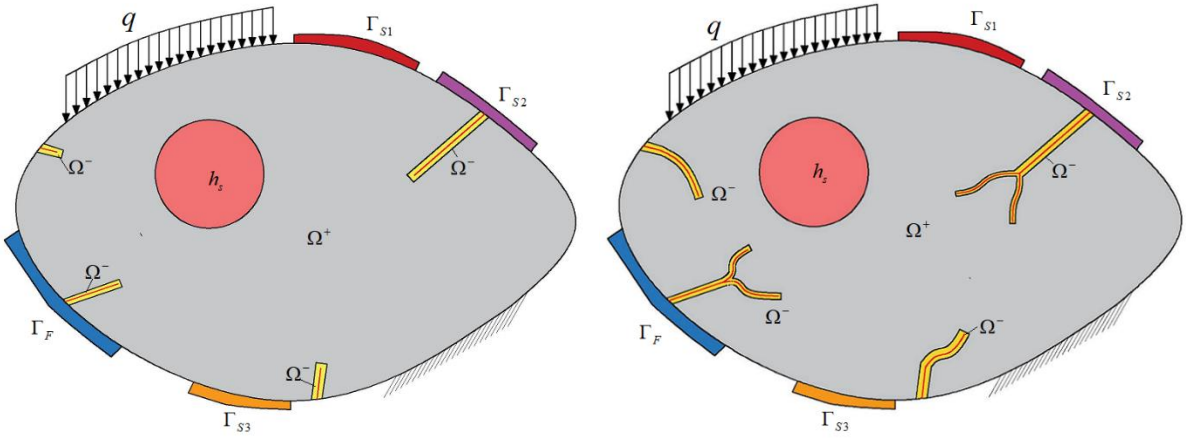

Figure 4.1. Adaptive refinement strategy.

4.3 Coupling grids with different grid size

Using this new technique, one is able to couple any two peridynamic grids with various grid-spacing. This technique is usable for both mechanical and the thermal parts of the procedure.

To illustrate, a 1D problem domain which is partially described by a coarse grid and partially by a fine grid is considered as depicted in Figure 4.2. Green squares are related to the main coarse grid while the yellow circles are the main nodes of the fine grid. The curved lines demonstrate the peridynamic bond interactions. In Figure 4.2, the m ratio is $m = 2$ i.e. each node interacts with two nodes on each side. Although various m values and horizon sizes can be adapted in this model, for the sake of simplicity the horizon size is taken as $\delta = 2\Delta x$. By adding some fictitious coarse and fine sets of nodes and activating them on the boundaries of the domain where the two grid spacing are supposed to be coupled, one can construct the linear system of the equations for a unique physical system. The distance, l_0, between the two portions is considered to be smaller than both δ^+ and δ^-.The fictitious nodes for the coarse and fine grid spacing are represented by unfilled-dashed squares and circles respectively. Moreover, the red square and circles shown in Figure 4.2 stand for the fictitious nodes activated where the two sets of grids are coupled. In fact, the activated fictitious nodes are used to make the real nodes located near the interface between the parts seem surrounded by a complete horizon (of their own type), as they are subjected to force interactions from the other part by means of the fictitious nodes. Hence, by using this method, the problem of surface effect in the interface zone between parts with different grid spacing may be reduced.

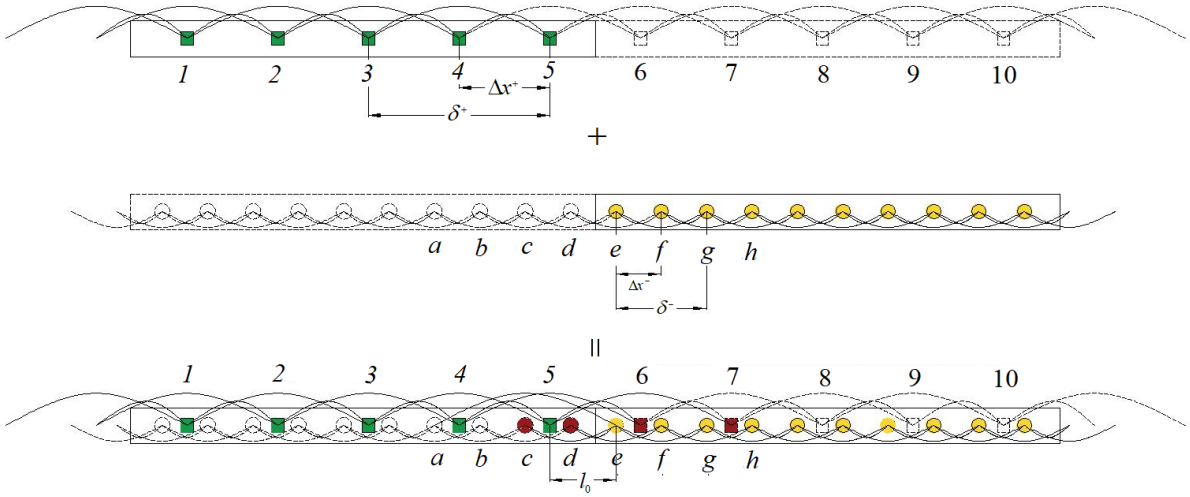

Figure 4.2. The coupling strategy in 1D problem.

By using the stiffness matrix, $\mathbf{K}$, for the equilibrium of the system, some non-standard terms emerge in the rows corresponding to the equilibrium of the real nodes, connected to the fictitious nodes. For the real nodes which are not connected to the fictitious nodes, usual equations illustrated in (Belytschko 1989; Bobaru et al. 2015) are used.

The stiffness matrix of a bond between two generic nodes, $\mathbf{x}_i$ and $\mathbf{x}_j$, based on small deformation assumption, is given by

$$\mathbf{k} = \frac{c_{ME,TH}}{|\boldsymbol{\xi}|}\beta(\boldsymbol{\xi})V_i V_j \begin{bmatrix} 1 & -1 \\ -1 & 1 \end{bmatrix} \tag{4.1}$$

As for instance, node *3*, in Figure 4.2, represents a node interacting only with the real nodes. The equilibrium of the equations for this node can be written as:

$$\begin{cases} -\alpha_{31}k_{ME}^{+}u_1 - \alpha_{32}k_{ME}^{+}u_2 + (\alpha_{31}+\alpha_{32}+\alpha_{34}+\alpha_{35})k_{ME}^{+}u_3 - \alpha_{34}k_{ME}^{+}u_4 - \alpha_{35}k_{ME}^{+}u_5 = F_3 \\ -\alpha_{31}k_{TH}^{+}\theta_1 - \alpha_{32}k_{TH}^{+}\theta_2 + (\alpha_{31}+\alpha_{32}+\alpha_{34}+\alpha_{35})k_{TH}^{+}\theta_3 - \alpha_{34}k_{TH}^{+}\theta_4 - \alpha_{35}k_{TH}^{+}\theta_5 = h_{s3} \end{cases} \tag{4.2}$$

in which

$$\alpha_{ij} = \frac{\beta\left(x_j - x_i\right)}{\left|x_j - x_i\right|} \tag{4.3}$$

F_i and $h_{s(i)}$ are the external force and heat source applied to node i respectively, $k_{ME}^{+} = c_{ME}^{+} V_i^{+} V_j^{+}$ and $k_{TH}^{+} = c_{TH}^{+} V_i^{+} V_j^{+}$.

In contrast, for the nodes connected to active fictitious nodes, some non-standard terms appear in the equilibrium equations. As for instance, the equilibrium equation of node 4 is

$$\begin{cases} -\alpha_{42}k_{ME}^{+}u_2 - \alpha_{43}k_{ME}^{+}u_3 + \left(\alpha_{42}+\alpha_{43}+\alpha_{45}+\alpha_{46}\right)k_{ME}^{+}u_4 - \alpha_{45}k_{ME}^{+}u_5 - \alpha_{46}k_{ME}^{+}u_6 = F_4 \\ -\alpha_{42}k_{TH}^{+}\theta_2 - \alpha_{43}k_{TH}^{+}\theta_3 + \left(\alpha_{42}+\alpha_{43}+\alpha_{45}+\alpha_{46}\right)k_{TH}^{+}\theta_4 - \alpha_{45}k_{TH}^{+}\theta_5 - \alpha_{46}k_{TH}^{+}\theta_6 = h_{s(4)} \end{cases} \tag{4.4}$$

The displacement and temperature at node *6* (u_6 , θ_6), can be obtained by a linear interpolation between node *e* and *f*. Therefore, Eq. (4.4) takes the following form:

$$\begin{cases} -\alpha_{42}k_{ME}^{+}u_2 - \alpha_{43}k_{ME}^{+}u_3 + \left(\alpha_{42}+\alpha_{43}+\alpha_{45}+\alpha_{46}\right)k_{ME}^{+}u_4 - \alpha_{45}k_{ME}^{+}u_5 - \alpha_{46}k_{ME}^{+}\left(c_e u_e + c_f u_f\right) = F_4 \\ -\alpha_{42}k_{TH}^{+}\theta_2 - \alpha_{43}k_{TH}^{+}\theta_3 + \left(\alpha_{42}+\alpha_{43}+\alpha_{45}+\alpha_{46}\right)k_{TH}^{+}\theta_4 - \alpha_{45}k_{TH}^{+}\theta_5 - \alpha_{46}k_{TH}^{+}\left(c_e\theta_e + c_f\theta_f\right) = h_{s(4)} \end{cases} \tag{4.5}$$

in which, c_e and c_f are the linear combination coefficients related to the values of the geometric parameters of the two grids.

Similarly, the equilibrium equations for node *5* assumes the following form:

$$\begin{cases} -\alpha_{53}k_{ME}^{+}u_3 - \alpha_{54}k_{ME}^{+}u_4 + \left(\alpha_{53}+\alpha_{54}+\alpha_{56}+\alpha_{57}\right)k_{ME}^{+}u_5 - \alpha_{56}k_{ME}^{+}\left(c_e u_e + c_f u_f\right) - \alpha_{57}k_{ME}^{+}\left(c_g u_g + c_h u_h\right) = F_5 \\ -\alpha_{53}k_{TH}^{+}\theta_3 - \alpha_{54}k_{TH}^{+}\theta_4 + \left(\alpha_{53}+\alpha_{54}+\alpha_{56}+\alpha_{57}\right)k_{TH}^{+}\theta_5 - \alpha_{56}k_{TH}^{+}\left(c_e\theta_e + c_f\theta_f\right) - \alpha_{57}k_{TH}^{+}\left(c_g\theta_g + c_h\theta_h\right) = h_{s(5)} \end{cases} \tag{4.6}$$

In an analogous way, for a node located in the fine grid zone and connected to the activated fictitious nodes e.g. *e* equilibrium equations is given by:

$$\begin{cases} -\alpha_{ec}\bar{k}_{ME}u_c - \alpha_{ed}\bar{k}_{ME}u_d + \left(\alpha_{ec}+\alpha_{ed}+\alpha_{ef}+\alpha_{eg}\right)\bar{k}_{ME}u_e - \alpha_{ef}\bar{k}_{ME}u_f - \alpha_{eg}\bar{k}_{ME}u_g = F_e \\ -\alpha_{ec}\bar{k}_{TH}\theta_c - \alpha_{ed}\bar{k}_{TH}\theta_d + \left(\alpha_{ec}+\alpha_{ed}+\alpha_{ef}+\alpha_{eg}\right)\bar{k}_{TH}\theta_e - \alpha_{ef}\bar{k}_{TH}\theta_f - \alpha_{eg}\bar{k}_{TH}\theta_g = h_{s(e)} \end{cases} \tag{4.7}$$

And hence it becomes

$$\begin{cases} -\alpha_{ec}\bar{k}_{ME}\left(c_4u_4+c_5u_5\right) - \alpha_{ed}\bar{k}_{ME}\left(c_5u_5+c_eu_e\right) + \left(\alpha_{ec}+\alpha_{ed}+\alpha_{ef}+\alpha_{eg}\right)\bar{k}_{ME}u_e - \alpha_{ef}\bar{k}_{ME}u_f - \alpha_{eg}\bar{k}_{ME}u_g = F_e \\ -\alpha_{ec}\bar{k}_{TH}\left(c_4\theta_4+c_5\theta_5\right) - \alpha_{ed}\bar{k}_{TH}\left(c_5\theta_5+c_e\theta_e\right) + \left(\alpha_{ec}+\alpha_{ed}+\alpha_{ef}+\alpha_{eg}\right)\bar{k}_{TH}\theta_e - \alpha_{ef}\bar{k}_{TH}\theta_f - \alpha_{eg}\bar{k}_{TH}\theta_g = h_{s(e)} \end{cases} \tag{4.8}$$

where $\bar{k}_{ME}$ and $\bar{k}_{TH}$ represent $\bar{k}_{ME} = \bar{c}_{ME}\bar{V}_i\bar{V}_j$ and $\bar{k}_{TH} = \bar{c}_{TH}\bar{V}_i\bar{V}_j$. Finally, writing the equilibrium equations for every node, one can construct the linear systems of equations for mechanical part of the problem as follows:

$$
\begin{bmatrix}
\vdots & \cdots & \cdots & \cdots & \cdots \\
\cdots & -\alpha_{42}k_{ME}^{+} & -\alpha_{43}k_{ME}^{+} & \left(\alpha_{42}+\alpha_{43}+\alpha_{45}+\alpha_{46}\right)k_{ME}^{+} & -\alpha_{45}k_{ME}^{+} \\
\cdots & 0 & -\alpha_{53}k_{ME}^{+} & -\alpha_{54}k_{ME}^{+} & \left(\alpha_{53}+\alpha_{54}+\alpha_{56}+\alpha_{57}\right)k_{ME}^{+} \\
\cdots & 0 & 0 & -\alpha_{ec}c_4k_{ME}^{-} & -\alpha_{ec}c_5k_{ME}^{-}-\alpha_{ed}c_5k_{ME}^{-} \\
\cdots & 0 & 0 & 0 & -\alpha_{fd}c_5k_{ME}^{-} \\
\cdots & \cdots & \cdots & \cdots & \cdots
\end{bmatrix}
$$

$$
\begin{bmatrix}
\cdots & \cdots & \cdots & \cdots & \vdots \\
-\alpha_{46}c_ek_{ME}^{+} & -\alpha_{46}c_fk_{ME}^{+} & 0 & 0 & \cdots \\
-\alpha_{56}c_ek_{ME}^{+} & -\alpha_{56}c_fk_{ME}^{+} & -\alpha_{57}c_gk_{ME}^{+} & -\alpha_{57}c_hk_{ME}^{+} & \cdots \\
-\alpha_{ed}c_ek_{ME}^{-}+\left(\alpha_{ec}+\alpha_{ed}+\alpha_{ef}+\alpha_{eg}\right)k_{ME}^{-} & -\alpha_{ef}k_{ME}^{-} & -\alpha_{eg}k_{ME}^{-} & 0 & \cdots \\
-\alpha_{fd}c_ek_{ME}^{-}-\alpha_{fe}k_{ME}^{-} & \left(\alpha_{fd}+\alpha_{fe}+\alpha_{fg}+\alpha_{fh}\right)k_{ME}^{-} & -\alpha_{fg}k_{ME}^{-} & -\alpha_{fh}k_{ME}^{-} & \cdots \\
\cdots & \cdots & \cdots & \cdots & \vdots
\end{bmatrix}
\begin{bmatrix}
\vdots \\ u_2 \\ u_3 \\ u_4 \\ u_5 \\ u_e \\ u_f \\ u_g \\ u_h \\ \vdots
\end{bmatrix}
=
\begin{bmatrix}
\vdots \\ F_2 \\ F_3 \\ F_4 \\ F_5 \\ F_e \\ F_f \\ F_g \\ F_h \\ \vdots
\end{bmatrix}
$$

(4.9)

In a similar way, linear systems of equations for the thermal part is given by:

$$
\begin{bmatrix}
\vdots & \cdots & \cdots & \cdots & \cdots \\
\cdots & -\alpha_{42}k_{TH}^{+} & -\alpha_{43}k_{TH}^{+} & \left(\alpha_{42}+\alpha_{43}+\alpha_{45}+\alpha_{46}\right)k_{TH}^{+} & -\alpha_{45}k_{TH}^{+} \\
\cdots & 0 & -\alpha_{53}k_{TH}^{+} & -\alpha_{54}k_{TH}^{+} & \left(\alpha_{53}+\alpha_{54}+\alpha_{56}+\alpha_{57}\right)k_{TH}^{+} \\
\cdots & 0 & 0 & -\alpha_{ec}c_4k_{TH}^{-} & -\alpha_{ec}c_5k_{TH}^{-}-\alpha_{ed}c_5k_{TH}^{-} \\
\cdots & 0 & 0 & 0 & -\alpha_{fd}c_5k_{TH}^{-} \\
\cdots & \cdots & \cdots & \cdots & \cdots
\end{bmatrix}
$$

$$
\begin{bmatrix}
\cdots & \cdots & \cdots & \cdots & \vdots \\
-\alpha_{46}c_ek_{TH}^{+} & -\alpha_{46}c_fk_{TH}^{+} & 0 & 0 & \cdots \\
-\alpha_{56}c_ek_{TH}^{+} & -\alpha_{56}c_fk_{TH}^{+} & -\alpha_{57}c_gk_{TH}^{+} & -\alpha_{57}c_hk_{TH}^{+} & \cdots \\
-\alpha_{ed}c_ek_{ME}^{-}+\left(\alpha_{ec}+\alpha_{ed}+\alpha_{ef}+\alpha_{eg}\right)k_{TH}^{-} & -\alpha_{ef}k_{TH}^{-} & -\alpha_{eg}k_{TH}^{-} & 0 & \cdots \\
-\alpha_{fd}c_ek_{TH}^{-}-\alpha_{fe}k_{TH}^{-} & \left(\alpha_{fd}+\alpha_{fe}+\alpha_{fg}+\alpha_{fh}\right)k_{TH}^{-} & -\alpha_{fg}k_{TH}^{-} & -\alpha_{fh}k_{TH}^{-} & \cdots \\
\cdots & \cdots & \cdots & \cdots & \vdots
\end{bmatrix}
\begin{bmatrix}
\vdots \\ \theta_2 \\ \theta_3 \\ \theta_4 \\ \theta_5 \\ \theta_e \\ \theta_f \\ \theta_g \\ \theta_h \\ \vdots
\end{bmatrix}
=
\begin{bmatrix}
\vdots \\ h_{s(2)} \\ h_{s(3)} \\ h_{s(4)} \\ h_{s(5)} \\ h_{s(e)} \\ h_{s(f)} \\ h_{s(g)} \\ h_{s(h)} \\ \vdots
\end{bmatrix}
\tag{4.10}
$$

It can be noticed that the stiffness matrixes of the system in Eq. (4.9) and (4.10) are not symmetrical. However, for quasi-static materials, crack propagation can be investigated by using explicit time integrations e.g. central difference or Verlet. In order to consider the inertia, one may simply attribute the mass to each node proportional to its volume by a lumped mass matrix. Moreover, to conserve the total mass in the system, it is essential that the distance between the parts of the model, l_0 , is calculated as follows:

$$
l_0 = (\Delta x^{+} + \Delta x^{-})/2 \tag{4.11}
$$

For 2D and 3D cases, the same approach is applicable. As shown in Figure 4.3, the square domain is discretized by two sets of grid spacing. In Figure 4.3, the fine and coarse grids are disconnected and we use $m = 2$ although different values of m can be considered. The distance between the coarse and fine grids are represented by Δx^- and Δx^+ respectively. Accordingly, the horizon sizes of the two parts are: $\delta^+ = 2\Delta x$ and $\delta^- = 2\Delta x^-$.

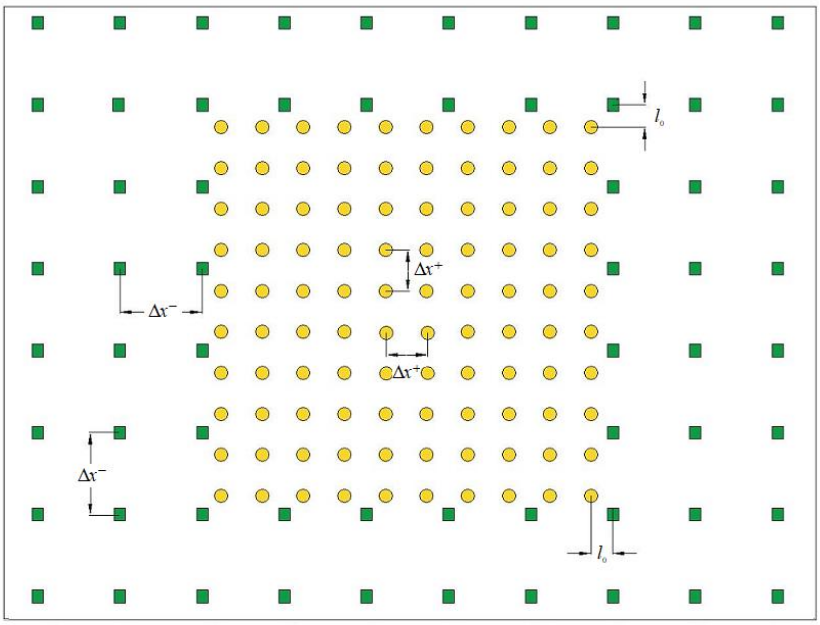

(a)

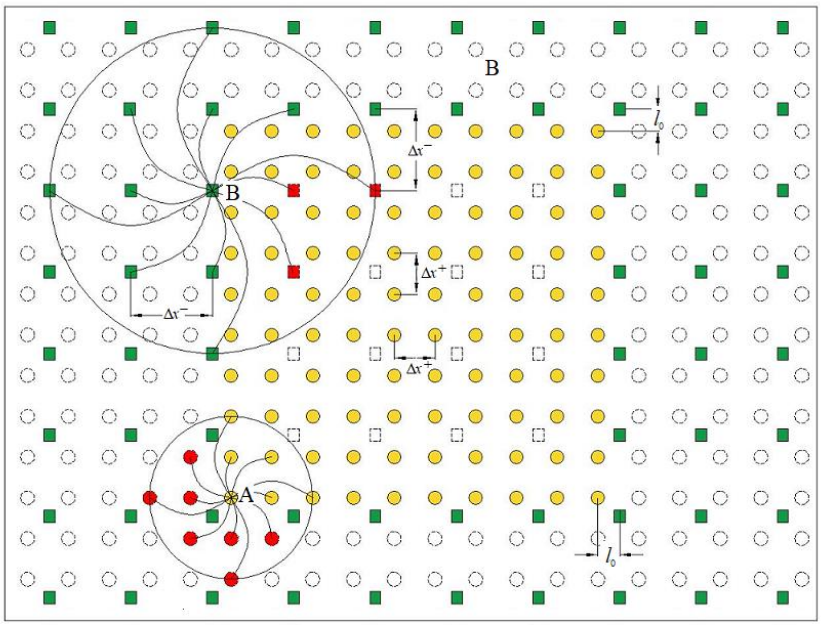

(b)

Figure 4.3. (a) Two still disconnected portions of a 2D model discretized by two different grid spacing, and (b) introduction of fictitious nodes to connect the portions.

In Figure 4.3, node A used as an indication of fine grid. This node should interact with all the real and the fictitious nodes of its own type located in its horizon. δ^- . The red circle nodes are the activated fictitious nodes which their values should be determined by the linear interpolation of the four real nearest family nodes surrounding them. Furthermore, node B is an indication of the coarse grid as shown in Figure 4.3. It also interacts with the family nodes of its own type located in its horizon. Red square nodes are the activated fictitious nodes which their displacement are interpolated by the bi-linear interpolation of the four real nearest family nodes surrounding them. After finding the displacement of the fictitious activated nodes, one

is able to calculate the forces acting on the real nodes. Since the forces of the coupling bonds are acting only on the real nodes, the rows corresponding to the equilibrium of the real nodes connected to coupling bonds will contain some non-standard terms. The presented coupling method can easily be extended to the 3D cases as a generalization of the 2D case.

4.4 Adaptive refinement

The proposed coupling method is applicable to thermal shock crack propagation problems. By means of this new method, one may apply the fine grid in the zones where cracks are prone to nucleate or propagate, while in the remaining parts of the body a coarser grid is used. Moreover, it is very efficient to expand the fine grid adaptively where large strain gradients are present. Hence, it is needed to know when to substitute a few nodes, located in the coarse grid zone, to a larger number of nodes of the fine grid. Considering two generic nodes in the coarse grid zone as $\mathbf{x}_i$ and $\mathbf{x}_j$, one may write the stretch of the bond linking them at the time, t_n , as follows (see Figure 4.4 (a))

$$s_{ij}^n = \frac{\left\|(\mathbf{x}_j + \mathbf{u}_j^n) - (\mathbf{x}_i + \mathbf{u}_i^n)\right\|}{\left\|\mathbf{x}_j - \mathbf{x}_i\right\|} - 1 \tag{4.12}$$

The stretch of the bonds corresponding to the coarse grid, should be checked at each time step. Nodes $\mathbf{x}_i$ and $\mathbf{x}_j$ known as critical nodes when the stretch of the bond between them lays within the following range:

$$\chi s_0 \le s_{ij}^n - \alpha T_{avg} \le s_0, \quad 0 < \chi < 1 \tag{4.13}$$

where, α is the thermal expansion coefficient. To assure that no crack reaches the horizons of the coarse grid, the complete zone within the horizon of the critical nodes should be substituted by the fine grid. Hence, nodes $\mathbf{x}_i$ and $\mathbf{x}_j$ with their family nodes are switched to the fine grid nodes at time instant t_{n+1} Figure 4.4 (b). The higher values of χ, the narrower zone of a coarse grid is modified by the fine grid. In contrast, a larger zone of the coarse grid should be transformed to a fine grid by using the smaller values of χ . Since in the explicit time marching, displacements, mass and velocity have to be assigned to the previously non-existing nodes. Therefore, the aforementioned new method is used to determine the values of displacement and velocities by using linear and bi-linear interpolation in 1D and 2D problems respectively.

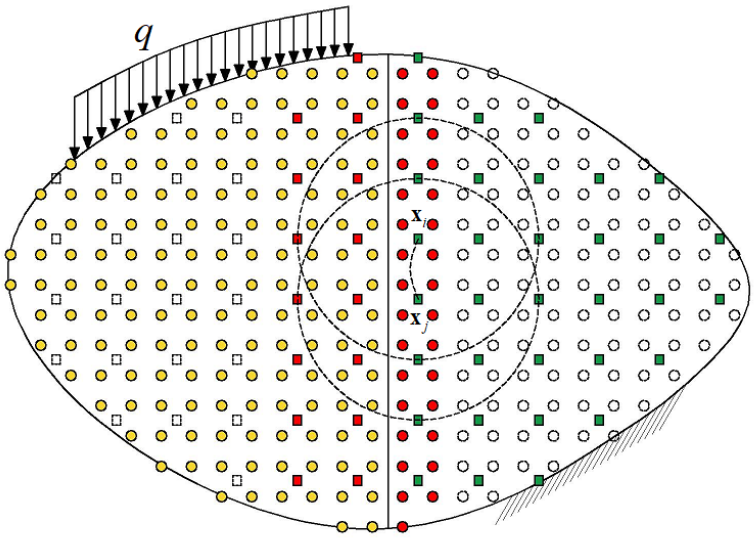

(a)

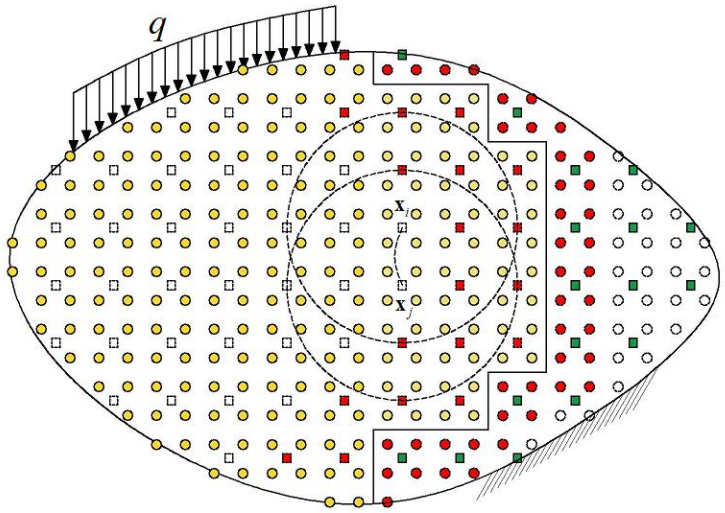

(b)

Figure 4.4. Variation of the model within two consecutive time steps;(a) the curved bond is the one that identifies two critical nodes of the coarse grid, (b) the coupled model after the refinement.

4.5 The step by step procedure of the method

1. Defining of constant parameters:
    - Mechanical constants: E , ν , ρ , Δt_{ME} , δ , c_{ME} , C .
    - Thermal constants: c_v , γ , α , θ_0 , θ_∞ , Δt_{TH} , δ , c_{TH} .
    - As recommended in (Kilic and Madenci 2010), for the mechanical part the time step of 1 ($\Delta t_{ME} = 1$) can be used. Furthermore, in thermomechanical coupling the total time step, Δt , should be less than both mechanical and thermal time steps , $\Delta t < \min\left\{\Delta t_{ME}, \Delta t_{TH}\right\}$.
2. Pre-processing:

- Build the grid sets, define node type, horizon sets, mark the fictitious nodes, define pre-cracks.
- Applying the mechanical and the thermal initial conditions.

3. Thermal analysis for step (n+1) and evaluate, θ^{n+1}, by Eq.(2.98).
4. Evaluate the displacements of the real nodes using the dynamic relaxation scheme through Eqs. (2.86)-(2.89).
5. Calculate displacement of the fictitious nodes, $\mathbf{u}_i^{n+1}$,using linear or bilinear interpolation.
6. Evaluate the accelerations of the real nodes, $\ddot{\mathbf{u}}_i^{n+1}$, by Eq. (2.83).
7. Calculate the stretch of the active bonds in the fine grid zone by Eq. (2.56).
8. Check if the stretch of the bonds exceeds its critical value, based on Eq, (2.79), the bond should be broken and removed from the calculations.
9. Evaluate the damage level of the real nodes in the fine grid zone using Eq.(2.80).
10. Calculate the stretch of the active bonds in the coarse grid zone by Eq.(4.12).
11. Check if the stretch of the bonds in coarse grid is within the range defined in Eq. (4.13), mark the node to be switched from coarse to fine.
12. Apply the refinement technique as described in Section 4.4.
13. Save the updated accelerations, velocities, displacements and temperature values as the initial values for the next time step
14. Repeat from step 3 for the next time step.

The whole solution procedure can be cast in a flowchart shown in Figure 4.5.

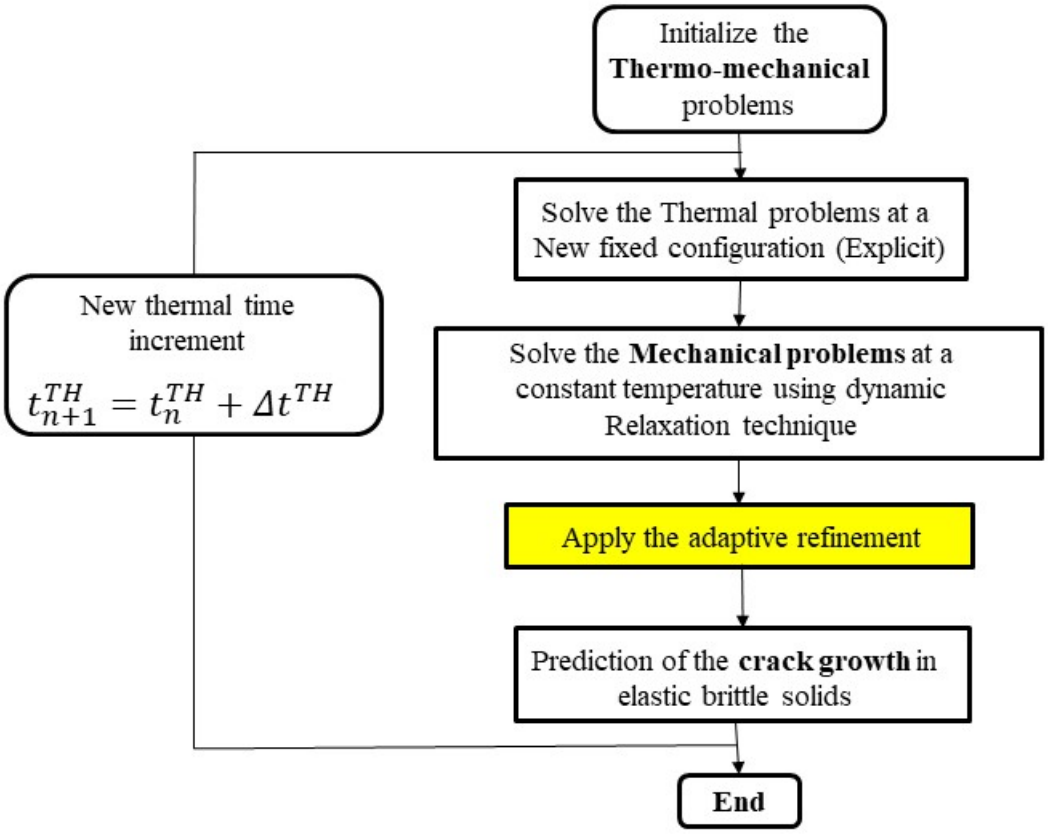

Figure 4.5. Step by step procedure of the method.

All the codes are developed using standard C++ language which facilitates using the code on different platforms.The run times reported later are measured on an Intel Core i7-6700HQ 2.60 GHz CPU, on a 64 bit Windows 10 Enterprise system. I/O times are excluded from the timings. The Microsoft Visual C++ 2015 compiler has been code are parallelized using OpenMP directives.

employed to compile the codes. To achieve maximum performance, most parts of the

4.6 Numerical Examples

4.6.1 *Example I*: Thermomechanical Analysis of a plate with a Hole

In this example, deformation of a plate with a hole, due to non-uniform heating, is investigated: no crack propagation is simulated (see Figure 4.6). Therefore, we first determine the temperature distribution all over the domain and boundaries. Correspondingly, deformation is evaluated by using adaptive dynamic relaxation method. This benchmark has been investigated in (Oterkus 2015). The Problem is solved in plane-stress conditions with $E = 200 \times 10^9$ Pa, $\alpha = 16 \times 10^{-6}$ 1/K, $\rho = 7850$ kg/m^3 and $\nu = 1/3$. The plate has a thermal conductivity $\gamma = 20$ W/m K, and specific heat $c_v = 500$ J/kg K. The initial temperature of the plate is 20 $^\circ$C. The right and left boundaries are subjected to constant temperatures as: $\theta^*(x = -L/2, y, t) = 500\,^\circ$C and $\theta^*(x = L/2, y, t) = 20\,^\circ$C. The remaining boundaries are insulated.

To impose the mechanical boundary conditions, the left and the right side of the plate is subjected to zero displacement constraints as: $u(x = -L/2, y, t) = 0, u(x = L/2, y, t) = 0$, whereas other boundaries are free of tractions. This example is solved for a duration of $t = 1000$ s with the time integration interval of $\Delta t = 0.01$ s, which results in 100000 steps.

The plate is discretised with three models: Uniform, Non-uniform I and Non-uniform II. In the Uniform model the grid spacing is $\Delta x = \Delta y = 5 \times 10^{-4}$ m. Non-uniform I is a coupled model with $\Delta x^+ = 10^{-3}$ m and $\Delta x^- = 5 \times 10^{-4}$ m. Additionally, Non-uniform II is a coupled model with $\Delta x^+ = 10^{-3}$ m and $\Delta x^- = 0.25 \times 10^{-4}$ m. The fine parts are shown in Figure 4.6 by Ω^- . The fine parts are chosen randomly without any symmetric axis. The fine grid zones in Figure 4.6 are neither parallel nor perpendicular to the plate sides. To obtain the converged solution, initially

this model is simulated with the Uniform grid model. Finding the proper value of Δx , we compare the contour plots of the temperature, horizontal and vertical displacements in Figure 4.7-Figure 4.9. The results of the Non-uniform I and Non-uniform II model are in an excellent agreement with the Uniform one. Moreover, the plate is simulated in Abaqus 6.13 by the finite element method (FEM). Then, the temperature profile and displacements contour plots are compared with the BB-PD results. The comparison indicates remarkable agreement.

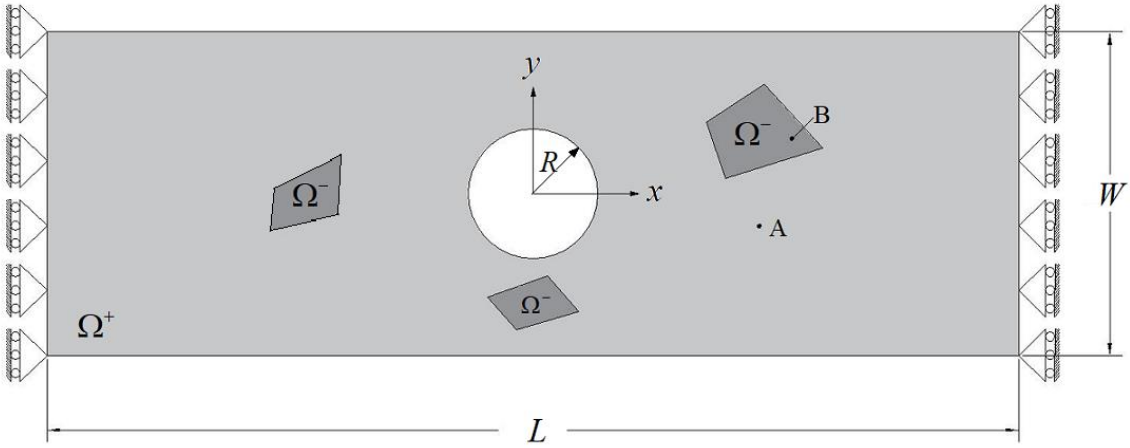

Figure 4.6. Problem domain, boundary conditions, and the zones with fine grid in *Example I*.

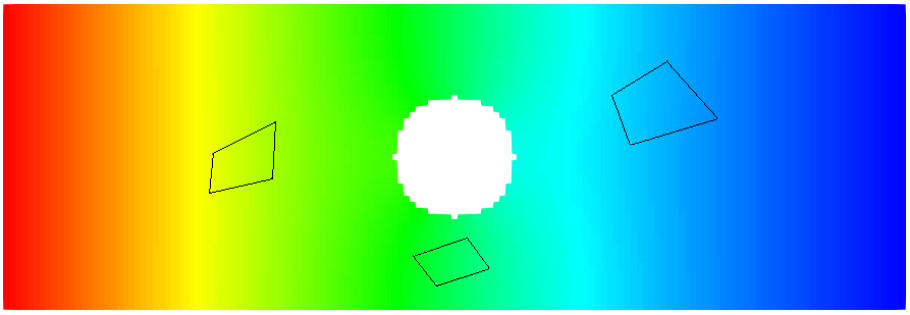

(a)

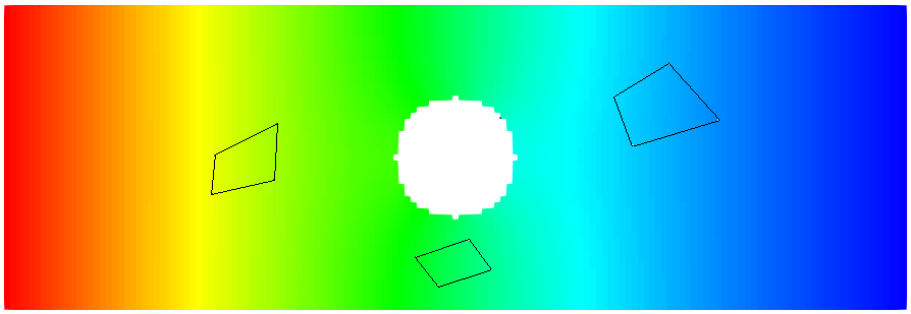

(b)

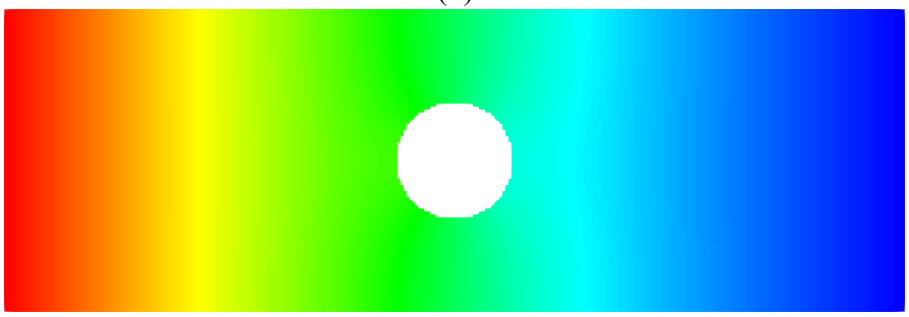

(c)

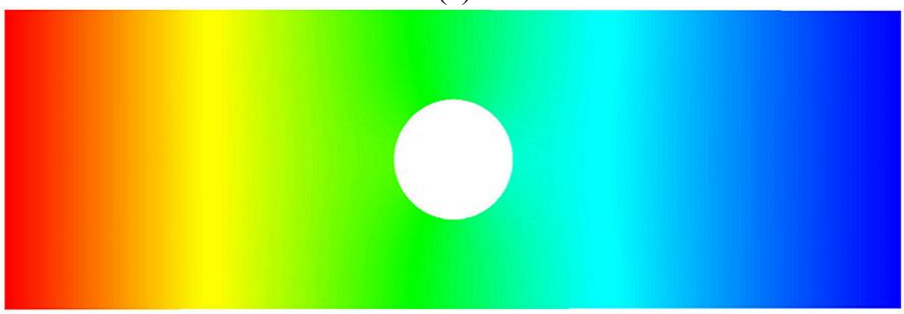

(d)

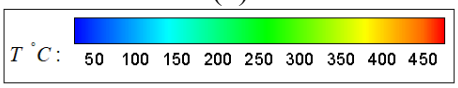

Figure 4.7. Temperature predictions after 1000 s: (a) Non-uniform I PD (b) Non-uniform II PD (c) Uniform PD and (d) FEM models.

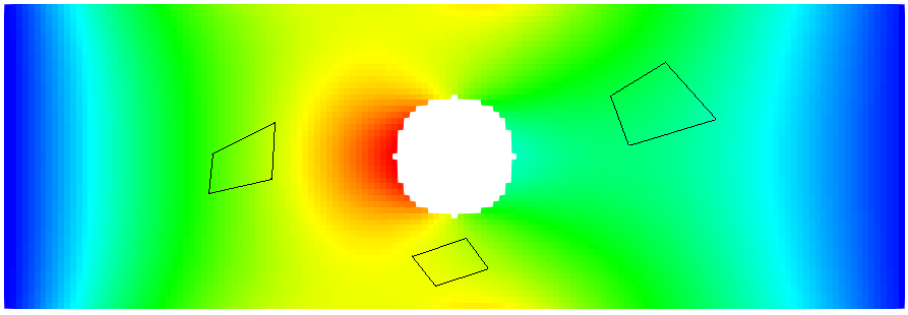

(a)

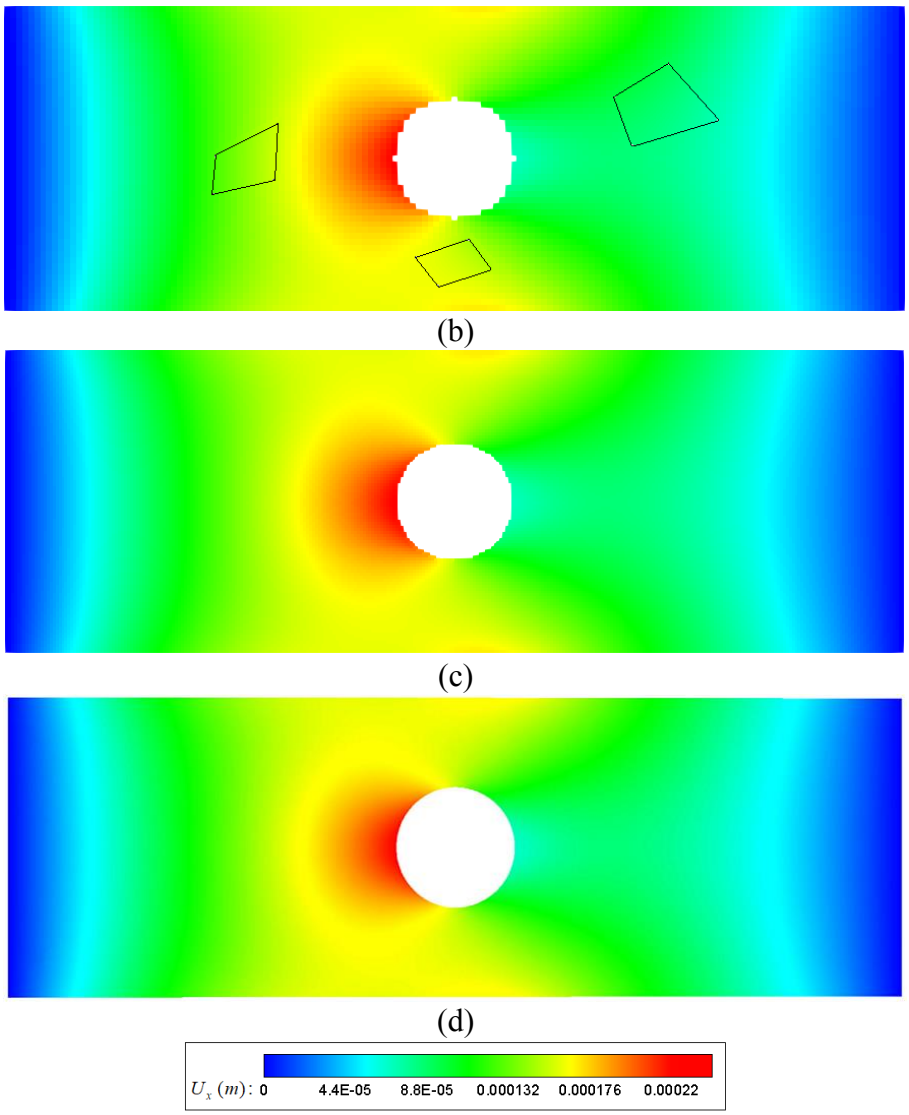

Figure 4.8. Horizontal displacement predictions after 1000 s: (a) Non-uniform I PD (b) Non-uniform II PD(c) Uniform PD and (d) FEM models.

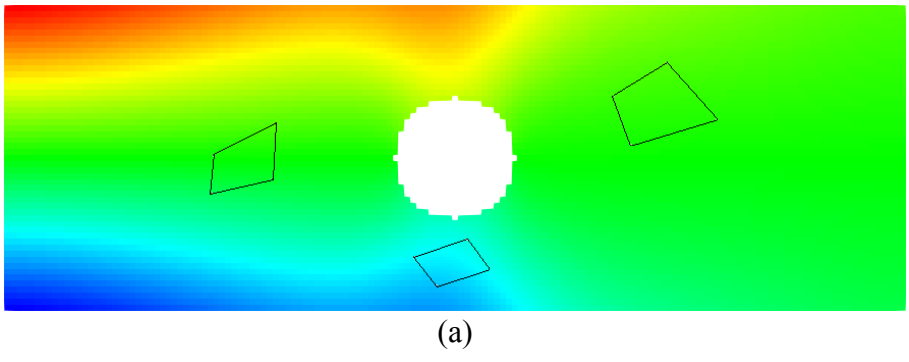

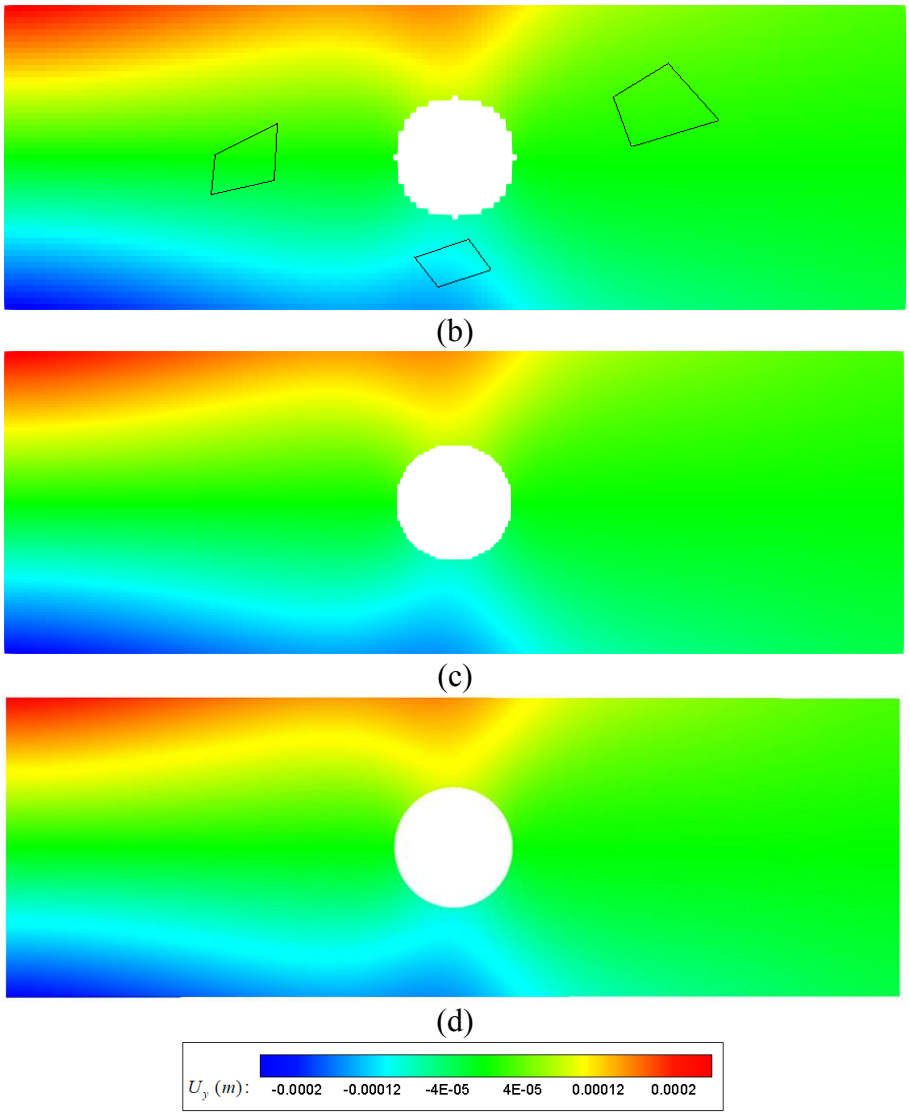

Figure 4.9. Vertical displacement predictions after 1000 s: (a) Non-uniform I PD (b) Non-uniform II PD(c) Uniform PD and (d) FEM models.

For further validation of the present method, two nodes, $\mathbf{x}_A = (0.035, 0.005)$ and $\mathbf{x}_B = (0.04, 0.0085)$ are chosen to investigate the time history of the horizontal displacement and temperature by three models. The time history of the horizontal displacement for nodes $\mathbf{x}_B$ and $\mathbf{x}_A$ are shown in Figure 4.10 (a) and Figure 4.10 (b) respectively. The results for both of the nodes are in an acceptable agreement; however, better agreement of the three models

can be observed for node B. Moreover, time history of the temperature for nodes $\mathbf{x}_B$ and $\mathbf{x}_A$ are depicted in Figure 4.10 (c) and Figure 4.10 (d) respectively. The results are in an excellent agreement and no significant numerical perturbation can be observed.

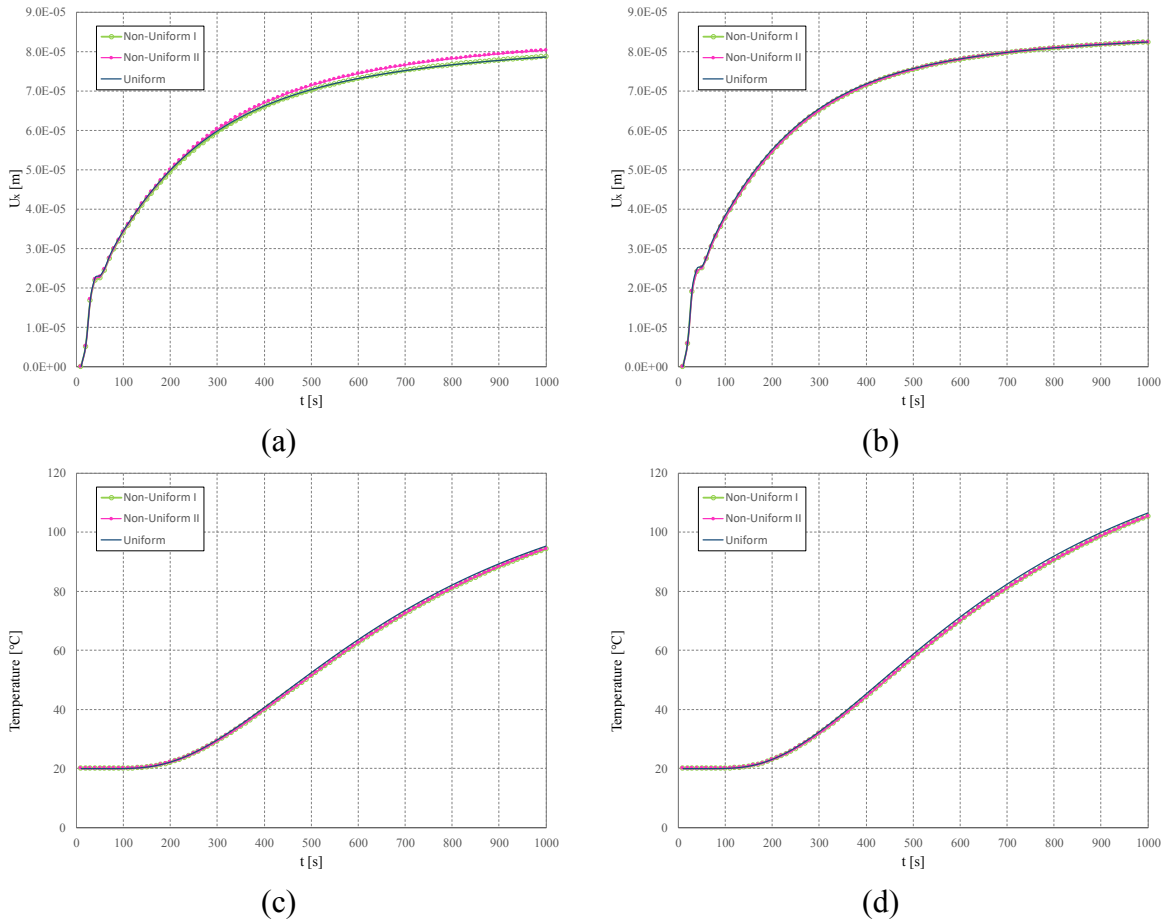

Figure 4.10. The time history of (a) horizontal displacement of node $\mathbf{x}_B$ (b) horizontal displacement of node $\mathbf{x}_A$ (c) temperature of node $\mathbf{x}_B$ (b) temperature of node $\mathbf{x}_A$.

4.6.2 *Example II*: Pre-cracked disk specimen under central thermal shock

In this example, we investigate the thermo-mechanical crack propagation in a pre-cracked disk using the adaptive multi-grid peridynamic method. This example has already been used as an experimental test to measure the thermal-shock resistance of different materials such as ceramics (Awaji et al. 2002; Honda et al. 2009; Honda et al. 2002). In this test, the center of a

disk is heated at its both sides over the circular area as depicted in Figure 4.11. Due to the central constant heat flux and the existence of the pre-crack, the inhomogeneous temperature distribution occurs over the disk which leads to the inhomogeneous thermal expansion and stress in the domain. The thermal shock fracture takes place when the emerged tensile stress reaches a certain value.

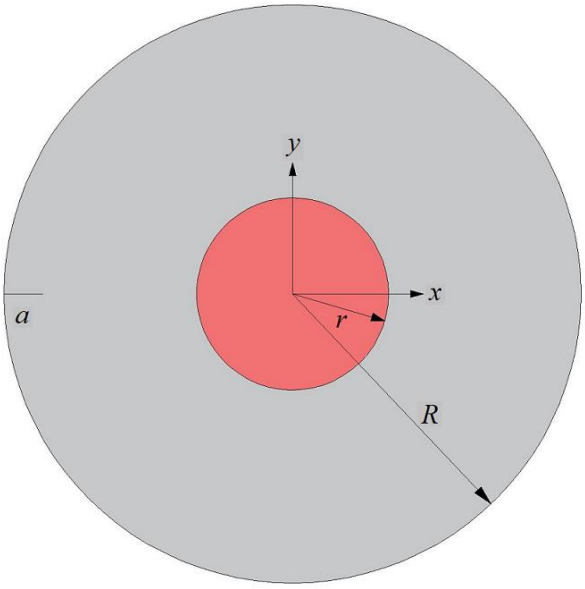

Figure 4.11. Geometry and boundary conditions for the thermal shock fracture problem in a disk. The red area denotes an imposed body heat flux.

Based on the experiments done in (Awaji et al. 2002; Honda et al. 2009; Honda et al. 2002), three different crack paths are observed in Figure 4.12. The first type of the crack path is a straight line from the pre-crack to the opposite side of the disk as depicted in Figure 4.12 (a). The second type of the crack path begins from the pre-notched crack tip propagates into two branches inside the heating area as shown in Figure 4.12 (b). The third type of the crack path resembles the second one; however, the crack branches outside of the heating area as depicted

in Figure 4.12 (c). This example also has been solved using phase filed numerical solution in (Chu et al. 2017) and all three types of crack paths have been observed.

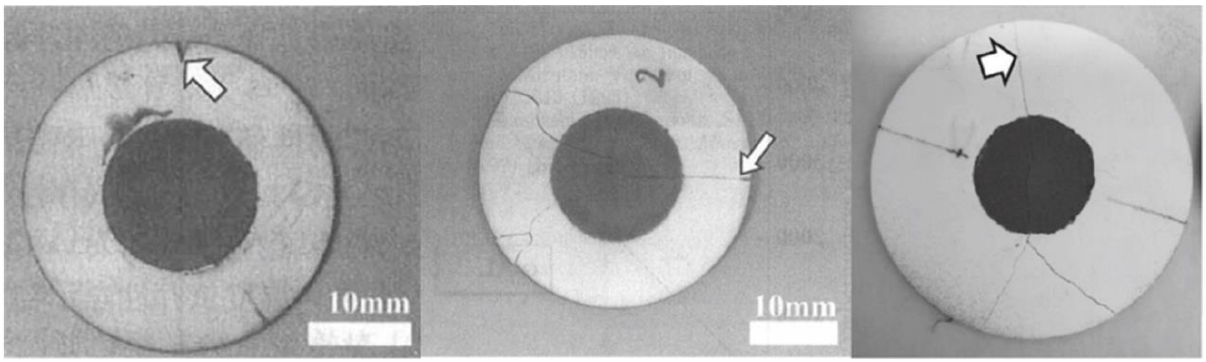

Figure 4.12. Three types of crack paths in experiments from (Honda et al. 2009; Honda et al. 2002) (a) Crack grows straightly through the heating area (b) crack branches in the heating area (c) crack branches outside of the heating area

As shown in Figure 4.11, the radius of the disk and the pre-notched crack size are chosen as: $R = 0.015$ m and $a = 0.002$ m. Regarding the data available in literature (Honda et al. 2002), the problem is solved in plane-stress conditions with $E = 380 \times 10^9$ Pa, $\alpha = 6.6 \times 10^{-6}$ 1/K, $\rho = 3900$ kg/m^3 , $G_c = 26.95$ J/m^2 and $\nu = 1/3$. The plate has a thermal conductivity $\gamma = 21$ W/m K, and specific heat $c_v = 961.5$ J/kg K. An adiabatic boundary condition is imposed around the disk. The value of the central heat flux in Eq. (2.98)is $h_s = \gamma$ (kW/m^3), the radius of the heating area is r as depicted in Figure 4.11.

Initially, a uniform peridynamic model is taken as the reference solution with the grid spacing of $\Delta x = 0.0003$ m. Then, the adaptive refinement solution is considered by using a refined model ($\Delta x^- = 0.0003$ m and $\Delta x^+ = 0.0006$ m). This example is solved for a duration of $t = 0.059$ s with the time integration interval of $\Delta t = 10^{-5}$ s, which results in 59000 steps. Moreover, the radius of the heating part and the heat flux for this example are taken as: $\gamma = 750000$ (kW/m^3) and $r = 5$ mm.

The contour plots of the damage obtained by the proposed method and Uniform model at 6 different instants are depicted in Figure 4.13. A very good agreement is observed between the crack paths obtained using both uniform and non-uniform model.

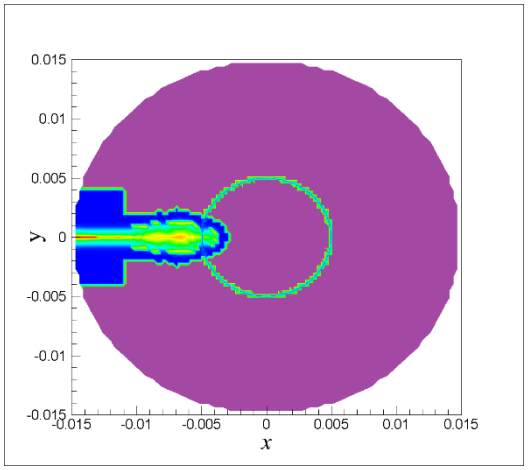

$t = 0.585$ s

(a)

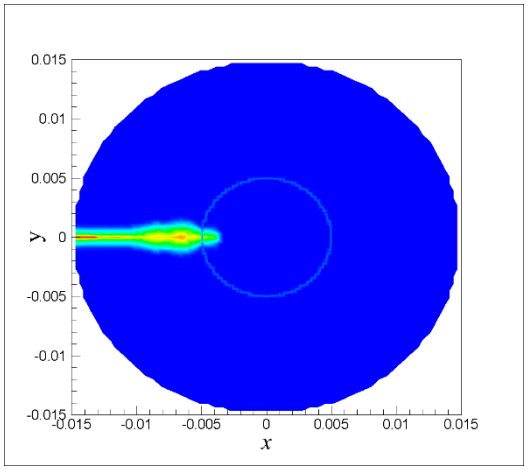

$t = 0.585$ s

(g)

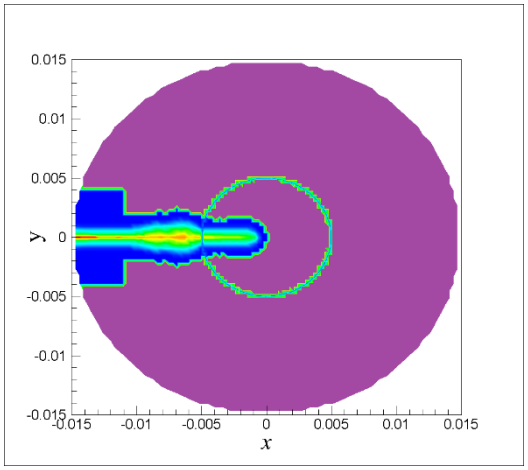

$t = 0.586$ s

(b)

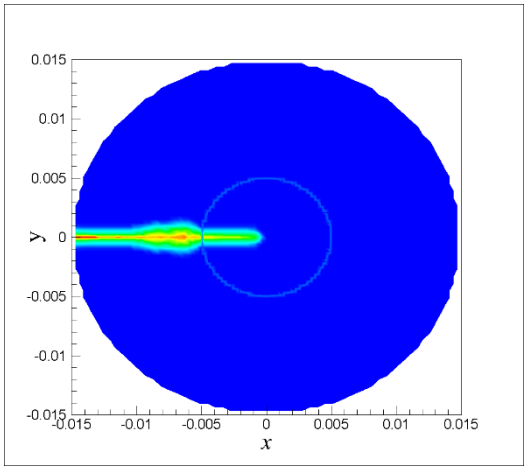

$t = 0.586$ s

(h)

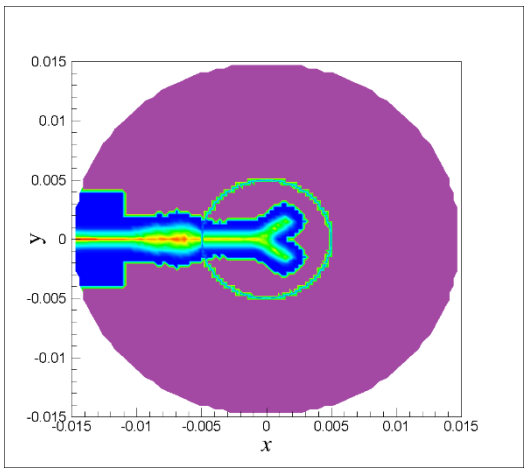

$t = 0.587$ s

(c)

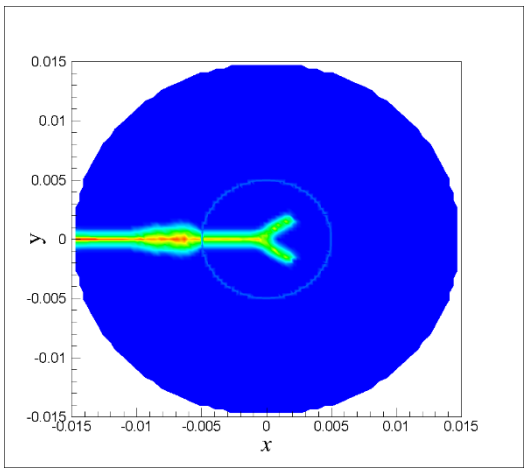

$t = 0.587$ s

(i)

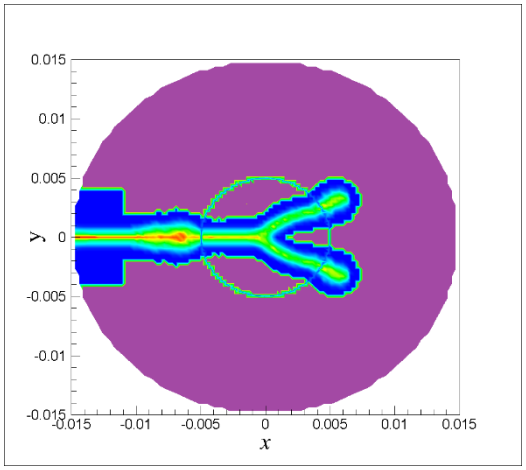

$t = 0.588$ s

(d)

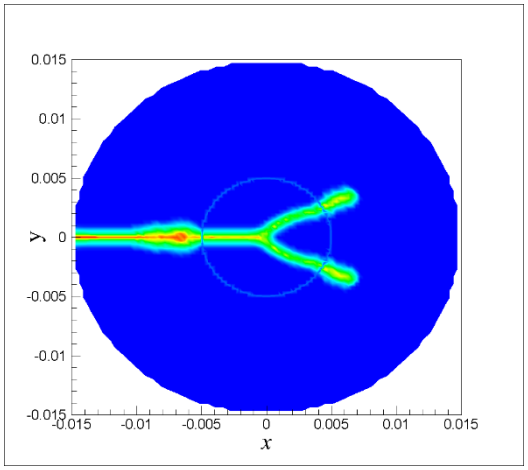

$t = 0.588$ s

(j)

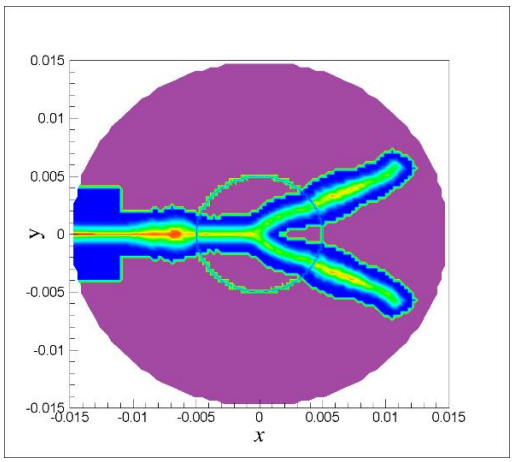

$t = 0.589$ s

(e)

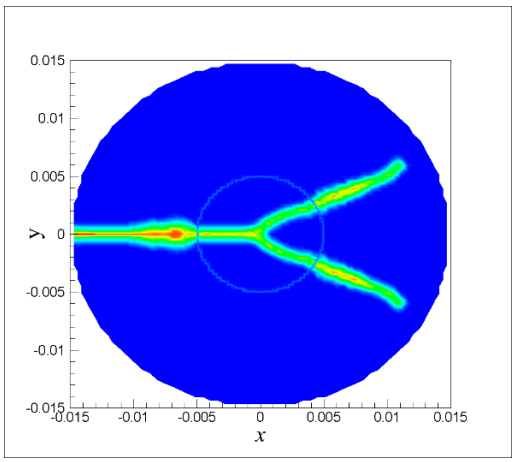

$t = 0.589$ s

(k)

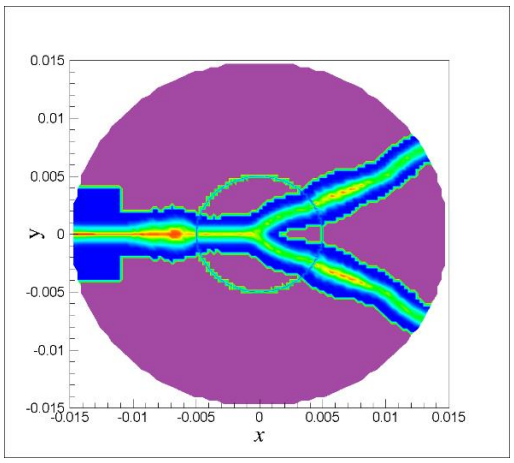

$t = 0.59$ s

(e)

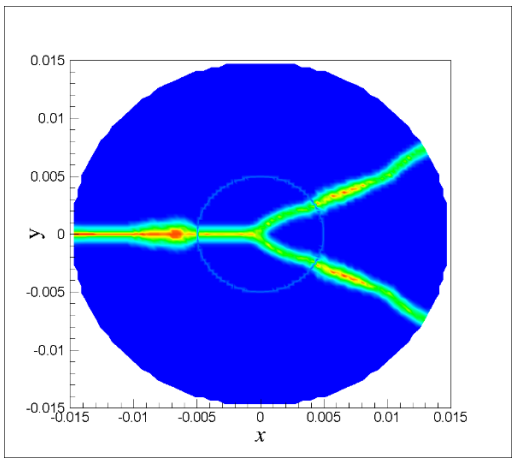

$t = 0.59$ s

(l)

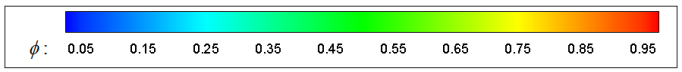

Figure 4.13. Example II. Damage at different time instances (a)-(e) in the adaptive refinement model (f)-(l) in the Uniform model.

Moreover, horizontal and vertical displacement components for the temperature distribution reported in (Figure 4.14) and their comparison to the refined model are shown in Figure 4.15. Remarkable agreement between the uniform and the refined model is achieved.

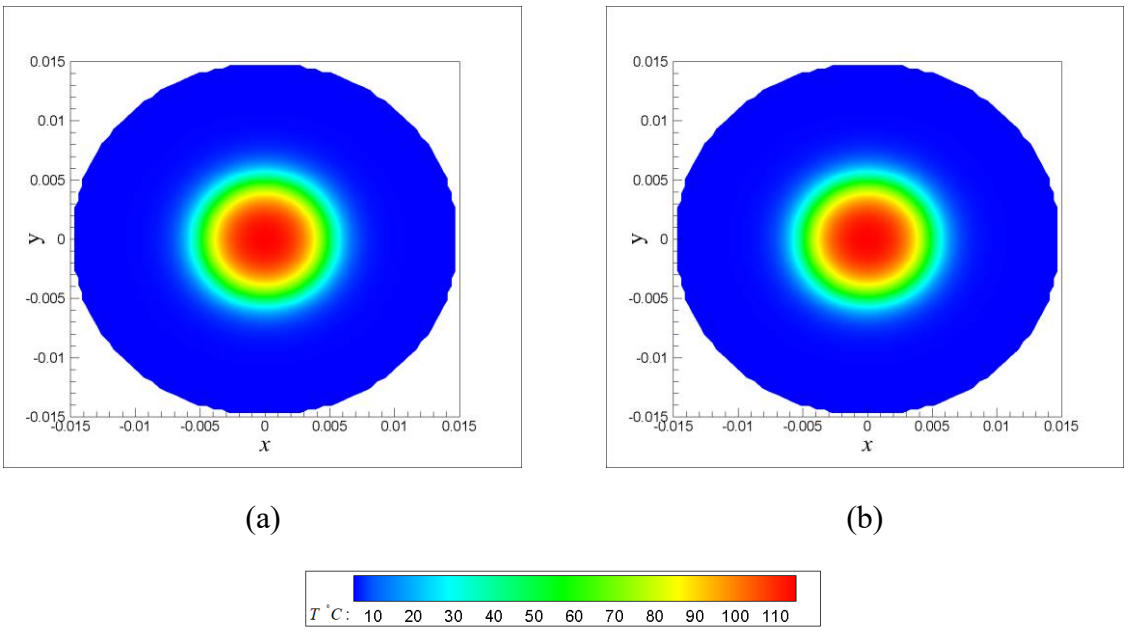

Figure 4.14. *Example II*: Temperature predictions after 0.59 s: (a) adaptive refinement model (b) the Uniform model.

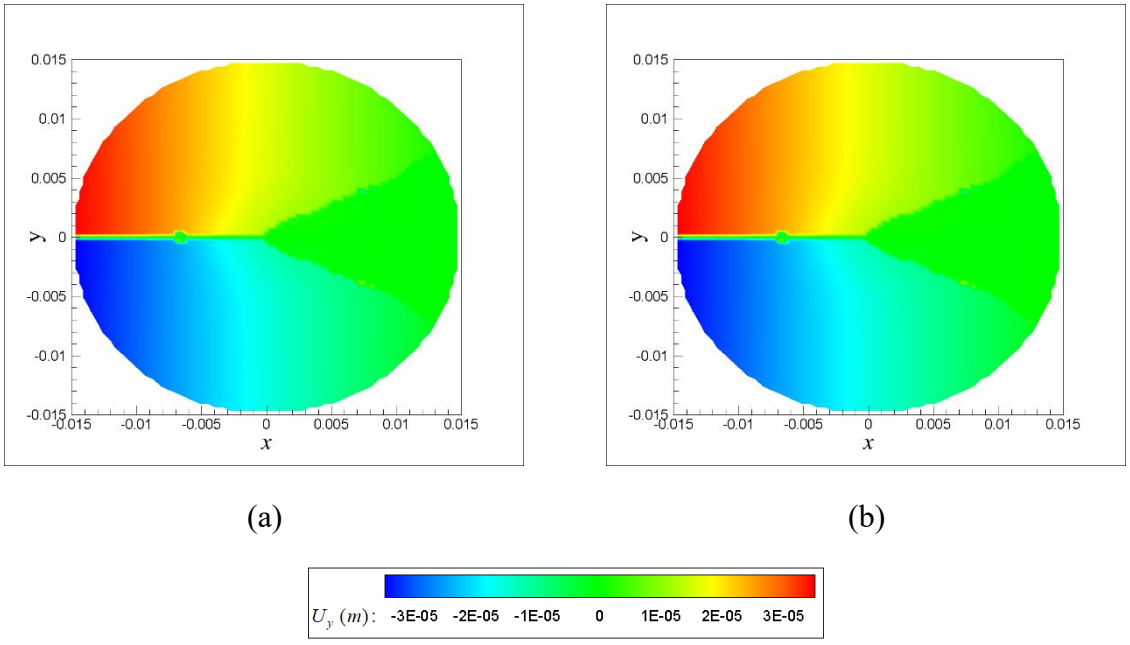

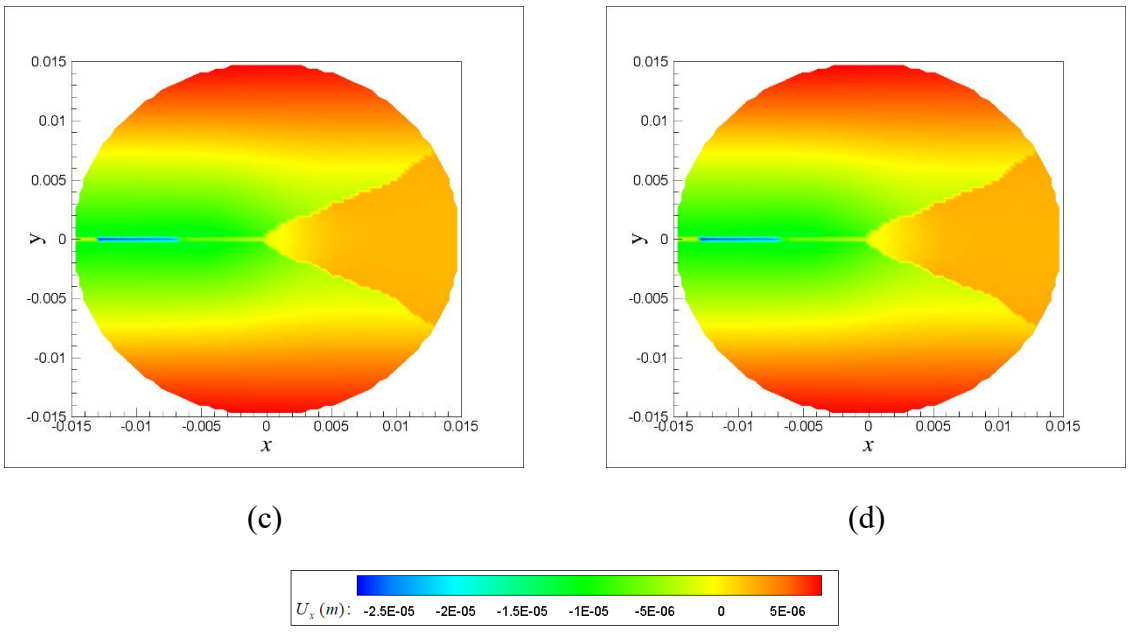

Figure 4.15. *Example II*: Vertical displacement predictions after 0.59 s (a) adaptive refinement model (b) the Uniform model and horizontal displacement predictions after 0.59 s (c) adaptive refinement model (d) the Uniform model.

In Table 4.1, the runtime of each simulation and the number of real nodes are reported.

Table 4.1. Comparison of the computational resources used by Uniform and refined models in *Example II*.

	Number of real nodes		
		Refined	
	Uniform	Coarse	Fine
$t = 0$ s	7825	3741	343
$t = 0.59$ s		1833	2996
Run time	521.60 s	175.31 s	

For a better comparison to the experimental results and the phase field numerical solution, one can change the radius of the heating part, r , and the heat flux, γ , to observe different crack paths.

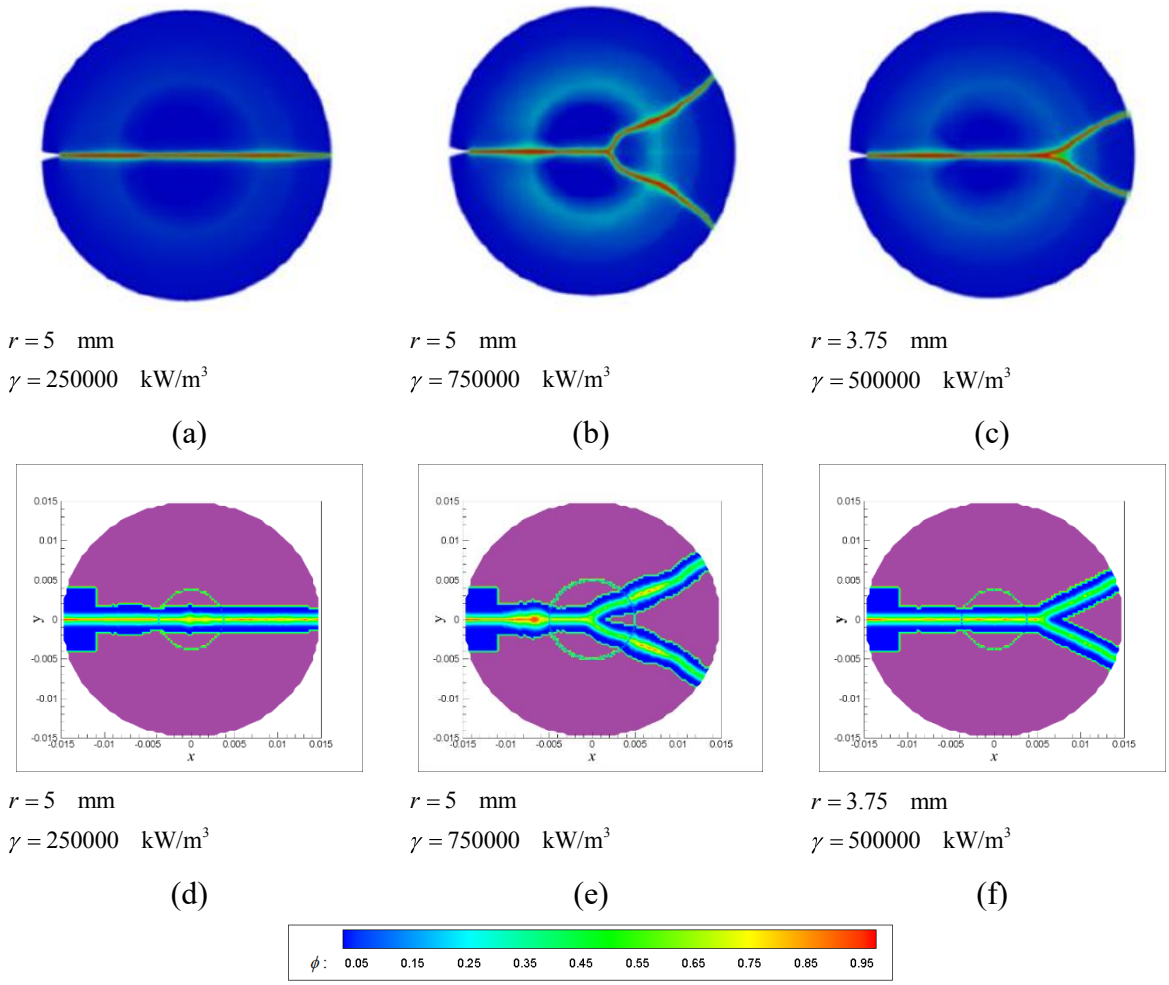

Figure 4.16. (a)-(c) Crack path results of the phase-field solution (d)-(e) adaptive refinement solution when the disk is broken completely with different heating radius r and heat flux γ for the central thermal shock of a disk.

In Figure 4.16 (d), these parameters are: $r = 5$ mm and $\gamma = 250000$ (kW/m^3) for both phase filed and peridynamic adaptive refinement models. We observe that the crack grows in a straight line without any branching. In Figure 4.16 (e), the heating parameters are changed to $r = 5$ mm and $\gamma = 750000$ (kW/m^3) and we observe in both simulations the branching occurs inside the heating area. In the third case (Figure 4.16 (f)), the heating parameters are taken as: $r = 3.75$ mm and $\gamma = 500000$ (kW/m^3) and the branching of the crack takes place outside of the heating area. In all three cases, the obtained crack path by the present solution is in a

remarkable agreement with the Phase field solution and the experimental results obtained by (Chu et al. 2017) in Figure 4.12.

4.6.3 Example III: Quenching test of rectangular specimen under central thermal shock

In this example, complex crack patterns induced by thermal shocks using the adaptive refinement peridynamic method is investigated. The quenching test is a benchmark to measure the thermal-shock resistance of different kinds of materials. In the experiments done by (Shao et al. 2011), rectangular ceramic slabs are heated to the certain temperature and then dropped into a water bath. Accordingly, some parallel cracks start to grow from the lateral surface of the slab due to the quenching phenomenon. The slabs with a higher initial temperature show extreme shrinkage and hence, more cracks with longer depth emerge on the boundaries of the slabs. For the first time, a method based on energy minimization has been established to calculate the periodic array and selective crack growth by (Jenkins 2005). Furthermore, other numerical simulation of this example can be traced in the literature (See (Bourdin et al. 2014; Chu et al. 2017; D'Antuono and Morandini 2017; Giannakeas et al. 2018; Wang et al. 2018b)); however, due to the complexity of the crack patterns, a large number of elements or nodes is needed which increase the computational time drastically. Hence, we consider two models for this example, one Uniform model with only fine grid spacing ($\Delta x = 0.00014\,\text{m}$), and an adaptive refined model ($\Delta x^{-} = 0.00014\,\text{m}$ and $\Delta x^{+} = 0.00028\,\text{m}$) then the efficiency of the refined model is investigated by comparing these two models with the experiment data.

The rectangular slab has the length of $L = 0.05$ m and width of $W = 0.01$ m as shown in Figure 4.17.

Based on the experimental model in (Shao et al. 2011), the problem is solved in plane strain conditions with $E = 340\times10^{9}$ Pa, $\alpha = 7.2\times10^{-6}$ 1/K, $\rho = 3950$ kg/m^3 , $G_c = 42.27$ J/m^2 and $\nu = 1/4$. The plate has a thermal conductivity $\gamma = 18$ W/m K, and specific heat $c_v = 880$ J/kg K. Convection boundary condition is imposed around the plate as represented in Figure 4.17. This example is solved for a duration of $t = 1$ s with the time integration interval of $\Delta t = 10^{-5}$ s, which results in 100000 steps.

The initial temperature is taken as $\theta_0 = 680$ K while the temperature of the surfaces contacted with water is $\theta_\infty = 300$ K.

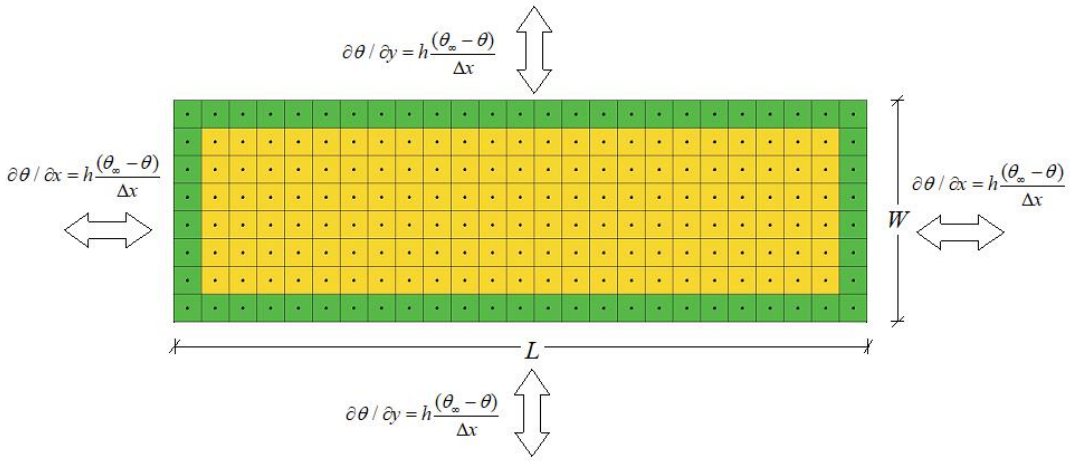

Figure 4.17. *Example III*: Numerical model of the ceramic specimen subjected to 2D quenching.

The contour plots of the damage obtained by the proposed numerical solution and the uniform model at $t = 1$ s are represented in Figure 4.18. Qualitatively, an acceptable agreement is obtained between the crack paths of the two models. Moreover, the experimental results of (Shao et al. 2011) depicted in Figure 4.19 are in a very good agreement with both PD numerical models.

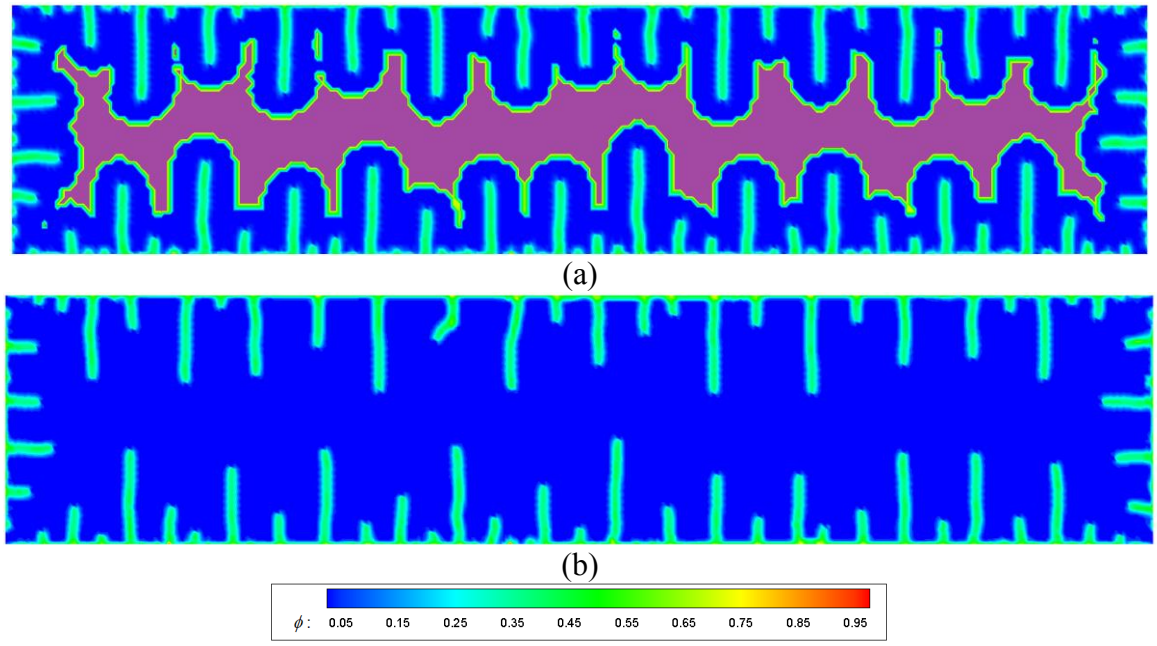

Figure 4.18. *Example III*: Damage predictions after 1.00 s: (a) adaptive refinement model (damage only related to the fine grid) (b) the Uniform model.

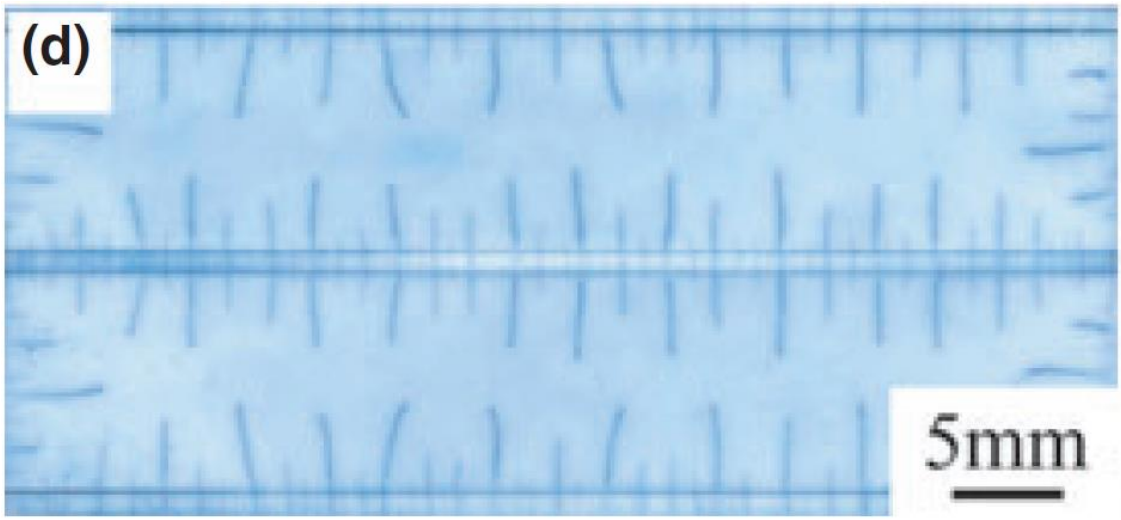

Figure 4.19. Experimental results of quenching test by (Shao et al. 2011).

In order to compare the crack paths quantitatively, one may analyse the crack frequency chart as shown in Figure 4.20. For this analysis only the cracks which their length is greater than 10% of the plate half-width are considered. In the study by (D'Antuono and Morandini 2017), this example has been solved by OSB-PD numerical solution and the results have been

compared to the experimental solution. By using OSB-PD, the number of total cracks with the length of 0.05-0.45 mm is 52 while this number in the experimental model is 56. In this study, 55 and 57 cracks have been obtained using the adaptive refined model and the Uniform model respectively and we observe that a better agreement with the experimental results is achieved. Analyzing Figure 4.20, one can obtain that the crack frequency trend line (dotted line) in the adaptive refined model is much more in agreement with the experimental data.

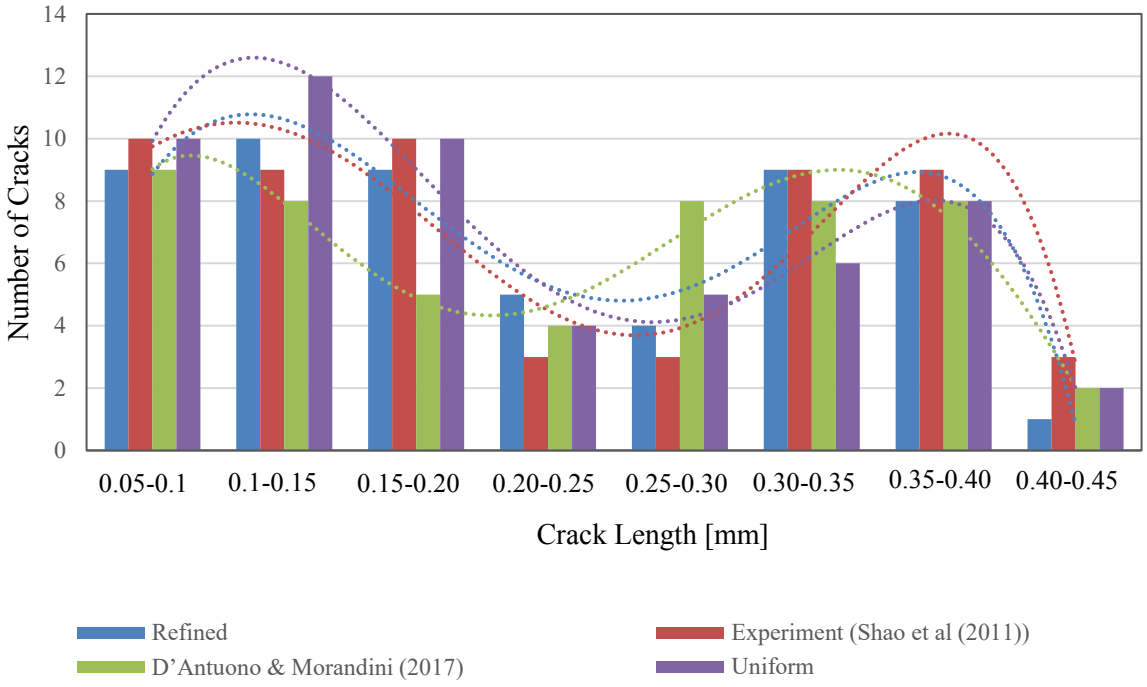

Figure 4.20. *Example III*: Crack frequency diagram and 5th order interpolation of the results

Additionally, in Table 4.2, the runtime of each simulation and the number of real nodes are reported. Consequently, the proposed refinement technique not only reduces the total run time of the code but also conforms well to the experimental data.

Table 4.2. Comparison of the computational resources used by Uniform and refined models in *Example III*.

	Number of real nodes		
		Refined	
	Uniform	Coarse	Fine
$t = 0$ s	24921	3741	0
$t = 1.0$ s		1799	17000
Run time	2016.31 s	817.60 s	

Moreover, temperature field at $t = 1$ s and its comparison to the refinement model are represented in Figure 4.21. Very good agreement between the Uniform and the refined model is achieved.

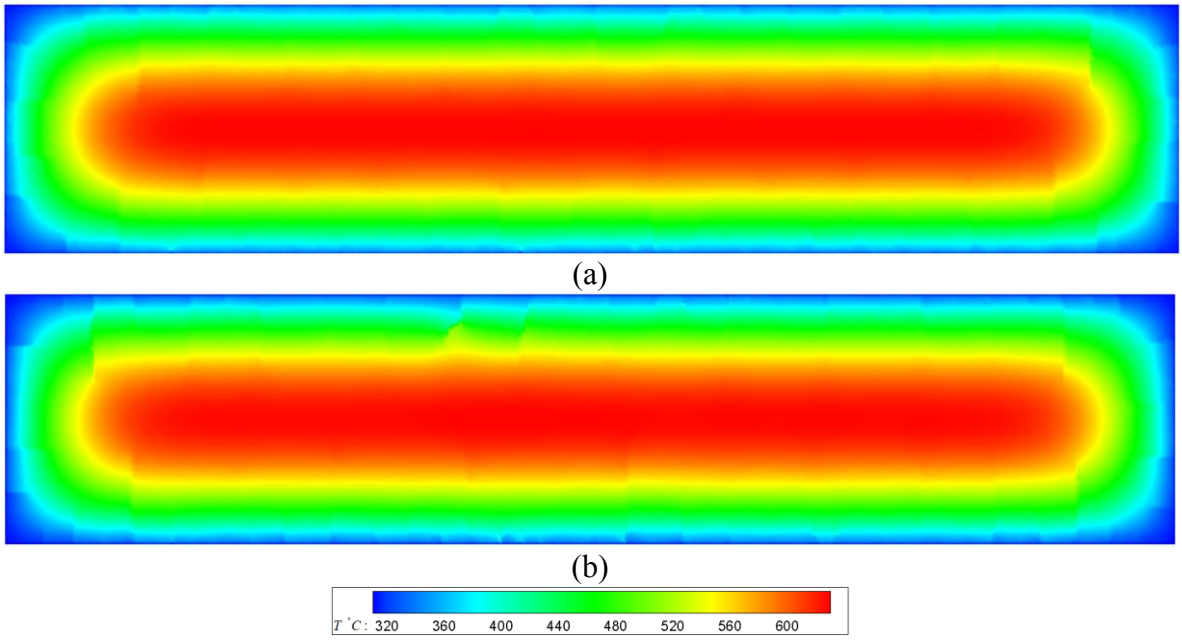

Figure 4.21. Example III: Temperature predictions after 1.00 s: (a) adaptive refinement model (b) the Uniform model.

4.6.4 Example IV: Pre-cracked disk specimen under central thermal shock

To further validate the proposed numerical solution, the thermal shock in a circular ceramic plate is investigated in this example. In the experiments done by (Liu et al. 2015), thin

circular ceramic plates are heated to the certain temperature and then dropped into a water bath. These thin plates are stacked together by two thick circular plates on the outside to set the adiabatic condition at the interior surfaces of the thin circular specimens.

The circular slab has the radius $R = 0.065$ m as shown in Figure 4.22. Based on the experimental model in (Liu et al. 2015), the problem is solved in plane-stress conditions with $E = 370 \times 10^9$ Pa, $\rho = 3980$ kg/m^3, $G_c = 12.16$ J/m^2 and $\nu = 1/3$. The convection boundary condition is imposed around the layer of the plate with the thickness of δ as represented in Figure 4.22. The plate has a temperature-dependent thermal conductivity, specific heat and thermal expansion as shown in Figure 4.23.

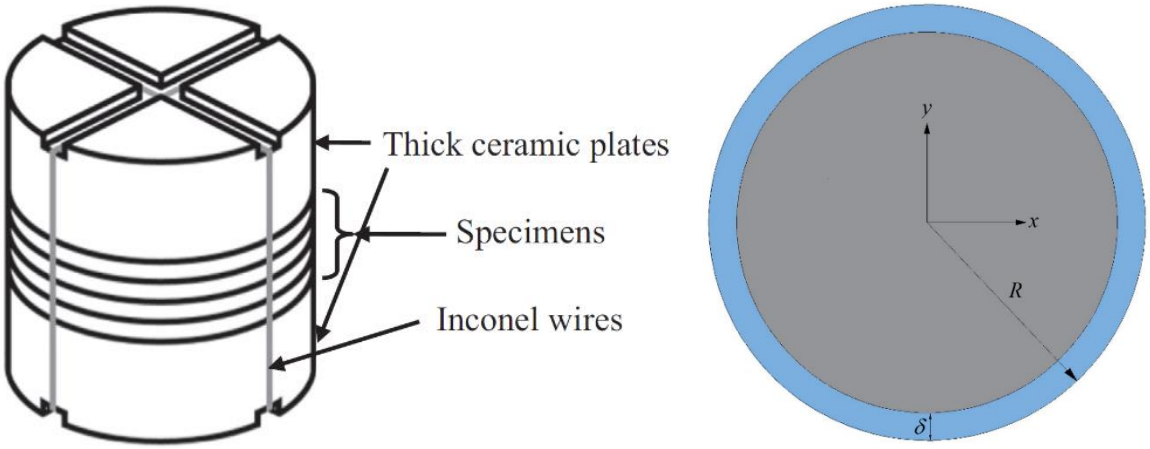

Figure 4.22. Geometrical and loading conditions in *example IV*: (a) schematic diagram (Liu et al. 2015) and (b) numerical model.

The material of the thin circular ceramic specimens is 99% Al2O3. The initial temperature is taken as $\theta_0 = 250\,°\text{C}$ while the temperature of the surfaces contacted with water is $\theta_\infty = 15$ °C. This example is solved for a duration of $t = 0.45$ s with the time integration interval of $\Delta t = 10^{-5}$ s, which results in 45000 steps.

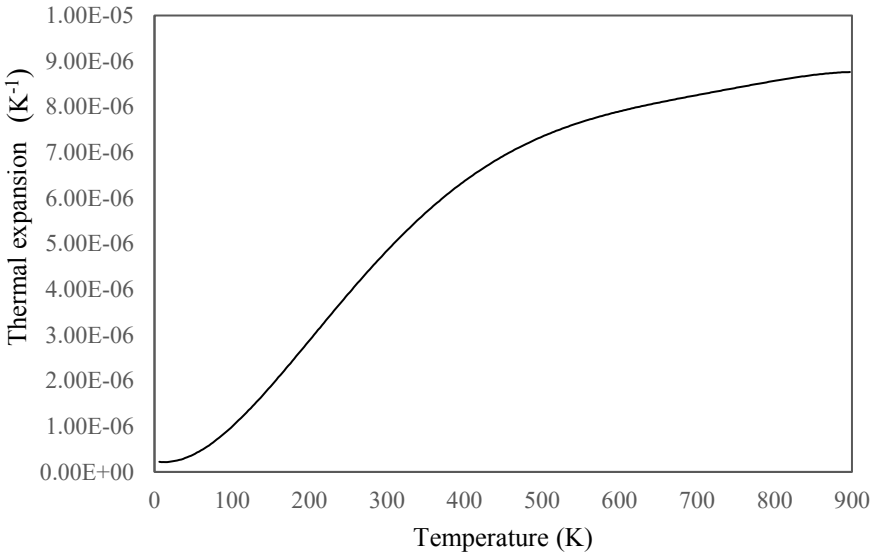
1.00E-05
9.00E-06
8.00E-06
7.00E-06
6.00E-06
5.00E-06
4.00E-06
3.00E-06
2.00E-06
1.00E-06
0.00E+00
Thermal expansion (K-1)
0
100
200
300
400
500
600
700
800
900
Temperature (K)

(a)

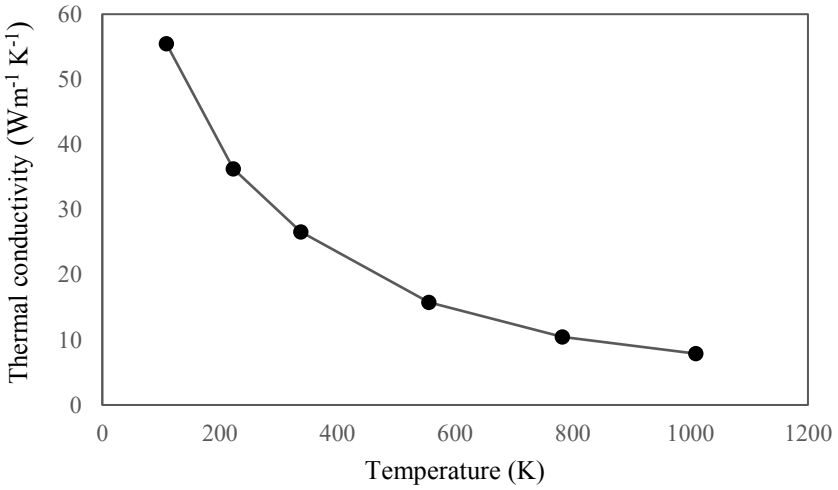
60
50
40
30
20
10
0
Thermal conductivity (Wm-1 K-1)
0
200
400
600
800
1000
1200
Temperature (K)

(b)

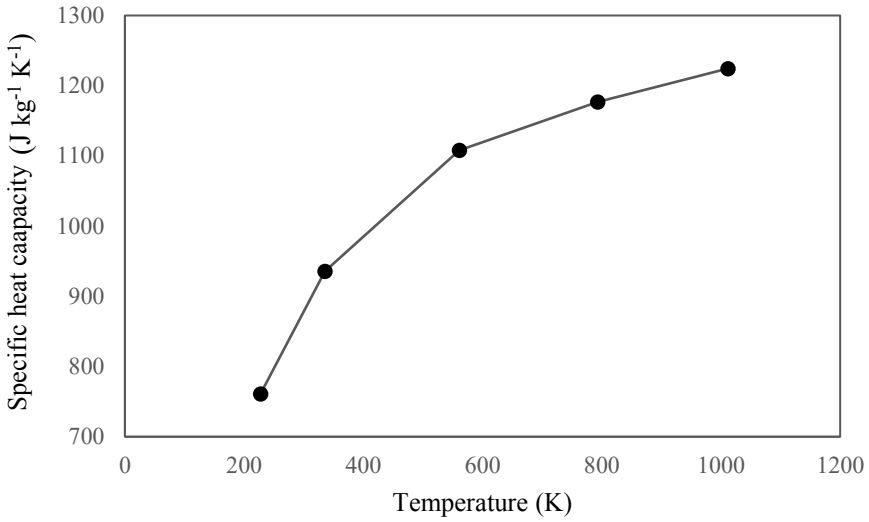

(c)

Figure 4.23. The temperature-dependent thermal properties of (a) thermal expansion, , (b) the thermal conductivity, γ, and (c) the specific heat capacity, c_v, in 99% Al2O3 ceramics versus temperature.

The contour plots of the damage obtained by the proposed numerical solution and Uniform model at $t = 0.45$ s are represented in Figure 4.24. The numerical results illustrate that complex multiple crack paths are initiated from the edge of the circular ceramic specimen and propagate towards the center of the specimen. Acceptable qualitative and quantitative agreement is obtained between the crack paths of the two numerical models and experimental one. Moreover, the number of total cracks in both simulations as well as the experimental model is 15. Also, the number of long cracks, which their length is more than 50% of the radius of the specimen, is equal to 4 in all the models.

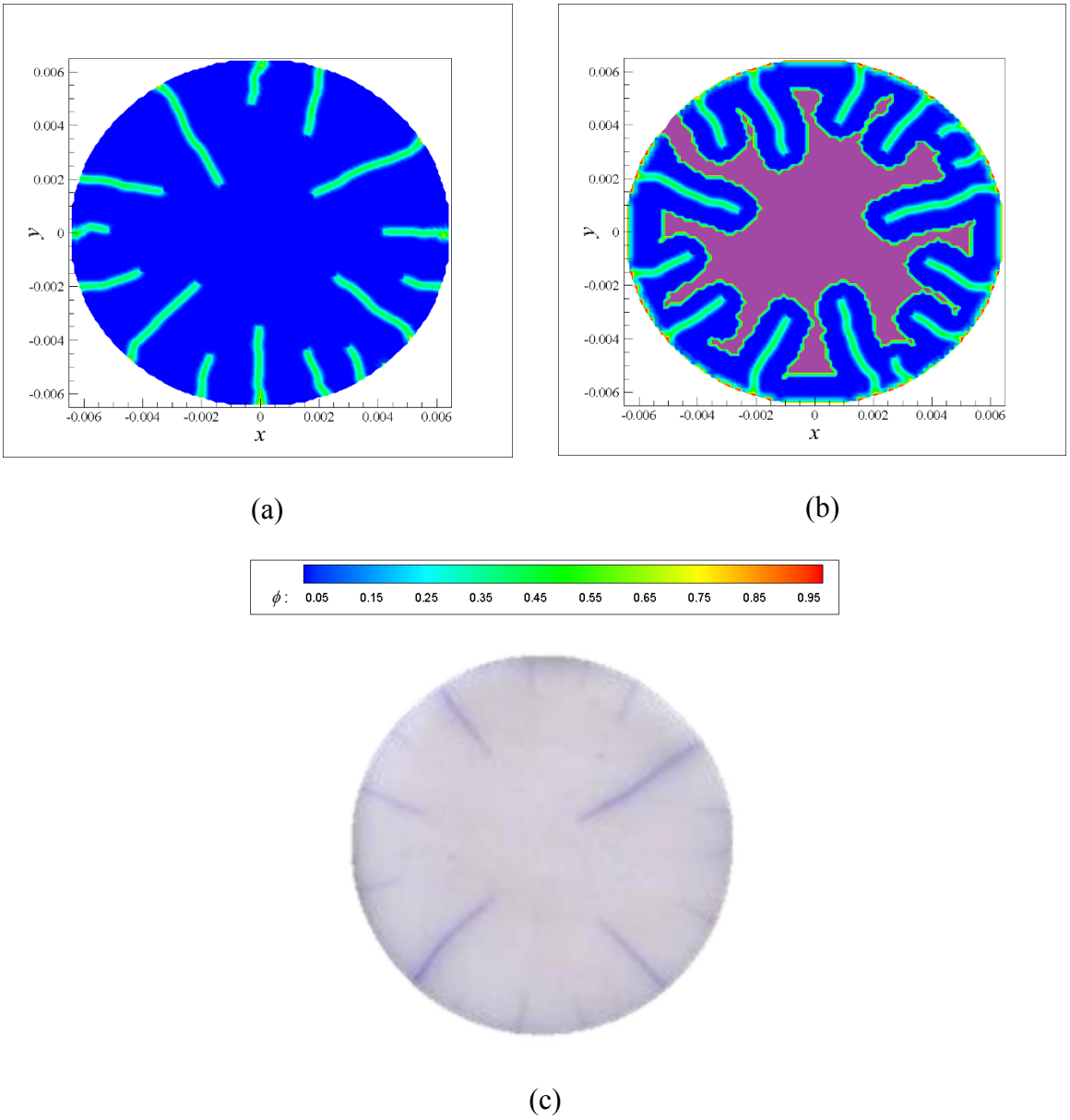

Figure 4.24. Example III: Damage predictions after 0.45 s: (a) the Uniform model (b) adaptive refinement model (damage only related to the fine grid) (c) experimental model by (Liu et al. 2015).

Additionally, in Table 4.3, the runtime of each simulation and the number of real nodes are reported. In this example also the total runtime of the simulation is significantly reduced by using the proposed adaptive refinement technique.

Table 4.3. Comparison of the computational resources used by Uniform and refined models in Example IV.

	Number of real nodes		
		Refined	
	Uniform	Coarse	Fine
$t = 0$ s	17181	4281	0
$t = 0.45$ s		1504	10904
Run time	706.04 s	226.34 s	

Then, the temperature profile and displacements contour plots for the adaptive refined model and the Uniform model are compared with each other as shown in Figure 4.25 and Figure 4.26. The comparison indicates striking agreement.

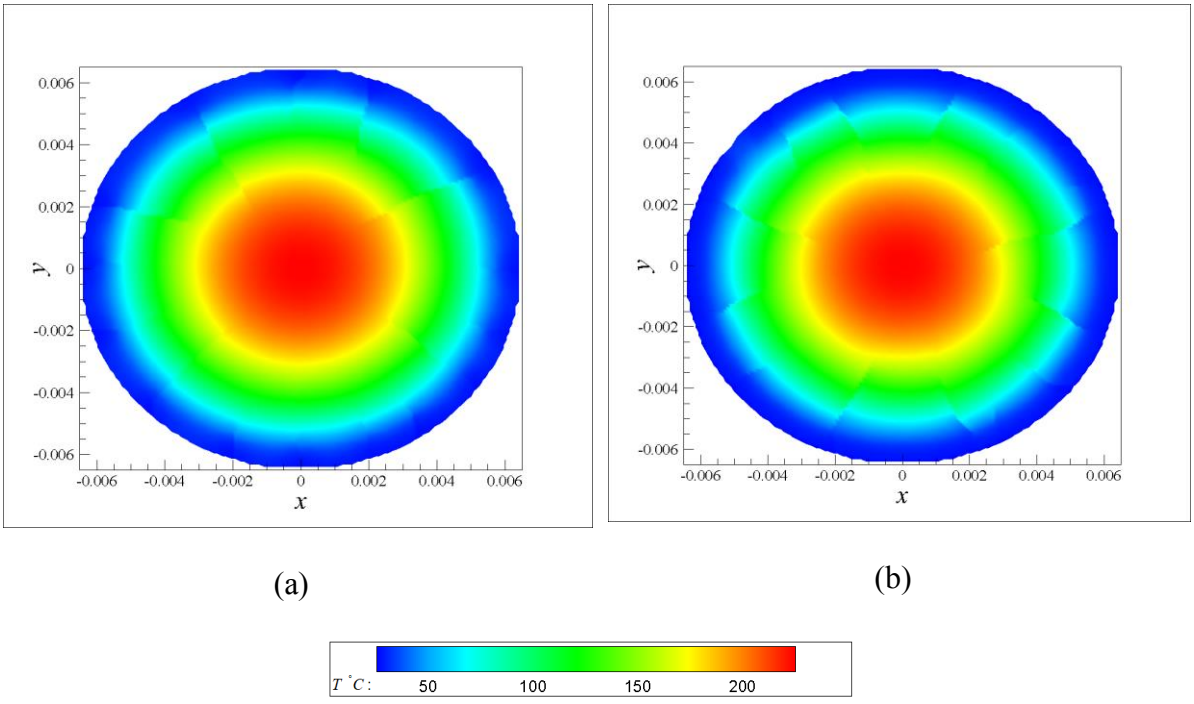

Figure 4.25. *Example IV*: Temperature predictions after 0.45 s: (a) adaptive refinement model (b) the Uniform model.

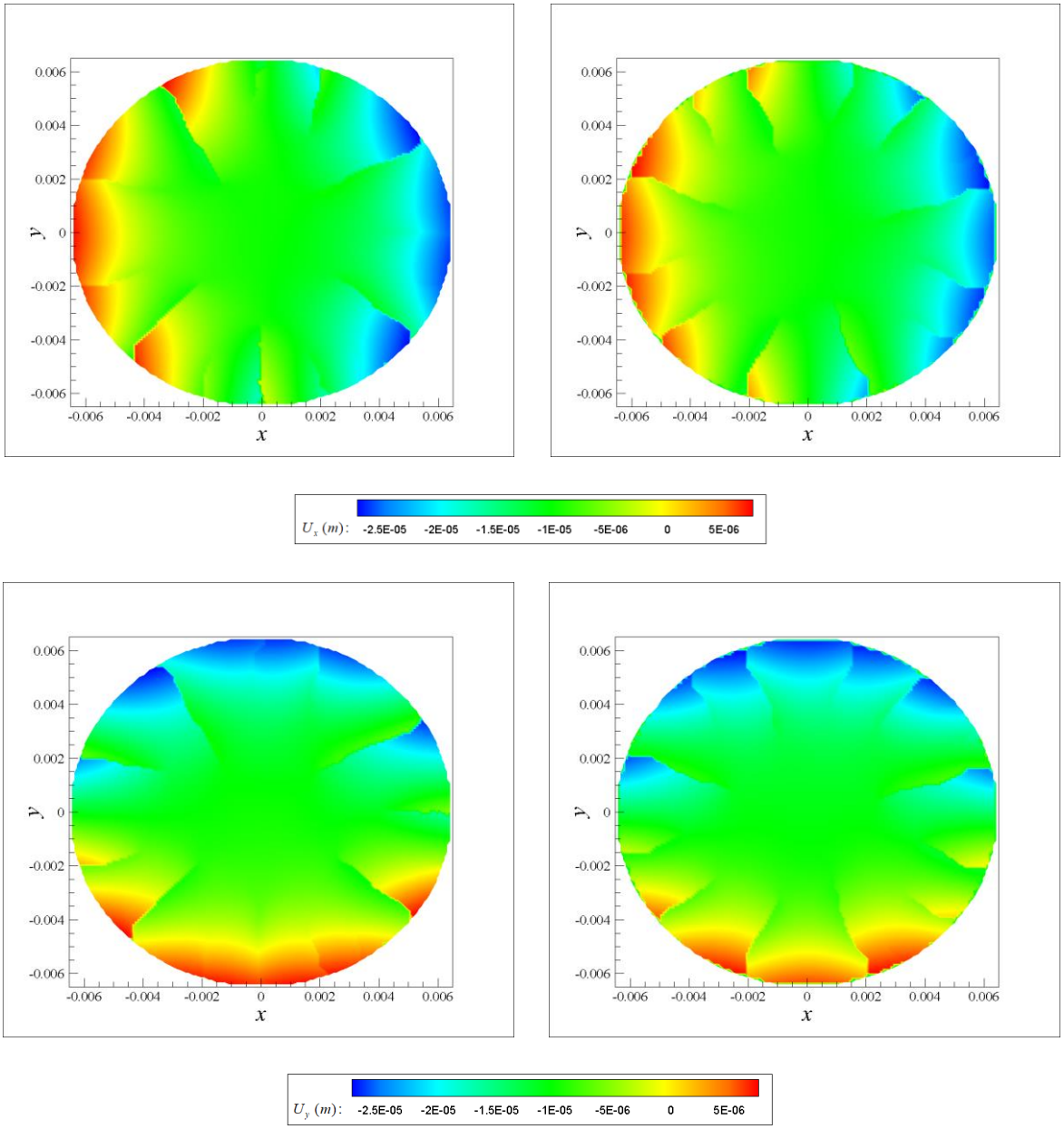

Figure 4.26. *Example IV*: Horizontal displacement predictions after 0.45 s (a) adaptive refinement model (b) the Uniform model and vertical displacement predictions after 0.45 s (c) adaptive refinement model (d) the Uniform model.

Chapter 5 Application of the Peridynamic differential operator to the solution of sloshing problems in tanks

5.1 Introduction

In this chapter we aim at applying the Peridynamic differential operator (PDDO) to incompressible inviscid fluid flow with moving boundaries. Based on the potential flow theory, a Lagrangian formulation is employed to cope with nonlinear free-surface waves of sloshing water in 2D and 3D rectangular and square tanks. In fact, PDDO recasts the local differentiation operator through a nonlocal integration scheme. This makes the method capable of determining the derivatives of a field variable, more precisely than direct differentiation, when jump discontinuities or gradient singularities come into the picture. The issue of gradient singularity can be found in tanks containing vertical/horizontal baffles. The application of PDDO helps us to obtain the velocity field with a high accuracy at each time step that leads to a suitable geometry updating for the procedure. Domain/boundary nodes are updated by using a second order finite difference time algorithm. The method is applied to the solution of different examples including tanks with baffles. The accuracy of the method is scrutinized by comparing the numerical results with analytical, numerical, and experimental results available in the literature. Based on our investigations PDDO can be considered a reliable and suitable

approach to cope with sloshing problems in tanks. The study paves the way to apply the method for a wider range of problems such as compressible fluid flow.

5.2 The Peridynamic differential operator (PDDO) for 2D problems

We consider a scalar field, $f = f(\mathbf{x})$, over a material point $\mathbf{x}$. The variation of this scalar field depends on the interaction of material point $\mathbf{x}$ and other material points $\mathbf{x}'$ located in a finite distance known as horizon length δ .

As explained in (Madenci et al. 2016), by considering the Taylor series expansion of a scalar field, $f(\mathbf{x}') = f(\mathbf{x}+\boldsymbol{\xi})$, PDDO in a two-dimensional domain, $\mathbf{x} = (x, y)$ can be constructed as

$$f(\mathbf{x}+\boldsymbol{\xi}) = \sum_{n_x=0}^{2}\sum_{n_y=0}^{2-n_x} \frac{1}{n_x!\,n_y!}\xi_x^{\,n_x}\xi_y^{\,n_y}\frac{\partial^{n_x+n_y} f(\mathbf{x})}{\partial x^{n_x}\partial y^{n_y}} + R(\mathbf{x}) \tag{5.1}$$

in which, $R(\mathbf{x})$ denotes the reminder, $n_x, n_y = 0,1,2$ and $\boldsymbol{\xi} = (\xi_x, \xi_y) = \mathbf{x}' - \mathbf{x}$. In Eq.(5.1) if $R(x) \to 0$, it can be expressed by

$$f(\mathbf{x}+\boldsymbol{\xi}) = f(\mathbf{x}) + \xi_x\frac{\partial f(\mathbf{x})}{\partial x} + \xi_y\frac{\partial f(\mathbf{x})}{\partial y} + \frac{1}{2}\xi_x^{\,2}\frac{\partial^2 f(\mathbf{x})}{\partial x^2} + \frac{1}{2}\xi_y^{\,2}\frac{\partial^2 f(\mathbf{x})}{\partial y^2} + \xi_x\xi_y\frac{\partial^2 f(\mathbf{x})}{\partial x\partial y} \tag{5.2}$$

One may multiply Peridynamic functions, $g^{p_x p_y}(\boldsymbol{\xi})$, which possess an orthogonality property, to each term of Eq. (5.2) and then integrate it over the horizon of each node, H_x , in which the family members of node $\mathbf{x}$ are located in, by

$$\int_{H_x} f(\mathbf{x}+\boldsymbol{\xi}) g^{p_x p_y}(\boldsymbol{\xi}) dV = f(\mathbf{x}) \int_{H_x} g^{p_x p_y}(\boldsymbol{\xi}) dV + \frac{\partial f(\mathbf{x})}{\partial x} \int_{H_x} \xi_x g^{p_x p_y}(\boldsymbol{\xi}) dV$$
$$+ \frac{\partial f(\mathbf{x})}{\partial y} \int_{H_x} \xi_y g^{p_x p_y}(\boldsymbol{\xi}) dV + \frac{\partial^2 f(\mathbf{x})}{\partial x^2} \int_{H_x} \frac{1}{2} {\xi_x}^2 g^{p_x p_y}(\boldsymbol{\xi}) dV + \frac{\partial^2 f(\mathbf{x})}{\partial y^2} \int_{H_x} \frac{1}{2} {\xi_y}^2 g^{p_x p_y}(\boldsymbol{\xi}) dV$$
$$+ \frac{\partial^2 f(\mathbf{x})}{\partial x \partial y} \int_{H_x} \xi_x \xi_y g^{p_x p_y}(\boldsymbol{\xi}) dV \tag{5.3}$$

where, p_x and p_y represent the order of differentiation with respect to x and y. Since in this study derivatives up to second order are needed (the solution of a Laplace equation shall be of concern), $p_x, p_y = 0,1,2$ through the integration. Thus, PDDO in 2D problems is expressed as

$$\frac{\partial^{p_x+p_y} f(\mathbf{x})}{\partial x^{p_x} \partial y^{p_y}} = \int_{H_x} f(\mathbf{x}+\boldsymbol{\xi}) g^{p_x p_y}(\boldsymbol{\xi}) dV \tag{5.4}$$

Peridynamic functions, $g^{p_x p_y}$, in Eq. (5.4) should possess an orthogonality property as

$$\frac{1}{n_x! n_y!} \int_{H_x} {\xi_x}^{n_x} {\xi_y}^{n_y} g^{p_x p_y}(\boldsymbol{\xi}) dV = \delta_{n_x p_x} \delta_{n_y p_y} \tag{5.5}$$

where $\delta_{n_x p_x}$ and $\delta_{n_y p_y}$ stand for Kronecker delta. The construction of Peridynamic functions, $g^{p_x p_y}$, is given by

$$g^{p_x p_y}(\boldsymbol{\xi}) = \sum_{q_x=0}^{2} \sum_{q_y=0}^{2-q_x} a_{q_x}^{p_x} a_{q_y}^{p_y} w_{q_x q_y}(\|\boldsymbol{\xi}\|) {\xi_x}^{q_x} {\xi_y}^{q_y} \tag{5.6}$$

in which, $w_{q_x q_y}(\|\boldsymbol{\xi}\|)$, are the weight functions which correspond to each term ${\xi_x}^{q_x}, {\xi_y}^{q_y}$ in the polynomial expansion. As, explained in (Madenci et al. 2016) , the weight function determines the degree of non-local interaction between the nodes and their family nodes. Although $w_{q_x q_y}(\|\boldsymbol{\xi}\|)$ can be different for each term of Taylor series expansion, for the sake of

simplification, $w_{q_x q_y}(\|\boldsymbol{\xi}\|)$ can be the same for each term as $w_{p_x p_y}(\|\boldsymbol{\xi}\|) = w(\|\boldsymbol{\xi}\|)$. Hence, Eq. (5.6) can be expressed by

$$g^{p_x p_y}(\boldsymbol{\xi}) = w(\|\boldsymbol{\xi}\|)(a_{00}^{p_x p_y} + a_{10}^{p_x p_y}\xi_x + a_{01}^{p_x p_y}\xi_y + a_{20}^{p_x p_y}\xi_x^{\,2} + a_{02}^{p_x p_y}\xi_y^{\,2} + a_{11}^{p_x p_y}\xi_x\xi_y) \tag{5.7}$$

in which the weight function, $w(\|\boldsymbol{\xi}\|)$, is constructed based on a Gaussian distribution as follows

$$w(\|\boldsymbol{\xi}\|) = e^{-(2|\xi|/\delta)^2} \tag{5.8}$$

where δ represents the horizon length. In order to find unknown coefficients, $a_{q_x}^{p_x} a_{q_y}^{p_y}$, in Eq.(5.7), one may put Eq. (5.7) in Eq. (5.5)and generate a linear system of equations as:

$$\sum_{q_x=0}^{2}\sum_{q_y=0}^{2-q_x}\sum_{q_x+q_y=0}^{2} A_{(n_x n_y)(q_x q_y)} a_{q_x q_y}^{p_x p_y} = b_{n_x n_y}^{p_x p_y} \tag{5.9}$$

To simplify Eq.(5.9), the coefficient matrix, $\mathbf{A}$, the matrix of unknown coefficients, $\mathbf{a}$, and the vector $\mathbf{b}$ can be formed as:

$$\mathbf{A} = \int_{H_x} w(\|\boldsymbol{\xi}\|) \begin{bmatrix} 1 & \xi_x & \xi_y & \xi_x^{\,2} & \xi_y^{\,2} & \xi_x\xi_y \\ \xi_x & \xi_x^{\,2} & \xi_x\xi_y & \xi_x^{\,3} & \xi_x\xi_y^{\,2} & \xi_x^{\,2}\xi_y \\ \xi_y & \xi_x\xi_y & \xi_y^{\,2} & \xi_x^{\,2}\xi_y & \xi_y^{\,3} & \xi_x\xi_y^{\,2} \\ \xi_x^{\,2} & \xi_x^{\,3} & \xi_x^{\,2}\xi_y & \xi_x^{\,4} & \xi_x^{\,2}\xi_y^{\,2} & \xi_x^{\,3}\xi_y \\ \xi_y^{\,2} & \xi_x\xi_y^{\,2} & \xi_y^{\,3} & \xi_x^{\,2}\xi_y^{\,2} & \xi_y^{\,4} & \xi_x\xi_y^{\,3} \\ \xi_x\xi_y & \xi_x^{\,2}\xi_y & \xi_x\xi_y^{\,2} & \xi_x^{\,3}\xi_y & \xi_x\xi_y^{\,3} & \xi_x^{\,2}\xi_y^{\,2} \end{bmatrix} dV \tag{5.10}$$

$$\mathbf{a} = \begin{bmatrix} a_{00}^{00} & a_{00}^{10} & a_{00}^{01} & a_{00}^{20} & a_{00}^{02} & a_{00}^{11} \\ a_{10}^{00} & a_{10}^{10} & a_{10}^{01} & a_{10}^{20} & a_{10}^{02} & a_{10}^{11} \\ a_{01}^{00} & a_{01}^{10} & a_{01}^{01} & a_{01}^{20} & a_{01}^{02} & a_{01}^{11} \\ a_{20}^{00} & a_{20}^{10} & a_{20}^{01} & a_{20}^{20} & a_{20}^{02} & a_{20}^{11} \\ a_{02}^{00} & a_{02}^{10} & a_{02}^{01} & a_{02}^{20} & a_{02}^{02} & a_{02}^{11} \\ a_{11}^{00} & a_{11}^{10} & a_{11}^{01} & a_{11}^{20} & a_{11}^{02} & a_{11}^{11} \end{bmatrix} \tag{5.11}$$

and

$$\mathbf{b}=\begin{bmatrix}1&0&0&0&0&0\\0&1&0&0&0&0\\0&0&1&0&0&0\\0&0&0&2&0&0\\0&0&0&0&2&0\\0&0&0&0&0&1\end{bmatrix} \tag{5.12}$$

Therefore, to satisfy the orthogonality property of PD functions, we just need to solve Eq. (5.9) as

$$\mathbf{a}=\mathbf{A}^{-1}\mathbf{b} \tag{5.13}$$

Having found the constant coefficients of the PD functions, $a_{q_xq_y}^{p_xp_y}$, one can compute Peridynamic derivatives explicitly using Eq (5.4):

$$\begin{Bmatrix} f(\mathbf{x}) \\ \dfrac{\partial f(\mathbf{x})}{\partial x} \\ \dfrac{\partial f(\mathbf{x})}{\partial y} \\ \dfrac{\partial^2 f(\mathbf{x})}{\partial x^2} \\ \dfrac{\partial^2 f(\mathbf{x})}{\partial y^2} \\ \dfrac{\partial^2 f(\mathbf{x})}{\partial x\partial y} \end{Bmatrix} = \int_{H_x} f(\mathbf{x}+\boldsymbol{\xi}) \begin{Bmatrix} g^{00}(\boldsymbol{\xi}) \\ g^{10}(\boldsymbol{\xi}) \\ g^{01}(\boldsymbol{\xi}) \\ g^{20}(\boldsymbol{\xi}) \\ g^{02}(\boldsymbol{\xi}) \\ g^{11}(\boldsymbol{\xi}) \end{Bmatrix} dV \tag{5.14}$$

As a result, PDDO enables the determination of different order of partial derivatives of the spatial functions using the simple integration in Eq.(5.14). This feature provides accurate derivatives without performing any numerical differentiation or employing any kernel functions.

In the subsequent section, the way of applying the recalled formulation to the solution of free-surface fluid problems as well as proper satisfaction of boundary conditions are explained.

5.3 Governing Lagrangian equations in 2D domain

Let consider a 2D domain, Ω, containing incompressible inviscid fluid as depicted in Figure 5.1. The portions of the boundary for this domain is taken as $\partial\Omega = \Gamma_S \bigcup \Gamma_F$, in which, Γ_S denotes the fluid-tank interface whereas Γ_F indicates the free surface of the fluid (see Figure 5.1). In fluid dynamics, for an irrotational velocity field, potential flow theory can be used. This theory describes the velocity field as the gradient of a scalar function

$$\mathbf{u} = \nabla\varphi \tag{5.15}$$

For an incompressible fluid e.g. water, the divergence of the velocity is

$$\nabla\mathbf{u} = 0 \tag{5.16}$$

Consequently, velocity potential, φ, has to satisfy the Laplace equation

$$\nabla^2\varphi = 0 \qquad \text{in } \Omega \tag{5.17}$$

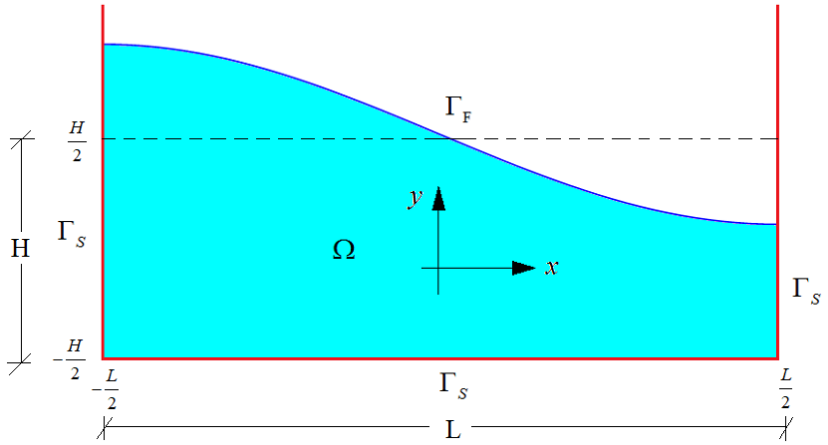

Figure 5.1. Problem domain and its boundaries.

We define the fluid boundary conditions in terms of velocity potential. The boundary conditions at the fluid-tank interface can be expressed as

$$\mathbf{n}^T\mathbf{u} = \mathbf{n}^T\mathbf{u}_S \tag{5.18}$$

where $\mathbf{n}$ is the outward vector normal to the fluid boundaries (Figure 5.2) and $\mathbf{u}_S$ represents the external predefined velocity exerted to the fluid-tank interface so that the boundary condition on Γ_S is given by

$$\frac{\partial\varphi}{\partial n} = \mathbf{n}^T\mathbf{u}_S \text{, on } \Gamma_S \tag{5.19}$$

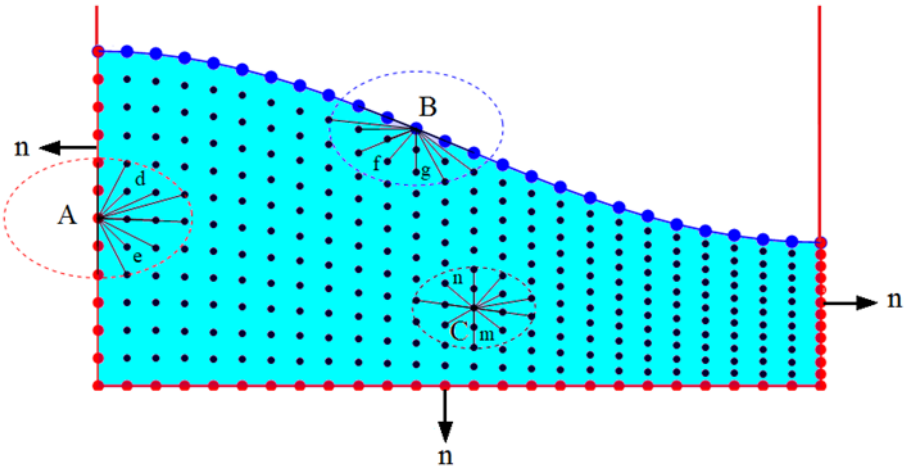

Figure 5.2. Discretization of the domain and boundary nodes.

On the other hand at the free surface, Γ_F, dynamic free surface boundary conditions (DFSBC) based on Lagrangian theory can be expressed by (Wu and Chang 2011)

$$\frac{d\varphi}{dt} = g(y + \frac{H}{2}) + \frac{1}{2}(\nabla\varphi.\nabla\varphi) \text{ , on } \Gamma_F \tag{5.20}$$

in which, H represents the water depth. In the above formula, precise evaluation of $\nabla\varphi$ is crucial to obtain a desirable convergence solution over the time. In the following section this evaluation will be explained comprehensively.

5.4 The solution procedure in 2D domain

In order to discretize the field equation and the boundary conditions, the family of each node should be determined. Then the degree of interaction with the family nodes is specified by the weight function expressed in Eq.(5.8). The horizon shapes can be taken arbitrarily although here they are considered to be circles with a radius of $\delta = m\Delta x$. In which Δx stands for the average distance between distributed nodes. The size and shape of the family nodes depend

on the efficiency of the computational solution; however, it should satisfy the nonlocal characteristics of the field equations. The PD function, $g^{p_x p_y}(\boldsymbol{\xi})$, is unique for each node and its value relates to the distribution of family nodes.

To illustrate numerical implementation, the two-dimensional differential field equation is expanded as

$$\left(\frac{\partial^2}{\partial^2 x}+\frac{\partial^2}{\partial^2 y}\right)\varphi(x,y)=0 \quad x,y\in\Omega \tag{5.21}$$

in which, $\varphi(\mathrm{x},\mathrm{y})$ is the unknown field variable. The boundary conditions expressed in Section 5.3 can be rewritten in the following form

$$\begin{aligned}
&\frac{\partial}{\partial y}\varphi(\mathrm{x},\mathrm{y}=-\frac{H}{2})=\mathrm{p}(\mathrm{x})\\
&\frac{\partial}{\partial x}\varphi(\mathrm{x}=-\frac{L}{2},\mathrm{y})=q(\mathrm{y})\\
&\frac{\partial}{\partial x}\varphi(\mathrm{x}=\frac{L}{2},\mathrm{y})=r(\mathrm{y})\\
&\varphi(\mathrm{x},\mathrm{y})=s(\mathrm{x},\mathrm{y}) \quad (\mathrm{x},\mathrm{y})\in\Gamma_{\mathrm{F}}
\end{aligned} \tag{5.22}$$

where $p(x)$, $q(y)$, $r(y)$ and $s(x,y)$ are known functions.

The integration is performed by a summation over all the family nodes within the horizon of $\mathbf{x}_i$ Thus, based on Eq.(5.21), a system of algebraic equations in terms of the PD unknowns, $\varphi(\mathrm{x}_j,\mathrm{y}_j)$, can be formed as

$$\sum_j\left[g^{20}(x_j-x_i,\mathrm{y}_j-y_i)+g^{02}(x_j-x_i,\mathrm{y}_j-y_i)\right]\varphi(\mathrm{x}_j,y_j)\,\mathrm{V}_j=0 \tag{5.23}$$

where V_j represents the volume of each node. i and j are the index of the collocation points and their family pointes respectively.

As for instance, $\mathbf{x}_C$ in Figure 5.2, represents a node positioned in the fluid domain, Ω . Recasting Eq (5.21) in terms of the integral operators introduced in Eq.(5.14), and evaluating the equation at $\mathbf{x}_C$ results in

$$\int_{H_{X(\mathrm{C})}} \varphi(\mathbf{x}+\boldsymbol{\xi}) g^{20}(\boldsymbol{\xi})\, dV + \int_{H_{X(\mathrm{C})}} \varphi(\mathbf{x}+\boldsymbol{\xi}) g^{02}(\boldsymbol{\xi})\, dV = 0 \tag{5.24}$$

The above equation based on Eq. (5.23) can be discretized as follows:

$$\cdots + k_{CC}\varphi_C V_C + k_{Cm}\varphi_m V_m + k_{Cn}\varphi_n V_n + \cdots = 0 \tag{5.25}$$

where, $k_{Cj} = g^{20}_{Cj}(\boldsymbol{\xi}_{Cj}) + g^{02}_{Cj}(\boldsymbol{\xi}_{Cj})$, and $\boldsymbol{\xi}_{Cj} = \mathbf{x}_j - \mathbf{x}_C$

Likewise, the boundary conditions are imposed at boundary points. Therefore, the boundary conditions given in Eq. (5.19)and Eq. (5.20) can be expressed in terms of PD unknowns, $\varphi(\mathrm{x}_j, \mathrm{y}_j)$, as

$$\begin{aligned}
&\sum_{j=1} \varphi(x_j, y_j) g^{01}(\mathrm{x}_j - x_i, \mathrm{y}_j - y_i)\, \mathrm{V}_j = \mathrm{p}(\mathrm{x}_i) \quad \text{for} \quad \mathrm{y}_i = -\frac{H}{2} \\
&\sum_{j=1} \varphi(x_j, y_j) g^{10}(\mathrm{x}_j - x_i, \mathrm{y}_j - y_i)\, \mathrm{V}_j = q(y_i) \quad \text{for} \quad x_i = -\frac{L}{2} \\
&\sum_{j=1} \varphi(x_j, y_j) g^{10}(\mathrm{x}_j - x_i, \mathrm{y}_j - y_i)\, \mathrm{V}_j = r(y_i) \quad \text{for} \quad x_i = \frac{L}{2} \\
&\sum_{j=1} \varphi(x_j, y_j) g^{00}(\mathrm{x}_j - x_i, \mathrm{y}_j - y_i)\, \mathrm{V}_j = s(\mathrm{x}_i, y_i) \quad \text{for} \quad (x_i, y_i) \in \Gamma_{\mathrm{F}}
\end{aligned} \tag{5.26}$$

Then, we perform the same procedure for $\mathbf{x}_A$ and $\mathbf{x}_B$ which are representative of two nodes with Neumann and Dirichlet boundary condition, respectively. Consequently, recasting the boundary relations given in Eq. (5.22) and evaluating at the nodes respectively leads to:

$$n_x \int_{H_{X(\mathrm{A})}} \varphi(\mathbf{x}+\boldsymbol{\xi}) g^{10}(\boldsymbol{\xi})\, dV + n_y \int_{H_{X(\mathrm{A})}} \varphi(\mathbf{x}+\boldsymbol{\xi}) g^{01}(\boldsymbol{\xi})\, dV = q(y_{(\mathrm{A})}) \tag{5.27}$$

and

$$\int_{H_{X(\mathrm{B})}} \varphi(\mathbf{x}+\boldsymbol{\xi}) g^{00}(\boldsymbol{\xi})\, dV = s(x_{(B)}) \tag{5.28}$$

Therefore, discretizing the above equations results in:

$$\cdots + k_{AA}\varphi_A V_A + k_{Ad}\varphi_d V_d + k_{Ae}\varphi_e V_e + \cdots = q(y_{(A)}) \tag{5.29}$$

and

$$\cdots + k_{BB}\varphi_B V_B + k_{Bg}\varphi_g V_g + k_{Bf}\varphi_f V_f + \cdots = s(\mathrm{x}_{(\mathrm{B})}) \tag{5.30}$$

where, $k_{Aj} = n_x g^{10}_{Aj}(\xi_{Aj}) + n_y g^{01}_{Aj}(\xi_{Cj})$, and $k_{Bj} = g^{00}_{Bj}(\xi_{Bj})$.

By merging Eq. (5.23) and Eq.(5.26), a linear algebraic system based on the PDDO approach can be formed as

$$\mathbf{k}\,\boldsymbol{\varphi} = \bar{\mathbf{u}} \tag{5.31}$$

in which $\mathbf{k}$ is the global matrix, $\boldsymbol{\varphi}$ is velocity potential unknown values whereas $\bar{\mathbf{u}}$ is the point-wise boundary/domain condition. To illustrate, one may expand Eq. (5.31) as

$$\begin{bmatrix} \vdots & \vdots & \vdots & \vdots & \vdots & \vdots & \vdots & \vdots & \vdots & \vdots & \vdots & \vdots & \vdots \\ \cdots & k_{AA}V_A & k_{Ad}V_d & k_{Ae}V_e & \cdots & 0 & 0 & 0 & \cdots & 0 & 0 & 0 & \cdots \\ \cdots & 0 & 0 & 0 & \cdots & k_{BB}V_B & k_{Bg}V_B & k_{Bf}V_B & \cdots & 0 & 0 & 0 & \cdots \\ \cdots & 0 & 0 & 0 & \cdots & 0 & 0 & 0 & \cdots & k_{CC}V_C & k_{Cm}V_C & k_{Cn}V_C & \cdots \\ \vdots & \vdots & \vdots & \vdots & \vdots & \vdots & \vdots & \vdots & \vdots & \vdots & \vdots & \vdots & \vdots \end{bmatrix} \begin{bmatrix} \vdots \\ \varphi_A \\ \varphi_d \\ \varphi_e \\ \vdots \\ \varphi_B \\ \varphi_g \\ \varphi_f \\ \vdots \\ \varphi_C \\ \varphi_m \\ \varphi_n \\ \vdots \end{bmatrix} = \begin{bmatrix} \vdots \\ \overline{u}_A \\ \vdots \\ \overline{u}_B \\ \vdots \\ \overline{u}_C \\ \vdots \end{bmatrix}$$

(5.32)

The rows of $\mathbf{k}$ represent each collocation point located in the domain/boundaries while the columns of $\mathbf{k}$ are associated with the family points. $\mathbf{k}$ is a square matrix and the entries of $\mathbf{k}$, when node j is a family point of point i, is given by

$$\begin{cases} \forall(x_i, \mathrm{y}_i) \in \Omega \rightarrow k_{ij} = g_{ij}^{02}(\boldsymbol{\xi}) + g_{ij}^{20}(\boldsymbol{\xi}) \\ \forall(x_i, \mathrm{y}_i) \in \Gamma_S \rightarrow k_{ij} = g_{ij}^{10}(\boldsymbol{\xi})\,\mathrm{n}_x + g_{ij}^{01}(\boldsymbol{\xi})\,\mathrm{n}_y \\ \forall(x_i, \mathrm{y}_i) \in \Gamma_F \rightarrow k_{ij} = g_{ij}^{00}(\boldsymbol{\xi}) \end{cases} \tag{5.33}$$

Correspondingly, boundary/domain conditions, $\overline{\mathbf{u}}$, for all types of nodes are defined as

$$\begin{cases} \forall(x_i, \mathrm{y}_i) \in \Omega \rightarrow \overline{u}_i = 0 \\ \forall(x_i, \mathrm{y}_i) \in \Gamma_S \rightarrow \overline{u}_i = p(x_i) \text{ or } q(\mathrm{y}_i) \text{ or } \mathrm{r}(\mathrm{y}_i) \rightarrow \overline{u}_i = u_{x(i)}\,\mathrm{n}_x + u_{y(i)}\,\mathrm{n}_y \\ \forall(x_i, \mathrm{y}_i) \in \Gamma_F \rightarrow \overline{u}_i = s(\mathrm{x}_i, \mathrm{y}_i) \rightarrow \overline{u}_i = \left(\varphi_i\right)_0 + \int_{t_0}^{t} g(y_i + \frac{H}{2}) + \frac{1}{2}(\nabla\varphi_i.\nabla\varphi_i)dt \end{cases} \tag{5.34}$$

By replacing Eqs. (5.33) and (5.34) into Eq. (5.32), and solving a linear system of equations the unknown values of the $\boldsymbol{\varphi}$ vector would be obtained by

$$\boldsymbol{\varphi} = \mathbf{k}^{-1}\,\bar{\mathbf{u}} \tag{5.35}$$

Having found the velocity potential, one can calculate the velocity field vector, $\mathbf{u}$, based on Eq. (5.14), by performing integration over family nodes as follows

$$\begin{aligned}(u_x)_i &= \frac{\partial \varphi}{\partial x} = \int_{H_i} g^{10}(\boldsymbol{\xi})\,\varphi dV \\ (u_y)_i &= \frac{\partial \varphi}{\partial y} = \int_{H_i} g^{01}(\boldsymbol{\xi})\,\varphi dV\end{aligned} \tag{5.36}$$

where i index stands for the collocation point number. The velocity field vector, $\mathbf{u}$, should be calculated numerically with respect to (5.36), as

$$\begin{aligned}(u_x)_i &= \frac{\partial \varphi}{\partial x} = \sum_{j=1}^{r} g_{ij}^{10}(\boldsymbol{\xi})\,\varphi_j V_j \\ (u_y)_i &= \frac{\partial \varphi}{\partial y} = \sum_{j=1}^{r} g_{ij}^{01}(\boldsymbol{\xi})\,\varphi_j V_j\end{aligned} \tag{5.37}$$

in which j and r are the index of family pointes and the total number of points located in a horizon, respectively. Hence, spatial derivatives of potential flow function (velocity) is determined accurately using the simple integration in Eq. (5.37).

In many numerical solutions this procedure is done by getting derivatives from the approximated potential flow field function which reduces the accuracy especially near the corners of a tank or near the baffle structures of complex shape.

5.4.1 Time marching

We assume the total solution time has been divided into small increments. Accordingly, Laplace equation with the aforementioned boundary conditions is solved in each time step to predict the velocity potential and the velocity field in the entire domain. Therefore, the rigid body movements of the tank, as well as the liquid free-surface boundary conditions are updated. Nonlinear terms are taken into account to predict the new DFSBC for the next time step.

Consequently, by using a second order finite difference scheme in time domain, DFSBC is formulated as (Wu et al. 2016; Wu and Chang 2011)

$$\forall(\mathrm{x}_i,\mathrm{y}_i)\in\Gamma_{\mathrm{F}}\rightarrow(\varphi_i)^{(n)}=(\varphi_i)^{(n-2)}+2\,\Delta t\left[\left(-g\,(y+\frac{H}{2})+\frac{1}{2}\nabla\varphi.\nabla\varphi\right)_i\right]^{(n-1)} \tag{5.38}$$

Therefore, one may recast Eq. (5.34) as

$$\begin{cases}\forall(x_i,\mathrm{y}_i)\in\Omega\rightarrow\bar{u}_i=0\\ \forall(x_i,\mathrm{y}_i)\in\Gamma_S\rightarrow\bar{u}_i=p(x_i)\text{ or }q(\mathrm{y}_i)\text{ or r}(\mathrm{y}_i)\rightarrow\bar{u}_i=u_{x(i)}\,\mathrm{n}_x+u_{y(i)}\,\mathrm{n}_y\\ \forall(x_i,\mathrm{y}_i)\in\Gamma_F\rightarrow\bar{u}_i=s(\mathrm{x}_i,\mathrm{y}_i)\rightarrow\bar{u}_i=(\varphi_i)^{(n-2)}+2\,\Delta t\left[\left(-g\,(y+\frac{H}{2})+\frac{1}{2}\nabla\varphi.\nabla\varphi\right)_i\right]^{(n-1)}\end{cases} \tag{5.39}$$

In order to find the new configuration of the domain, kinematic free-surface boundary condition is expressed as

$$\nabla\varphi=\frac{d\mathbf{x}}{dt} \tag{5.40}$$

Using Eq. (5.40) and the second order finite difference scheme which is denominated as a

leap-frog time marching approach, we are able to obtain the new configuration of the nodes as

$$\mathbf{x}^{n} = \mathbf{x}^{(n-2)} + 2\,\Delta t(\nabla\varphi)^{(n-1)} \tag{5.41}$$

5.4.2 The step by step procedure of the method

After defining the problem geometry, to give an insight into the implementation of the method, we clarify the step by step procedure.

1. The method is capable of dealing with irregular distribution of nodes; nonetheless, we suggest to use a regular distribution of nodes at the first time step.
2. Choosing a set of family nodes for each node based on its horizon length, δ.
3. Evaluate the $\mathbf{k}$ using Eq. (5.33).
4. Evaluate the $\bar{\mathbf{u}}$ as defined in Eq. (5.39).
5. Solve the linear algebraic system in Eq. (5.35), and determine the velocity potential value, φ, for each node.
6. Evaluate the velocity of each node using Eq. (5.37).
7. Update the velocity potential values of the free surface nodes based on Eq. (5.38).
8. Calculate the final configuration using Eq. (5.41).
9. Replace the configuration, $\mathbf{x}^{(n-1)}$, at (n-1) time step with the configuration at (n-2) time step, $\mathbf{x}^{(n-2)}$.
10. Replace the velocity potential vector, $\varphi^{(n-1)}$, at (n-1) time step with the velocity potential vector at (n-2) time step, $\varphi^{(n-2)}$.
11. Repeat the procedure from step 3.

The whole solution procedure can be cast in a flowchart shown in Figure 5.3.

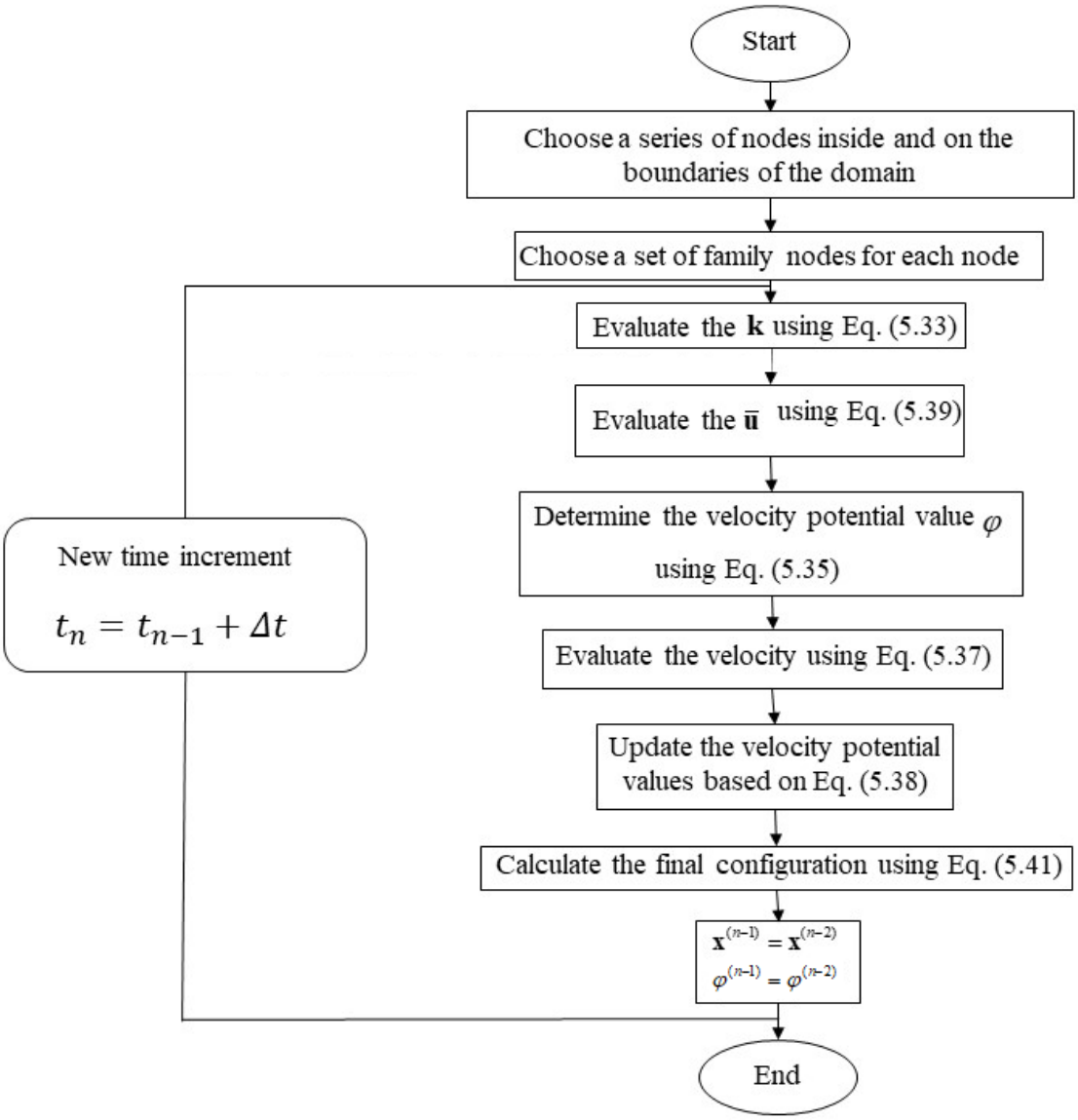

Figure 5.3. Step by step procedure of the method.

All the codes are developed using standard Wolfram Mathematica language on an Intel Core i7-6700HQ 2.60 GHz CPU, on a 64 bit Windows 10 Enterprise system.

5.5 Governing Lagrangian equations and the solution procedure in 3D domain

By considering the second order Taylor series expansion of scalar field, $f(\mathbf{x}') = f(\mathbf{x}+\boldsymbol{\xi})$, PDDO in a three-dimensional domain, $\mathbf{x} = (x, \mathrm{y}, \mathrm{z})$ can be constructed as

$$f(\mathbf{x}+\boldsymbol{\xi}) = \sum_{n_x=0}^{2} \sum_{n_y=0}^{2-n_x} \sum_{n_z=0}^{2-n_x-n_x} \frac{1}{n_x!\,n_y!\,n_z!} \xi_x^{\,n_x} \xi_y^{\,n_y} \xi_z^{\,n_z} \frac{\partial^{n_x+n_y+n_z} f(\mathbf{x})}{\partial x^{n_x} \partial y^{n_y} \partial z^{n_z}} + R(\mathbf{x}) \tag{5.42}$$

Similar to the 2D procedure, $\mathbf{A}$, the matrix of unknown coefficients, $\mathbf{a}$, and the vector $\mathbf{b}$ for 3D domain can be formed as:

$$\mathbf{A} = \int_{H_x} w(\|\boldsymbol{\xi}\|) \begin{bmatrix}
1 & \xi_x & \xi_y & \xi_z & \xi_x^{\,2} & \xi_y^{\,2} & \xi_z^{\,2} & \xi_x\xi_y & \xi_x\xi_z & \xi_y\xi_z \\
\xi_x & \xi_x^{\,2} & \xi_x\xi_y & \xi_x\xi_z & \xi_x^{\,3} & \xi_x\xi_y^{\,2} & \xi_x\xi_z^{\,2} & \xi_x^2\xi_y & \xi_x^2\xi_z & \xi_x\xi_y\xi_z \\
\xi_y & \xi_x\xi_y & \xi_y^{\,2} & \xi_y\xi_z & \xi_y\xi_x^{\,2} & \xi_y^{\,3} & \xi_y\xi_z^{\,2} & \xi_x\xi_y^{\,2} & \xi_x\xi_y\xi_z & \xi_y^2\xi_z \\
\xi_z & \xi_x\xi_z & \xi_y\xi_z & \xi_z^{\,2} & \xi_z\xi_x^{\,2} & \xi_z\xi_y^{\,2} & \xi_z^{\,3} & \xi_x\xi_y\xi_z & \xi_x\xi_z^{\,2} & \xi_y\xi_z^{\,2} \\
\xi_x^{\,2} & \xi_x^{\,3} & \xi_x^2\xi_y & \xi_x^2\xi_z & \xi_x^4 & \xi_x^{\,2}\xi_y^{\,2} & \xi_x^{\,2}\xi_z^{\,2} & \xi_x^3\xi_y & \xi_x^3\xi_z & \xi_x^{\,2}\xi_y\xi_z \\
\xi_y^{\,2} & \xi_x\xi_y^{\,2} & \xi_y^{\,3} & \xi_z\xi_y^{\,2} & \xi_x^{\,2}\xi_y^{\,2} & \xi_y^4 & \xi_y^{\,2}\xi_z^{\,2} & \xi_x\xi_y^3 & \xi_x\xi_y^2\xi_z & \xi_y^{\,3}\xi_z \\
\xi_z^{\,2} & \xi_x\xi_z^{\,2} & \xi_y\xi_z^{\,2} & \xi_z^3 & \xi_x^{\,2}\xi_z^{\,2} & \xi_y^{\,2}\xi_z^{\,2} & \xi_z^4 & \xi_x\xi_y\xi_z^2 & \xi_x\xi_z^3 & \xi_y\xi_z^3 \\
\xi_x\xi_y & \xi_x^2\xi_y & \xi_x\xi_y^{\,2} & \xi_x\xi_y\xi_z & \xi_x^3\xi_y & \xi_x\xi_y^3 & \xi_x\xi_y\xi_z^2 & \xi_x^{\,2}\xi_y^{\,2} & \xi_x^{\,2}\xi_y\xi_z & \xi_x\xi_y^2\xi_z \\
\xi_x\xi_z & \xi_x^2\xi_z & \xi_x\xi_y\xi_z & \xi_x\xi_z^{\,2} & \xi_x^3\xi_z & \xi_x\xi_y^2\xi_z & \xi_x\xi_z^3 & \xi_x^{\,2}\xi_y\xi_z & \xi_x^{\,2}\xi_z^{\,2} & \xi_x\xi_y\xi_z^2 \\
\xi_y\xi_z & \xi_x\xi_y\xi_z & \xi_y^2\xi_z & \xi_y\xi_z^{\,2} & \xi_x^{\,2}\xi_y\xi_z & \xi_y^{\,3}\xi_z & \xi_y\xi_z^3 & \xi_x\xi_y^2\xi_z & \xi_x\xi_y\xi_z^2 & \xi_y^{\,2}\xi_z^{\,2}
\end{bmatrix} dV \tag{5.43}$$

$$\mathbf{a} = \begin{bmatrix} a_{000}^{000} & a_{000}^{100} & a_{000}^{010} & a_{000}^{001} & a_{000}^{200} & a_{000}^{020} & a_{000}^{002} & a_{000}^{110} & a_{000}^{101} & a_{000}^{011} \\ a_{100}^{000} & a_{100}^{100} & a_{100}^{010} & a_{100}^{001} & a_{100}^{200} & a_{100}^{020} & a_{100}^{002} & a_{100}^{110} & a_{100}^{101} & a_{100}^{011} \\ a_{010}^{000} & a_{010}^{100} & a_{010}^{010} & a_{010}^{001} & a_{010}^{200} & a_{010}^{020} & a_{010}^{002} & a_{010}^{110} & a_{010}^{101} & a_{010}^{011} \\ a_{001}^{000} & a_{001}^{100} & a_{001}^{010} & a_{001}^{001} & a_{001}^{200} & a_{001}^{020} & a_{001}^{002} & a_{001}^{110} & a_{001}^{101} & a_{001}^{011} \\ a_{200}^{000} & a_{200}^{100} & a_{200}^{010} & a_{200}^{001} & a_{200}^{200} & a_{200}^{020} & a_{200}^{002} & a_{200}^{110} & a_{200}^{101} & a_{200}^{011} \\ a_{020}^{000} & a_{020}^{100} & a_{020}^{010} & a_{020}^{001} & a_{020}^{200} & a_{020}^{020} & a_{020}^{002} & a_{020}^{110} & a_{020}^{101} & a_{020}^{011} \\ a_{002}^{000} & a_{002}^{100} & a_{002}^{010} & a_{002}^{001} & a_{002}^{200} & a_{002}^{020} & a_{002}^{002} & a_{002}^{110} & a_{002}^{101} & a_{002}^{011} \\ a_{110}^{000} & a_{110}^{100} & a_{110}^{010} & a_{110}^{001} & a_{110}^{200} & a_{110}^{020} & a_{110}^{002} & a_{110}^{110} & a_{110}^{101} & a_{110}^{011} \\ a_{101}^{000} & a_{101}^{100} & a_{101}^{010} & a_{101}^{001} & a_{101}^{200} & a_{101}^{020} & a_{101}^{002} & a_{101}^{110} & a_{101}^{101} & a_{101}^{011} \\ a_{011}^{000} & a_{011}^{100} & a_{011}^{010} & a_{011}^{001} & a_{011}^{200} & a_{011}^{020} & a_{011}^{002} & a_{011}^{110} & a_{011}^{101} & a_{011}^{011} \end{bmatrix} \tag{5.44}$$

and

$$\mathbf{b} = \begin{bmatrix} 1 & 0 & 0 & 0 & 0 & 0 & 0 & 0 & 0 & 0 \\ 0 & 1 & 0 & 0 & 0 & 0 & 0 & 0 & 0 & 0 \\ 0 & 0 & 1 & 0 & 0 & 0 & 0 & 0 & 0 & 0 \\ 0 & 0 & 0 & 1 & 0 & 0 & 0 & 0 & 0 & 0 \\ 0 & 0 & 0 & 0 & 2 & 0 & 0 & 0 & 0 & 0 \\ 0 & 0 & 0 & 0 & 0 & 2 & 0 & 0 & 0 & 0 \\ 0 & 0 & 0 & 0 & 0 & 0 & 2 & 0 & 0 & 0 \\ 0 & 0 & 0 & 0 & 0 & 0 & 0 & 1 & 0 & 0 \\ 0 & 0 & 0 & 0 & 0 & 0 & 0 & 0 & 1 & 0 \\ 0 & 0 & 0 & 0 & 0 & 0 & 0 & 0 & 0 & 1 \end{bmatrix} \tag{5.45}$$

Therefore, to satisfy the orthogonality property of PD functions, we just need to solve

$$\mathbf{a} = \mathbf{A}^{-1}\mathbf{b} \tag{5.46}$$

Having found the constant coefficients of the PD functions, $a_{q_x q_y q_z}^{p_x p_y p_z}$, one can compute Peridynamic derivatives explicitly as:

$$\begin{Bmatrix} f(\mathbf{x}) \\ \dfrac{\partial f(\mathbf{x})}{\partial x} \\ \dfrac{\partial f(\mathbf{x})}{\partial y} \\ \dfrac{\partial f(\mathbf{x})}{\partial z} \\ \dfrac{\partial^2 f(\mathbf{x})}{\partial x^2} \\ \dfrac{\partial^2 f(\mathbf{x})}{\partial y^2} \\ \dfrac{\partial^2 f(\mathbf{x})}{\partial z^2} \\ \dfrac{\partial^2 f(\mathbf{x})}{\partial x \partial y} \\ \dfrac{\partial^2 f(\mathbf{x})}{\partial x \partial z} \\ \dfrac{\partial^2 f(\mathbf{x})}{\partial y \partial z} \end{Bmatrix} = \int_{H_x} f(\mathbf{x}+\boldsymbol{\xi}) \begin{Bmatrix} g^{000}(\boldsymbol{\xi}) \\ g^{100}(\boldsymbol{\xi}) \\ g^{010}(\boldsymbol{\xi}) \\ g^{001}(\boldsymbol{\xi}) \\ g^{200}(\boldsymbol{\xi}) \\ g^{020}(\boldsymbol{\xi}) \\ g^{002}(\boldsymbol{\xi}) \\ g^{110}(\boldsymbol{\xi}) \\ g^{101}(\boldsymbol{\xi}) \\ g^{011}(\boldsymbol{\xi}) \end{Bmatrix} dV \tag{5.47}$$

For an incompressible fluid in a 3D domain, differential field equation is expanded as

$$\left(\frac{\partial^2}{\partial^2 x} + \frac{\partial^2}{\partial^2 y} + \frac{\partial^2}{\partial^2 z} \right) \varphi(x, y, z) = 0 \quad x, y, z \in \Omega \tag{5.48}$$

Similar to the 2D formulation, a linear algebraic system for 3D problems can be formed as

$$\mathbf{k}\,\boldsymbol{\varphi} = \bar{\mathbf{u}} \tag{5.49}$$

The entries of $\mathbf{k}$, when node j is a family point of point i, is given by

$$\begin{cases} \forall (x_i, \mathrm{y}_i, \mathrm{z}_i) \in \Omega \rightarrow k_{ij} = g_{ij}^{200}(\boldsymbol{\xi}) + g_{ij}^{020}(\boldsymbol{\xi}) + g_{ij}^{002}(\boldsymbol{\xi}) \\ \forall (x_i, \mathrm{y}_i, \mathrm{z}_i) \in \Gamma_S \rightarrow k_{ij} = g_{ij}^{100}(\boldsymbol{\xi})\,\mathrm{n}_x + g_{ij}^{010}(\boldsymbol{\xi})\,\mathrm{n}_y + g_{ij}^{001}(\boldsymbol{\xi})\,\mathrm{n}_z \\ \forall (x_i, \mathrm{y}_i, \mathrm{z}_i) \in \Gamma_F \rightarrow k_{ij} = g_{ij}^{000}(\boldsymbol{\xi}) \end{cases} \tag{5.50}$$

Correspondingly, boundary/domain conditions, $\bar{\mathbf{u}}$, for all types of nodes are defined as

$$\begin{cases} \forall(x_i, \mathrm{y}_i, \mathrm{z}_i) \in \Omega \rightarrow \bar{u}_i = 0 \\ \forall(x_i, \mathrm{y}_i, \mathrm{z}_i) \in \Gamma_S \rightarrow \bar{u}_i = u_{x(i)}\,\mathrm{n}_x + u_{y(i)}\,\mathrm{n}_y + u_{z(i)}\,\mathrm{n}_z \\ \forall(x_i, \mathrm{y}_i, \mathrm{z}_i) \in \Gamma_F \rightarrow \bar{u}_i = g(\mathrm{z}_i + \frac{H}{2}) + \frac{1}{2}(\nabla\varphi_i.\nabla\varphi_i) \end{cases} \tag{5.51}$$

Solving a linear system of equations the unknown values of the $\boldsymbol{\varphi}$ vector would be obtained by Eq.(5.35).

The velocity field vector, $\mathbf{u}$, in 3D problems should be calculated numerically as

$$\begin{aligned} (u_x)_i &= \frac{\partial\varphi}{\partial x} = \sum_{j=1}^{r} g_{ij}^{100}(\xi)\,\varphi_j V_j \\ (u_y)_i &= \frac{\partial\varphi}{\partial y} = \sum_{j=1}^{r} g_{ij}^{010}(\xi)\,\varphi_j V_j \\ (u_z)_i &= \frac{\partial\varphi}{\partial z} = \sum_{j=1}^{r} g_{ij}^{001}(\xi)\,\varphi_j V_j \end{aligned} \tag{5.52}$$

5.6 Benchmark

To check the convergence rate (CR), we employ the PDDO method to solve a problem governed by Laplace equation in the domain shown in Figure 5.4. Dirichlet boundary conditions, derived from an exact solution, not expanded by polynomial basis, are imposed as:

$$u_{ex} = \sin(x)\cosh(y) \tag{5.53}$$

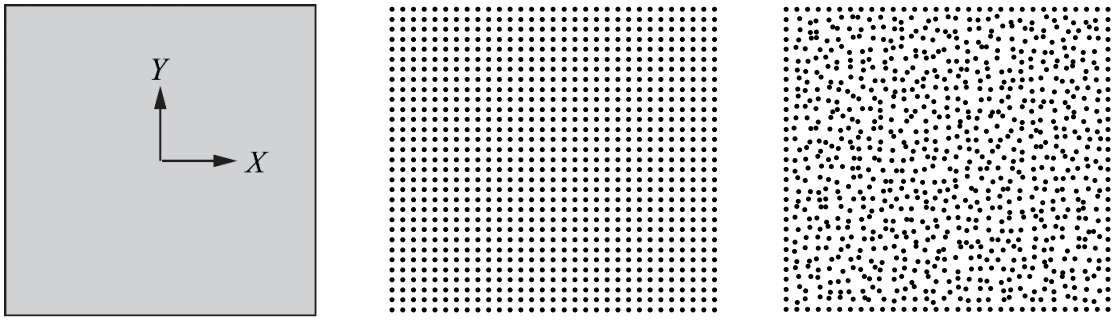

(a) (b) (c)

Figure 5.4. (a) The domain, (b) regular distribution of nodes and, (c) irregular distribution of nodes with 35% irregularity.

To evaluate the accuracy of the method, we compute the error in the L^2 displacement norm and H^1 semi-norm given by:

$$e_{L^2} = \left(\frac{\sum_{i=1}^{N} \left| u_i^{ex} - \bar{u}_i \right|^2}{\sum_{i=1}^{N} \left| u_i^{ex} \right|^2} \right)^{1/2}, \quad e_{H^1} = \left(\frac{\sum_{i=1}^{N} \left| \varepsilon_i^{ex} - \bar{\varepsilon}_i \right|^2}{\sum_{i=1}^{N} \left| \varepsilon_i^{ex} \right|^2} \right)^{1/2} \tag{5.54}$$

The convergence plot with respect to both L^2 norm and H^1 semi-norm are depicted in Figure 5.5 which shows the method monotonically converges to the exact solution by a CR of more than 2.

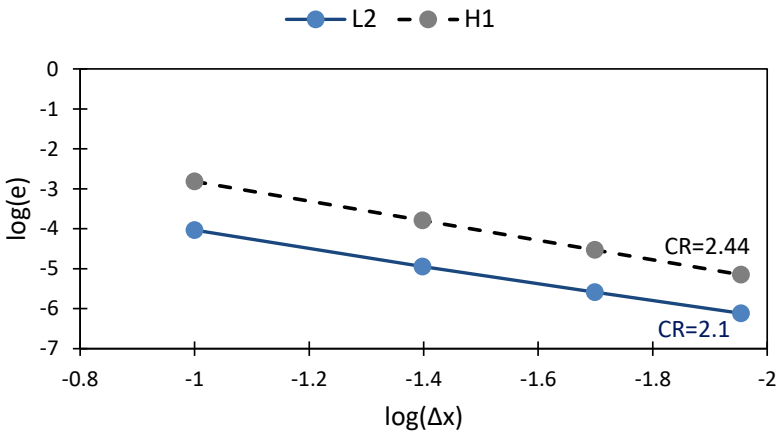

(a)

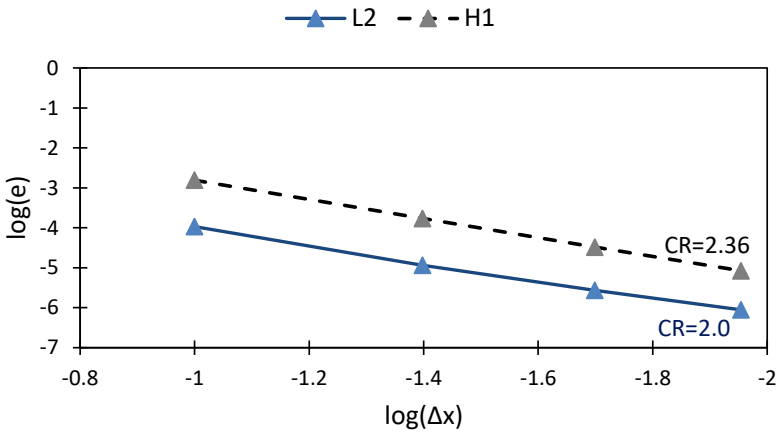

(b)

Figure 5.5. Convergence plot for (a) regular and (b) irregular discretization of domain.

5.7 Examples

5.7.1 Standing wave in a rectangular tank

Water sloshing with an initial free surface profile is a simple benchmark that has been validated by different numerical methods (Idelsohn et al. 2004; Lo and Young 2004; Radovitzky and Oritz 1998; Ramaswamy and Kawahara 1986; Suzuki et al. 2007; Zandi et

al. 2012). In this problem, an initial cosine wave is assigned to the free surface in a rectangular tank as depicted in Figure 5.6.

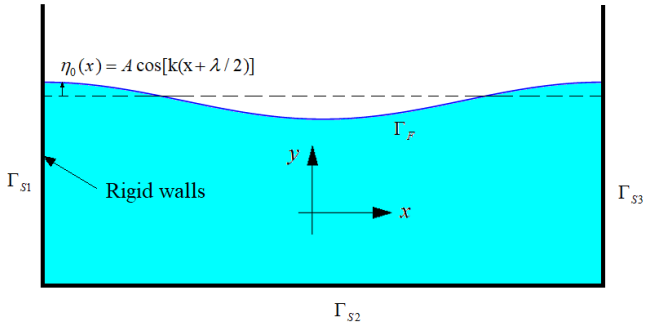

Figure 5.6. The standing wave problem.

The initial boundary condition is given to the free surface of the tank as

$$\eta_0(x) = A\cos[k(x+\lambda/2)] \tag{5.55}$$

in which, A and λ are the wave amplitude and the wavelength respectively, whereas $\eta_0(x)$ is the initial free surface displacement. Additionally, the wave number is represented by $k = 2\pi/\lambda$.

In (Wu and Taylor 1994) an analytical solution is proposed to evaluate the wave elevation at the center of the tank by taking account the nonlinear effects. The wave elevation is $\eta(t) = \eta_1(t) + \eta_2(t)$, where for the first term we have

$$\eta_1(t) = -A\cos(\omega_2 t) \tag{5.56}$$

and the second term is expressed by

$$\eta_2(t) = -\frac{1}{8g}\left\{2(A\omega_2)^2\cos(2\omega_2 t) + \frac{A^2}{\omega_2^2}[k_2^2 g^2 + \omega_2^4 - (k_2^2 g^2 + 3\omega_2^4)\cos(\omega_4 t)]\right\} \tag{5.57}$$

where

$$\omega_n = [k_n g \tan(k_n H)]^{1/2} \tag{5.58}$$

$$k_n = n\pi / \lambda \tag{5.59}$$

In this simulation, the length and the depth of the water in the equilibrium state are $L = 2$ and $H = 0.5$ m respectively. Water density and gravity constant are set to $\rho = 1000$ kg/m^3 and $g = 9.81$ m/s^2. Moreover, wave amplitude and the wavelength are considered as $A = 0.1H$ and $\lambda = 2$ m, respectively. The boundary condition values in terms of the PD unknowns, $\varphi(\mathrm{x}_j, \mathrm{y}_j)$, for this example are expressed as (See Figure 5.1).

$$\begin{aligned}
&\sum_{j=1} \varphi(x_j, y_j) g^{01}(\mathrm{x}_j - x_i, \mathrm{y}_j - y_i)\, \mathrm{V}_j = 0 \quad \text{for} \quad (x_i, y_i) \in \Gamma_{S2} \\
&\sum_{j=1} \varphi(x_j, y_j) g^{10}(\mathrm{x}_j - x_i, \mathrm{y}_j - y_i)\, \mathrm{V}_j = 0 \quad \text{for} \quad (x_i, y_i) \in \Gamma_{S1} \\
&\sum_{j=1} \varphi(x_j, y_j) g^{10}(\mathrm{x}_j - x_i, \mathrm{y}_j - y_i)\, \mathrm{V}_j = 0 \quad \text{for} \quad (x_i, y_i) \in \Gamma_{S3} \\
&\sum_{j=1} \varphi(x_j, y_j) g^{00}(\mathrm{x}_j - x_i, \mathrm{y}_j - y_i)\, \mathrm{V}_j = (\varphi_i)^{(n-2)} + 2\Delta t \left[\left(-g\,(y + \frac{H}{2}) + \frac{1}{2} \nabla\varphi . \nabla\varphi \right)_i \right]^{(n-1)} \quad \text{for} \quad (x_i, y_i) \in \Gamma_{\mathrm{F}}
\end{aligned} \tag{5.60}$$

where

$$\left(\nabla\varphi . \nabla\varphi\right)_i^{(n-1)} = \left(\sum_{j=1}^{r} g_{ij}^{10}(\xi)\, \varphi_j V_j \right)^2 + \left(\sum_{j=1}^{r} g_{ij}^{01}(\xi)\, \varphi_j V_j \right)^2 \tag{5.61}$$

And y_i in Eq. (5.60) at $t = 0$ (s) is given by

$$y_0 = A\cos[\mathrm{k}(\mathrm{x}_i + \lambda / 2)] + \frac{H}{2} \tag{5.62}$$

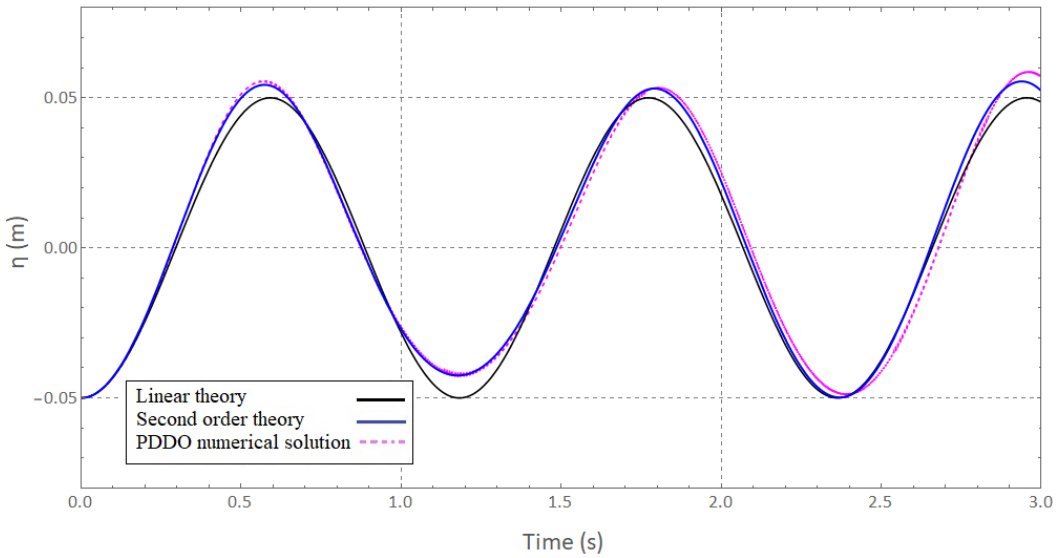

Figure 5.7. Comparison of the calculated wave heights at the center of the tank.

The wave height at the center of thank is shown in Figure 5.7. In this example, Δt is taken 0.01 s, and the domain is discretized with a uniform 41×11 grid of nodes with a grid spacing $\Delta x = 0.05$ m. The result obtained by PDDO is in a good agreement with the second order theory, $\eta(t) = \eta_1 + \eta_2$; however, there is a disparity between linear theory, $\eta(t) = \eta_1$ and the PDDO solution. Thus, PDDO has a good accuracy to model nonlinear effects of the motion.

Based on Bernoulli's equation, the total pressure consists of hydrodynamic and hydrostatic pressure as

$$p = \underbrace{-\rho\frac{\partial\varphi}{\partial t} - \frac{1}{2}\rho(\nabla\varphi.\nabla\varphi)}_{\text{hydrodynamic pressure}} \underbrace{-\rho g(y+\frac{H}{2})}_{\text{hydrostatic pressure}} \tag{5.63}$$

Hence, using the second order finite difference method which is clarified in Section 5.4.1, one may evaluate the hydrodynamic pressure in each time step as

$$p^n_{Hydrodynamic} = -\rho\frac{\varphi^{n+1}-\varphi^{n-1}}{2\Delta t} - \frac{1}{2}\rho\left(\nabla\varphi^n.\nabla\varphi^n\right) \tag{5.64}$$

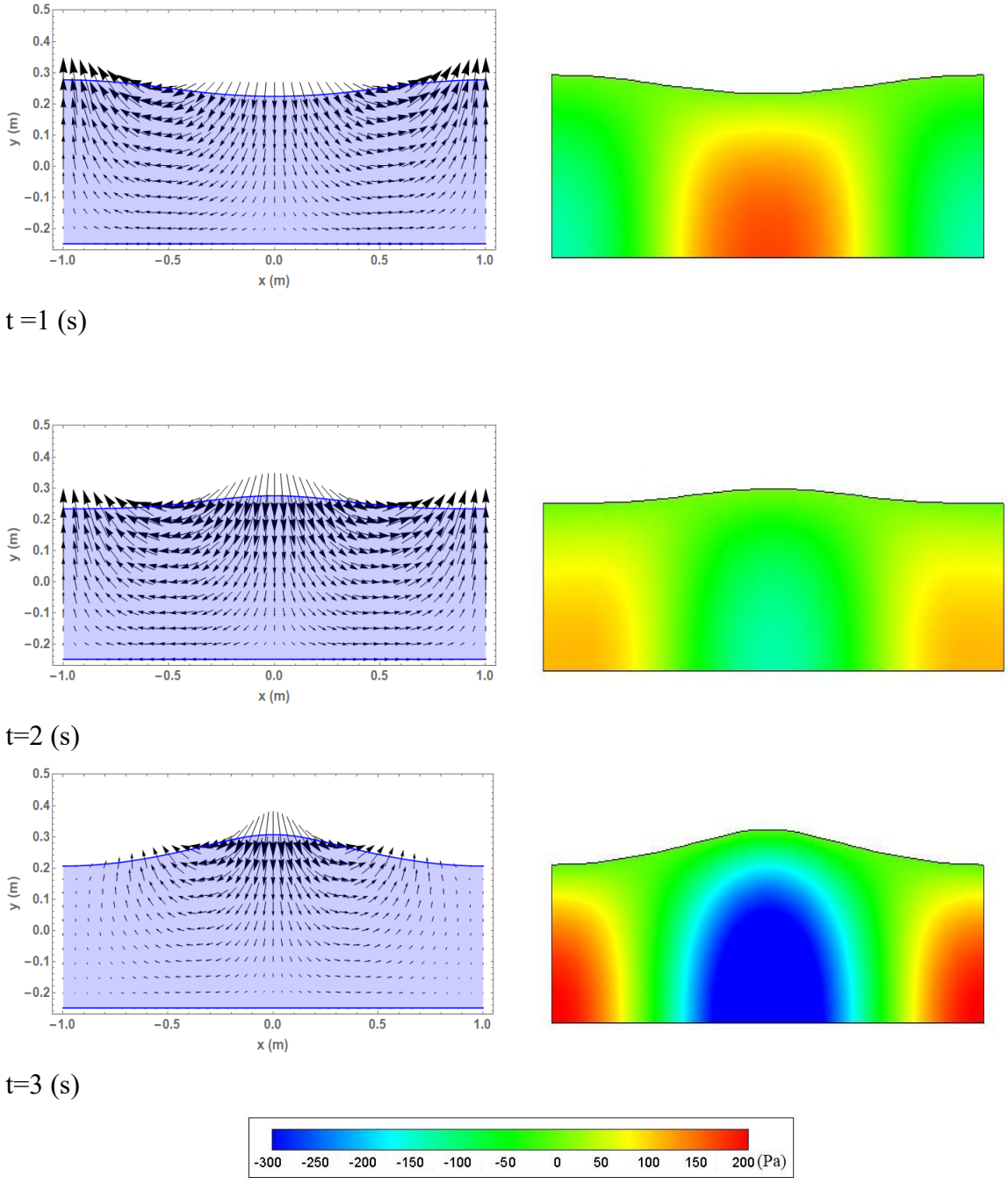

Figure 5.8. Velocity vector-plots and hydrodynamic pressure at different time steps.

Snapshots of hydrodynamic pressure for three different time steps are depicted in Figure 5.8. In the same figure, the velocity vector plots at different time steps, derived from Eq. (5.37), are reported. The results show that the boundary conditions are imposed accurately in time.

5.7.2 Non-linear liquid sloshing under harmonic excitation

5.7.2.1 Sloshing under resonant excitation

In this section, liquid sloshing is investigated to have a better insight of PDDO accuracy with respect to the Meshless Local Petrov-Galerkin (MPLG) approach (see (Pal 2012b)).

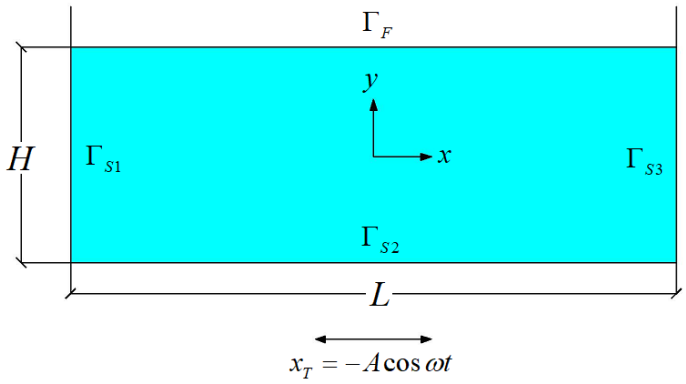

Figure 5.9. Sloshing under harmonic excitation domain.

The geometrical dimensions of the tank are set as those chosen by Pal (Pal 2012b) so that: $H = 1.0$ m and $L = 2.0$ m. The lowest natural angular frequency of the tank is $\omega_0 = 3.76$ rad/s (Pal 2012b). A periodic cosine excitation with a shaking frequency of $\omega = 1.0\,\omega_0$ is considered on the x direction as

$$x_T = -A\cos\omega t \tag{5.65}$$

where $A = 0.0000971$ m is the displacement amplitude. This example is solved with the time step of $\Delta t = 0.01$ s; however this value in MLPG solution is taken as $\Delta t = 0.003$ s which is 3.3 times smaller than the PDDO model.

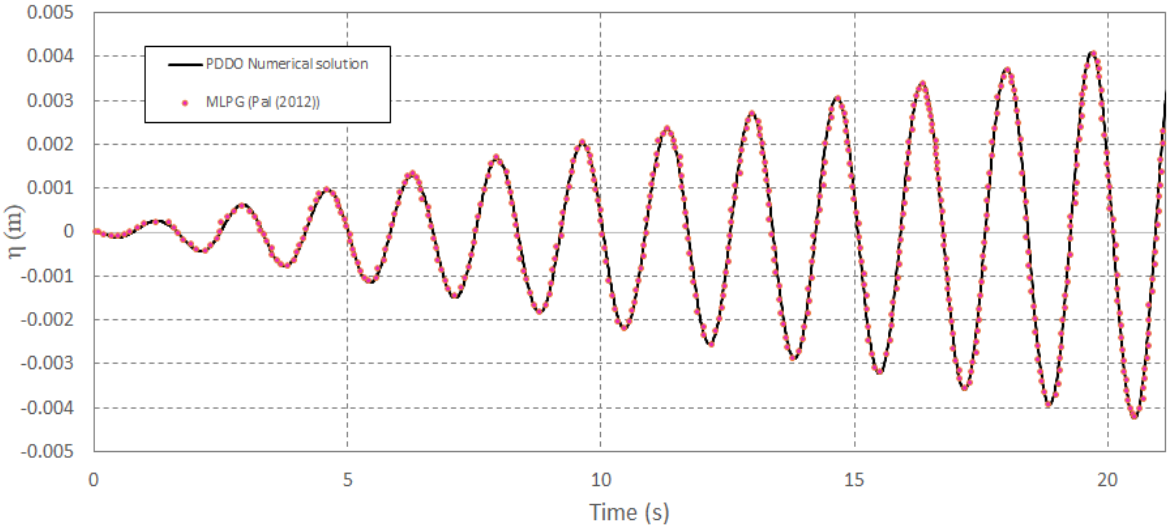

Figure 5.10. Comparison of the calculated wave heights at the left wall of the tank.

The discrete form of boundary conditions can be expressed by (See Figure 5.9)

$$\sum_{j=1}\varphi(x_j,y_j)g^{01}(\mathrm{x}_j-x_i,\mathrm{y}_j-y_i)\,\mathrm{V}_j=0 \quad \text{for} \quad \text{for} \quad (x_i,y_i)\in\Gamma_{S2}$$

$$\sum_{j=1}\varphi(x_j,y_j)g^{10}(\mathrm{x}_j-x_i,\mathrm{y}_j-y_i)\,\mathrm{V}_j=A\omega\sin\omega t \quad \text{for} \quad (x_i,y_i)\in\Gamma_{S1}$$

$$\sum_{j=1}\varphi(x_j,y_j)g^{10}(\mathrm{x}_j-x_i,\mathrm{y}_j-y_i)\,\mathrm{V}_j=-A\omega\sin\omega t \quad \text{for} \quad (x_i,y_i)\in\Gamma_{S3}$$

$$\sum_{j=1}\varphi(x_j,y_j)g^{00}(\mathrm{x}_j-x_i,\mathrm{y}_j-y_i)\,\mathrm{V}_j=(\varphi_i)^{(n-2)}+2\Delta t\left[\left(-g\,(y+\frac{H}{2})+\frac{1}{2}\nabla\varphi.\nabla\varphi\right)_i\right]^{(n-1)} \quad \text{for} \quad (x_i,y_i)\in\Gamma_{\mathrm{F}}$$

(5.66)

where

$$\left(\nabla\varphi.\nabla\varphi\right)_i^{(n-1)}=\left(\sum_{j=1}^{r}g_{ij}^{10}(\xi)\,\varphi_j V_j\right)^2+\left(\sum_{j=1}^{r}g_{ij}^{01}(\xi)\,\varphi_j V_j\right)^2 \tag{5.67}$$

For this example we discretize the solution domain with a uniform grid of 17×9 nodes which results in 153 nodes. As reported in (Pal 2012a), for the MLPG solution a uniform grid of 41×21 nodes, which results in 861 nodes, is employed. The free-surface elevation at the left

wall of the tank is shown in Figure 5.10. The PDDO solution is in good agreement with the solution of MLPG.

5.7.2.2 Sloshing with high nonlinearity under resonant excitation

In this example, liquid sloshing problem with strong nonlinearity is simulated and compared with experimental measurements, numerical results obtained with the volume of fluid method (VOF) (Liu and Lin 2008), and the linear analytical solution. The geometrical dimensions of the tank are set as those chosen by Liu and Lin (Liu and Lin 2008) as $H = 0.15$ m and $L = 0.57$ m. The lowest natural angular frequency of the tank is $\omega_0 = 6.0578$ rad/s (Liu and Lin 2008). A periodic sinusoidal excitation with a shaking frequency of $\omega = 1.0\,\omega_0$ is considered on the x direction as

$$x_T = -A \sin \omega t \tag{5.68}$$

where $A = 0.005$ m is the displacement amplitude. Three gauges are set in the center, near the left boundary and right boundary of the tank (Figure 5.11). to measure the free surface displacement. Resonance effect occurs since the frequency of oscillation is equal to the natural frequency of the tank. The discrete form of boundary conditions can be expressed by (see Figure 5.11)

$$\sum_{j=1}\varphi(x_j,y_j)g^{01}(\mathrm{x}_j-x_i,\mathrm{y}_j-y_i)\mathrm{V}_j=0 \qquad \text{for} \quad (x_i,y_i)\in\Gamma_{S2}$$

$$\sum_{j=1}\varphi(x_j,y_j)g^{10}(\mathrm{x}_j-x_i,\mathrm{y}_j-y_i)\mathrm{V}_j=A\omega\sin\omega t \qquad \text{for} \quad (x_i,y_i)\in\Gamma_{S1}$$

$$\sum_{j=1}\varphi(x_j,y_j)g^{10}(\mathrm{x}_j-x_i,\mathrm{y}_j-y_i)\mathrm{V}_j=-A\omega\sin\omega t \quad \text{for} \quad (x_i,y_i)\in\Gamma_{S3}$$

$$\sum_{j=1}\varphi(x_j,y_j)g^{00}(\mathrm{x}_j-x_i,\mathrm{y}_j-y_i)\mathrm{V}_j=(\varphi_i)^{(n-2)}+2\Delta t\left[\left(-g\,(y+\frac{H}{2})+\frac{1}{2}\nabla\varphi.\nabla\varphi\right)_i\right]^{(n-1)} \qquad \text{for} \quad (x_i,y_i)\in\Gamma_{\mathrm{F}}$$

(5.69)

where

$$\left(\nabla\varphi.\nabla\varphi\right)_i^{(n-1)}=\left(\sum_{j=1}^{r}g_{ij}^{10}(\xi)\,\varphi_jV_j\right)^2+\left(\sum_{j=1}^{r}g_{ij}^{01}(\xi)\,\varphi_jV_j\right)^2 \tag{5.70}$$

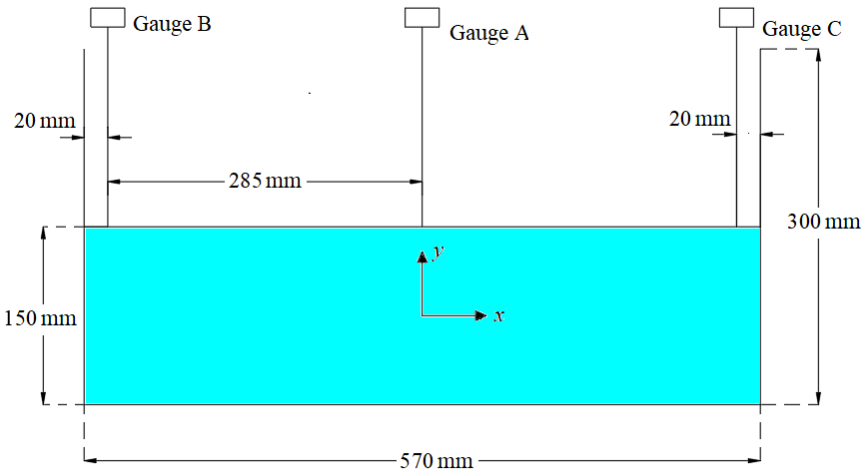

Figure 5.11. Side view of experimental setup and main dimensions (Liu and Lin 2008).

The wave elevation histories of different probes are shown in Figure 5.12. This example is solved up to 6.7 s and the time step is chosen as $\Delta t = 0.01\,\mathrm{s}$.

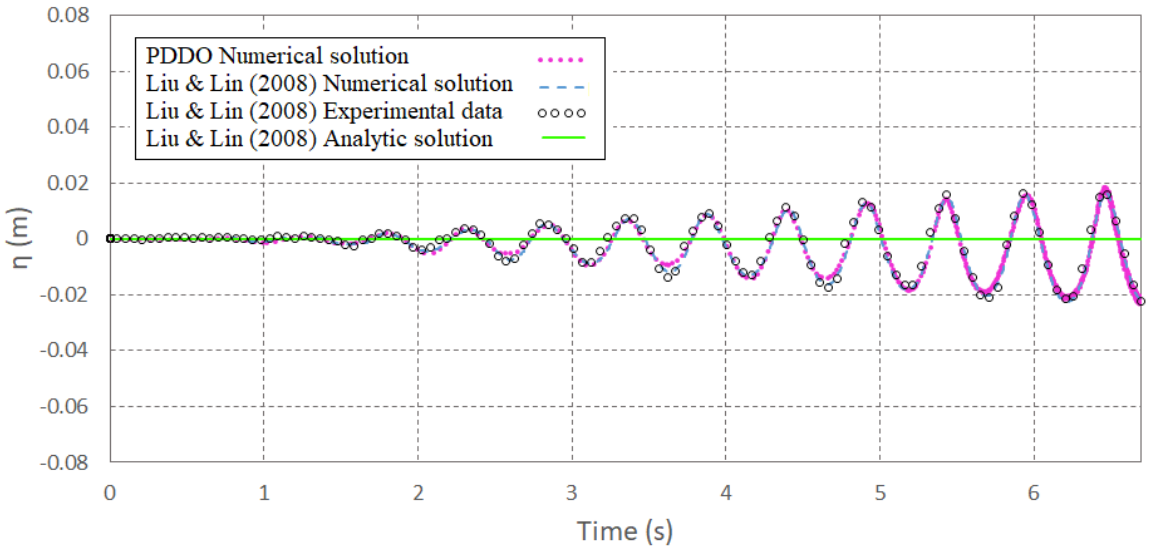
PDDO Numerical solution
Liu & Lin (2008) Numerical solution
Liu & Lin (2008) Experimental data
Liu & Lin (2008) Analytic solution
η (m)
Time (s)
0.08
0.06
0.04
0.02
0
-0.02
-0.04
-0.06
-0.08
0
1
2
3
4
5
6

(a)

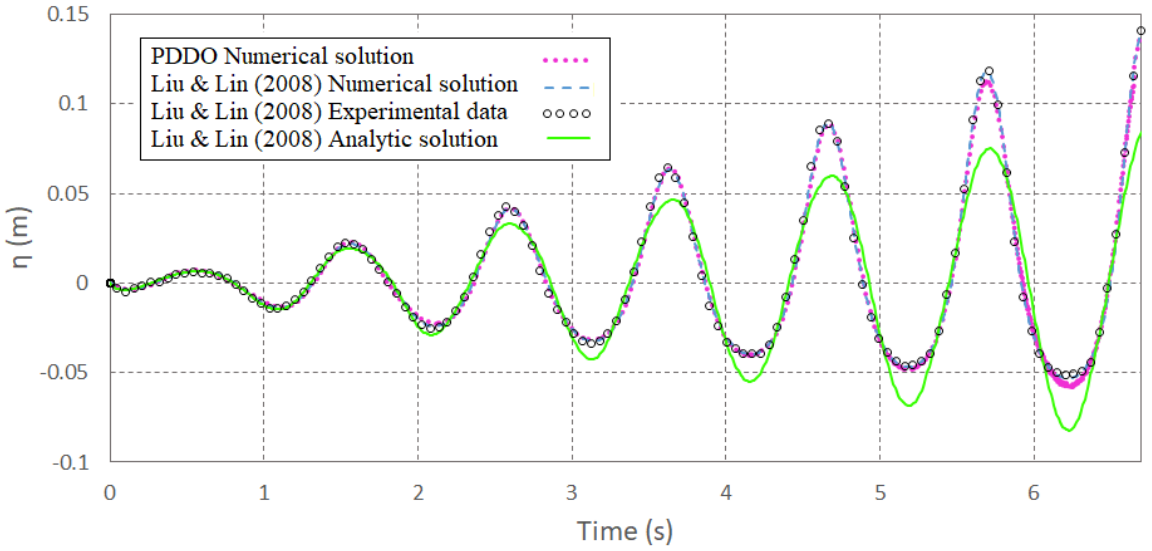
PDDO Numerical solution
Liu & Lin (2008) Numerical solution
Liu & Lin (2008) Experimental data
Liu & Lin (2008) Analytic solution
η (m)
Time (s)
0.15
0.1
0.05
0
-0.05
-0.1
0
1
2
3
4
5
6

(b)

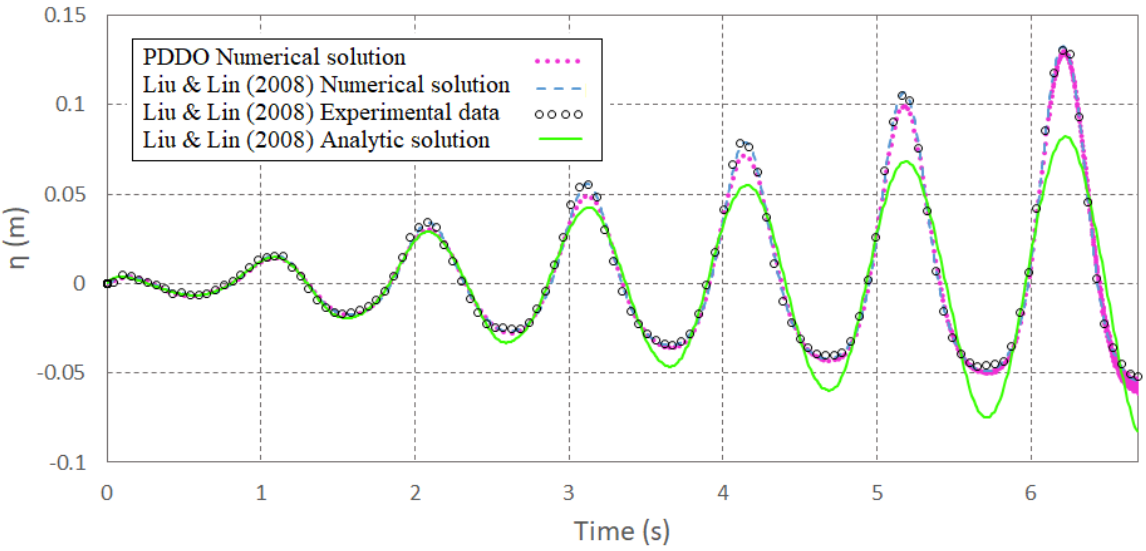

(c)

Figure 5.12. Comparisons of the time series of surface elevation η at the position of (a) probe A; (b) probe B; and (c) probe C.

The solution domain is discretized with a 12×5 uniform grid of nodes which results in 60 nodes. However, as reported in (Liu and Lin 2008), for VOF solution a 114×64 grid of nodes, that contributes to 7296 nodes, is employed. The results of PDDO are in a remarkable agreement with the experimental data of Liu & Lin (Liu and Lin 2008) and the VOF solution (Liu and Lin 2008), whereas the linear analytical solution does not conform with them. Hence, we can conclude that PDDO is a precise tool for predicting nonlinear effects of motion. The maximum elevation of the free surface at t=6.18 s is almost two times greater than the initial water depth. Therefore, this example is a good indication of strong nonlinearity of the free surface fluid sloshing. The walls of the tank are set to be infinitely high; however, in the experiment test the wall heights are 30 cm as depicted in Figure 5.11.

The snap shots of the free surface profile with their velocity vector plots in different time intervals, $t = 6.22 : 6.74$ s in Figure 5.13.

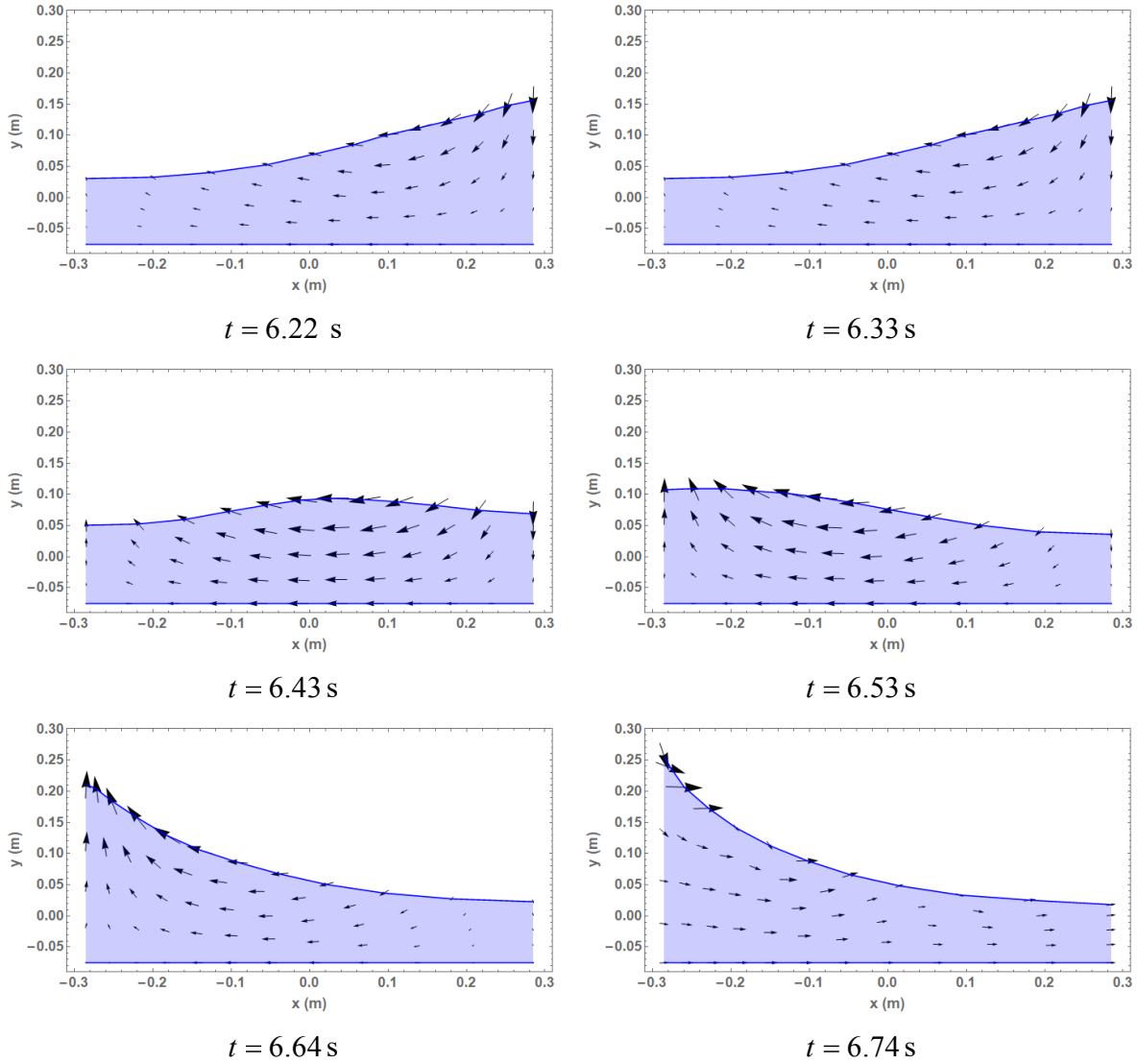

Figure 5.13. Snapshots of free surface profiles with velocity vector-plots in the two-dimensional sloshing case in the time interval of t =6.22:6.74 s.

One of the ways to evaluate the stability and efficiency of the proposed numerical solution is to investigate the histograph of the condition number (CN) of the global stiffness matrix as reported in Figure 5.14. The (CN) of the global stiffness matrix can be evaluated as (Wu et al. 2016)

$$CN = \left\|\mathbf{k}\right\|_2 \left\|\mathbf{k}^{-1}\right\|_2 \tag{5.71}$$

in which $\|\bullet\|$ stands for 2-norm of a matrix. Figure 5.14 shows that as the analysis proceeds in time CN grows significantly. This is due to the irregularity of discretization when a new configuration for the solution domain is obtained. The maximum value of (CN) is 2500 which is low enough to guarantee the stability of the linear system of equations. As can be seen, PDDO generates a well-conditioned sparse system of equations in time. In the same figure, the CN obtained by Wu et al (Wu et al. 2016) using a local polynomial collocation method with the same discretization is reported.

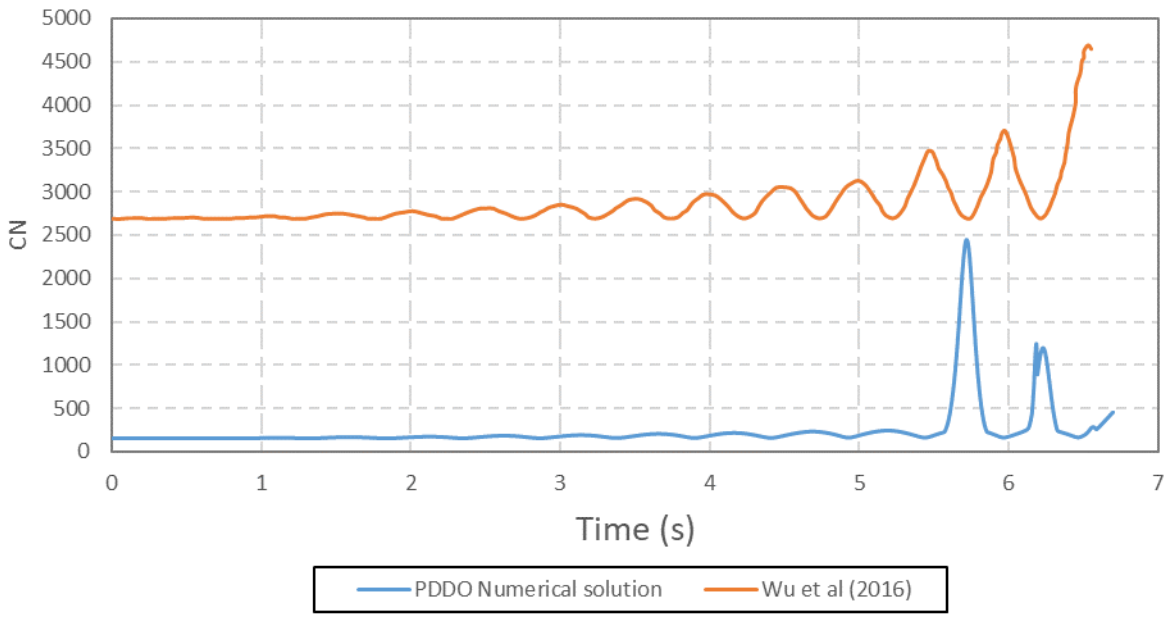

Figure 5.14. The histograph of the global stiffness matrix for non-linear liquid sloshing under surge excitation.

5.7.3 Liquid sloshing in a tank with baffles

5.7.3.1 2D liquid sloshing in a tank with a horizontal baffle

In order to prevent the violent free surface fluctuation, one may install horizontal and vertical baffles inside the liquid tanks. On the other hand, installing a rigid baffle can generate a sharp gradient of velocity potential near the tip of baffle which might be a source of instability for

the solution which use direct differentiation procedures. Using PDDO culminates in determining the derivatives of the velocity potential accurately at each time step and avoiding the instability of the solution. For the sake of verification, we consider a problem which can be found in the study by Liu & Lin (Liu and Lin 2009); shown in (Figure 5.15). The tank length and the water depth in the equilibrium state are $L = 1.0$ m and $H = 0.5$ m, respectively. A rigid baffle with the length of $0.4L$ is placed at a depth of 0.4 m from the initial free surface and on the left boundary of the tank.

A periodic sinusoidal excitation, $x_T = -A\sin\omega t$, with a shaking angular frequency of $\omega = 5.29\,\text{rad/s}$ is considered, where $A = 0.002$ m. In this example, a 51×26 uniform grid of nodes is employed. The problem is solved up to 10.0 s and the time step is taken $\Delta t = 0.01$ s.

The discrete form of boundary conditions are

$$\sum_{j=1}\varphi(x_j,y_j)g^{01}(\mathrm{x}_j-x_i,\mathrm{y}_j-y_i)\,\mathrm{V}_j = 0 \quad \text{for} \quad (x_i,y_i)\in\Gamma_{S2}$$

$$\sum_{j=1}\varphi(x_j,y_j)g^{10}(\mathrm{x}_j-x_i,\mathrm{y}_j-y_i)\,\mathrm{V}_j = A\omega\sin\omega t \quad \text{for} \quad (x_i,y_i)\in\Gamma_{S1}$$

$$\sum_{j=1}\varphi(x_j,y_j)g^{10}(\mathrm{x}_j-x_i,\mathrm{y}_j-y_i)\,\mathrm{V}_j = -A\omega\sin\omega t \quad \text{for} \quad (x_i,y_i)\in\Gamma_{S3}$$

$$\sum_{j=1}\varphi(x_j,y_j)g^{01}(\mathrm{x}_j-x_i,\mathrm{y}_j-y_i)\,\mathrm{V}_j = 0 \quad \text{for} \quad (x_i,y_i)\in\Gamma_{S4}$$

$$\sum_{j=1}\varphi(x_j,y_j)g^{01}(\mathrm{x}_j-x_i,\mathrm{y}_j-y_i)\,\mathrm{V}_j = 0 \quad \text{for} \quad (x_i,y_i)\in\Gamma_{S5}$$

$$\sum_{j=1}\varphi(x_j,y_j)g^{00}(\mathrm{x}_j-x_i,\mathrm{y}_j-y_i)\,\mathrm{V}_j = (\varphi_i)^{(n-2)} + 2\Delta t\left[\left(-g\,(y+\frac{H}{2})+\frac{1}{2}\nabla\varphi.\nabla\varphi\right)_i\right]^{(n-1)} \quad \text{for} \quad (x_i,y_i)\in\Gamma_{\mathrm{F}} \tag{5.72}$$

As for instance, $\mathbf{x}_A$ and $\mathbf{x}_B$ in Figure 5.15 (b), represent nodes positioned on the two surfaces of the baffle. In Eq. (5.72) each node interacts only with its family nodes located on the same side of the baffle as depicted in Figure 5.15 (b) (visibility criterion).

In Figure 5.16, we compare the results of PDDO for displacement with those obtained by Liu & Lin (Liu and Lin 2009) at the free surface.

Good agreement is observed between two numerical solutions; however, using horizontal baffle does not influence the resonance phenomenon significantly. Hence, the elevation of the free surface wave grows over time with the current frequency.

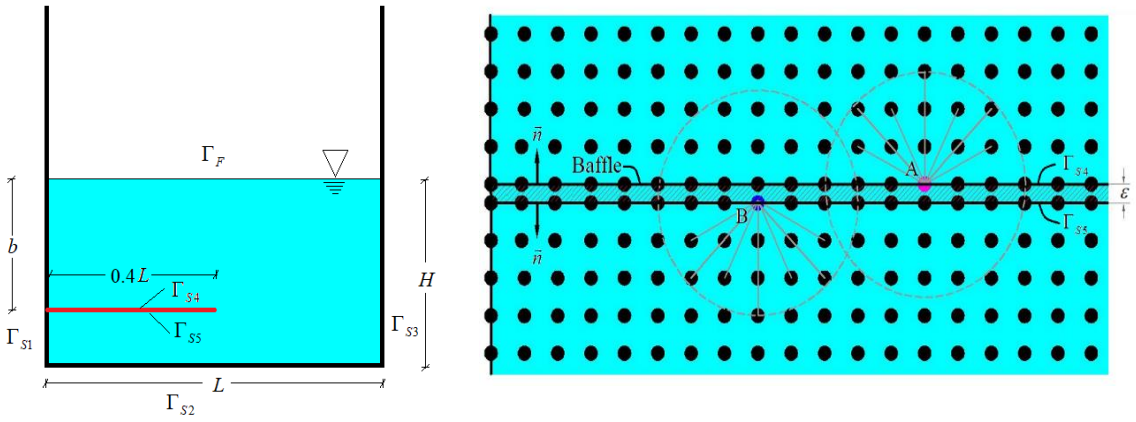

(a) (b)

Figure 5.15. (a) 2D rectangular tank with a horizontal baffle (b) zoom in the baffle area.

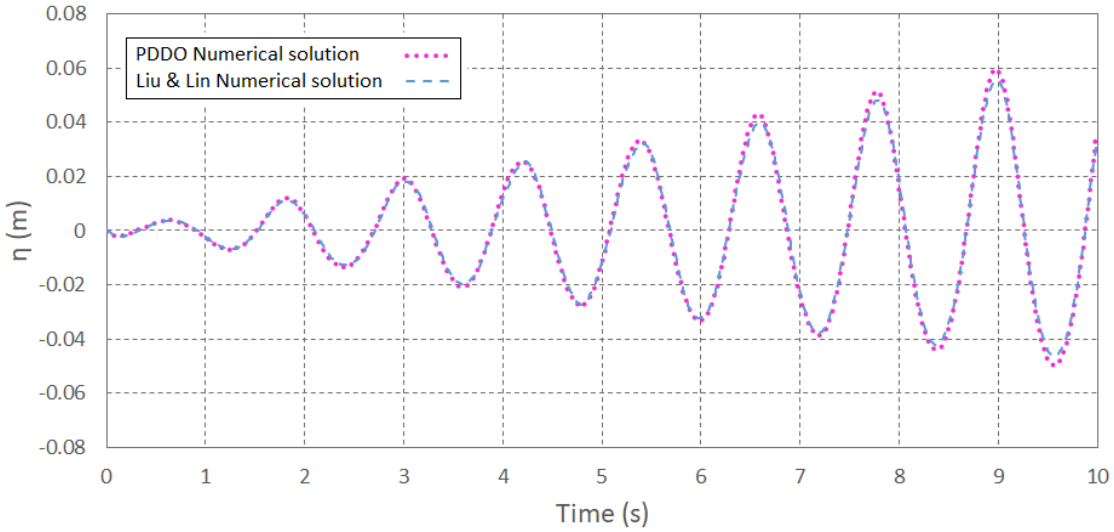

Figure 5.16. Comparisons of the time series of surface elevation η at the right boundary of the baffled tank.

5.7.3.2 2D liquid sloshing in a tank with a vertical baffle

The same tank with a vertical baffle is simulated in this section. A vertical baffle is set at the center of the tank (as depicted in Figure 5.17) and the excitation is the same as the previous problem. The height of the baffle is $0.75H$. The grid and the time step are equal to those used in the previous example. This example is solved both with and without the baffle and the results of the free surface displacement on the right boundary are in an acceptable agreement with Liu & Lin (Liu and Lin 2009) numerical solution. The discrete form of boundary conditions are

$$\sum_{j=1}\varphi(x_j,y_j)g^{01}(\mathrm{x}_j-x_i,\mathrm{y}_j-y_i)\mathrm{V}_j=0 \quad \text{for} \quad (x_i,y_i)\in\Gamma_{S2}$$

$$\sum_{j=1}\varphi(x_j,y_j)g^{10}(\mathrm{x}_j-x_i,\mathrm{y}_j-y_i)\mathrm{V}_j=A\omega\sin\omega t \quad \text{for} \quad (x_i,y_i)\in\Gamma_{S1}$$

$$\sum_{j=1}\varphi(x_j,y_j)g^{10}(\mathrm{x}_j-x_i,\mathrm{y}_j-y_i)\mathrm{V}_j=-A\omega\sin\omega t \quad \text{for} \quad (x_i,y_i)\in\Gamma_{S3}$$

$$\sum_{j=1}\varphi(x_j,y_j)g^{01}(\mathrm{x}_j-x_i,\mathrm{y}_j-y_i)\mathrm{V}_j=-A\omega\sin\omega t \quad \text{for} \quad (x_i,y_i)\in\Gamma_{S4}$$

$$\sum_{j=1}\varphi(x_j,y_j)g^{01}(\mathrm{x}_j-x_i,\mathrm{y}_j-y_i)\mathrm{V}_j=A\omega\sin\omega t \quad \text{for} \quad (x_i,y_i)\in\Gamma_{S5}$$

$$\sum_{j=1}\varphi(x_j,y_j)g^{00}(\mathrm{x}_j-x_i,\mathrm{y}_j-y_i)\mathrm{V}_j=(\varphi_i)^{(n-2)}+2\Delta t\left[\left(-g\,(y+\frac{H}{2})+\frac{1}{2}\nabla\varphi.\nabla\varphi\right)_i\right]^{(n-1)} \tag{5.73}$$

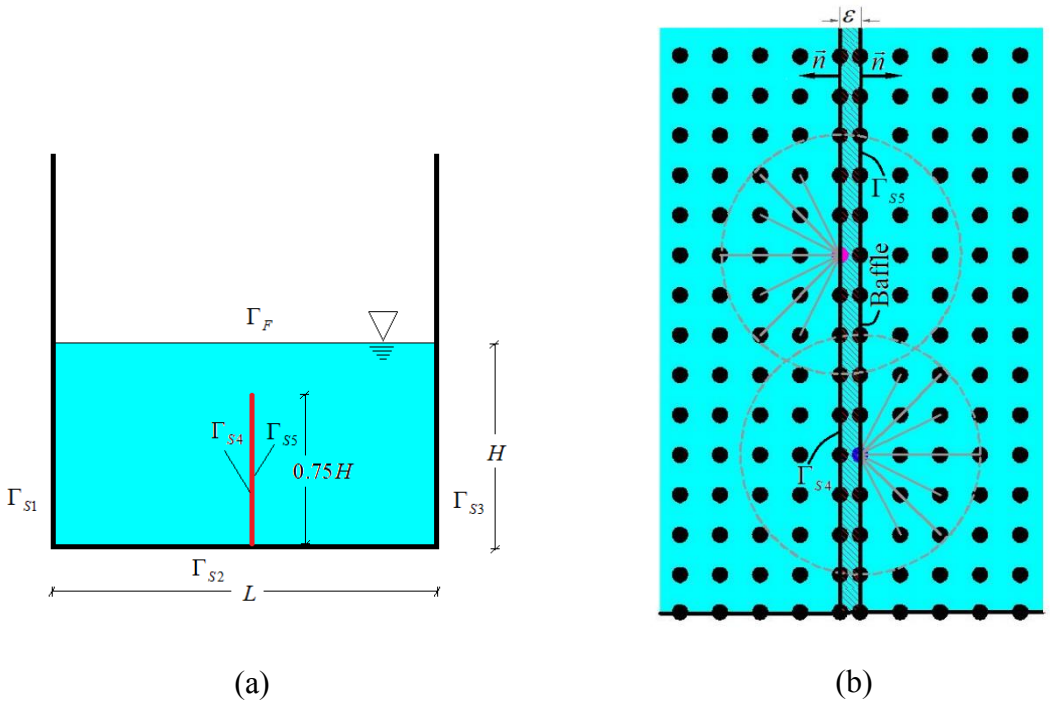

(a) (b)

Figure 5.17. (a) 2D rectangular tank with a vertical baffle (b) zoom in the baffle area.

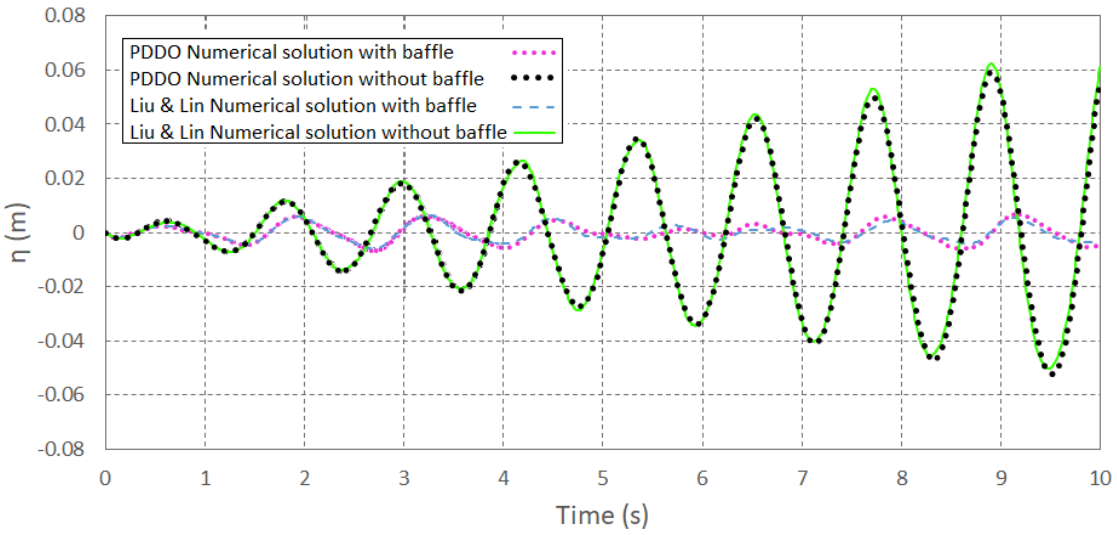

Figure 5.18. Comparisons of the time series of surface elevation η at the right boundary of the tank.

As shown in Figure 5.18, by using a vertical baffle, the amplitude of the wave is significantly diminished. Velocity vector-plots of both simulations are depicted in Figure 5.19. It can be observed that vertical baffle obstructs the sloshing water so that the resonance phenomenon cannot occur with the current frequency.

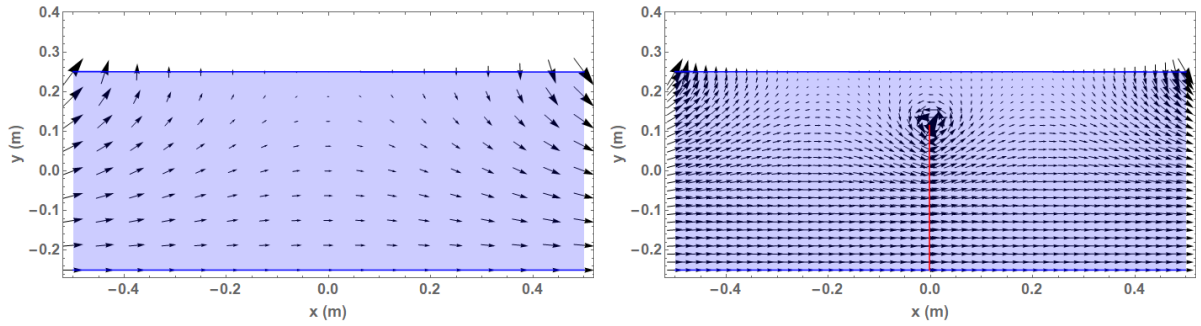

(a) (d)

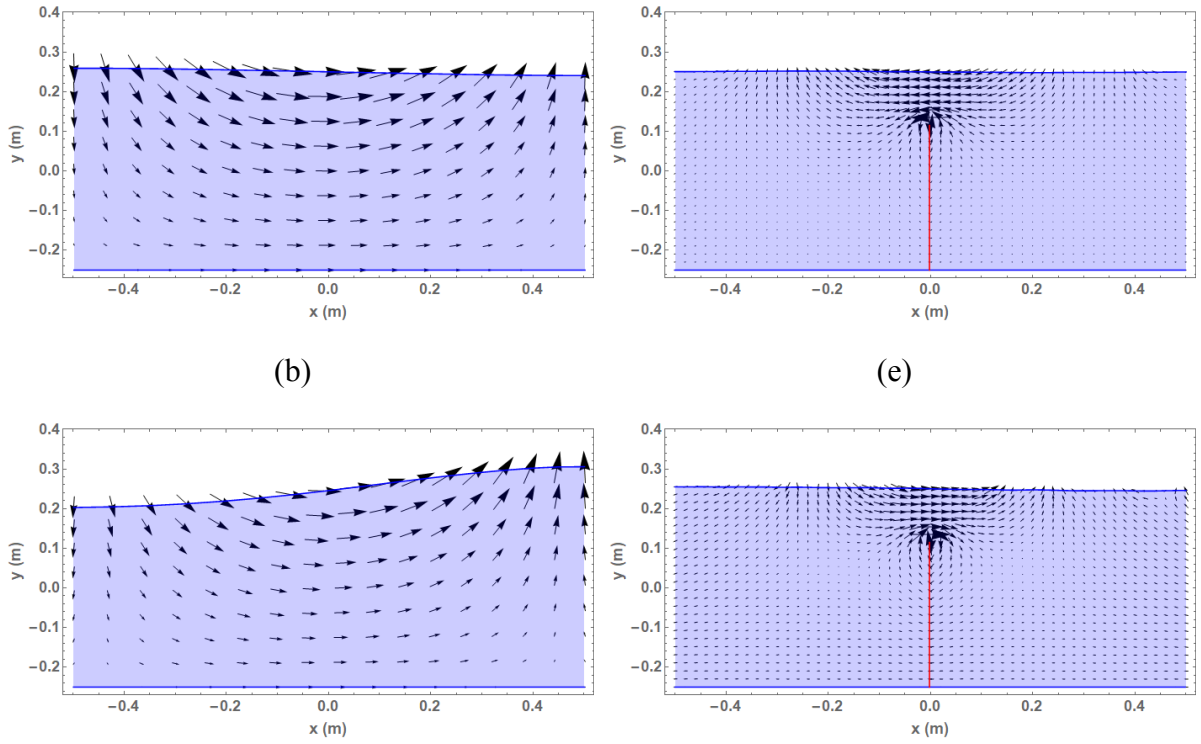

Figure 5.19. Comparison of free surface profiles without baffles (a-c) and with a vertical baffle (d-f) at t= 0, 5 and 10 (s).

5.7.4 Solitary wave propagation

In this section, a solitary wave propagation in a rectangular tank is simulated. In such problems, an initial configuration and velocity is imposed to the surface (see Figure 5.20). The wave goes back to its former position after colliding with the right wall.

The solution of this problem by various numerical methods (Durate et al. 2004; González et al. 2007; Lo and Young 2004; Nithiarasu 2005; Ramaswamy and Kawahara 1987a; Zandi et al. 2012), experiments (Maxworthy 1976), and analytical solutions (Byatt-Smith 1971) can be found in the literature.

In this example, the length and the depth of the water in the equilibrium state are $L = 160$ m and $H = 10$ m, respectively. Water density and gravity acceleration are set to $\rho = 1000$ kg/m^3 and $g = 9.81$ m/s^2. The discrete form of boundary conditions can be expressed by

$$\sum_{j=1} \varphi(x_j, y_j) g^{01}(\mathrm{x}_j - x_i, \mathrm{y}_j - y_i)\, \mathrm{V}_j = 0 \quad \text{for} \quad (x_i, y_i) \in \Gamma_{S2}$$
$$\sum_{j=1} \varphi(x_j, y_j) g^{10}(\mathrm{x}_j - x_i, \mathrm{y}_j - y_i)\, \mathrm{V}_j = 0 \quad \text{for} \quad (x_i, y_i) \in \Gamma_{S1}$$
$$\sum_{j=1} \varphi(x_j, y_j) g^{10}(\mathrm{x}_j - x_i, \mathrm{y}_j - y_i)\, \mathrm{V}_j = 0 \quad \text{for} \quad (x_i, y_i) \in \Gamma_{S3}$$
$$\sum_{j=1} \varphi(x_j, y_j) g^{00}(\mathrm{x}_j - x_i, \mathrm{y}_j - y_i)\, \mathrm{V}_j = (\varphi_i)^{(n-2)} + 2\Delta t \left[\left(-g\,(y + \frac{H}{2}) + \frac{1}{2} \nabla\varphi . \nabla\varphi \right)_i \right]^{(n-1)} \quad \text{for} \quad (x_i, y_i) \in \Gamma_{\mathrm{F}} \tag{5.74}$$

where

$$\left(\nabla\varphi . \nabla\varphi\right)_i^{(n-1)} = \left(\sum_{j=1}^{r} g_{ij}^{10}(\xi)\, \varphi_j V_j + u_0 \right)^2 + \left(\sum_{j=1}^{r} g_{ij}^{01}(\xi)\, \varphi_j V_j + v_0 \right)^2 \tag{5.75}$$

The initial boundary condition is given to the free surface of the tank as

$$\eta_0(x) = A \operatorname{sech}^2 \left(\sqrt{\frac{3A}{4H^3}}\, x \right) \tag{5.76}$$

in which, A is the wave amplitude. The initial velocity components, based on Laitone's work (Laitone 1960), are given by

$$u_0 = \sqrt{gH}\, \frac{\eta_0}{H} \operatorname{sech}^2 \left(\sqrt{\frac{3\eta_0}{4H^3}}\, x \right) \tag{5.77}$$

$$v_0 = \sqrt{3gH} \left(\frac{\eta_0}{H} \right)^{(3/2)} \left(\frac{y}{H} \right) \operatorname{sech}^2 \left(\sqrt{\frac{3\eta_0}{4H^3}}\, x \right) \tanh \left(\sqrt{\frac{3\eta_0}{4H^3}}\, x \right) \tag{5.78}$$

Aforementioned initial velocity components should be added to the velocities obtained In Eq. (5.37).

This problem is solved for different values of η_0 / H using a 81×6 uniform grid of nodes.

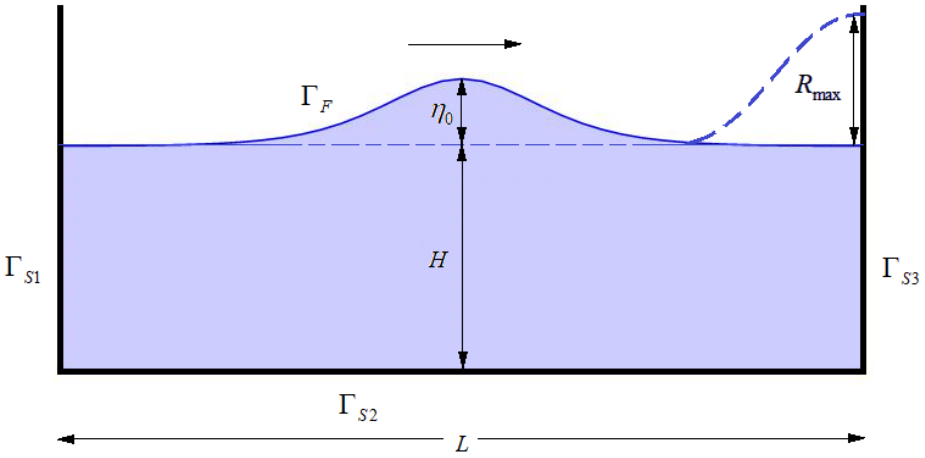

Figure 5.20. Solitary wave propagation in a 2D rectangular tank.

In Figure 5.21 the maximum run-up at the right wall is represented using different approaches. To evaluate the maximum run-up, Byatt-Smith (Byatt-Smith 1971) proposed an analytical first order equation as

$$\frac{R_{\max}}{H} = 2\left(\frac{\eta_0}{H}\right) + \frac{1}{2}\left(\frac{\eta_0}{H}\right)^2 + O\left(\frac{\eta_0}{H}\right)^3 \tag{5.79}$$

Comparing this analytical solution with other numerical approaches and experimental data, one may observe that it shows a slight deviation (less than 3%) of $\frac{R_{\max}}{H}$ vs $\frac{\eta_0}{H}$ the results obtained by PDDO are in agreement with the experimental data of Maxworthy (Maxworthy 1976). Moreover, other numerical approaches proposed by Zandi et al (Zandi et al. 2012) and Lo & Young (Lo and Young 2004) are in a good agreement with PDDO numerical solution which shows the capability of this method to predict the precise maximum run-up.

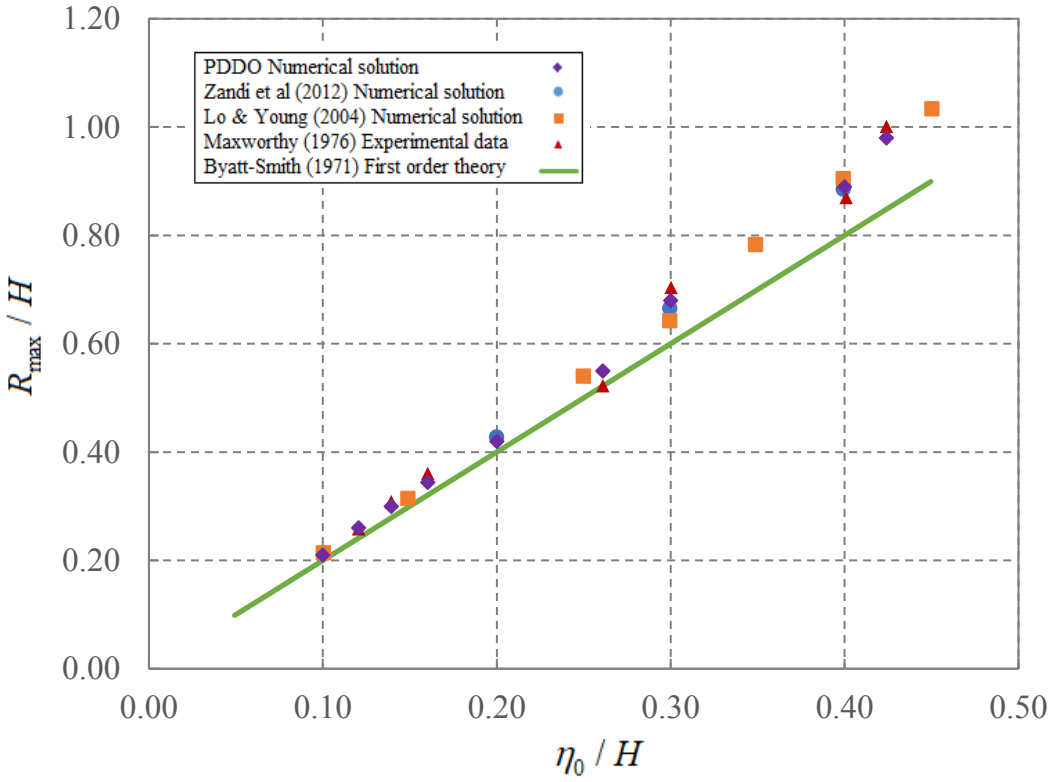

Figure 5.21. The maximum run-up height at the right wall vs initial wave height.

5.7.5 3D nonlinear liquid sloshing under sway and surge excitations in a square tank

In this section, liquid sloshing is simulated in a 3D square tank as depicted in Figure 5.22.a. Experimental data on this test can be found in (Wu et al. 2015). This benchmark has been solved by other numerical solutions such as harmonic polynomial cell (HPC) method (Shao and Faltinsen 2014) and recently investigated by polynomial collocation method (Wu et al. 2016). The length and the width of the tank are $L = B = 1.0$ m while the still water depth is 0.25 m. A periodic oscillation, with the angle of $\varphi = 30^{\circ}$ (See Figure 5.22.b), is considered having velocity projections in x and y directions as

$$u_x = -A\omega\cos(\varphi)\sin(\omega t),\quad u_y = -A\omega\sin(\varphi)\cos(\omega t) \tag{5.80}$$

where, ω represents the angular frequency of the excitation and A stands for the oscillation amplitude. In (5.80) u_x and u_y denote surge and sway velocities respectively.

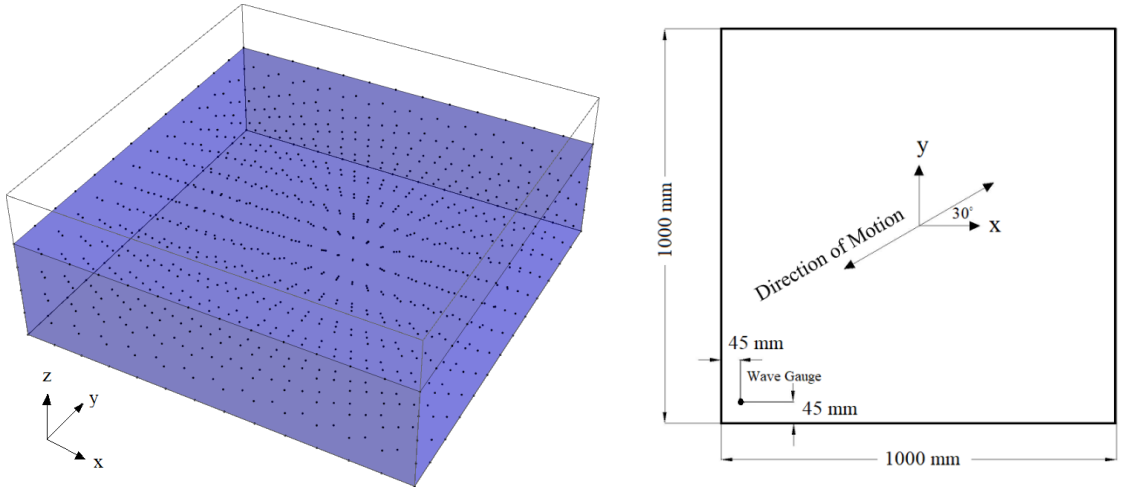

(a) (b)

Figure 5.22. . (a) Distribution of the nodes over the square tank (b) Top view of the square tank.

The boundary condition values in terms of PD unknowns, $\varphi(\mathrm{x}_j, \mathrm{y}_j)$, in this problem is given by

$$\sum_{j=1} \varphi(x_j, y_j, z_j) g^{001}(\mathrm{x}_j - x_i, \mathrm{y}_j - y_i, z_j - z_i)\mathrm{V}_j = 0 \quad \text{for} \quad z_i = -\frac{H}{2}$$

$$\sum_{j=1} \varphi(x_j, y_j, z_j) g^{100}(\mathrm{x}_j - x_i, \mathrm{y}_j - y_i, z_j - z_i)\mathrm{V}_j = A\omega\cos(\varphi)\sin(\omega t) \quad \text{for} \quad x_i = -\frac{L}{2}$$

$$\sum_{j=1} \varphi(x_j, y_j, z_j) g^{100}(\mathrm{x}_j - x_i, \mathrm{y}_j - y_i, z_j - z_i)\mathrm{V}_j = -A\omega\cos(\varphi)\sin(\omega t) \quad \text{for} \quad x_i = \frac{L}{2}$$

$$\sum_{j=1} \varphi(x_j, y_j, z_j) g^{010}(\mathrm{x}_j - x_i, \mathrm{y}_j - y_i, z_j - z_i)\mathrm{V}_j = A\omega\sin(\varphi)\cos(\omega t) \quad \text{for} \quad y_i = -\frac{B}{2}$$

$$\sum_{j=1} \varphi(x_j, y_j, z_j) g^{010}(\mathrm{x}_j - x_i, \mathrm{y}_j - y_i, z_j - z_i)\mathrm{V}_j = -A\omega\sin(\varphi)\cos(\omega t) \quad \text{for} \quad y_i = \frac{B}{2}$$

$$\sum_{j=1} \varphi(x_j, y_j, z_j) g^{000}(\mathrm{x}_j - x_i, \mathrm{y}_j - y_i, z_j - z_i)\mathrm{V}_j = (\varphi_i)^{(n-2)} + 2\Delta t\left[\left(-g(z + \frac{H}{2}) + \frac{1}{2}\nabla\varphi.\nabla\varphi\right)_i\right]^{(n-1)} \quad \text{for} \quad (x_i, y_i, z_i) \in \Gamma_{\mathrm{F}}$$

(5.81)

in which,

$$\left(\nabla\varphi.\nabla\varphi\right)_i^{(n-1)}=\left(\sum_{j=1}^{r}g_{ij}^{100}(\xi)\,\varphi_j V_j\right)^2+\left(\sum_{j=1}^{r}g_{ij}^{010}(\xi)\,\varphi_j V_j\right)^2+\left(\sum_{j=1}^{r}g_{ij}^{001}(\xi)\,\varphi_j V_j\right)^2 \tag{5.82}$$

The lowest natural angular frequency of the tank is $\omega_0 = 4.4957$ rad/s (Wu et al. 2016). The excitation frequency is $\omega = 0.9\omega_0$, where $A = 0.005$ m. A 14×14 uniform grid is emplyed in the $x-y$ direction and 5 uniform vertical nodes are set in the z direction. It should be pointed out that for this example PDDO uses 980 nodes while in the model proposed by (Wu et al. 2016) 1005 nodes are emplyed. This example is solved up to 28.0 s and the time step is chosen as $\Delta t = 0.01$ s.

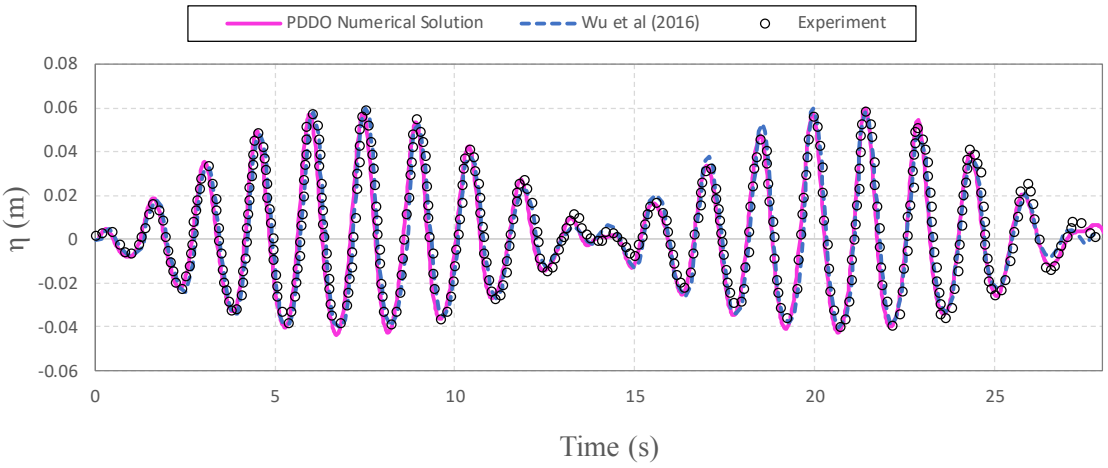

(a)

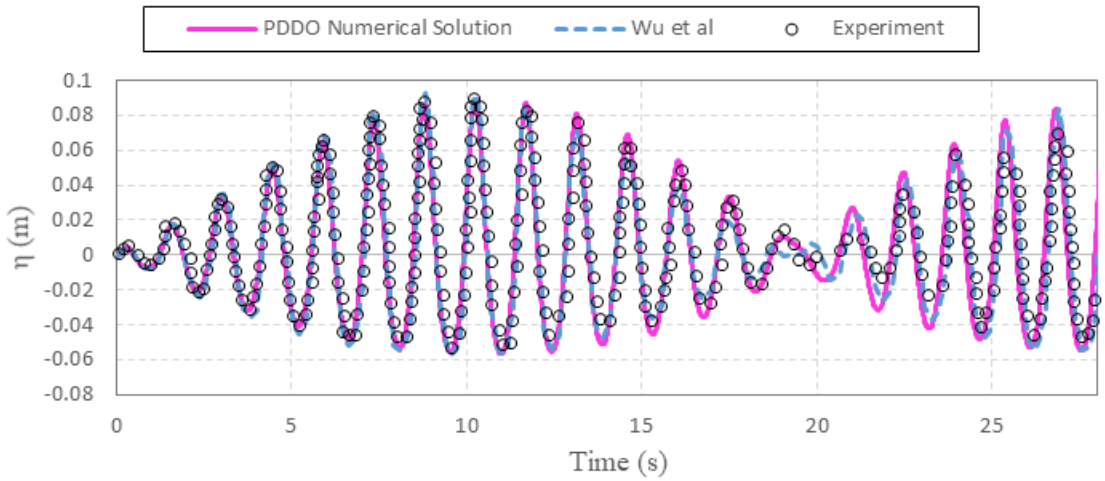

(b)

Figure 5.23. Comparison of the surface elevations in the square obtained by the present method, polynomial collocation method and the experimental data (a) $\omega = 0.9\omega_0$ (b) $\omega = 0.93\omega_0$.

The wave Gauge is set with a distance of 0.0636 m from the left-lower corner of the tank on its diagonal as depicted in Figure 5.22.b. Comparison between PDDO numerical solution, polynomial collocation method in (Wu et al. 2016) and experimental data in (Wu et al. 2015) is shown in Figure 5.23. Excellent agreement is obtained between the three sets of results. The snap shots of the free surface elevation at different times, $t = 22.2\ s : 22.8\ \text{s}$, for $\omega = 0.9\omega_0$ have been depicted in Figure 5.24. It can be observed that the left-lower corner of the tank has its lowest and highest elevation at *t*=22.2 s and *t*=22.8 s respectively while for the right-upper corner the elevation goes from its highest level at *t*=22.2 to its lowest elevation at *t*=22.8 s.

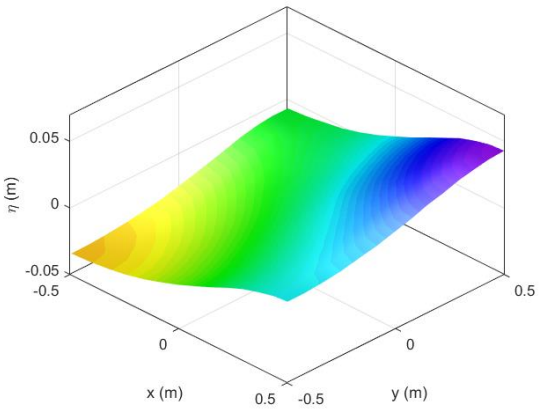

t=22.2 s

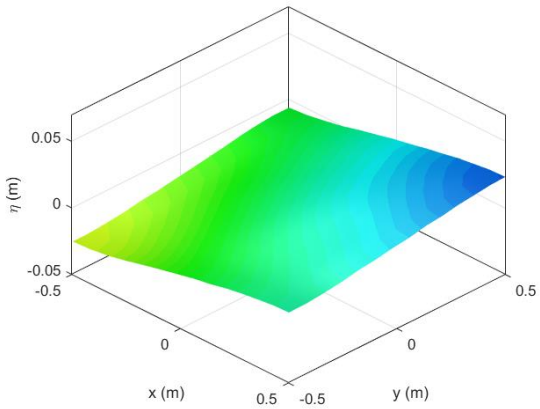

t=22.3 s

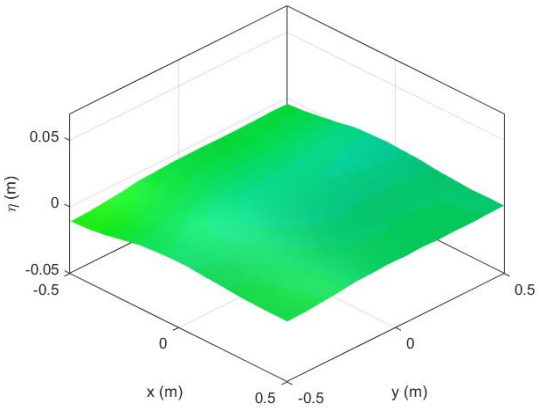

t=22.4 s

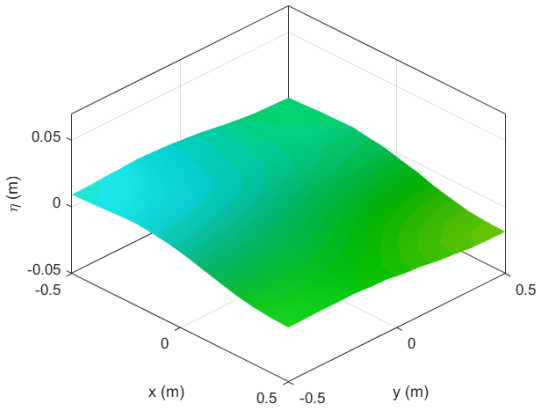

t=22.5 s

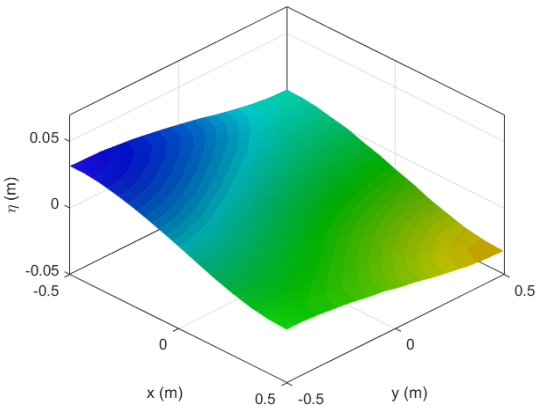

t=22.6 s

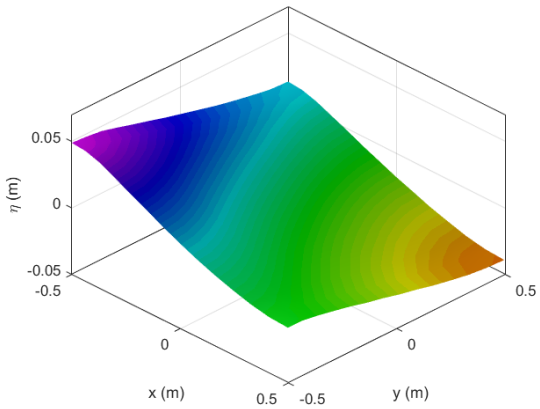

t=22.7 s

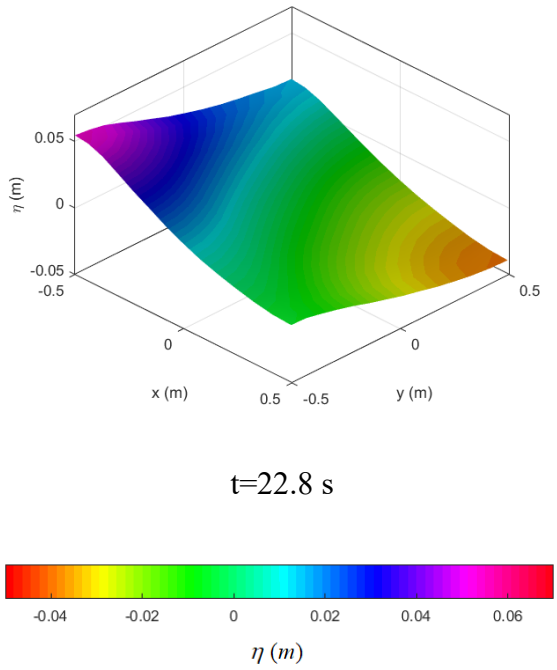

Figure 5.24. Snapshots of free surface elevation in different time intervals, $t = 22.2\ s : 22.8\ s$, for a 3-D square tank and $\omega = 0.9\omega_1$.

5.7.6 3D nonlinear liquid sloshing in a cylindrical water tank

In this example, a 3D cylindrical water tank is simulated by PDDO. The results are then validated with the results of the BEM and experimental data given in (Chen et al. 2007b). A tank with radius of $R = 0.3$ m, and still water depth of $h = 0.1$ m, is considered as shown in Figure 5.25. Based on the linear theorem, first natural frequency of the cylindrical tank is given by ((Chen et al. 2007b)):

$$\omega_1 = \sqrt{\frac{\lambda_1 g}{R} \tanh\left(\lambda_1 \frac{h}{R}\right)} \tag{5.83}$$

where λ_1 stands for the first root of the first derivative of the first-order Bessel function $J_1'(\lambda_1)$. In this example, these parameters are evaluated as $\lambda_1 = 1.84$ and thus $\omega_0 = 5.74$ rad/s.

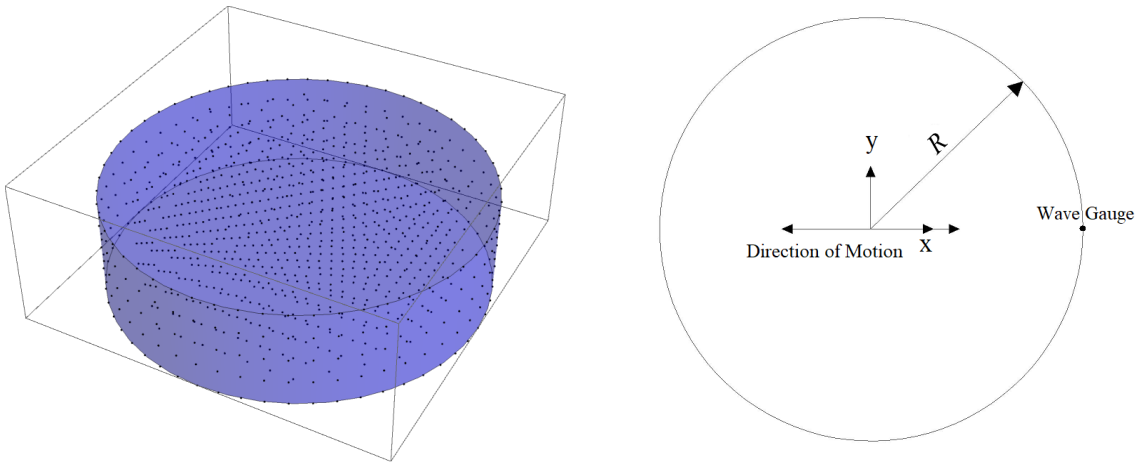

(a) (b)

Figure 5.25. (a) Distribution of the nodes over the cylinder tank (b) Top view of the cylinder tank.

257 nodes are emplyed in the $x-y$ direction and 5 uniform vertical nodes are set in the z direction. The total number of nodes used for this example is 1285. Note that although the number of nodes in this study is greater than the elements in (Chen et al. 2007b), the time step used in this study is $\Delta t = 0.01$ s which is ten times higher than the time step employed in (Chen et al. 2007b). A harmonic excitation with the velocity oscillation of $u_e = A\omega \sin \omega t$ is considered; with $A = 0.0005$ m, $\omega = 5.16$ rad/s for the first case, and 5.74 rad/s for the second case. In Figure 5.26, the wave elevation history at lateral wall $(0, R)$ is compared with the experimental data and the results given by Chen et al. (2007). It may be noted that the results of the PDDO are in good agreement with the BEM results while the results of both methods are in far agreement with the experimental data. The reason may be traced under the fact that the wave elevation is relatively small while the solution is performed in a nonlinear style. This may introduced some round-off errors in both numerical solutions. An acceptable agreement between PDDO numerical results and experimental results is observed especially when the

frequency of sloshing is equal to $\omega_0 = 5.74$ rad/s. A resonance effect can be observed since the wave amplitude grows with the time (Figure 5.26 (b)).

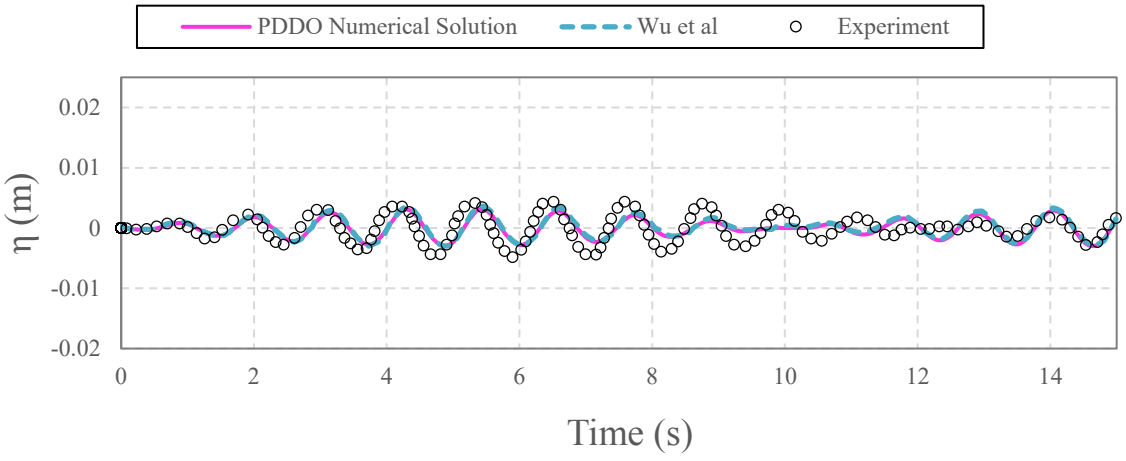

(a)

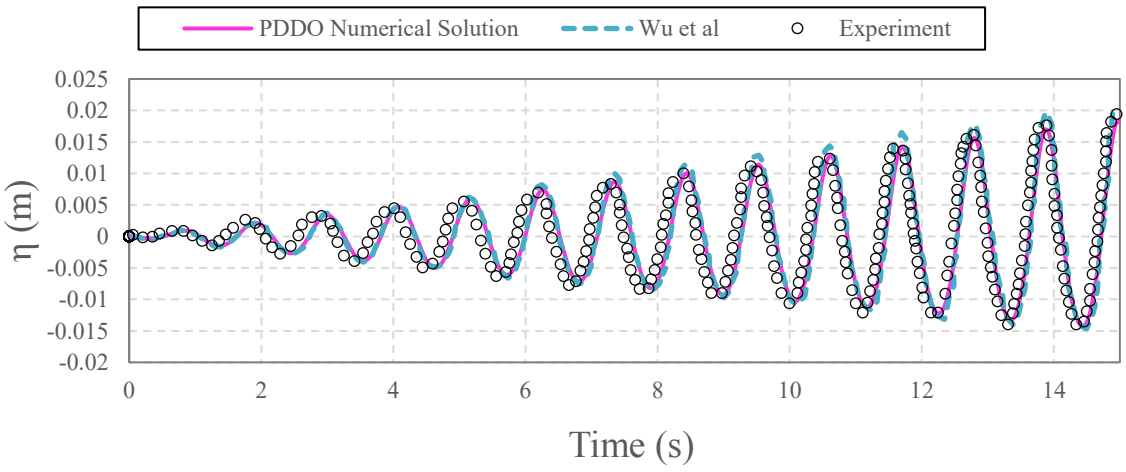

(b)

Figure 5.26. Comparison of the surface elevations at lateral wall (*R*,*0*) obtained by the PDDO method (Chen et al. 2007b) and experimental data with forced frequency: (a) $\omega = 5.16$ rad/s (b) $\omega = 5.74$ rad/s.

The snap shots of the free surface elevation at different times, $t = 13.15\mathrm{T} : 13.65\mathrm{T}$, for $\omega = 5.74$ rad/s have been depicted in Figure 5.27.

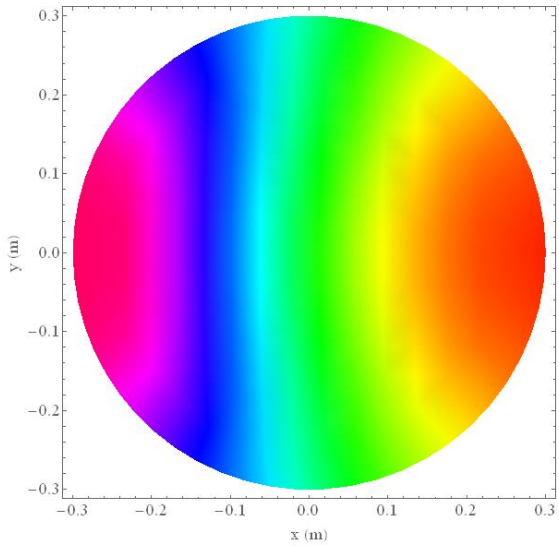

t=13.15T

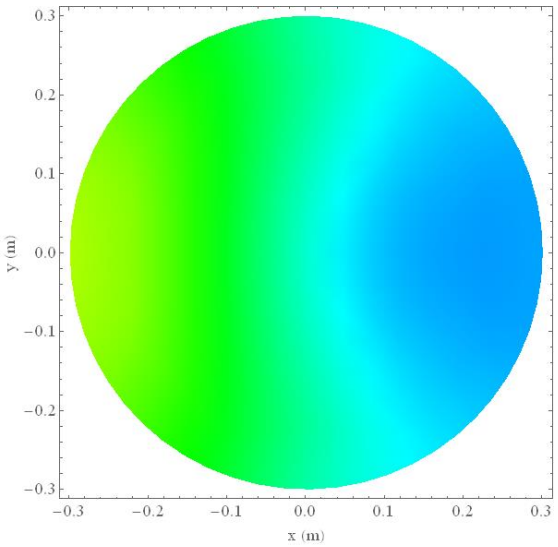

t=13.45T

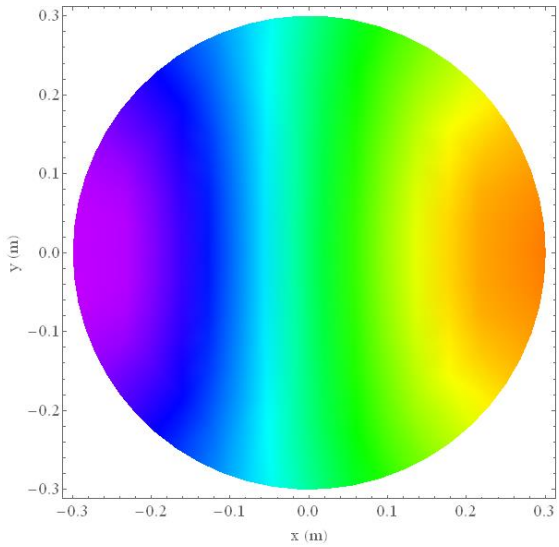

t=13.25T

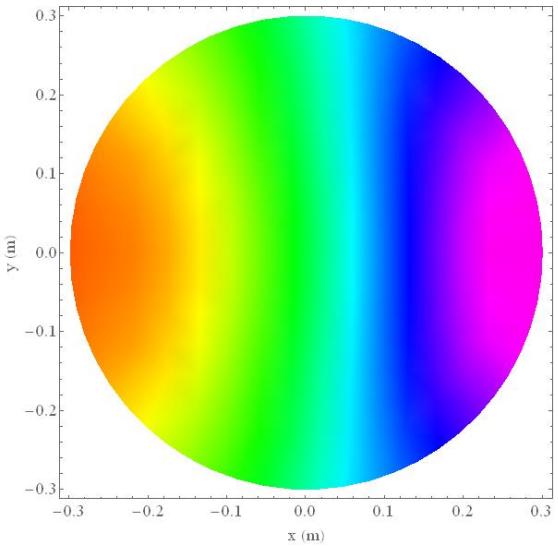

t=13.55T

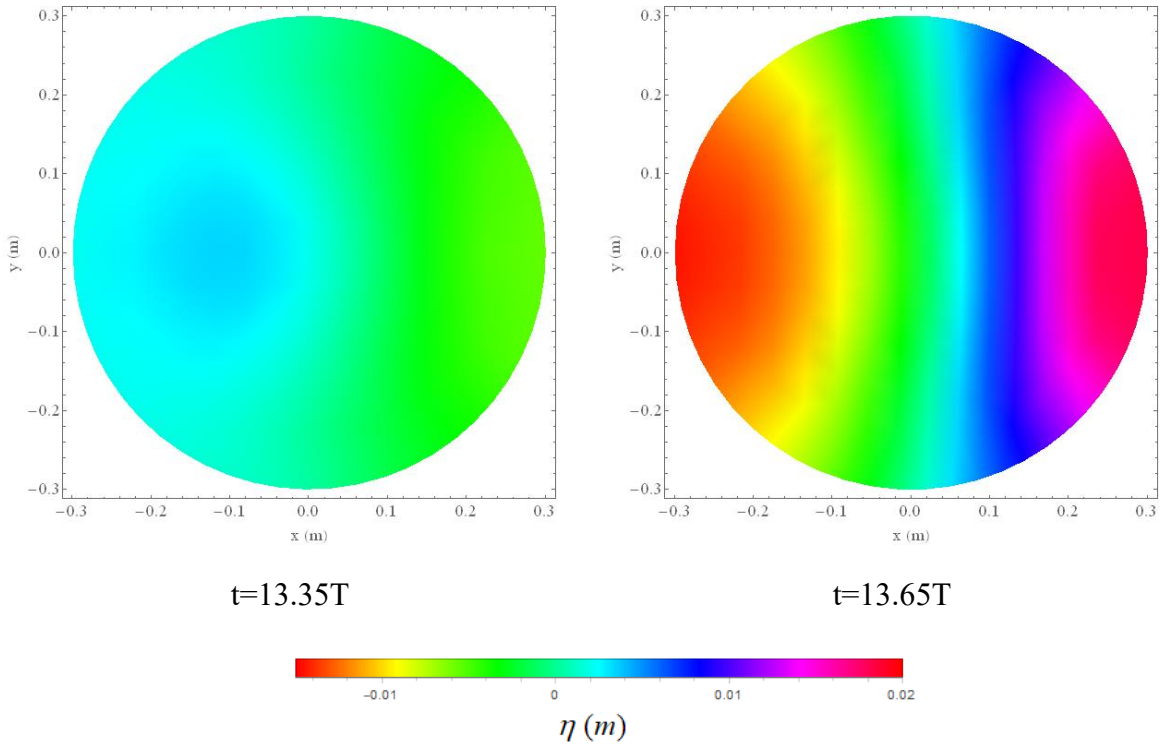

Figure 5.27. Snapshots of free surface elevation in different time intervals, $t = 13.15\,\mathrm{T} : 13.65\,\mathrm{T}$, for a 3-D cylinder tank and $\omega = 5.74\,\mathrm{rad/s}$.

Chapter 6 Conclusions

In the present dissertation, a comprehensive study on engineering problems with discontinuities using the bond-based peridynamic model and the PDDO mesh-free method is studied. The main goal is to increase the accuracy and to reduce the computational cost of engineering simulations. Accordingly, Chapters 1 and 2 have been devoted to the literature review and to an overview of the bond-based peridynamic formulation and of its discretization. The main contributions of the work are presented in Chapters 3, 4 and 5. The following conclusions can be drawn from each chapter:

- ***Chapter 3***

Chapter 3 compares three fatigue degradation strategies to be used in the simulation of fatigue crack propagation. The constitutive law of the material under static load is bilinear. The increment of damage due to fatigue is added to that due to the static increment of the opening displacement and is defined in three different ways. A mathematical cylinder model is employed to carry out a comparison of the computational efficiency of the three fatigue degradation strategies.

Fatigue degradation strategy 1 assumes that the fatigue damage rate is a function of the opening displacement δ and of the current value of the total damage *D*. In fatigue degradation strategy 2 the damage directly affects the critical value of the opening displacement δ_c . Finally fatigue degradation strategy 3 assumes that the fatigue damage rate is a function only of the opening displacement δ .

Then the three laws are implemented in a code using bond based peridynamics to simulate fatigue crack propagation, and the sensitivity of the results to variations of the main discretization parameters is assessed. Both the cylinder model and the BBPD code provide the same assessment of the three fatigue degradation strategies. Two main conclusions can be obtained by the current work:

1) The third fatigue degradation strategy is the best, among those investigated, to be used in BBPD codes.
2) The cylinder model appears to provide reliable indications about the computational performance of the fatigue laws.

- ***Chapter 4***

Chapter 4 presents an effective way to use a variable grid size in a weakly coupled thermo-mechanical peridynamic model. The proposed numerical method is equipped with stretch control criterion to transform the grid discretization adaptively in time. Hence, finer grid spacing is only applied in limited zones where it is required. This method is capable of predicting complex crack patterns without any *a priori* hypothesis on crack onset and geometry. By introducing fine grid discretization over the boundaries of the model the surface (softening) effect is reduced significantly. The accuracy and performance of the model are examined through problems such as thermo-elastic and thermal-shock induced fracture in ceramics. Accordingly, the proposed numerical solution results are compared qualitatively and quantitatively to the experimental data, standard peridynamic with uniform grid size and FEM numerical solutions. A remarkable agreement is observed between all sets of results. The results confirm that the method is capable of producing the

results of a standard peridynamic model with uniform discretization at a much smaller computational cost.

- ***Chapter 5***

In this study, Peridynamic differential operator for the first time is applied to the solution of problems of liquid sloshing in tanks and makes use of potential flow theory and Lagrangian description. PDDO is capable to recast partial derivatives of a function through a nonlocal integral operator whose kernel is free of using any correction function. The method is capable to produce a well-conditioned system of equations for the problem which is important for marching in time. In order to validate the method, 2D challenging liquid sloshing problems with strong non linearity have been solved and the results are compared with the other numerical/analytical/experimental results available in literature. Excellent agreement is obtained between the PDDO numerical solution and experimental/numerical results that exhibits nonlinear wave effects. To further validate the method, we investigate liquid sloshing in rectangular tanks containing horizontal and vertical baffles. The PDDO method is then applied to the solution of solitary wave propagation problem and the results are in a good agreement with experimental data and other numerical results available in literature. Moreover, 3D application of PDDO numerical method in sway and surge liquid sloshing is presented to show the robustness of the strategy. The examples are solved with a coarse grid of nodes with respect to some other approaches such as MLPG, VOF, and local polynomial collocation methods. The newly proposed method is unique in its combination of high accuracy, high stability and low computational cost.

6.1 Future works

It must be pointed out that several future works can be carried out following the outcomes of the present study. Some of them are listed as:

- Extension of the fatigue crack growth and thermal sock problems to 3D problems.
- Three fatigue strategies described in Chapter 3, can be investigated in a SB-PD framework.
- Inspired by the work of this dissertation, the author aim at parallelize the implementation of the present refinement approach explained in Chapter 4.
- Fully-coupled Thermo-mechanical problems can be investigated using the adaptive refinement technique explained in Chapter 4.
- Adaptive refinement technique described in Chapter 4, paves the way to future studies on concurrent multiscale modeling of materials and structures using peridynamic theory.
- For further studies, PDDO can be applied to more complex problems such as viscus liquid sloshing in rectangular tank with/without baffles.

References

Agwai AG (2011) A Peridynamic Approach for Coupled Fields. Ph.D thesis, The University of Arizona.

Akyildiz H, Unal NE (2005) Experimental investigation of pressure distribution on a rectangular tank due to the liquid sloshing *Ocean Engineering* **32**:1503-1516.

Akyildiz H, Unal NE (2006) Sloshing in a three-dimensional rectangular tank: numerical simulation and experimental validation *Ocean Engineering* **33**:2135-2149.

Alfano G, Crisfield MA (2001) Finite element interface models for the delamination analysis of laminated composites: Mechanical and computational issues *International Journal for Numerical Methods in Engineering* **50**:1701-1736.

Alfano G, Crisfield MA (2003) Solution strategies for the delamination analysis based on a combination of local-control arc-length and line searches *International Journal for Numerical Methods in Engineering* **58**:999-1048.

Allix O, Corigliano A (1996) Modeling and simulation of crack propagation in mixed modes interlaminar fracture specimens *International journal of Fracture* **77**:111-140.

Asp LE, Sjögren A, Greenhalgh ES (2001) Delamination growth and thresholds in a carbon/epoxy composite under fatigue loading *Journal of Composites Technology & Research* **23**:55-68.

Awaji H, Honda S, Yamamoto N, Endo T, Hirosaki N (2002) Thermal Shock Strength and Thermal Shock Fracture Toughness of Ceramics. In: Fracture Mechanics of Ceramics: Volume 13. Crack-Microstructure Interaction, R-Curve Behavior, Environmental Effects in Fracture, and Standardization. Springer US, Boston, MA, pp 363-379

Baber F, Guven I (2017) Solder joint fatigue life prediction using peridynamic approach *Microelectronics Reliability* **79**:20-31.

Bahr HA, Weiss HJ, Maschke HG, Meissner F (1988) Multiple crack propagation in a strip caused by thermal shock *Theoretical and Applied Fracture Mechanics* **10**:219-226.

Bak BLV, Turon A, Lindgaard E, Lund E (2016) A Simulation Method for High-Cycle Fatigue-Driven Delamination using a Cohesive Zone Model *International Journal for Numerical Methods in Engineering* **106**:163–191.

Bak BLV, Turon A, Lindgaard E, Lund E (2017) A benchmark study of simulation methods for high-cycle fatigue-driven delamination based on cohesive zone models *Composite Structures* **164**:198-206.

Barenblatt GI (1962) The Mathematical Theory of Equilibrium of Crack in Brittle Fracture*,Advances in Applied Mechanics* **7**:55-129.

Baydoun M, Fries T (2012) Crack propagation criteria in three dimensions using the XFEM and an explicit–implicit crack description *International Journal of Fracture* **178**:51-70.

Bažant ZP, Ohtsubo H, Aoh K (1979) Stability and post-critical growth of a system of cooling or shrinkage cracks *International Journal of Fracture* **15**:443-456.

Bazazzadeh S, Shojaei A, Zaccariotto M, Galvanetto U (2019) Application of the Peridynamic differential operator to the solution of sloshing problems in tanks *Engineering Computations*:(DOI 10.1108/EC-1112-2017-0520).

Belytschko T (1989) The Finite Element Method: Linear Static and Dynamic Finite Element Analysis: Thomas J. R. Hughes *Computer-Aided Civil and Infrastructure Engineering* **4**:245-246.

Belytschko T, Black T (1999) Elastic crack growth in finite elements with minimal remeshing *International Journal for Numerical Methods in Engineering* **45**:601-620.

Benedetti I, Aliabadi MH (2010) A fast hierarchical dual boundary element method for three-dimensional elastodynamic crack problems *International Journal for Numerical Methods in Engineering* **84**:1038-1067.

Benedetti I, Aliabadi MH (2013) A three-dimensional cohesive-frictional grain-boundary micromechanical model for intergranular degradation and failure in polycrystalline materials *Computer Methods in Applied Mechanics and Engineering* **265**:36-62.

Benedetti I, Aliabadi MH (2015) Multiscale modeling of polycrystalline materials: A boundary element approach to material degradation and fracture *Computer Methods in Applied Mechanics and Engineering* **289**:429-453.

Benedetti I, Milazzo A, Aliabadi MH (2009) A fast dual boundary element method for 3D anisotropic crack problems *International Journal for Numerical Methods in Engineering* **80**:1356-1378.

Benito JJ, Urena F, Gavete L (2001) Influence of several factors in the generalized finite difference method *Applied Mathematical Modelling* **25**:1039-1053.

Blackman BRK, Hadavinia H, Kinloch AJ, Williams JG (2003) The use of a cohesive zone model to study the fracture of fibre composites and adhesively-bonded joints *International journal of fracture* **119**:25-46.

Blumenauer H, Pusch G (1993) Technische Bruchmechanik. Wiley-VCH Verlag, Weinheim.

Bobaru F, Duangpanya M (2010) The peridynamic formulation for transient heat conduction *International Journal of Heat and Mass Transfer* **53**:4047-4059.

Bobaru F, Duangpanya M (2012) A peridynamic formulation for transient heat conduction in bodies with evolving discontinuities *Journal of Computational Physics* **231**:2764-2785.

Bobaru F, Foster JT, Geubelle PH, Silling SA (2015) Handbook of Peridynamic Modeling. Taylor & Francis,

Bobaru F, Foster JT, Geubelle PH, Silling SA (2016) Handbook of peridynamic modeling. CRC Press,

Bobaru F, Ha YD (2011) Adaptive refinement and multiscale modeling in 2D peridynamics *International Journal for Multiscale Computational Engineering* **9**:635–659.

Bobaru F, Yang M, Alves Leonardo F, Silling Stewart A, Askari E, Xu J (2008) Convergence, adaptive refinement, and scaling in 1D peridynamics *International Journal for Numerical Methods in Engineering* **77**:852-877.

Boroomand B, Bazazzadeh S, Zandi SM (2016) On the use of Laplace's equation for pressure and a mesh-free method for 3D simulation of nonlinear sloshing in tanks *Ocean Engineering* **122**:54-67.

Boroomand B, Bazazzadeh S, Zandi SM (2017) On the use of Laplace's equation for pressure and a mesh-free method for 3D simulation of nonlinear sloshing in tanks; Reply to the discussion *Ocean Engineering* **134**:176-177.

Boroomand B, Soghrati S, Movahedian B (2010) Exponential basis functions in solution of static and time harmonic elastic problems in a meshless style *International Journal for Numerical Methods in Engineering* **81**:971-1018.

Bourdin B, Marigo J-J, Maurini C, Sicsic P (2014) Morphogenesis and Propagation of Complex Cracks Induced by Thermal Shocks *Physical Review Letters* **112**:014301.

Branco R, Antunes F, Costa JA (2015) Review on 3D-FE adaptive remeshing techniques for crack growth modelling *Engineering Fracture Mechanics* **141**:170–195.

Byatt-Smith JGB (1971) An integral equation for unsteady surface waves and a comment on the Boussinesq equation *Journal of Fluid Mechanics* **49**:625–633.

Chen BF, Nokes R (2005) Time-independent finite difference analysis of fully nonlinear and viscous fluid sloshing in a rectangular tank *Journal of Computational Physics* **209**:47-81.

Chen J-T, Lee Y-T, Yu S-R, Shieh S-C (2009) Equivalence between the Trefftz method and the method of fundamental solution for the annular Green's function using the addition theorem and image concept *Engineering Analysis with Boundary Elements* **33**:678-688.

Chen J, Crisfield MA, Kinloch AJ, Busso EP, Matthews FL, Qiu Y (1999) Predicting progressive delamination of composite material specimens via interface elements *Mechanics of Composite Materials and Structures* **6**:301-317.

Chen JT, Wu CS, Lee YT, Chen KH (2007a) On the equivalence of the Trefftz method and method of fundamental solutions for Laplace and biharmonic equations *Computers & Mathematics with Applications* **53**:851-879.

Chen YH, Hwang WS, Ko CH (2007b) Sloshing behaviours of rectangular and cylindrical liquid tanks subjected to harmonic and seismic excitations *Earthquake Engineering & Structural Dynamics* **36**:1701-1717.

Chen Z, Bobaru F (2015) Peridynamic modeling of pitting corrosion damage *Journal of the Mechanics and Physics of Solids* **78**:352-381.

Chen Z, Zhang G, Bobaru F (2016) The influence of passive film damage on pitting corrosion *Journal of The Electrochemical Society* **163**:C19-C24.

Cheng Z, Zhang G, Wang Y, Bobaru F (2015) A peridynamic model for dynamic fracture in functionally graded materials *Composite Structures* **133**:529-546.

Choun Y-S, Yun C-B (1996) Sloshing characteristics in rectangular tanks with a submerged block *Computers and Structures* **61**:401-413.

Choun Y-S, Yun C-B (1999) Sloshing an alysis of rectangular tanks with a submerged structure by using small-amplitude wave theory *Earthquake Engineering and Structure Dynamics* **28**:763-783.

Chu D, Li X, Liu Z (2017) Study the dynamic crack path in brittle material under thermal shock loading by phase field modeling *International Journal of Fracture* **208**:115-130.

Crisfield MA, Alfano G (2002) Adaptive hierarchical enrichment for delamination fracture using a decohesive zone model *International Journal for Numerical Methods in Engineering* **54**:1369-1390.

D'Antuono P, Morandini M (2017) Thermal shock response via weakly coupled peridynamic thermo-mechanics *International Journal of Solids and Structures* **129**:74-89.

Day AS (1965) An introduction to dynamic relaxation *The Engineering* **219**:218-221.

Degrieck J, Van Paepegem W (2001) Fatigue damage modeling of fibre-reinforced composite materials: Review *Applied Mechanics Reviews* **54**:279-300.

Dipasquale D, Zaccariotto M, Galvanetto U (2014) Crack propagation with adaptive grid refinement in 2D peridynamics *International Journal of Fracture* **190**:1-22.

Dugdale DS (1960) Yielding of steel sheets containing slits *Journal of the Mechanics and Physics of Solids* **8**:100 –104.

Durate F, Gormaz R, Natesan S (2004) Arbitrary Lagrangian–Eulerian method for Navier–Stokes equations with moving boundaries *Computer Methods in Applied Mechanics and Engineering* **193**:4819–4836.

Faltinsen OM (1987) A numerical nonlinear method of sloshing in tanks with two-dimensional flow *Journal of Ship Research* **22**:193-202.

Faltinsen OM, Rognebakke OF, Timokha AN (2005) Classification of three-dimensional nonlinear sloshing in a square-base tank with finite depth *Journal of Fluids and Structures* **2**:81-103.

Frandsen JB (2004) Sloshing motions in excited tanks *Journal of Computational Physics* **196**:53-87.

Galvanetto U, Robinson P, Cerioni A, Armas CL (2009) A Simple Model for the Evaluation of Constitutive Laws for the Computer Simulation of Fatigue-Driven Delamination in Composite Materials *SDHM: Structural Durability & Health Monitoring* **5**:161-190.

Gerstle W, Sau N, Silling S (2007) Peridynamic modeling of concrete structures *Nuclear Engineering and Design* **237**:1250-1258.

Ghajari M, Iannucci L, Curtis P (2014) A peridynamic material model for the analysis of dynamic crack propagation in orthotropic media *Computer Methods in Applied Mechanics and Engineering* **276**:431-452.

Giannakeas IN, Papathanasiou TK, Bahai H (2018) Simulation of thermal shock cracking in ceramics using bond-based peridynamics and FEM *Journal of the European Ceramic Society* **38**:3037-3048.

Gingold RA, Monaghan JJ (1977) Smoothed particle hydrodynamics: theory and application to non-spherical stars *Monthly Notices of the Royal Astronomical Society* **181**:375–389.

González D, Cueto E, Chinesta F, Doblaré M (2007) A natural element updated Lagrangian strategy for free-surface fluid dynamics *Journal of Computational Physics* **223**:127–150.

Griffith AA (1921) VI. The phenomena of rupture and flow in solids *Philosophical Transactions of the Royal Society of London* **221**:163-198.

Gu X, Zhang Q, Xia X (2017a) Voronoi-based peridynamics and cracking analysis with adaptive refinement *International Journal for Numerical Methods in Engineering* **112**:2087-2109.

Gu Y, Wang L, Chen W, Zhang C, He X (2017b) Application of the meshless generalized finite difference method to inverse heat source problems *International Journal of Heat and Mass Transfer* **108**:721–729.

Ha YD, Bobaru F (2010) Studies of dynamic crack propagation and crack branching with peridynamics *International Journal of Fracture* **162**:229-244.

Ha YD, Bobaru F (2011) Characteristics of dynamic brittle fracture captured with peridynamics *Engineering Fracture Mechanics* **78**:1156-1168.

Hasselman DPH (1963) Elastic Energy at Fracture and Surface Energy as Design Criteria for Thermal Shock *Journal of the American Ceramic Society* **46**:535-540.

Hasselman DPH (1969) Unified Theory of Thermal Shock Fracture Initiation and Crack Propagation in Brittle Ceramics *Journal of the American Ceramic Society* **52**:600-604.

Hillerborg A, Modeer M, Petersson P-E (1976) Analysis of crack formation and crack growth in concrete by means of fracture mechanics and finite elements *Cement and Concrete Research* **6**:773-781.

Honda S, Ogihara Y, Kishi T, Hashimoto S, Iwamoto Y (2009) Estimation of thermal shock resistance of fine porous alumina by infrared radiation heating method *Journal of the Ceramic Society of Japan* **117**:1208-1215.

Honda S, Suzuki T, Nishikawa T, Awaji H, Akimune Y, Hirosaki N (2002) Estimation of Thermal Shock Properties for Silicon Nitride Having High Thermal Conductivity *Journal of the Ceramic Society of Japan* **110**:38-43.

Hu W, Ha YD, Bobaru F (2012) Peridynamic model for dynamic fracture in unidirectional fiber-reinforced composites *Computer Methods in Applied Mechanics and Engineering* **217**:247-261.

Hu W, Wang Y, Yu J, Yen C-F, Bobaru F (2013) Impact damage on a thin glass plate with a thin polycarbonate backing *International Journal of Impact Engineering* **62**:152-165.

Hu YL, Carvalho NVD, Madenci E (2015) Peridynamic modeling of delamination growth in composite laminates *Composite Structures* **132**:610-620.

Hu YL, Madenci E (2017) Peridynamics for fatigue life and residual strength prediction of composite laminates *Composite Structures* **160**:169-184.

Huang D, Lu G, Qiao P (2015) An improved peridynamic approach for quasi-static elastic deformation and brittle fracture analysis *International Journal of Mechanical Sciences* **94-95**:111-122.

Ibrahim RA (2005) Liquid Sloshing Dynamics: Theory and Applications. Cambridge University Press, NewYork, USA.

Idelsohn SR, Onate E, Pin FD (2003) A Lagrangian meshless finite element method applied to fluid–structure interaction problems *Computers & Structures* **81**:655-671.

Idelsohn SR, Oñate E, Pin FD (2004) The particle finite element method: a powerful tool to solve incompressible flows with free surfaces and breaking waves *International Journal for Numerical Methods in Engineering* **61**:964–989.

Jenkins DR (2005) Optimal spacing and penetration of cracks in a shrinking slab *Physical Review E* **71**:056117.

Jiang CP, Wu XF, Li J, Song F, Shao YF, Xu XH, Yan P (2012) A study of the mechanism of formation and numerical simulations of crack patterns in ceramics subjected to thermal shock *Acta Materialia* **60**:4540-4550.

Jung J, Seok J (2016) Fatigue crack growth analysis in layered heterogeneous material systems using peridynamic approach *Composite Structures* **152**:403-407.

Jung J, Seok J (2017) Mixed-mode fatigue crack growth analysis using peridynamic approach *International Journal of Fatigue* **103**:591-603.

Juntti M, Asp LE, Olsson A (1999) Assessment of evaluation methods for the mixed-mode bending test *Journal of Composites Technology & Research* **21**:37-48.

Kilic B, Madenci E (2009) Prediction of crack paths in a quenched glass plate by using peridynamic theory *International Journal of Fracture* **156**:165-177.

Kilic B, Madenci E (2010) An adaptive dynamic relaxation method for quasi-static simulations using the peridynamic theory *Theoretical and Applied Fracture Mechanics* **53**:194-204.

Kingery WD (1955) Factors Affecting Thermal Stress Resistance of Ceramic Materials *Journal of the American Ceramic Society* **38**:3-15.

Konstanze K (2014) Simulation of high-cycle fatigue-driven delamination in composites using a cohesive zone model. Ph.D thesis, Imperial College London.

Kuhn G, Partheymüller P (1999) 3D crack growth simulations with the boundary element method. Southampton.

Laitone EV (1960) The second approximation to cnoidal and solitary waves *Journal of Fluid Mechanics* **9**:430–444.

Le QV (2014) Relationship between microstructure and mechanical properties in Bi2Sr2CaCu2Ox round wires using peridynamic simulation. Ph.D thesis, Raleigh (NC): North Carolina State University.

Lee J, Oh SE, Hong J-W (2017) Parallel programming of a peridynamics code coupled with finite element method *International Journal of Fracture* **203**:99-114.

Leray D, Vadean A, Daidie A (2008) Fast computation of preloaded bolted circular joint aiming at fatigue bolt sizing: Hypotheses and modeling *Engineering Computations* **25**:42-54.

Levine SR, Opila EJ, Halbig MC, Kiser JD, Singh M, Salem JA (2002) Evaluation of ultra-high temperature ceramics foraeropropulsion use *Journal of the European Ceramic Society* **22**:2757-2767.

Li J, Song F, Jiang C (2015) A non-local approach to crack process modeling in ceramic materials subjected to thermal shock *Engineering Fracture Mechanics* **133**:85-98.

Li S, Liu WK (1998) Synchronized reproducing kernel interpolant via multiple wavelet expansion *Computational Mechanics* **21**:28-47.

Li S, Liu WK (1999a) Reproducing kernel hierarchical partition of unity, Part I—formulation and theory *International Journal for Numerical Methods in Engineering* **45**:251-288.

Li S, Liu WK (1999b) Reproducing kernel hierarchical partition of unity, Part II—applications *International Journal for Numerical Methods in Engineering* **45**:289-317.

Liu D, Lin P (2008) A numerical study of three-dimensional liquid sloshing in tanks *Journal of Computational Physics* **227**:3921-3939.

Liu D, Lin P (2009) Three-dimensional liquid sloshing in a tank with baffles *Ocean engineering* **36**:202-212.

Liu Y, Wu X, Guo Q, Jiang C, Song F, Li J (2015) Experiments and numerical simulations of thermal shock crack patterns in thin circular ceramic specimens *Ceramics International* **41**:1107-1114.

Lo DC, Young DL (2004) Arbitrary Lagrangian–Eulerian finite element analysis of free surface flow using a velocity-vorticity formulation *Journal of Computational Physics* **195**:175–201.

Madenci E, Barut A, Futch M (2016) Peridynamic differential operator and its applications *Computer Methods in Applied Mechanics and Engineering* **304**:408-451.

Madenci E, Dorduncu M, Barut A, Futch M (2017) Numerical solution of linear and nonlinear partial differential equations using the peridynamic differential operator *Numerical Methods for Partial Differential Equations* **33**:1726–1753.

Madenci E, Oterkus E (2014) Peridynamic Theory and Its Applications. Springer-Verlag New York.

Maxworthy T (1976) Experiments on collisions between solitary waves *Journal of Fluid Mechanics* **76**:177-185.

Menouillard T, Belytschko T (2011) Analysis and computations of oscillating crack propagation in a heated strip *International Journal of Fracture* **167**:57-70.

Mi Y, Crisfield MA (1996) Analytical derivation of load/displacement relationship for the DCB and MMB and proof of the FEA formulation. IC-AERO Report 97-02, Department of Aeronautics, Imperial College , London, UK.

Miranda ACO, Meggiolaro MA, Castro JTP, Martha LF, Bittencourt TN (2003) Fatigue life and crack path predictions in generic 2D structural components *Engineering Fracture Mechanics* **70**:1259-1279.

Mitra S, Wang CZ, Reddy JN, Khoo BC (2012) A 3D fully coupled analysis of nonlinear sloshing and ship motion *Ocean Engineering* **39**:1-13.

Moës N, Belytschko T (2002) Extended finite element method for cohesive crack growth *Engineering Fracture Mechanics* **69**:813-833.

Mossaiby F, Shojaei A, Zaccariotto M, Galvanetto U (2017) OpenCL implementation of a high performance 3D Peridynamic model on graphics accelerators *Computers & Mathematics with Applications* **74**:1856-1870.

Nemat-Nasser S (1978) Stability of a system of interacting cracks *International Journal of Engineering Science* **16**:277-285.

Nemat-Nasser S, Keer LM, Parihar KS (1978) Unstable growth of thermally induced interacting cracks in brittle solids *International Journal of Solids and Structures* **14**:409-430.

Nguyen VP, Rabczuk T, Bordas S, Duflot M (2008) Meshless methods: A review and computer implementation aspects *Mathematics and Computers in Simulation* **79**:763-813.

Nithiarasu P (2005) An arbitrary Lagrangian–Eulerian (ALE) formulation for free surface flows using the characteristic-based split (CBS) scheme *International Journal for Numerical Methods in Fluids* **48**:1415–1428.

Opeka MM, Talmy IG, Zaykoski JA (2004) Oxidation-based materials selection for 2000°C + hypersonic aerosurfaces: Theoretical considerations and historical experience *Journal of Materials Science* **39**:5887–5904.

Ostergaard MG, Ibbotson AR, Roux OL, Prior AM (2011) Virtual testing of aircraft structures *CEAS Aeronautical Journal* **1**:83.

Oterkus E, Guven I, Madenci E (2010) Fatigue failure model with peridynamic theory. 12th IEEE Intersociety Conference on Thermal and Thermomechanical Phenomena in Electronic Systems, Las Vegas, NV, USA.

Oterkus S (2015) Peridynamics for the solution of multiphysics problems. University of Arizona.

Oterkus S, Madenci E (2017) Peridynamic modeling of fuel pellet cracking *Engineering Fracture Mechanics* **176**:23-37.

Oterkus S, Madenci E, Agwai A (2014a) Fully coupled peridynamic thermomechanics *Journal of the Mechanics and Physics of Solids* **64**:1-23.

Oterkus S, Madenci E, Agwai A (2014b) Peridynamic thermal diffusion *Journal of Computational Physics* **265**:71-96.

Padture NP, Gell M, Jordan EH (2002) Thermal Barrier Coatings for Gas-Turbine Engine Applications *Science* **296**:280-284.

Pal P (2012a) Slosh Dynamics of Liquid-Filled Rigid Containers: Two-Dimensional Meshless Local Petrov-Galerkin Approach *Journal of Engineering Mechanics* **138**:567-581.

Pal P (2012b) Slosh dynamics of liquid-filled rigid containers: two-dimensional meshless local Petrov-Galerkinapproach *Journal of Engineering Mechanics* **138**:567-581.

Peerlings RHJ, Brekelmans WAM, Borst R, Geers MGD (2000) Gradientenhanced damage modelling of high-cycle fatigue *International Journal for Numerical Methods in Engineering* **49**:1547 -1569.

Point N, Sacco E (1996) A delamination model for laminated composites *International Journal of Solids and Structures* **33**:483-509.

Qiu Y, Crisfield MA, Alfano G (2001) An interface element formulation for the simulation of delamination with buckling *Engineering Fracture Mechanics* **68**:1755-1776.

Radovitzky R, Oritz M (1998) Lagrangian finite element analysis of Newtonian fluid flow *International Journal for Numerical Methods in Engineering* **43**:607-619.

Ramaswamy B, Kawahara M (1986) Lagrangian finite element method for the analysis of two-dimensional sloshing problems *International Journal for Numerical Methods in Fluids* **6**:659-670.

Ramaswamy B, Kawahara M (1987a) Arbitrary Lagrangian-Eulerian finite element method for unsteady, convective, incompressible viscous free surface fluid flow *International Journal for Numerical Methods in Fluids* **7**:1053–1075.

Ramaswamy B, Kawahara M (1987b) Lagrangian finite element analysis applied to viscous free surface fluid flow *International Journal for Numerical Methods in Fluids* **7**:953-984.

Ren B, Li C, Yan X, Lin MC, Bonet J, Hu S-M (2014) Multiple-Fluid SPH Simulation Using a Mixture Model *ACM Trans Graph* **33**:1-11.

Ren H, Zhuang X, Cai Y, Rabczuk T (2016) Dual-horizon peridynamics *International Journal for Numerical Methods in Engineering* **108**:1451-1476.

Richard HA, Sander M (2016) Fatigue Crack Growth vol 227. Springer International Publishing, Switzerland.

Robinson P, Galvanetto U, Tumino D, Bellucci G, Violeau D (2005) Numerical simulation of fatigue-driven delamination using interface elements *International journal for numerical methods in engineering* **63**:1824-1848.

Rokhi MM, Shariati M (2013) Implementation of the extended finite element method for coupled dynamic thermoelastic fracture of a functionally graded cracked layer *Journal of the Brazilian Society of Mechanical Sciences and Engineering* **35**:69-81.

Salete E, Benito JJ, Ureña F, Gavete L, Ureña M, García A (2017) Stability of perfectly matched layer regions in generalized finite difference method for wave problems *Journal of Computational and Applied Mathematics* **312**:231-239.

Schellekens, Borst R (1993) A non-linear finite element approach for the analysis of mode I free edge delamination in composites *International Journal of Solids and Structures* **30**:1239-1253.

Schneider GA (1991) Thermal shock criteria for ceramics *Ceramics International* **17**:325-333.

Seleson P, Beneddine S, Prudhomme S (2013) A force-based coupling scheme for peridynamics and classical elasticity *Computational Materials Science* **66**:34-49.

Seleson P, Ha YD, Beneddine S (2015) Concurrent coupling of bond-based peridynamics and the Navier equation of classical elasticity by blending **13**:91-113.

Shao J, Li S, Li Z, Liu M (2015) A comparative study of different baffles on mitigating liquid sloshing in a rectangular tank due to a horizontal excitation *Engineering Computations* **32**:1172-1190.

Shao JR, Li HQ, Liu GR, Liu MB (2012) An improved SPH method for modeling liquid sloshing dynamics *Computers & Structures* **100-101**:18-26.

Shao Y-L, Faltinsen OM (2014) A harmonic polynomial cell (HPC) method for 3D Laplace equation with application in marine hydrodynamics *Journal of Computational Physics* **274**:312-332.

Shao Y, Zhang Y, Xu X, Zhou Z, Li W, Liu B (2011) Effect of Crack Pattern on the Residual Strength of Ceramics After Quenching *Journal of the American Ceramic Society* **94**:2804-2807.

Shi J, Chopp D, Lua J, Sukumar N, Belytschko T (2010) Abaqus implementation of extended finite element method using a level set representation for three-dimensional fatigue crack growth and life predictions. *Engineering Fracture Mechanics* **77**:2840-2863.

Shingareva I, Celaya CL (2007) On frequency–amplitude dependences for surface and internal standing waves *Journal of Computational and Applied Mathematics* **200**:459-470.

Shobeyri G, Yourdkhani M (2017) A new meshless approach in simulating free surface flows using continuous MLS shape functions and Voronoi diagram *Engineering Computations* **34**:2565-2581.

Shojaei A, Boroomand B, Mossaiby F (2015) A simple meshless method for challenging engineering problems *Engineering Computations* **32**:1567-1600.

Shojaei A, Mossaiby F, Zaccariotto M, Galvanetto U (2018) An adaptive multi-grid peridynamic method for dynamic fracture analysis *International Journal of Mechanical Sciences* **144**:600-617.

Shojaei A, Mudric T, Zaccariotto M, Galvanetto U (2016) A coupled meshless finite point/Peridynamic method for 2D dynamic fracture analysis *International Journal of Mechanical Sciences* **119**:419-431.

Shojaei A, Zaccariotto M, Galvanetto U (2017) Coupling of 2D discretized Peridynamics with a meshless method based on classical elasticity using switching of nodal behaviour *Engineering Computations* **34**:1334-1366.

Silling SA (2000) Reformulation of elasticity theory for discontinuities and long-range forces *Journal of the Mechanics and Physics of Solids* **48**:175-209.

Silling SA, Askari A (2014) Peridynamic model for fatigue cracking. Report, SAND2014-18590, Albuquerque (NM, United States): Sandia National Laboratories (SNL-NM).

Silling SA, Askari E (2005a) A meshfree method based on the peridynamic model of solid mechanics *Computers & Structures* **83**:1526–1535.

Silling SA, Askari E (2005b) A meshfree method based on the peridynamic model of solid mechanics *Computers & Structures* **83**:1526-1535.

Silling SA, Epton M, Weckner O, Xu J, Askari E (2007) Peridynamic States and Constitutive Modeling *Journal of Elasticity* **88**:151-184.

Suzuki Y, Koshizuka S, Oka Y (2007) Hamiltonian moving-particle semi-implicit (HMPS) method for incompressible fluid flows *Computer Methods in Applied Mechanics and Engineering* **196**:2876–2894.

Tang SB, Zhang H, Tang CA, Liu HY (2016) Numerical model for the cracking behavior of heterogeneous brittle solids subjected to thermal shock *International Journal of Solids and Structures* **80**:520-531.

Tarasovs S, Ghassemi A (2014) Self-similarity and scaling of thermal shock fractures *Physical Review E* **90**:012403.

Underwood P (1983) Dynamic relaxation *Computational Methods for Transient* **1**

Wang Y, Zhou X, Kou M (2018a) A coupled thermo-mechanical bond-based peridynamics for simulating thermal cracking in rocks *International Journal of Fracture* **211**:13-42.

Wang Y, Zhou X, Kou M (2018b) Peridynamic investigation on thermal fracturing behavior of ceramic nuclear fuel pellets under power cycles *Ceramics International* **44**:11512-11542.

Wildman RA, O'Grady JT, Gazonas GA (2017) A hybrid multiscale finite element/peridynamics method *International Journal of Fracture* **207**:41-53.

Wu CH, Faltinsen OM, Chen BF (2015) Time-Independent Finite Difference and Ghost Cell Method to Study Sloshing Liquid in 2D and 3D Tanks with Internal Structures *Communications in Computational Physics* **13**:780-800.

Wu GX, Taylor RE (1994) Finite element analysis of two dimensional non-linear transient water waves *Applied Ocean Research* **16**:363–372.

Wu N-J, Hsiao S-C, Wu H-L (2016) Mesh-free simulation of liquid sloshing subjected to harmonic excitations *Engineering Analysis with Boundary Elements* **64**:90-100.

Wu N, Chang K (2011) Simulation of free-surface waves in liquid sloshing using a domain-type meshless method *International Journal for Numerical Methods in Fluids* **67**:269–288.

Xu J, Askari A, Weckner O, Silling S (2008) Peridynamic analysis of impact damage in composite laminates *Journal of Aerospace Engineering* **21**:187-194.

Xu Z, Zhang G, Chen Z, Bobaru F (2018) Elastic vortices and thermally-driven cracks in brittle materials with peridynamics *International Journal of Fracture* **209**:203-222.

Yu K, Xin XJ, Lease KB (2011) A new adaptive integration method for the peridynamic theory *Modelling and Simulation in Materials Science and Engineering* **19**:045003.

Zaccariotto M, Luongo F, Sarego G, Galvanetto U (2015a) Examples of applications of the peridynamic theory to the solution of static equilibrium problems *The Aeronautical Journal* **119**:677-700.

Zaccariotto M, Mudric T, Tomasi D, Shojaei A, Galvanetto U (2018) Coupling of FEM meshes with Peridynamic grids *Computer Methods in Applied Mechanics and Engineering* **330**:471-497.

Zaccariotto M, Sarego G, Dipasquale D, Galvanetto U (2015b) Strategies for fatigue damage modeling with peridynamics. 8th International Congress of Croatian Society of Mechanics, Opatija, Croatia.

Zaccariotto M, Tomasi D, Galvanetto U (2017) An enhanced coupling of PD grids to FE meshes *Mechanics Research Communications* **84**:125-135.

Zamani A, Eslami MR (2010) Implementation of the extended finite element method for dynamic thermoelastic fracture initiation *International Journal of Solids and Structures* **47**:1392-1404.

Zandi SM, Boroomand B, Soghrati S (2012) Exponential basis functions in solution of incompressible fluid problems with moving free surfaces *Journal of Computational Physics* **23**:505–527.

Zandi SM, Rafizadeh A, Shanehsazzadeh A (2017) Numerical simulation of non-breaking solitary wave run-up using exponential basis functions *Environmental Fluid Mechanics* **17**:1-20.

Zhang C, Li Y, Meng Q (2015) Fully nonlinear analysis of second-order sloshing resonance in a three-dimensional tank *Computers & Fluids* **116**:88-104.

Zhang G, Bobaru F (2016) Modeling the evolution of fatigue failure with peridynamics *Romanian Journal of Technical Sciences - Applied Mechanics,* **61**:22-40.

Zhang G, Le Q, Loghin A, Subramaniyan A, Bobaru F (2016a) Validation of a peridynamic model for fatigue cracking *Engineering Fracture Mechanics* **162**:76-94.

Zhang T, Ren YF, Fan CM, Li PW (2016b) Simulation of two-dimensional sloshing phenomenon by generalized finite difference method *Engineering Analysis with Boundary Elements* **63**:82-91.

Zhang T, Yu-Fei R, Zhi-Qiang Y, Chia-Ming F, Po-Wei L (2016c) Application of generalized finite difference method to propagation of nonlinear water waves in numerical wave flume *Ocean Engineering* **123**:278-290.

Zienkiewicz OC, Taylor RL (2000) vol 3. Butterworth-Heineman, JordanHill, Oxford, UK.